

TOKYO METROPOLITAN UNIVERSITY

DOCTORAL THESIS

**Investigation of Diffuse X-ray
Emission from the Massive
Star-Forming Region RCW 38**

Author:

Aoto FUKUSHIMA

Supervisor:

Dr. Yuichiro EZOE

*A thesis submitted in fulfillment of the requirements
for the degree of Doctor of Philosophy*

in the

**Experimental Astrophysics Laboratory
Department of Physics**

February 17, 2023

Abstract

Massive stars are known to have a great impact on surrounding environments through their powerful ultraviolet radiation, fast stellar winds, and supernova explosions. In the 2000s, diffuse X-ray emission was revealed in some massive star-forming regions (MSFRs). It is expected to provide clues to probe the physical properties of the environments around young massive stars hidden in dense, giant molecular clouds. However, many aspects of diffuse emission, such as the origins and the determinants of the emission mechanism, still need to be better understood. We have studied the nearby young MSFR RCW 38. A previous study suggested hard diffuse X-ray emission from *Chandra* observation. We observed the same region with the *Suzaku* satellite which has a low background and is highly sensitive to spatially extended emission. To detect and consider point source contributions, we also used *Chandra* data. We divided the area according to the radius from the cluster center and analyzed the X-ray spectra. In the inner region ($r < 2'.0$), the non-thermal emission (power law with a photon index of ~ 2) was suggested, although a two-temperature thermal plasma model (~ 0.9 and ~ 5 keV) could not be rejected. In the outer region ($r = 2'.0$ – $5'.5$), the two-temperature thermal plasma model was favorable. The observed high-temperature components in RCW 38 are hotter than other MSFRs observed with *Suzaku*. By comparing the diffuse X-ray properties associated with multiple MSFRs, we confirmed that the observed temperature and brightness have a positive correlation with the density of the surrounding interstellar medium (ISM). That supports that the surrounding ISM determines the hardness of the diffuse emission. In RCW 38, it is suggested that stellar winds or supernova remnants of massive stars collide with the dense ISM, which converts kinetic energy into extremely hot plasmas and/or non-thermal particles. These insights provide important clues for advancing a unified understanding of the diffuse X-ray emission of MSFRs.

Contents

Abstract	iii
1 Introduction	1
2 Review	5
2.1 Star formation	5
2.1.1 Interstellar medium (ISM)	5
2.1.2 Star-forming processes	14
2.2 Stellar evolution and types	21
2.2.1 Stellar classification	21
2.2.2 Evolution processes	23
2.3 X-ray emission from astronomical objects	27
2.3.1 Absorption	27
2.3.2 Non-thermal emission	29
2.3.3 Thermal emission	33
2.3.4 X-rays from various stars	36
2.3.5 Diffuse X-rays from massive star-forming regions (MSFRs)	42
3 Instrumentation	45
3.1 <i>Chandra</i>	45
3.1.1 High Resolution Mirror Assembly (HRMA)	46
3.1.2 Advanced CCD Imaging Spectrometer (ACIS)	46
3.2 <i>Suzaku</i>	49
3.2.1 X-Ray Telescope (XRT)	52
3.2.2 X-ray Imaging Spectrometer (XIS)	54
4 Observations of MSFRs	59
4.1 Past reports of diffuse X-ray emission	59
4.1.1 Evidenced for thermal emission	59
4.1.2 Possibility of non-thermal origins	66

4.2	RCW 38	71
4.2.1	Basic properties and previous results	72
4.2.2	Motivations	77
4.2.3	Observations	79
5	Data analysis and results	87
5.1	Background estimation	87
5.1.1	Non-X-ray background (NXB)	87
5.1.2	Astrophysical foreground and backgrounds	88
5.2	<i>Chandra</i> spectra of point sources	92
5.2.1	Definition of extraction regions	92
5.2.2	Spectral fitting to X-ray point sources	93
5.3	Spectral analysis of diffuse X-ray emission with <i>Suzaku</i>	101
5.3.1	Background and point-source contributions	101
5.3.2	Spectral fitting in the inner region	107
5.3.3	Spectral fitting in the outer region	109
6	Discussion	117
6.1	Brief summary of obtained results	117
6.2	Contamination to diffuse components	117
6.2.1	Estimation of faint point source contribution	118
6.2.2	Possible uncertainties	118
6.3	Emission components	126
6.4	Comparison with previous non-thermal model	132
6.5	Thermal scenario	133
6.5.1	Thermal plasmas and energetics	133
6.5.2	Comparison with other MSFRs	134
7	Conclusion	139
	Acknowledgements	141
	Bibliography	143

List of Figures

2.1	Absolute temperature versus number density in various phases of ISM. The dashed line shows a constant pressure line.	6
2.2	Optical image of the Orion Nebula captured by the Hubble Space Telescope. The arrow shows the position of the Orion Trapezium Cluster. Credit: NASA, ESA, M. Robberto (STScI/ESA) and the Hubble Space Telescope Orion Treasury Project Team (STScI)	7
2.3	The reflection nebulae M 78 (NGC 2068) and NGC 2071 captured by the Wide Field Imager camera on the MPG/ESO 2.2 m telescope at the La Silla Observatory. A dark nebula is visualized on the right of M 78. Credit: ESO/Igor Chekalin	10
2.4	(top) Velocity-integrated CO map of the Galaxy. (bottom) Longitude-velocity map of CO emission integrated over a strip $\sim 4^\circ$ wide in latitude centered on the Galactic plane. Both are taken from Dame, Hartmann, and Thaddeus (2001).	11
2.5	The distribution in the Galactic plane of molecular clouds within 1 kpc of the Sun. The circle radii are proportional to the cube roots of the cloud masses and in most cases are close to the clouds' actual radii. Taken from Dame et al. (1987).	12
2.6	Stellar initial mass functions, mass fraction per logarithmic mass bin versus mass, summarized by Baldry and Glazebrook (2003). The integral of each curve is set to unity.	15
2.7	Classification scheme of young stellar objects and their spectra and views at each class, taken from Zhang (2018).	16
2.8	Accretion rate versus core mass, taken from Wolfire and Cassinelli (1987). The corresponding equivalent support temperature is shown on the right side. Each line indicates the limit of possible stellar mass at a given accretion rate.	20
2.9	The main spectral classes of stars according to the Harvard classification. Credit: University of Oregon Physics Department	22

2.10	Schematic HR diagram. Credit: ESO	24
2.11	Observed distribution of low- and intermediate-mass pre-main-sequence stars in the HR diagram (Palla and Stahler, 1993).	25
2.12	The absorption or scattering cross-section in the 0.125 eV to 10 keV, taken from Ryter (1996).	28
2.13	The geometry of an electron moving past an ion of charge Ze with a velocity of v	29
2.14	Spiral motion of an electron in a uniform magnetic field B	31
2.15	The geometries of an electron receiving energy from a photon in the observer's frame (left) and in the electron-rest frame (right). . .	32
2.16	Simplified level scheme for helium-like ions, taken from Porquet et al. (2001).	36
2.17	Contour map ($1^\circ \times 1^\circ$) of the Orion Nebula observed by <i>Einstein</i> (Ku and Chanan, 1979).	43
3.1	Schematic view of the <i>Chandra</i> X-ray observatory. Credit: NASA . .	45
3.2	(top) Photograph of the High Resolution Mirror Assembly (HRMA). Credit: NASA/CXC/SAO. (bottom) Schematic view of the HRMA, taken from The <i>Chandra</i> Proposers' Observatory Guide.	48
3.3	On-axis effective area versus energy of the HRMA, HRMA/Advanced CCD Imaging Spectrometer (ACIS), and HRMA/High Resolution Camera (HRC), taken from The <i>Chandra</i> Proposers' Observatory Guide.	49
3.4	Photograph of the ACIS. Credit: NASA/CXC/SAO.	50
3.5	ACIS pre-launch energy resolution versus X-ray energy for the front-illuminated (FI) and back-illuminated (BI) CCDs, taken from The <i>Chandra</i> Proposers' Observatory Guide.	50
3.6	(top) Schematic view of the X-ray observatory <i>Suzaku</i> . (bottom) Side view of <i>Suzaku</i> with the internal structures after deployment of the extensible optical bench. Both are taken from Mitsuda et al. (2007).	51
3.7	Background rates of detectors onboard X-ray astronomy satellites as a function of energy (Mitsuda et al., 2007). The rate is normalized with the effective area and the field of view (FOV).	52
3.8	Photograph of <i>Suzaku</i> 's X-Ray Telescope (XRT). Credit: NASA/GSFC	54

3.9	Image and point spread function of four XRT modules taken from Serlemitsos et al. (2007). All images are binned with 2×2 pixels, followed by smoothing with a Gaussian profile with $\sigma = 3$ pixels, where the pixel size is $24 \mu\text{m}$	55
3.10	Vignetting curves of the four XRTs using the Crab Nebula taken during 2005 August 22–27 (Serlemitsos et al., 2007). The model curves were calculated with a ray-tracing simulator.	55
3.11	Photograph of the four X-ray Imaging Spectrometer (XIS) before installation onto <i>Suzaku</i> . Credit: NASA/GSFC	56
3.12	Effective area of one XRT + XIS system, for both the FI and BI CCDs (Mitsuda et al., 2007).	56
4.1	(a) The JHK _s three color near-infrared (NIR) image of the central region ($23' \times 25'$) of M 17 from the Two Micron All Sky Survey. (b) Adaptively smoothed X-ray image of M 17, taken from the ACIS-I detector ($17' \times 17'$). Two colors correspond to 0.5–2 keV (red) and 2–8 keV (blue). Both images are derived from Townsley et al. (2003).	61
4.2	ACIS spectra of (a) soft diffuse emission and (b) point sources in M 17, taken from Townsley et al. (2003).	62
4.3	Adaptively binned XIS images of M 17 in the (a) 0.5–1.5 keV and (b) 1.5–5 keV bands, taken from Hyodo et al. (2008).	63
4.4	Adaptively smoothed three-color X-ray image of the Carina Nebula (Townsley et al., 2011a). The names of white-labeled objects indicate major massive stellar clusters, massive O/Wolf-Rayet (WR) stars, and the middle-age neutron star. The three green boxes show the FOV of the <i>Suzaku</i> XIS observations. Taken from Ezoe et al. (2019).	64
4.5	XIS spectra from the north (black) and south (red) of η Carinae, taken from Hamaguchi et al. (2007). The intensities are normalized. The above labels show detected emission lines.	66
4.6	Adaptively smoothed ACIS-I images of NGC 6334 in the (a) 0.5–2 keV and (b) 2–8 keV bands, taken from Ezoe et al. (2006b).	67
4.7	ACIS spectra of the diffuse component (circles) and summed point sources (crosses) in NGC 6334 (Ezoe et al., 2006b).	67
4.8	Examples of ACIS spectra of the diffuse component in (a) soft and (b) hard X-ray regions of NGC 6334 (Ezoe et al., 2006b).	68

4.9	(a) The JHK _s three color NIR image ($\sim 16' \times 16'$) of RCW 49 centered on its ionizing cluster Westerlund 2. (b) Adaptively smoothed X-ray image of RCW 49, taken from the ACIS-I detector ($17' \times 17'$).	70
4.10	ACIS spectra of the diffuse emission in RCW 49 (Townesley et al., 2005).	70
4.11	Observations of RCW 38 at various wavelengths (Wolk et al., 2008). (a) An optical image, (b) Mid-infrared (MIR) image, (c) A close-up NIR image, and (d) 6 cm radio continuum contours.	73
4.12	Extended X-ray contours overlaid on a K _s -band image of RCW 38, taken from Wolk et al. (2002). The image is $\sim 2.5'$ (~ 1.25 pc) on a side. O5.5 binary IRS 2 is centered on the contours.	74
4.13	(top) X-ray spectrum of the O star IRS 2. An absorbed thermal bremsstrahlung model is fitted to the data. (bottom) X-ray spectrum of the diffuse emission in RCW 38. The data are fitted to an absorbed power law with a small thermal component (solid line). Taken from Wolk et al. (2002).	75
4.14	X-ray spectra of the diffuse emission from four subregions of RCW 38, taken from Wolk et al. (2002).	76
4.15	Position plots of (a) RCW 38 cluster members and (b) nonmembers, taken from Wolk et al. (2006).	78
4.16	<i>Suzaku</i> XIS 0 + 3 image of RCW 38 in (a) 0.2–2 keV and (b) 2–10 keV. The two far-end corners of the ⁵⁵ Fe calibration sources are removed. The circles correspond to the regions with a radius of $2.0'$ and $5.5'$, respectively. The green dashed regions correspond to the <i>Chandra</i> ACIS-I FOV.	82
4.17	<i>Chandra</i> ACIS-I image of RCW 38. The image is smoothed by a Gaussian function with $\sigma = 2$ pixel. The circles are the same as in figure 4.16. The ellipse is the background region used in point-source spectral analysis.	83
4.18	Light curve of the <i>Chandra</i> RCW 38 observation. The dotted line shows the mean count rate. The blue points represent outliers more than 5σ from the mean value.	84
4.19	<i>Suzaku</i> XIS 0 + 3 image of the background region (RX J0852.0-4622 NW offset) in 0.2–10 keV. It is smoothed by a Gaussian function with $\sigma = 5$ pixel.	85

5.1	<i>Suzaku</i> XIS (a) FI and (b) BI spectra of RX J0852.0-4622 NW offset (black). The red spectra show NXB contribution, estimated from the night Earth observations.	89
5.2	<i>Suzaku</i> XIS spectra of the RX J0852.0-4622 NW offset. The NXB is subtracted. The solid lines and data correspond with XIS 0 (black), XIS 1 (red), XIS 2 (green), and XIS 3 (blue). For astrophysical foreground/backgrounds, we assumed local hot bubble (LHB, dotted light blue lines), transabsorption emission (TAE, dotted magenta lines), and cosmic X-ray background (CXB, dotted orange lines).	91
5.3	<i>Chandra</i> ACIS-I images of (a) the whole emission region and (b) a close-up view of the inner region. The images are smoothed by a Gaussian function with $\sigma = 2$ pixel. The cyan ellipses and circles show point source regions. The blue ellipse shows IRS 2.	94
5.4	<i>Chandra</i> ACIS-I spectra from the point sources in the (a) inner and (b) outer regions of RCW 38 (black). The red spectra show the background contribution extracted from the starless region	95
5.5	Background-subtracted <i>Chandra</i> ACIS-I spectra of point sources in the (a) inner and (b) outer regions of RCW 38. The blue and red dotted lines indicate low- and high-temperature thermal plasma models, respectively.	97
5.6	Histogram of absorption N_{H} derived through spectral fits of (a) the 209 bright cluster members and (b) the 157 faint cluster members within the RCW 38 ACIS-I observation (Wolk et al., 2006).	99
5.7	Histogram of plasma temperature kT for each cluster member, taken from Wolk et al. (2006).	100
5.8	X-ray point source density profile of the RCW 38 cluster member as a function of distance from the cluster center (Wolk et al., 2006).	100
5.9	<i>Suzaku</i> XIS (a) FI and (b) BI spectra from the inner region of RCW 38 (black). The red spectra show NXB contribution, estimated from the night Earth observations.	102
5.10	Same as figure 5.9 but for the outer region.	103
5.11	<i>Suzaku</i> XIS spectra of the (a) inner and (b) outer regions of RCW 38. The NXBs are subtracted. The orange lines indicate the best-fit models of foreground/background emission. The green and magenta lines indicate the contributions of point source emission from the inner and outer regions, respectively.	105

5.12	<i>Suzaku</i> XIS 0 + 3 images of the simulated point sources from the (a) inner and (b) outer regions of RCW 38. The exposure time was assumed to be 10,000 ks for photon statistics. The circles are the same as in figure 4.16.	106
5.13	<i>Suzaku</i> XIS spectra of the (a) inner and (b) outer regions of RCW 38. The NXBs are subtracted. Absorbed power law and thermal plasma models were assumed for the diffuse emission.	113
5.14	Same as figure 5.13 but a two-temperature absorbed thermal plasma model was assumed for the diffuse emission.	115
6.1	X-ray luminosity function of RCW 38, taken from Wolk et al. (2006). The solid line shows the 365 detected cluster members within the ACIS-I FOV. The dotted line shows the expected full distribution of X-ray luminosities assuming a lognormal distribution (after Feigelson et al., 2005).	119
6.2	Same as figure 5.13 but the point source contributions are scaled by a factor of 0.8 for the best-fitting model.	123
6.3	Same as figure 5.14 but the point source contributions are scaled by a factor of 0.8 for the best-fitting model.	125
6.4	Same as figure 5.13 but the point source contributions are scaled by a factor of 1.45 for the best-fitting model.	129
6.5	Same as figure 5.14 but the point source contributions are scaled by a factor of 1.45 for the best-fitting model.	131
6.6	(a) Very Large Telescope image of RCW 38 (from Wolk et al., 2006) and the morphology of the molecular clouds derived from Fukui et al. (2016). (b) <i>Chandra</i> RCW 38 image smoothed with the <code>csmooth</code> tool.	132
6.7	Unabsorbed age-corrected surface brightness versus absorption diagram for diffuse thermal plasma. The dashed lines show the prediction of $S_{\chi t^{-1/3}} \propto N_{\text{H}}^{5/3}$	137
6.8	Temperature versus absorption diagram of diffuse thermal emission. Colored and gray data indicate high- and low-temperature components, respectively. The dashed line shows the fitted model to the high-temperature components.	138

List of Tables

2.1	Properties of molecular clouds (Turner, 1988).	13
2.2	Classification of main-sequence stars and their characteristics according to the Harvard system.	22
2.3	Main-sequence massive star definition (Zinnecker and Yorke, 2007).	23
2.4	X-ray properties of young stellar objects (YSOs) and massive OB stars.	38
3.1	Overview of <i>Chandra</i> capabilities.	47
3.2	Overview of <i>Suzaku</i> capabilities (after Mitsuda et al., 2007).	53
4.1	Past reports of extended X-rays from MSFRs.	60
4.2	Log of observations.	81
5.1	Spectral fits to astrophysical foreground/backgrounds.	90
5.2	Spectral fits to X-ray point sources in RCW 38.	96
5.3	Parameters of the astrophysical foreground/background and point source emission assumed in the diffuse spectral analyses of tables 5.4 and 5.5.	111
5.4	Spectral fits to RCW 38 diffuse X-ray emission (non-thermal model).	112
5.5	Spectral fits to RCW 38 diffuse X-ray emission (thermal model).	114
6.1	Same as table 5.3 but for tables 6.2 and 6.3. Point source contributions are scaled by a factor of 0.8 for the best-fitting model.	121
6.2	Same as table 5.4 (non-thermal model) but the point source contributions are scaled by a factor of 0.8 for the best-fitting model.	122
6.3	Same as table 5.5 (thermal model) but the point source contributions are scaled by a factor of 0.8 for the best-fitting model.	124
6.4	Same as table 5.3 but for tables 6.5 and 6.6. Point source contributions are scaled by a factor of 1.45 for the best-fitting model.	127
6.5	Same as table 5.4 (non-thermal model) but the point source contributions are scaled by a factor of 1.45 for the best-fitting model.	128

6.6 Same as table 5.5 (thermal model) but the point source contributions are scaled by a factor of 1.45 for the best-fitting model. 130

List of Abbreviations

ACIS	Advanced CCD Imaging Spectrometer
ARF	Auxiliary Response File
BI	Back-Illuminated
CCD	Charge-Coupled Device
CIAO	Chandra Interactive Analysis of Observations
CXB	Cosmic X-ray Background
EM	Emission Measure
FI	Front-Illuminated
FIR	Far-InfraRed
FOV	Field Of View
HXD	Hard X-ray Detector
HR	Hertzsprung-Russell
HRC	High Resolution Camera
HRMA	High Resolution Mirror Assembly
ISM	InterStellar Medium
LHB	Local Hot Bubble
MIR	Mid-InfraRed
MSFR	Massive Star-Forming Region
NIR	Near-InfraRed
NXB	Non-X-ray Background
TAE	Trans-Absorption Emission
WR	Wolf-Rayet
XIS	X-ray Imaging Spectrometer
XRS	X-Ray Spectrometer
XRT	X-Ray Telescope
YSO	Young Stellar Object

Physical Constants

Boltzmann Constant	$k = 8.617\,333\,262 \times 10^{-5} \text{ eV K}^{-1}$ $= 1.380\,649 \times 10^{-16} \text{ erg K}^{-1}$
Constant of Gravitation	$G = 6.674\,30 \times 10^{-8} \text{ cm}^{-3} \text{ g}^{-1} \text{ s}^{-2}$
Dielectric Constant of Free Space	$\epsilon_0 = 8.854\,187\,813 \times 10^{-14} \text{ C}^2 \text{ J}^{-1} \text{ cm}^{-1}$ $= 1 \text{ esu}$
Electron Mass	$m_e = 9.109\,383\,702 \times 10^{-28} \text{ g}$
Elementary Charge	$e = 1.602\,176\,634 \times 10^{-19} \text{ C}$ $= 4.803\,204 \times 10^{-10} \text{ esu}$
Plank Constant	$h = 6.626\,070\,152 \times 10^{-27} \text{ erg s}$
Rydberg Constant	$R = 1.097\,37 \times 10^5 \text{ cm}^{-1}$
Solar Mass	$M_\odot = 1.9884 \times 10^{33} \text{ g}$
Solar Radius	$R_\odot = 6.957 \times 10^{10} \text{ cm}$
Solar Luminosity	$L_\odot = 3.828 \times 10^{33} \text{ erg s}^{-1}$
Speed of Light	$c = 2.997\,924\,58 \times 10^{10} \text{ cm s}^{-1}$ (in vacuum)
Stefan-Boltzmann Constant	$\sigma = 3.539\,164\,737\,76 \times 10^7 \text{ eV s}^{-1} \text{ cm}^{-2} \text{ K}^{-4}$ $= 5.670\,367 \times 10^{-5} \text{ ergs s}^{-1} \text{ cm}^{-2} \text{ K}^{-4}$
Total Recombination Rate	$\alpha = 3 \times 10^{-13} \text{ cm}^{-3} \text{ s}^{-1}$ (at 10^4 K)

Unit conversion

Energy	$1 \text{ J} = 1 \times 10^7 \text{ erg}$ $= 6.242 \times 10^{18} \text{ eV}$
Temperature	$1 \text{ eV} = 1.160\,45 \times 10^4 \text{ K}$
Time	$1 \text{ yr} = 3.155\,692\,5 \times 10^7 \text{ sec}$

Chapter 1

Introduction

In the universe, we can see countless stars shining. These stars form inside dense concentrations of interstellar gas and dust called molecular clouds. One trigger causes an imbalance of gravity in the interstellar molecular cloud. That causes the molecules to condense and promotes gravitational actions more and more. By repeating this, the clumps grow in size with increasing speed and evolve into stars. The mass of the initial stage largely determines the life of a star. In particular, massive stars ($>8M_{\odot}$) play the most important role in the evolution of the universe.

Massive stars synthesize elements through nuclear fusion reactions caused by their massive gravity and explode as supernovae at the end of their lives. Supernova explosions greatly impact the surrounding environment, such as scattering various elements into outer space and providing materials to create new stars. The shock waves of the explosions often promote the formation of new stars. Then, neutron stars or sometimes black holes appear after the explosions. Not only such a violent end but also high-speed stellar winds ($600\text{--}3,000\text{ km s}^{-1}$) and intense ultraviolet radiation ($10^{37}\text{--}10^{39}\text{ erg s}^{-1}$) affect surrounding stars, planets, and interstellar space throughout lifetimes.

Massive stars are thus essential astronomical objects for the thermodynamics and chemical evolution of galaxies. Despite their importance, massive stars and their formation processes and environments are less well understood than those of low-mass stars. The reasons for this are as follows: (1) massive stars evolve more quickly and important evolutionary phases are short-lived, (2) massive star-forming regions (MSFRs) are not close compared to those of low-mass stars, (3) massive stars are surrounded by dense molecular clouds throughout their lives, especially when they are young. In short, observational studies are very difficult.

Various signals come from astronomical objects: gamma rays, X-rays, ultraviolet, optical light, infrared, and radio waves as electromagnetic waves; cosmic rays, neutrinos, and gravitational waves as other energetic phenomena. In ancient times, astronomy was pioneered by observing optical light visible to the human eye. In the latter half of the 20th century, the wavelength range expanded, and astronomy developed greatly along with it.

In the 1960s, X-ray emission, the main method of this thesis, from outside the solar system was successfully detected for the first time using an observation rocket (Giacconi et al., 1962). Subsequently, the primary means changed to astronomical satellites for longer-duration observations, and it turned out that there were numerous X-ray sources in the universe. MSFRs are also one of the X-ray-emitting objects. X-rays (especially in the high-energy band) penetrate gas and dust at a higher transmittance than optical and even near-infrared (NIR) light. That means X-rays can be valuable probes for understanding massive stars and their surrounding environments.

The X-ray emission implies the existence of a high-energy phenomenon. In terms of temperature, X-rays exhibit high-temperature states of $\sim 10^6$ – 10^8 K, while the surface of the sun is $\sim 6,000$ K, mainly emitting optical light. Furthermore, X-rays themselves can become key players in the star-forming environment. For example, X-rays and extreme ultraviolet rays may heat and evaporate the exoplanetary atmosphere when planets have formed, contributing to water loss. Therefore, they may also be related to planetary habitability.

Decades of X-ray studies have shown diffuse X-ray emission as an inherent phenomenon in MSFRs. Using the *Einstein* satellite, Ku and Chanan (1979) found unexplained extended X-ray emission from the vicinity of the Orion Trapezium region. Similar emission was seen in other active MSFRs. X-rays from MSFRs were also extensively studied on subsequent satellites, such as *Tenma*, *Ginga*, *ROSAT*, and *ASCA*. With the observation accuracy at that time, it could not rule out the possibility that the extended emission was a superposition of undetected point sources. However, the *Chandra* satellite launched in 1999 had a telescope with unprecedented spatial resolution on board, which eventually showed the emission was truly diffuse.

Multiple observations of MSFRs have ensured the existence of diffuse X-ray emission associated with massive stars or their surrounding interstellar medium (ISM). However, what generates that diffuse X-ray emission? Although the most likely

origins are massive stellar winds or supernova remnants, they have not yet been settled. It is generally accepted that these high-energy phenomena heat the gas to several million K or more, producing hot plasma emitting thermal X-ray emission. Indeed, X-ray spectra from some MSFRs show emission line structures and bremsstrahlung emission that suggests hot plasma (e.g., Townsley et al., 2003). On the other hand, non-thermal diffuse X-ray emission has also been reported (e.g., Wolk et al., 2002). In the non-thermal case, 10 keV to several MeV and possibly TeV electrons should exist in the regions. Although the diffuse X-ray emission is thus expected to provide valuable clues for investigating MSFRs, we still do not have unified views on many points: whether the emission is thermal or non-thermal, what is its origin, and even relationships between basic properties of the star clusters and the nature of the emission.

We thus aim to reveal the diffuse X-ray emission in MSFRs. In particular, it is not well understood whether non-thermal diffuse X-ray emission truly exists and what produces such a hard and flat X-ray spectrum. Therefore, this thesis focuses mainly on RCW 38, a representative MSFR where previous studies have suggested non-thermal diffuse X-ray emission. The present thesis has the following structure. The basic features of MSFRs are reviewed in chapter 2. Chapter 3 describes the instrumentation utilized in our analysis. In chapter 4, we explain observations of RCW 38 and other MSFRs. Then, we present a detailed analysis of the diffuse emission of RCW 38 in chapter 5. The discussions and conclusions are given in chapters 6 and chapter 7, respectively.

Chapter 2

Review

X-ray observations of MSFRs provide a practical way to investigate massive stars and their surrounding environments, which play a key role in galaxy evolution. In this chapter, we review the formation and evolution of stars and introduce their types and the high-energy phenomena seen in MSFRs. Then, we review the information that X-rays provide us and what has been understood by X-ray observations so far, along with past results.

2.1 Star formation

2.1.1 Interstellar medium (ISM)

Not only stars but also gas and dust, called ISM, exist in the universe. ISM contains the raw materials for the formation of new stars. In the Galaxy, $\sim 90\%$ of the total mass (excluding dark matter) is stars, and $\sim 10\%$ exists as ISM. Of the ISM, $\sim 99\%$ is some form of gas, and $\sim 1\%$ is dust (Boulanger, Cox, and Jones, 2000). Its gas mass consists of $\sim 70\%$ hydrogen, $\sim 28\%$ helium, and $\sim 2\%$ heavier elements (Herbst, 1995; Ferriere, 2001). ISM exists in various densities and temperatures because of gravity and magnetic fields, in addition to heating and cooling mainly by radiation. According to its physical quantities, the ISM is classified into several phases, as shown in figure 2.1.

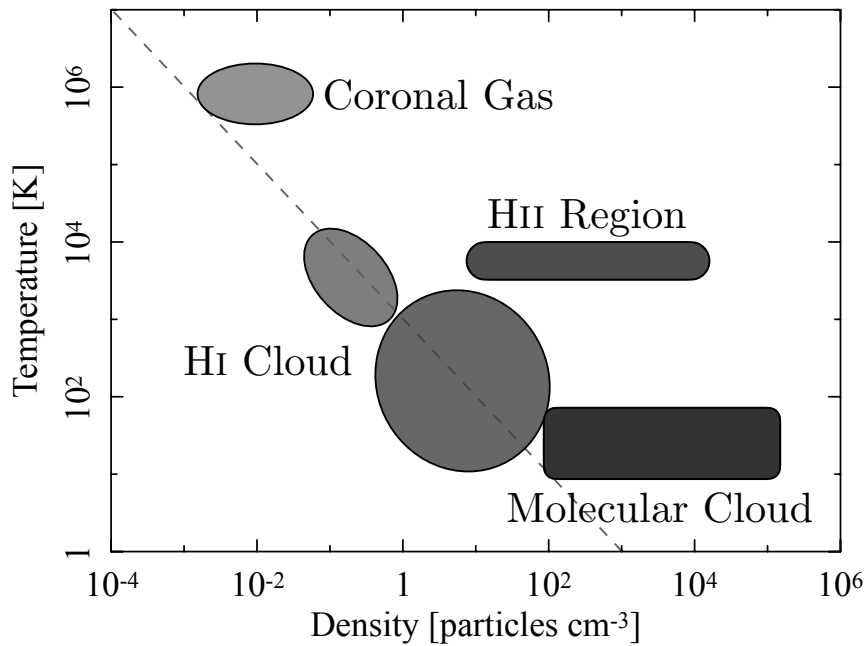


FIGURE 2.1: Absolute temperature versus number density in various phases of ISM. The dashed line shows a constant pressure line.

Coronal gas and H I clouds

The lowest-density ($\sim 10^{-2} \text{ cm}^{-3}$) phase is called coronal gas. It is an extremely high temperature ($\sim 10^6 \text{ K}$) and emits X-rays. Most hydrogen atoms are fully ionized in such hot gas. Since it is observed in supernova remnants and inside superbubbles, supernova explosions are believed to heat the gas. It is also observed inside the galactic disk and in the halo. Its volume occupancy is considered to be 20%–50%. In particular, the coronal gas occupies a large fraction of the volume in the center of the Galaxy (Williams, Mathur, and Nicastro, 2005).

H I clouds are interstellar gas clouds composed mainly of neutral atomic hydrogen gas, with densities of $\sim 10^{-2}$ – 10^2 cm^{-3} . The gas cloud has two phases: a warm neutral medium stable at $\sim 10^4 \text{ K}$ and a cold neutral medium at $\sim 10^2 \text{ K}$. They are roughly constant in pressure (proportional to temperature \times density) with each other and are quasi-equilibrium, including the coronal gas (Field, Goldsmith, and Habing, 1969). The warm neutral medium is observed by the 21 cm hyperfine-structure transition line of atomic hydrogen and the cold neutral medium by absorption lines at the same wavelength.

H II regions

H II regions are relatively stable in temperature ($\sim 6,000\text{--}10^4$ K) but have a wide range of density ($\sim 10\text{--}10^4$ cm $^{-3}$). They are composed of ionized hydrogen and surround thousands of stars. The intense ultraviolet emission from the massive stars ionizes the surrounding nebula and forms the H II region (Anderson et al., 2009). As a result, it strongly emits a H α line at a wavelength of 656.3 nm, which corresponds to red in the optical light band. Figure 2.2 shows an optical image of the Orion Nebula, one of the most nearby and representative H II regions. The central four stars “Trapezium” are ionizing the surroundings. They are main-sequence or zero-age main-sequence OB stars (θ^1 Orionis A–D). Star formation seems to be still ongoing around them (Palla and Stahler, 1999). In the end, supernova explosions and stellar winds from massive stars will disperse the surrounding gas, leaving behind only the clusters.

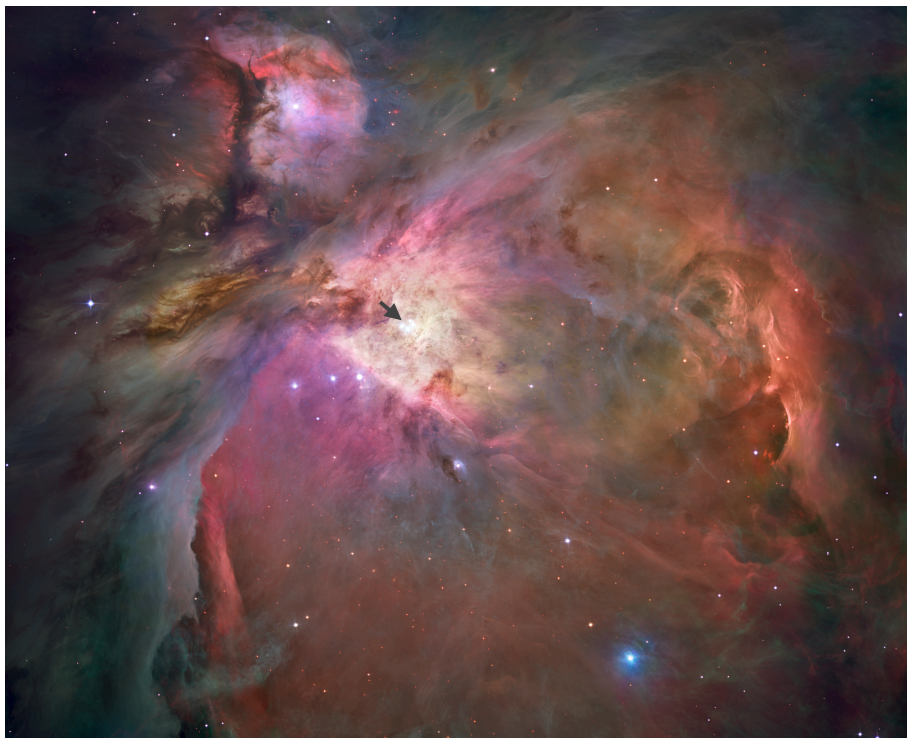


FIGURE 2.2: Optical image of the Orion Nebula captured by the Hubble Space Telescope. The arrow shows the position of the Orion Trapezium Cluster. Credit: NASA, ESA, M. Robberto (STScI/ESA) and the Hubble Space Telescope Orion Treasury Project Team (STScI)

Denser ($>10^4 \text{ cm}^{-3}$) regions are called the ultra-compact H II regions. They are strong far-infrared (FIR) sources because their warm dust converts embedded stellar luminosity into FIR emission. In the $100 \mu\text{m}$ band, they are one of the brightest objects in the Galaxy. Although 3–4 orders of magnitude weaker than this FIR emission, it emits free-free emission in the radio band, a good feature to distinguish it from other FIR sources. Radio observations achieve high spatial resolution imaging and can observe various morphologies, such as shell, cometary, bipolar, core-halo, irregular, and multi-peaks (Wood and Churchwell, 1989; Churchwell, 2002).

Precursors of H II regions are giant molecular clouds described below. Massive stars born in a giant molecular cloud form a boundary surface of ionized gas. This blows out the gas surrounding the stars at supersonic speeds. The newly ionized gas causes an ultra-compact (diameter $\lesssim 0.1 \text{ pc}$) H II region to expand and evolve into a compact ($\lesssim 0.5 \text{ pc}$) H II region and then into a more diffuse ($\sim 0.1\text{--}100 \text{ pc}$) H II region (see Habing and Israel, 1979; Kurtz, 2002; Kurtz, 2005). In large examples, super-giant H II regions exceeding 100 pc in size have been observed (e.g., NGC 604, see Yang et al., 1996).

From Spitzer (1978), the time evolution of the ionization surface radius R of an H II region is described as follows:

$$R = R_S \left(1 + \frac{7c_s t}{4R_S} \right)^{4/7}, \quad (2.1)$$

$$R_S = \left(\frac{3}{4\pi} \frac{N_u}{n_i^2 \alpha} \right)^{1/3}, \quad (2.2)$$

where R_S is the Strömgen radius (Strömgen, 2013) where the number of photoionization is equal to that of recombination, c_s is the sound speed, t is the time, N_u is the ionizing photons emitted by the star, n_i is the initial density of the ionized gas, and α is the total recombination rate of hydrogen ions in a unitary volume. These equations show that the hotter and brighter the central exciting stars, the larger the radius of the region. On the other hand, the denser the surrounding hydrogen gas, the smaller the radius. Furthermore, the dynamical age of an ultra-compact H II region can be roughly estimated from its size. For example, assuming an O7 star ($N_u = 10^{49} \text{ s}^{-1}$, $n_i = 10^5 \text{ cm}^{-3}$) as the ionizing source, it should take $\sim 2 \times 10^4 \text{ yr}$ to expand to 0.1 pc .

H II regions with star formation are found only in spiral and irregular galaxies,

not elliptical galaxies. This is because galaxy collisions form elliptical galaxies. Their giant molecular clouds and H II regions are severely agitated, leading to rapid star formation and gas starvation (Hau et al., 2008). Other than MSFRs, planetary nebulae formed by evolved low-mass stars can emit a H α line due to ionization by the central white dwarf.

Molecular clouds

Molecular clouds are the densest ($\sim 10^2\text{--}10^5\text{ cm}^{-3}$) and coldest ($\sim 10\text{--}10^2\text{ K}$). They account for only 1% of the ISM by volume. They are interstellar gas clouds in which hydrogen exists mainly in the molecular state. When there are light sources behind molecular clouds, they can become dark nebulae that cast shadows, and when they reflect the light of nearby stars, they can be visualized as reflection nebulae, as shown in figure 2.3. However, molecular hydrogen itself is symmetric, has no electric dipole, and does not emit a detectable electromagnetic signal except under extraordinary conditions, such as shock. Therefore, it is a standard method to observe rotational transition emission lines from molecules and dust mixed in the same region. The most frequently observed is the carbon monoxide line, which is thought to be the second most abundant molecule. It emits radio waves and the brightness is generally considered to be proportional to the hydrogen mass in the region.

Figure 2.4 shows the distribution of molecular clouds traced by CO ($J = 1\text{--}0$) in the Galaxy. The gas correlates with the spiral arms of the Galaxy, and most of them are found at low galactic latitudes. In particular, molecular clouds in the inner spiral arms appear as an intense ridge of emission $\sim 2^\circ$ wide in galactic latitude extending $\sim 60^\circ$ on either side of the Galactic center. The abundant molecular gas in the spiral arms suggests that molecular clouds must form and dissociate on timescales shorter than 10 million years (Williams, Blitz, and McKee, 1999). Figure 2.5 shows the distribution of molecular clouds around the Sun. These clouds orbit the Galaxy with the Sun and are well-known targets.

Molecular clouds are classified roughly into dark clouds ($\lesssim 10^4 M_\odot$) and giant molecular clouds ($\gtrsim 10^4 M_\odot$). Small molecular clouds isolated from surrounding clouds are called globules and are typically $< 10^2 M_\odot$. Table 2.1 shows the characteristics of each cloud, as summarized by Turner (1988). Dark clouds and giant molecular clouds have different features in terms of star formation. In the dark clouds, only low-mass stars with $1 M_\odot$ or less are formed, while in the giant

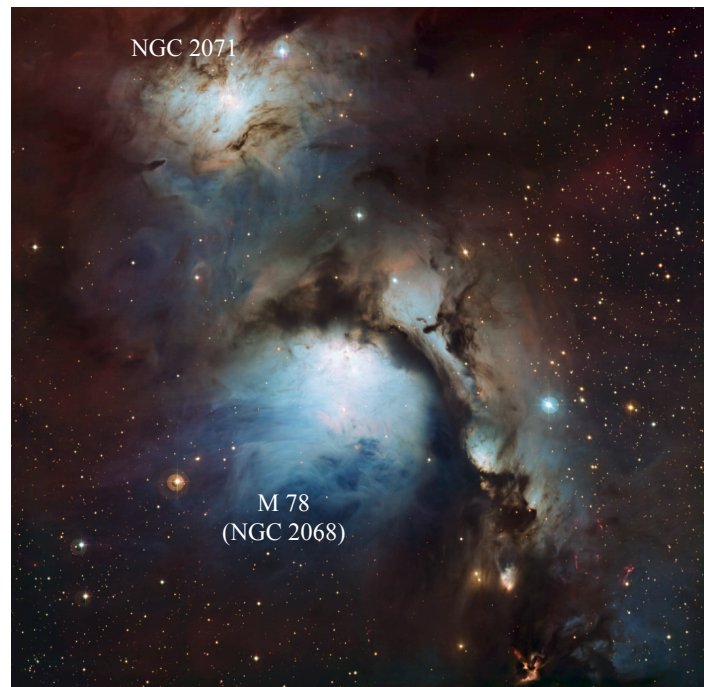


FIGURE 2.3: The reflection nebulae M 78 (NGC 2068) and NGC 2071 captured by the Wide Field Imager camera on the MPG/ESO 2.2 m telescope at the La Silla Observatory. A dark nebula is visualized on the right of M 78. Credit: ESO/Igor Chekalin

molecular clouds, intermediate-mass and massive stars with several M_{\odot} or more are also formed in addition to low-mass stars. Such intermediate-mass and massive stars ionize the surrounding gas with intense ultraviolet radiation. Therefore, MSFRs are usually accompanied by H II regions. The dense ($>10^4 \text{ cm}^{-3}$) part of the cloud is called the molecular cloud core, the direct parent body where star formation occurs.

As seen in figure 2.1, the pressure of ISMs is basically proportional to the product of density and temperature. It maintains a static state in balance with the surrounding pressure through expansion and contraction. In the molecular cloud core, however, when the concentration of matter exceeds a certain limit, self-gravity exceeds the internal pressure of the gas. As a result, the material can no longer maintain its shape and unilaterally begins to contract because of gravity. This is the initial stage of star formation. Such gravitational instability is called “Jeans instability”. In general, clouds with higher masses, smaller sizes, and cooler temperatures are more likely to induce star formation (Jeans, 1902).

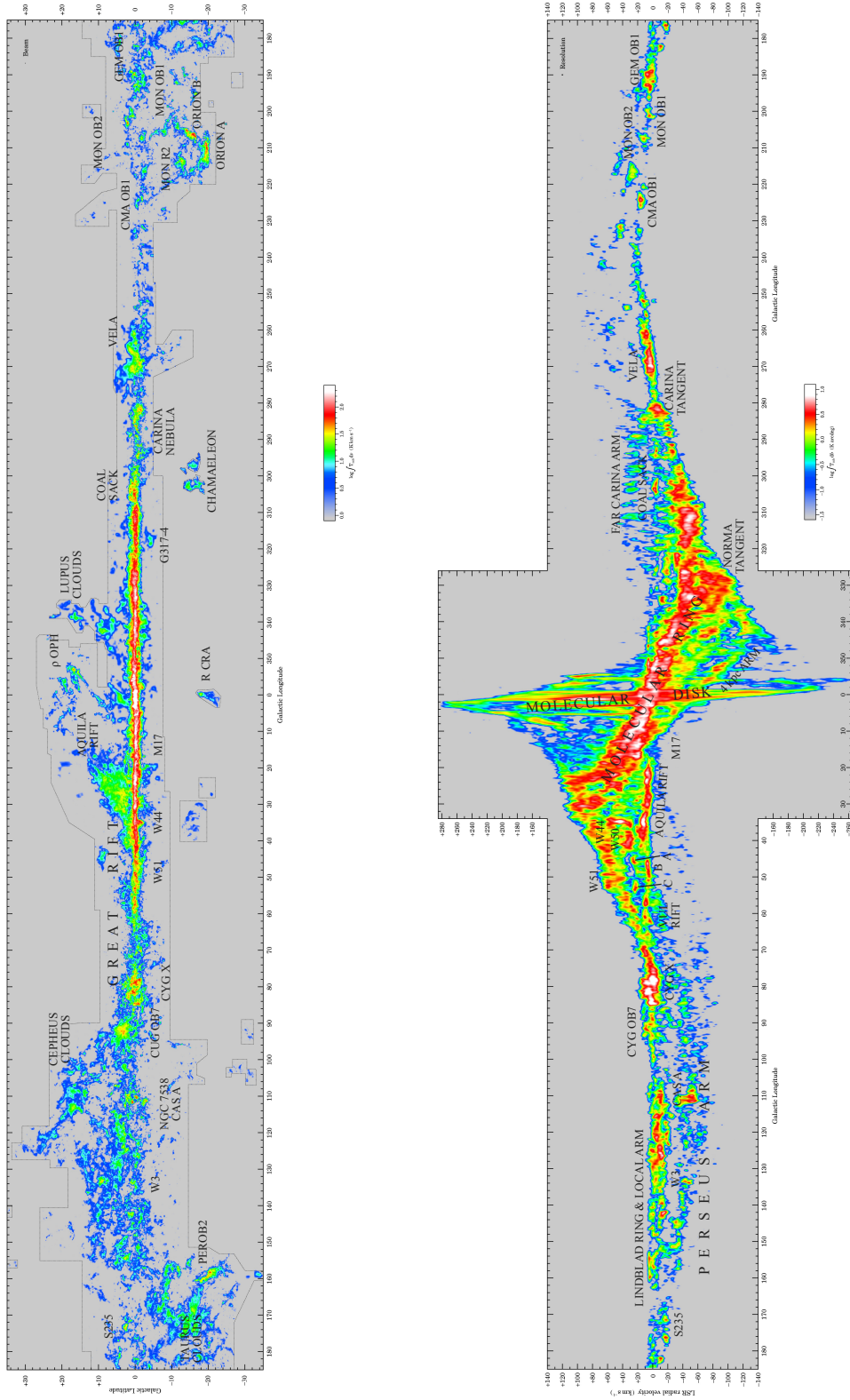


FIGURE 2.4: (top) Velocity-integrated CO map of the Galaxy. (bottom) Longitude-velocity map of CO emission integrated over a strip $\sim 4^\circ$ wide in latitude centered on the Galactic plane. The map has been smoothed in velocity to a resolution of 2 km s^{-1} and in longitude to a resolution of $12'$. Both are taken from Dame, Hartmann, and Thaddeus (2001). The molecular clouds are labeled with reference to Dame et al. (1987).

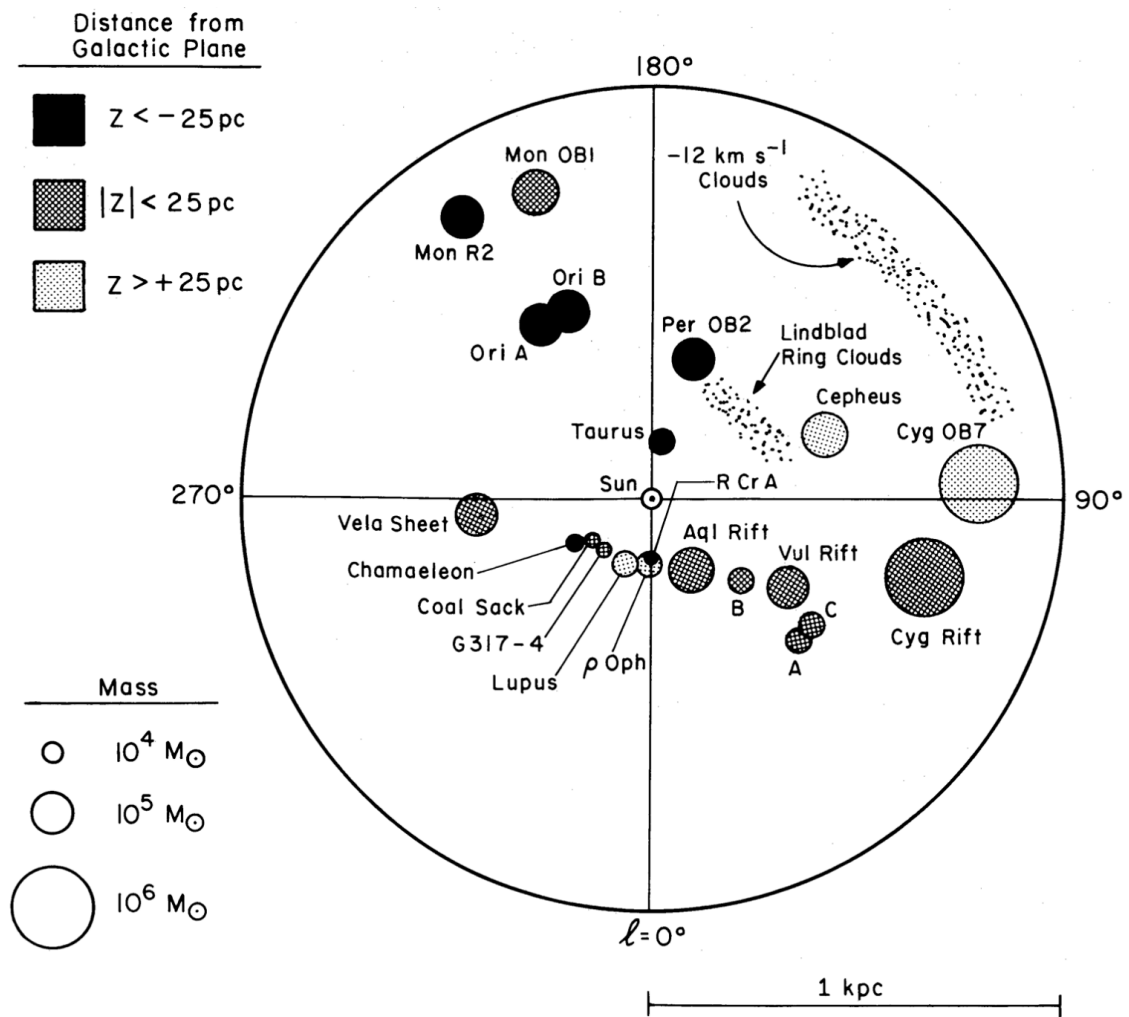


FIGURE 2.5: The distribution in the Galactic plane of molecular clouds within 1 kpc of the Sun. The circle radii are proportional to the cube roots of the cloud masses and in most cases are close to the clouds' actual radii. Taken from Dame et al. (1987).

TABLE 2.1: Properties of molecular clouds (Turner, 1988).

Property	Group A (cold)		Group B (warm)	
	Envelope	Core(s)	Envelope	Core(s)
Morphological types	Globules, Dark Clouds		Giant Molecular Clouds	
T (K)	10	10	10–20	20–100
n (cm^{-3})	10^2 – 10^3	10^4 – 10^5	10^2 – 10^3	3×10^4 – 10^6
Diameter (pc)	1–10	0.1–1	10–200	1–3
M (M_\odot)	10–1,000	1–100	10^3 – 10^5	10^2 – 5×10^3
Strong infrared?	No	No	No	Yes
Star formation?	Low-mass stars only ~ None earlier than A0		Copious low-mass stars Usually OB stars and clusters	
No. in galaxy	Globules: ~25,000 Dark Clouds: unknown		4,000	
Total mass (M_\odot)	unknown		4×10^9	
Motions (Δv)	0.5–3.0 km s^{-1} (supersonic)	0.2–0.4 km s^{-1} (subsonic)	3–15 km s^{-1} (supersonic)	

When the molecular cloud is stable, the following equation must be satisfied.

$$\frac{dP}{dr} = -G \frac{\rho M}{r^2}, \quad (2.3)$$

where P is the pressure of the gas, r is the radius of the gas sphere, G is the constant of gravitation, ρ is the density of the gas, and M is the mass of the gas inside the sphere of radius r . The mass that causes the instability is called “Jeans mass (M_J)” and is expressed by the following:

$$M_J = \left(\frac{4\pi}{3} \right) \rho \left(\frac{R_J}{2} \right)^3, \quad (2.4)$$

$$R_J = \frac{c_s}{\sqrt{G\rho}}, \quad (2.5)$$

where R_J is the Jeans length and c_s is the sound speed in the gas. Equation (2.3) collapses for perturbations of a scale larger than the R_J value. Practically, it is also necessary to consider the balance of magnetic fields and centrifugal forces due to turbulence and rotation, in addition to self-gravity and pressure. For example, a molecular cloud with a density of 10^4 cm^{-3} at 100 K would have $R_J \approx 1 \text{ pc}$ and $M_J \approx 10^3 M_\odot$.

It is also known that MSFRs have extremely dense ($>10^6 \text{ cm}^{-3}$), hot ($>100 \text{ K}$), and compact (diameter $<0.1 \text{ pc}$) cores, called hot cores (Kurtz et al., 2000; Tak, 2004). The hot cores are considered precursors to the ultra-compact H II regions (Churchwell, 2002). Namely, they are molecular gas clumps surrounding stellar clusters, including massive protostellar objects. The central stars heat the gas to such high temperatures. It is characterized by the prominent emission lines of complex organic molecules. The hot cores are often observed in the mid-infrared (MIR) band.

2.1.2 Star-forming processes

Since the 1970s, comprehension of star-forming regions has made great progress with significant improvements in radio and infrared observational technologies (see review for Evans II, 1999; Zinnecker and Yorke, 2007; Madau and Dickinson, 2014). However, they are still not fully understood, especially for massive star formation. In this subsection, we review standard star formation processes and unsolved problems, separately for low-mass and massive stars.

Low-mass stars

Low-mass stars are more common than massive stars. Salpeter (1955) showed that the number of stars in each mass range decreases rapidly as their mass increases. When $\zeta(m)\Delta m$ is defined as the number of stars with initial masses in the range m to $m + \Delta m$ within a specified volume of space, $\zeta(m)$ is called stellar initial mass function and is believed to have the following relationship:

$$\zeta(m) \propto m^{-\alpha}, \quad (2.6)$$

where α is a dimensionless exponent, originally proposed by Salpeter (1955) as $\alpha = 2.35$. The value has been modified by various other studies and found to be more complex (e.g., Miller and Scalo, 1979; Scalo, 1986; Scalo, 1998; Kroupa, 2001), as shown in figure 2.6. Note that the initial mass function here refers to the initial mass distribution when stars begin nuclear fusion, that is, when they become main-sequence stars. The number of observable massive stars is even lower than in figure 2.6 because massive stars have shorter lifetimes than low-mass stars.

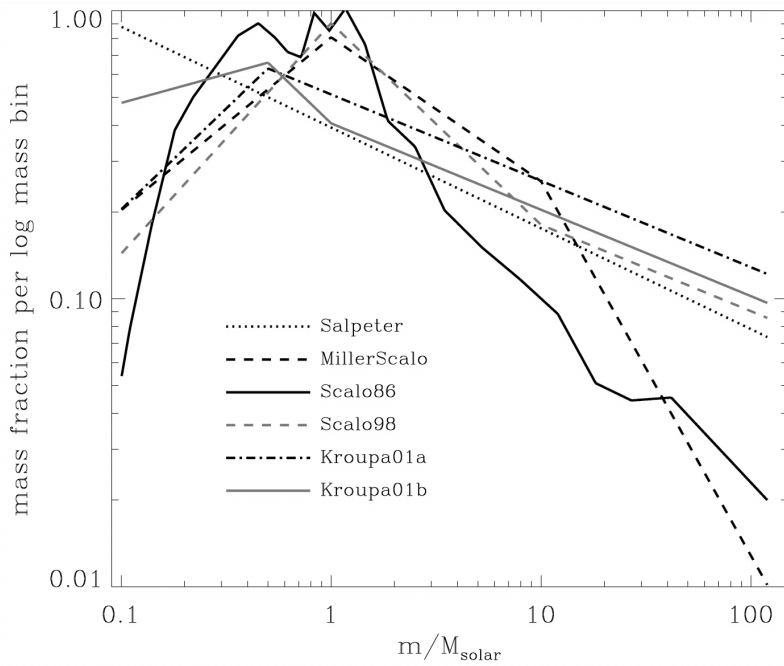


FIGURE 2.6: Stellar initial mass functions, mass fraction per logarithmic mass bin versus mass, derived from Salpeter (1955), Miller and Scalo (1979), Scalo (1986) and Scalo (1998), and Kroupa (2001), summarized by Baldry and Glazebrook (2003). The integral of each curve is set to unity.

In addition to the above numerical reason, no explosive events (e.g., massive stellar winds and supernova explosions) significantly change the environment of their parent molecular clouds in low-mass star-forming regions. Therefore, observational and theoretical studies of low-mass star-forming regions are much more advanced than those of MSFRs.

Low-mass star formation can be roughly divided into 3 phases, as shown in figure 2.7. The first step is the prestellar phase. As described in the previous subsection, a molecular cloud core that reaches the Jeans mass begins gravitational contraction. In general, the time scale of gravitational contraction is known to be the same order of magnitude as free-fall time (typically $\sim 10^6$ yr), although the force of contraction is reduced by the gas pressure. On the other hand, the total mass of molecular clouds in the Galaxy is estimated to be $M_{\text{H}_2} = 10^9 M_{\odot}$ from CO line observations. Consequently, the rate of star formation in the Galaxy is considered to be

$$\frac{M_{\text{H}_2}}{t_{\text{ff}}} \sim \frac{10^9 M_{\odot}}{10^6 \text{ yr}} = 10^3 M_{\odot} \text{ yr}^{-1}. \quad (2.7)$$

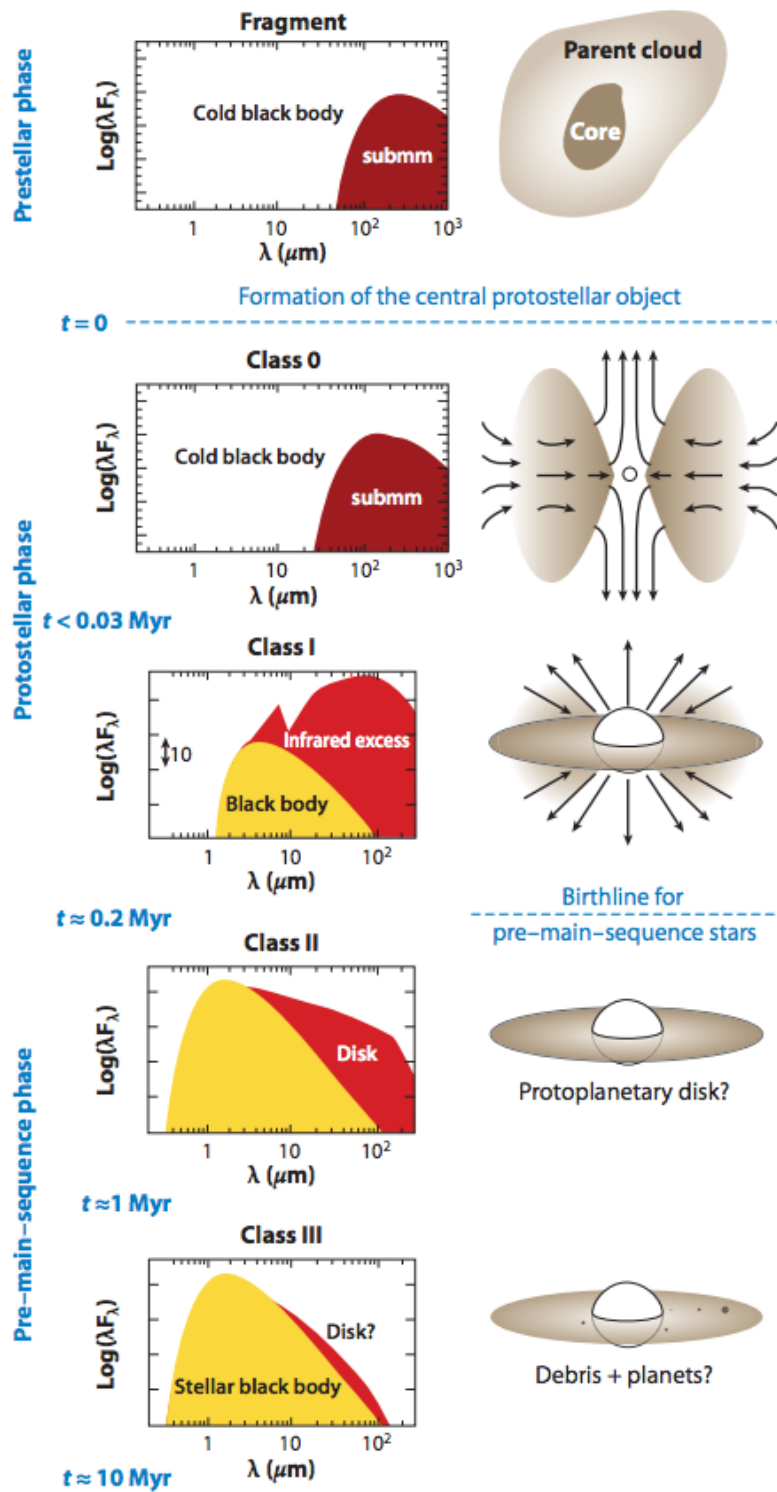


FIGURE 2.7: Classification scheme of young stellar objects and their spectra and views at each class, taken from Zhang (2018).

However, the star formation rate suggested by various observations is $\sim 3M_{\odot} \text{ yr}^{-1}$, which is different from the equation (2.7) by more than two orders of magnitude (Heyer and Dame, 2015; Licquia and Newman, 2015). The reason for this is unknown. The free-fall time may be up to two orders of magnitude larger than expected.

The second step of low-mass star formation is the protostellar phase. As gravitational contraction proceeds and the central density exceeds 10^{11} cm^{-3} , heat caused by the compression cannot escape into interstellar space. As a result, the gas temperatures rise drastically, and protostars are born. Protostars are the earliest stage of young stellar objects (YSOs). As shown in figure 2.7, YSOs are classified into four groups (class 0, I, II, and III) according to their infrared spectrum (Lada and Wilking, 1984; Andre, Ward-Thompson, and Barsony, 1993; Greene et al., 1994). This classification represents the evolutionary path of stars, with the higher number corresponding to older YSOs.

The protostellar phase corresponds to class 0 and class I, where gas accretes from disks that form around the protostars and significantly increase their mass. In class 0, protostellar masses are less than the envelopes. In class I, the masses exceed the envelopes and are considered the main accretion phase. The time scale of accretion duration is $\tau_{\text{acc}} \sim 10^5\text{--}10^6 \text{ yr}$ (Larson, 2003). The typical size of a protostellar core is several R_{\odot} . The accreting gas collides with the protostellar surfaces and forms shock waves. The temperatures of the shock fronts are estimated to reach $\sim 10^4 \text{ K}$ and should emit ultraviolet and optical light. However, they are not directly observable since they are deeply embedded in molecular clouds. Instead, the emission absorbed by interstellar dust is re-emitted in the infrared band. Since the core temperatures of protostars after mass accretion are $\sim 10^6 \text{ K}$, more than one order of magnitude is still required for nuclear fusion reactions.

The third step of low-mass star formation is the pre-main-sequence phase. The protostars, whose mass accretion has been stopped, continue to contract and release gravitational energy. This contraction process proceeds while maintaining a state of mechanical equilibrium. YSOs in this stage are called T-Tauri stars. In terms of spectral classification, they correspond to class II and class III (figure 2.7). The accretion disks gradually disappear as the T-Tauri stars evolve. T-Tauri stars that still have optically thick disks are called Classical T-Tauri stars, and those without them are called Weak T-Tauri stars. During this phase, nuclear fusions are initiated, resulting in sudden releases of energy that blow away much of what

remains of the envelopes and molecular cloud cores. Captured dust and gas form relatively small objects such as planets and comets as remnants of the disks and remain in orbit around the newly born main-sequence stars.

The time scale required for T-Tauri stars to evolve into main-sequence stars can be estimated by dividing their gravitational energy $U_G = GM^2/R$ by their luminosity $L = 4\pi R^2\sigma T^4$, where M is the mass of the central star, R is the radius of the star, σ is the Stephan-Boltzman constant, and T is the surface temperature of the star. This is called "Kelvin-Helmholtz" time scale and is expressed as

$$\tau_{\text{KH}} = \frac{U_G}{L} \simeq \frac{GM^2}{4\pi R^3\sigma T^4}. \quad (2.8)$$

In the case of the Sun, the time scale is estimated to be $\tau_{\text{KH}} \sim 10^7$ yr.

When the radius of the star contracts to $\sim R_\odot$, the core temperature rises to $\sim 10^7$ K and hydrogen burning finally begins. After this, the contraction stops, and the size of the star is kept almost constant for a long time since nuclear reaction energy maintains the pressure. That is the main-sequence phase, during which the hydrogen-burning nuclear reaction continues stably. The lifetime of the main-sequence phase is already determined by the initial mass. In the case of the Sun, its lifetime is $\sim 10^{10}$ yr (Goldsmith, 2001).

Massive stars

As for the low-mass star formation, the astronomical objects corresponding to each evolutionary stage of the standard scenario have been identified and established by observation. The same scenario can apply to intermediate-mass stars ($\sim 2\text{--}10M_\odot$), although there is less observational evidence. However, if the same accretionary evolution simply continued for a long time, the following difficulties would arise when considering massive star formation.

Lifetime

When protostars evolve into main-sequence stars through mass accretion, the relationship between accretion time τ_{acc} and Kelvin-Helmholtz time τ_{KH} is closely related to the determination of stellar mass. For low-mass stars, the relationship $\tau_{\text{acc}} < \tau_{\text{KH}}$ allows them to accrete enough mass before they evolve into main-sequence stars. On the other hand, massive accretion reverses the above relationship and thus $\tau_{\text{acc}} > \tau_{\text{KH}}$. That means

that mass accretion continues even after evolution to a main-sequence star. Here, a lifetime of a massive star is typically $\sim 10^6$ yr. Therefore, even if the accretion continues at a typical mass accretion rate of low-mass stars ($\sim 10^{-5} M_{\odot} \text{ yr}^{-1}$), the mass can only be increased to $\sim 30\text{--}40 M_{\odot}$ at most. Therefore, that cannot account for observed stars with higher mass. This limit is shown as line B in figure 2.8.

Feedback

After massive central stars evolve into main-sequence stars, they give intense radiation to surrounding accretion materials. This radiation is absorbed by dust and re-emitted, providing momentum in the outward direction. In order to continue accretion against this, an inward momentum of the accretion flow must exceed the outward momentum. Line C in figure 2.8 is the limit when free fall is assumed as the velocity of the accretion flow. In addition, massive stars expand H II regions to cover entire outer layers. Thus, the gas is heated to $\sim 10^4$ K and gravitationally unbound, which stops mass accretion. This limit is shown as line A in figure 2.8.

Eddington limit

Line E in figure 2.8 shows the Eddington limit (Rybicki and Lightman, 1979). In the region above this line, radiation pressure exceeds gravity and gas moves outward.

In summary, only region D in figure 2.8 is theoretically feasible stellar mass for a given accretion rate. Hence, at the same accretion rate as for typical low-mass stars ($\sim 10^{-6}\text{--}10^{-5} M_{\odot} \text{ yr}^{-1}$), spherically symmetric accretion would not be possible to form high-mass stars above $10\text{--}20 M_{\odot}$.

Several theories have been proposed to overcome the above difficulties and explain the process of massive star formation — for example, “turbulent core accretion model” (McKee and Tan, 2003; Hosokawa, Yorke, and Omukai, 2010; Myers et al., 2013), “competitive accretion model” (Bonnell et al., 2001; Clark et al., 2008), “collision and merger model” (Bonnell, Bate, and Zinnecker, 1998; Bally and Zinnecker, 2005), and “clump-fed model” (Wang et al., 2009). Here, the estimate in figure 2.8 assumed spherically symmetric accretion for simplicity. In fact, massive stars are considered to gain mass from their accretion disks in the same way as low-mass stars (Kraus et al., 2010). Namely, the disk direction is optically thick, and the radiation pressure should be weaker. Therefore, the most severe lower

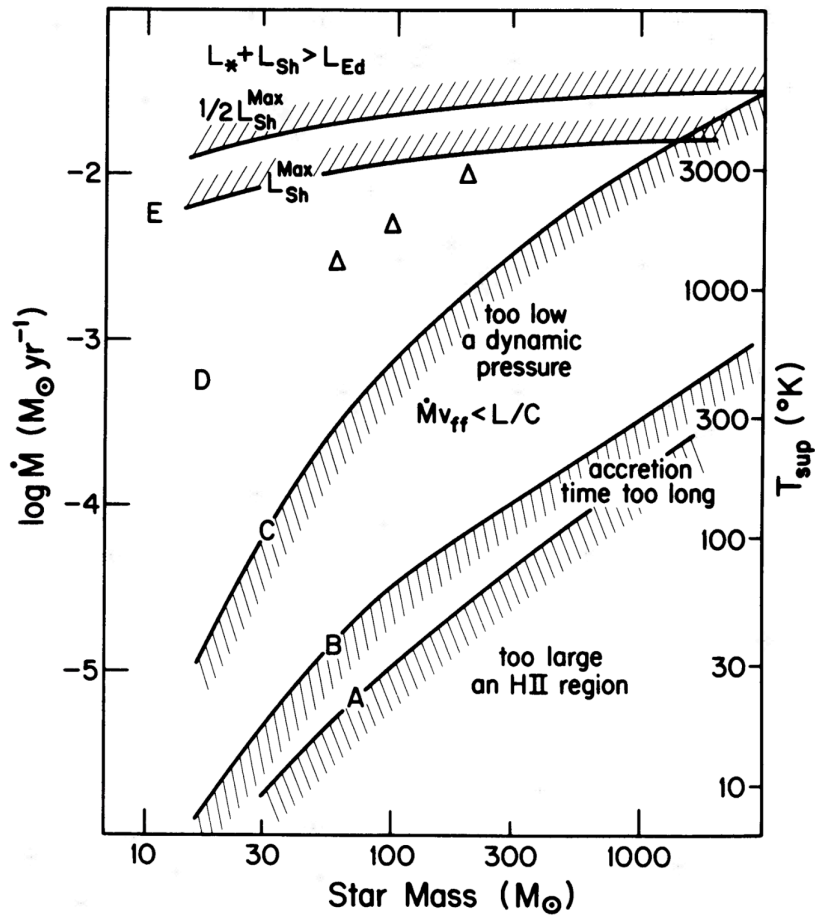


FIGURE 2.8: Accretion rate versus core mass, taken from Wolfire and Cassinelli (1987). The corresponding equivalent support temperature is shown on the right side. Each line indicates the limit of possible stellar mass at a given accretion rate (see text).

limit (line C) would be actually relieved, and that may be the breakthrough to explain massive star formation (Yorke and Bodenheimer, 1999; Krumholz et al., 2009; Kuiper et al., 2010; Tanaka and Nakamoto, 2011). However, they would still need to gain mass in some way, much more efficiently than low-mass stars.

Radio observations suggest cloud-cloud collision can cause strong compression and thus form massive stars. A growing body of evidence to support this hypothesis has been found in multiple MSFRs (e.g., Westerlund 2 by Furukawa et al., 2009; Ohama et al., 2010, RCW 38 by Fukui et al., 2016, M 17 by Nishimura et al., 2018, and NGC 6334 by Fukui et al., 2018). In any case, the key to forming massive stars is rapidly confining the gas in extremely compact space.

2.2 Stellar evolution and types

We described forming protostars from ISMs and their evolution to main-sequence stars. In this section, we review stellar evolution after the birth of main-sequence stars and their classification. Stellar types are still determined simply by the masses of the stars.

2.2.1 Stellar classification

The main-sequence stars are brightly shining stars undergoing nuclear fusion reactions in their cores. The emission spectrum is a continuum component approximated by blackbody radiation, plus absorption lines by atoms and molecules in the stellar atmosphere. Stars are classified as O, B, A, F, G, K, and M according to the type and intensity of their absorption lines, as shown in figure 2.9. This is called Harvard classification, which is directly in order of the surface temperature of the star (Hearnshaw, 1990). Each type varies continuously, and they are further divided into 10 classes and assigned a number from 0 to 9, starting with the highest temperature. Roughly, the high-temperature side is called an early stage, and the low-temperature side is called a late stage.

The atmospheres of most stars are known to have the same chemical abundance as the Sun and be in thermal equilibrium. Since the states of molecules, atoms, and ions are primarily determined by temperature, the intensity of each absorption line is also sensitive to temperature. This is why the Harvard classification is a temperature series. It is also a mass series, since the heavier the star, the higher the temperature. Table 2.2 summarizes the characteristics of O to M stars (Habets

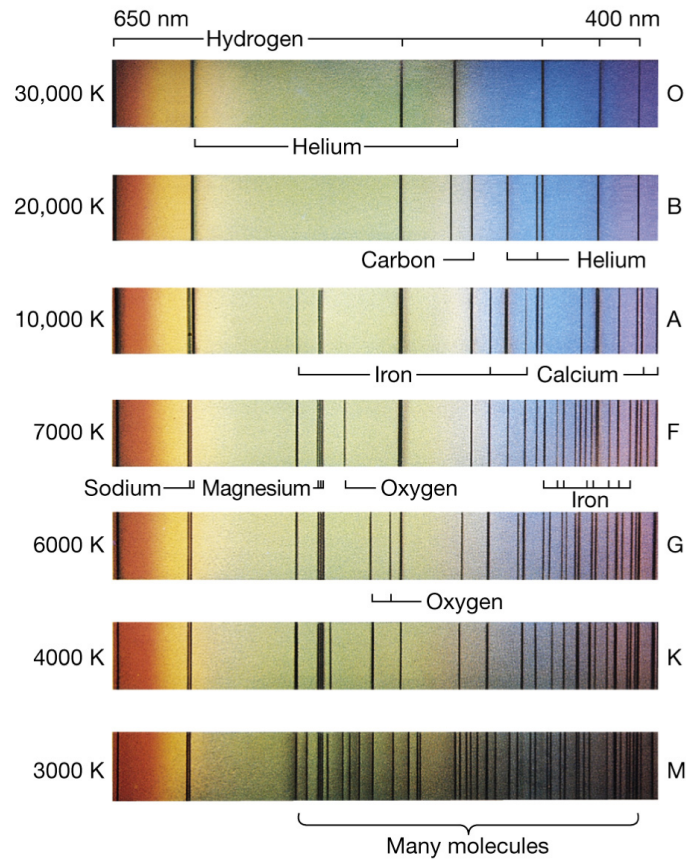


FIGURE 2.9: The main spectral classes of stars according to the Harvard classification. Credit: University of Oregon Physics Department

TABLE 2.2: Classification of main-sequence stars and their characteristics according to the Harvard system.

Spectral Type	Surface Temperature (K)	Mass (M_{\odot})	Radius (R_{\odot})	Bolometric Luminosity (L_{\odot})	Fraction (%)
O	>30,000	>16	>6.6	>30,000	<0.0001
B	10,000–30,000	2.1–16	1.8–6.6	25–30,000	0.13
A	7,500–10,000	1.4–2.1	1.4–1.8	5–25	0.60
F	6,000–7,500	1.04–1.4	1.15–1.4	1.5–5	3.0
G	5,200–6,000	0.8–1.04	0.96–1.15	0.6–1.5	7.6
K	3,700–5,200	0.45–0.8	0.7–0.96	0.08–0.6	12.1
M	2,400–3,700	0.08–0.45	<0.7	<0.08	76.5

TABLE 2.3: Main-sequence massive star definition (Zinnecker and Yorke, 2007).

Mass (M_{\odot})	Designation	Spectral Type
8–16	Early B-type massive stars	B3V to B0V
16–32	Late O-type massive stars	O9V to O6V
32–64	Early O-type massive stars	O5V to O2V
64–128	O/WR-type massive stars	WNL-H*

* WNL-H: N-rich late-type Wolf-Rayet (WR) stars, still on the H-burning (see Crowther, 2007).

and Heintze, 1981; Ledrew, 2001; Baraffe et al., 2003; Weidner and Vink, 2010). High-mass stars emit bluer (higher-energy) radiation, while low-mass stars emit relatively redder. Currently, stars with even lower mass than M stars have been discovered and classified into L and T stars (Kirkpatrick, 2005). Many of these are brown dwarfs and do not have enough mass to initiate a nuclear fusion reaction.

In addition to the above classification, the Morgan-Keenan classification takes into account the brightness of stars (Morgan, Keenan, and Kellman, 1943; Morgan and Keenan, 1973). The brightness of a star is often related to its size. Thus, the following symbols are added after the spectral types: 0 (hypergiants), I (supergiants), II (bright giants), III (normal giants), IV (subgiants), V (main-sequence stars), VI or sd (subdwarfs), and VII or D (white dwarfs). They may be further subdivided and labeled a, ab, or b from the bright side.¹ For example, the Sun can be written as G2V.

Massive stars, the main objects of the present thesis, are defined as above $8M_{\odot}$. Thus, they are classified as either O stars or early B stars, as shown in table 2.3. Wolf-Rayet (WR) stars are considered to be massive stars that have lost their outer layer of hydrogen due to powerful stellar winds. It is known to exhibit a unique spectral structure with a broad emission line.

2.2.2 Evolution processes

Hertzsprung-Russell (HR) diagram is imperative in understanding stellar evolution. The HR diagram plots the temperature (or spectral type) of stars against their luminosity (absolute magnitude). Figure 2.10 is a schematic HR diagram. It

¹See <https://lweb.cfa.harvard.edu/~pberlind/atlas/htmls/note.html> for details

shows the various evolutionary stages of stars. The main sequence is distributed along the line from the upper left (high brightness and high temperature) to the lower right (low brightness and low temperature) in the HR diagram and shows the most prominent features. Main-sequence stars spend most of their lives somewhere on this line according to their masses and convert hydrogen to helium through nuclear fusion reactions.

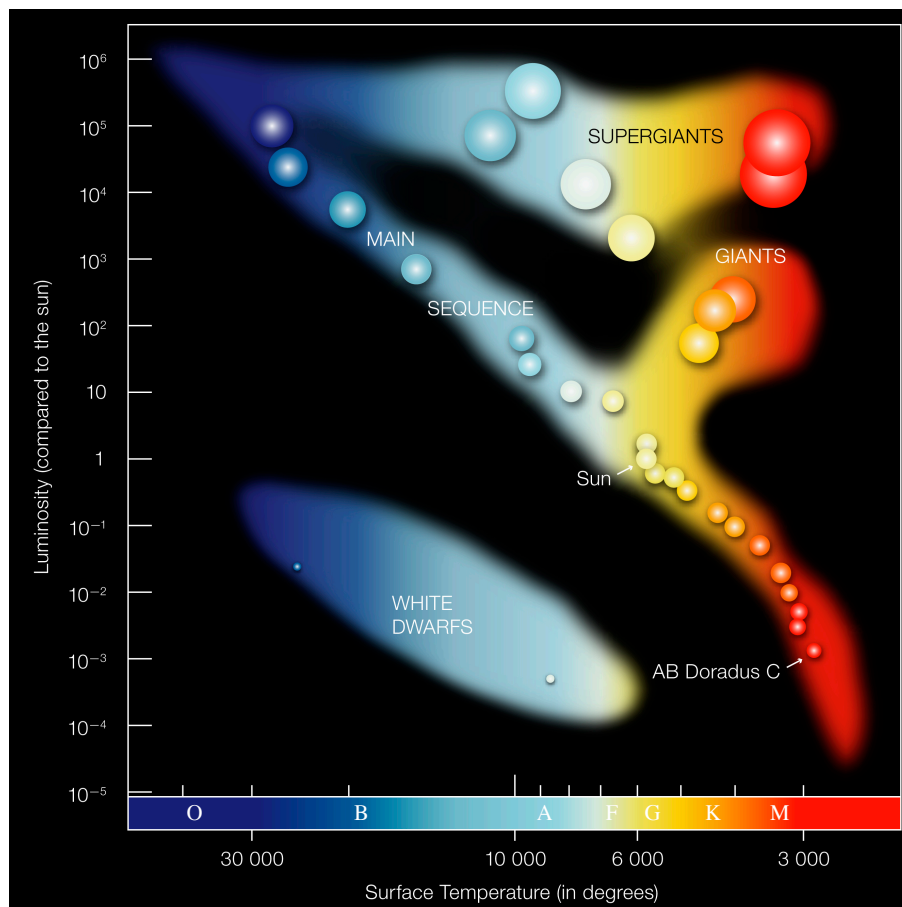


FIGURE 2.10: Schematic HR diagram. Credit: ESO

We here follow the stellar evolution with the HR diagram. Figure 2.11 shows the evolutionary paths of pre-main-sequence stars to main-sequence stars on the HR diagram. T-Tauri stars ($<2M_{\odot}$) exhibit F to M spectral types. They lose energy due to radiation from their surfaces and contract quasi-statically. The entire stars are nearly convective and their luminosity decreases as they contract while the surface temperature remains constant (Hayashi, 1961). Therefore, they move almost vertically downward from “birth-line” in figure 2.11 (Hayashi track, see

Stahler, 1988). After that, stars with masses below $0.5M_{\odot}$ directly become zero-age main-sequence stars. Stars with masses above $0.5M_{\odot}$ move to the upper left as radiation heat transfers exceed convection (Heney track, see Heney, Leleuvier, and Levée, 1955). Intermediate-mass pre-main-sequence stars ($2-8M_{\odot}$) are called Herbig Ae/Be stars and exhibit A or B spectral types. They evolve faster than low-mass stars and move quickly onto the Heney track. The birth-line of massive stars ($>8M_{\odot}$) is on the main sequence. In other words, they do not have a pre-main-sequence phase and have already evolved into main-sequence stars by the end of the mass accretion phase.

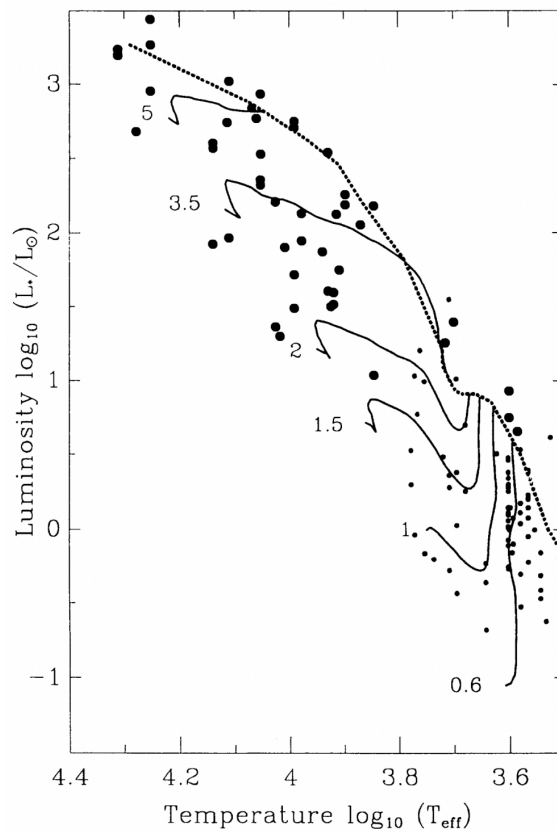


FIGURE 2.11: Observed distribution of low- and intermediate-mass pre-main-sequence stars in the HR diagram (Palla and Stahler, 1993). Large circles represent Herbig Ae/Be stars (Berrilli et al., 1992) and small dots represent T-Tauri stars (Strom et al., 1989). Each solid line is the evolutionary path for each stellar mass in solar units. The dotted line is the boundary where the pre-main-sequence stars exist and is called “birth-line”.

Stars after the main sequence not only release energy through nuclear fusion reactions but also begin to eject gas from some point in the pre-main-sequence phase.

Low- and intermediate-mass main-sequence stars eject their own mass at hundreds of km s^{-1} . Magnetic fields are formed on the stellar surface due to the dynamo mechanism (Choudhuri, Schussler, and Dikpati, 1995), and magnetohydrodynamic waves are excited on the stellar surface, originating from the movement of their convective layer. It is considered that stellar winds are driven by the energy transfer from the convective layer to the outer layer via these waves and turbulence (Suzuki et al., 2013). By contrast, massive stars are dominated by outward radiation pressure. The winds driven by the radiation pressure exceed $1,000 \text{ km s}^{-1}$ (Maeder and Meynet, 1987; Prinja, 1990), causing high mass loss and great effects on interstellar space. Thus, WR stars are believed to be stars after very high-mass (at least $25M_{\odot}$) main-sequence stars (or supergiants) have blown out their outer layers by this mechanism. WR stars are located in the upper left edge of the HR diagram.

After a sufficient amount of time, the central cores of the main-sequence stars run out of hydrogen. The central cores then contract, the heat is transferred to the outer hydrogen layer, and the nuclear fusion reaction proceeds in the outer layer. As a result, the outer layers expand against self-gravity and increase luminosity while the temperature decreases. The stellar winds slow down to tens of km s^{-1} . During this phase, they move to the upper right regions in the HR diagram and evolve into red giants or red supergiants. Depending on the masses of the stars, helium and heavier elements in the cores cause nuclear fusion reactions in succession.

In the case of low- and intermediate-mass giants, gas flows out from the outer layers, where gravitational constraints are weak. Then, the centers of the stars are gradually exposed. Due to the lack of mass, nuclear fusion proceeds only to light elements. They then evolve into hot and compact white dwarfs. They support gravity by electron degeneracy pressure and gradually cool down. They are located in the lower left of the HR diagram. That is the end of low- and intermediate-mass stars. However, when a white dwarf gains mass for some reason, such as mass accretion from another object or a merger with a second white dwarf, and gains $1.4M_{\odot}$, it is known to cause a supernova explosion (Maeda and Terada, 2016). Exploded objects in this way are called Type Ia supernovae.

In the case of massive giants (supergiants), nuclear fusion reactions proceed one after another, eventually producing a central iron core. Unlike lighter elements,

iron does not release heat through nuclear fusion. Then the stars lose their outward pressure and collapse rapidly due to gravity. The fallen outer layer collides with the core, and the recoil shocks cause supernova explosions. Exploded objects in this way are called Type II supernovae. The iron cores compressed by powerful forces become neutrons and remain extraordinarily dense neutron stars. They support their gravity by neutron degeneracy pressure. Therefore, they are even more compact than white dwarfs. Stars whose gravity overwhelms this degeneracy pressure become black holes (Heger et al., 2003).

2.3 X-ray emission from astronomical objects

As we have seen, observational studies of star formation proceeded mainly through radio, infrared, and optical light bands. X-rays can observe energetic astrophysics compared to those bands. X-rays from MSFRs were first discovered in the Orion Nebula by the *Uhuru* satellite launched in 1970 (Giacconi et al., 1974). It can be said that X-ray astronomy is a relatively new field among these wavelengths. In this section, we organize the key elements for studying MSFRs by X-rays and introduce the implications obtained from X-ray observations.

2.3.1 Absorption

Electromagnetic waves with energies of ~ 0.1 – 100 keV are called X-rays. This thesis mainly focuses on X-rays in the range of ~ 0.1 – 10 keV. The lower energy is sometimes expressed as “soft”, and the higher energy is “hard”. Since X-rays are absorbed by the Earth’s atmosphere, X-ray astronomical objects are generally observed from outside the atmosphere using instruments onboard rockets, balloons, and artificial satellites. On the other hand, X-rays have a high transmittance to ISMs in space.

Figure 2.12 shows the extinction cross-section of electromagnetic waves in the energy range from FIR to X-rays in the ISMs. The dominant extinction effect differs between the low-energy side and the high-energy side. On the low-energy side, extinction is due to the scattering of radiation by dust. Ultraviolet is the most opaque to ISMs. The wavelength of 91.2 nm (energy of 13.6 eV) corresponds to the Lyman limit (see subsection 2.3.3). When electromagnetic waves larger than this energy are incident, hydrogen begins to be ionized. Thus, on the higher energy side, the dominant extinction factor is the absorption of hydrogen and/or

other heavier elements. In the X-ray band, photoelectric absorption is caused by elements such as C, N, O, Ne, Mg, and Fe. X-rays have a high penetrating power equal to or higher than infrared rays. As mentioned in subsection 2.1.1, star-forming sites are generally very dense, and the thick ISMs often make it difficult for electromagnetic waves to reach us. In such environments, the high transmittance of X-rays is a valuable tool to probe inside the mysterious giant molecular clouds.

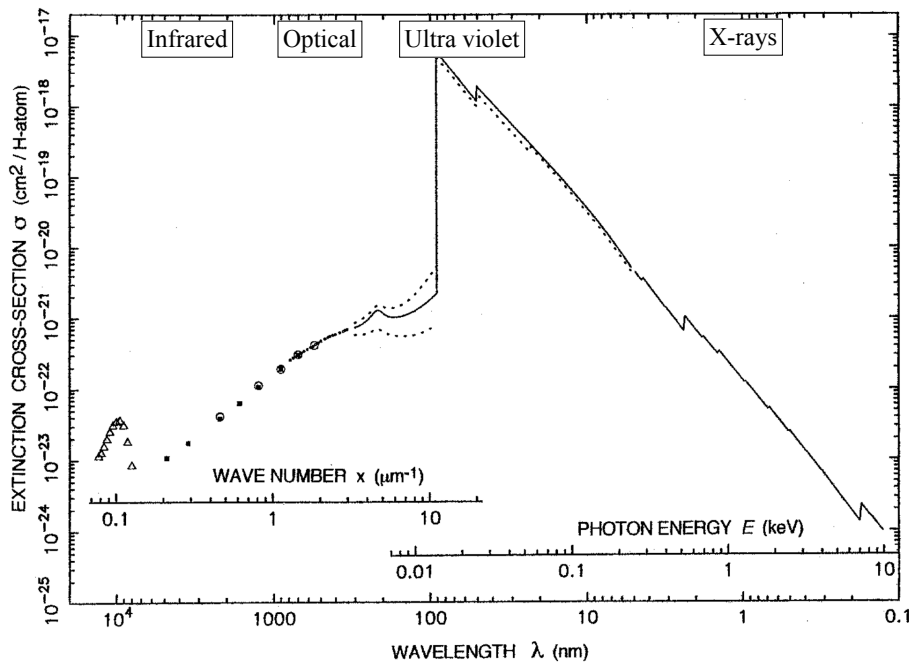


FIGURE 2.12: The absorption or scattering cross-section in the 0.125 eV to 10 keV, taken from Ryter (1996).

The degree of interstellar absorption experienced by observed X-rays is usually estimated by the hydrogen column density N_{H} (in units of atoms cm^{-2} or simply cm^{-2}) assuming cosmic elemental abundance. The column density is the amount of material per unit area integrated along the line of sight. Here, we denote photon absorption cross-section per hydrogen atom by σ_{H} . When X-ray intensity I_0 comes through an absorption column density N_{H} , observed X-ray intensity I is expressed as

$$I = I_0 e^{-\sigma_{\text{H}} N_{\text{H}}}, \quad (2.9)$$

where $\tau = \sigma_{\text{H}} N_{\text{H}}$ is called optical depth and is an indicator of whether it is optically thick ($\tau > 1$) or optically thin ($\tau < 1$). Typical interstellar absorption for

MSFRs is $N_{\text{H}} \sim 10^{21}\text{--}10^{23} \text{ cm}^{-2}$. Therefore, the ISMs are almost free from absorption above $\sim 2 \text{ keV}$, as shown in figure 2.12.

2.3.2 Non-thermal emission

The basic processes of X-ray emission from astronomical objects can be roughly classified into thermal and non-thermal emission. In this subsection, we summarize possible non-thermal X-ray emissions. Non-thermal emission is represented only by a continuous power-law model on the spectrum. This is because the energy distribution of non-thermal electrons, the main sources of the emission, can be approximated by a power law. The spectral energy distribution is usually expressed in terms of flux per unit frequency f_ν . This is approximated by a power of the frequency ν as $f_\nu \propto \nu^\alpha$, where α is called a spectral index which determines the spectral shapes. When using the number of photons per unit frequency $N (= f_\nu/E)$, it is approximated by a power of energy $E (= h\nu)$ as $N(E) \propto E^{-\Gamma}$, where h is Plank constant and Γ is called a photon index. The spectral index α and the photon index Γ are thus related by $\Gamma = 1 - \alpha$.

Bremsstrahlung

Bremsstrahlung is the electromagnetic wave emitted by accelerated charged particles. In space, when a charged particle passes near an atomic nucleus, the motion of the two charges emits X-rays as a time-varying electric dipole. As described below, the probability of the emission is inversely proportional to the square of the mass of the charged particles. Since protons are much heavier than electrons, the acceleration of the proton is almost negligible. Thus, electrons are the main source of the emission.

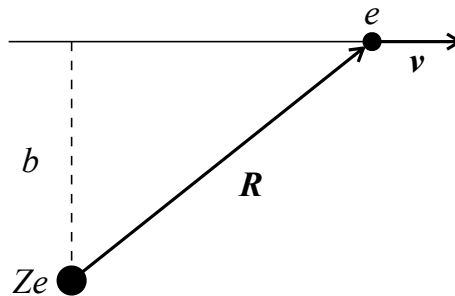


FIGURE 2.13: The geometry of an electron moving past an ion of charge Ze with a velocity of v .

When a single free electron (charge $-e$) passes nearby a single nucleus (charge Ze) with an impact parameter b and is accelerated, as shown in figure 2.13, they are considered an electric dipole and the power of the bremsstrahlung emission in the unit of angular frequency is given by

$$\frac{dW(b)}{d\omega} = \begin{cases} \frac{8Z^2e^6}{3\pi c^3 m^2 v^2 b^2} & (b \ll v/\omega) \\ 0 & (b \gg v/\omega), \end{cases} \quad (2.10)$$

where c is the speed of light, m is the mass of the electron, and v is the velocity of the electron (see Rybicki and Lightman, 1991). Assuming that electrons have uniform velocity v in a plasma with electron density n_e and ion density n_i , the number of electrons passing between impact parameters b and $b + db$ per unit time for a single ion is $2\pi b db \times v n_e$. Then, using the $b \ll v/\omega$ result of equation (2.10), the total emission per unit frequency per unit volume per unit time can be written as:

$$\begin{aligned} \frac{dW(b)}{d\omega dV dt} &= 2\pi v n_e n_i \int_{b_{\min}}^{\infty} \frac{dW(b)}{d\omega} b db \\ &= 2\pi v n_e n_i \int_{b_{\min}}^{b_{\max}} \frac{8Z^2e^6}{3\pi c^3 m^2 v^2 b^2} b db \\ &= \frac{16\pi e^6}{3\sqrt{3}c^3 m^2 v} n_e n_i Z^2 \frac{\sqrt{3}}{\pi} \ln \left(\frac{b_{\max}}{b_{\min}} \right) \\ &= \frac{16\pi e^6}{3\sqrt{3}c^3 m^2 v} n_e n_i Z^2 g_{ff}(v, \omega), \end{aligned} \quad (2.11)$$

where b_{\min} and b_{\max} is some minimum and maximum value of impact parameter, and $g_{ff} = \frac{\sqrt{3}}{\pi} \ln \left(\frac{b_{\max}}{b_{\min}} \right)$ is called ‘‘Gaunt factor’’ which is a certain function of the energy of the electron and frequency of the emission. This value is known to be on the order of ~ 1 (Brussaard and Hulst, 1962). Equation (2.11) is a model in which the electrons have a fixed velocity v . The energy spectrum of the bremsstrahlung is obtained by averaging over the actual electron velocity distribution.

Synchrotron emission

Synchrotron emission is included in bremsstrahlung. It is emitted by charged particles but is accelerated by a magnetic field. We assume a situation that an electron with relativistic velocity v receives Lorentz force and spirals around magnetic force lines, as shown in figure 2.14. If we denote $\beta = v/c$ and $\gamma = 1/\sqrt{1-\beta^2}$,

the typical frequency of a photon emitted in synchrotron emission by a single electron with energy $mc^2\gamma$ is given by

$$\nu_c = \frac{3\gamma^2 e B \sin\alpha}{2\pi mc}, \quad (2.12)$$

where α is the pitch angle between the magnetic field \mathbf{B} and the electron velocity \mathbf{v} . The peak frequency of the synchrotron emission spectrum from a single electron is known to be $0.29\nu_c$. Luminosity (in units of erg s^{-1}) of the synchrotron emission from a single electron is given as

$$\begin{aligned} P_{\text{synch}} &= \frac{4}{9} \frac{e^4 \beta^2 \gamma^2 B^2}{m^2 c^3} \\ &= \frac{4}{3} \sigma_T c \beta^2 \gamma^2 U_B, \end{aligned} \quad (2.13)$$

where $\sigma_T = 8\pi\{e^2/(mc^2)\}^2/3$ is Thomson scattering cross-section and $U_B = B^2/(8\pi)$ is the magnetic energy density.

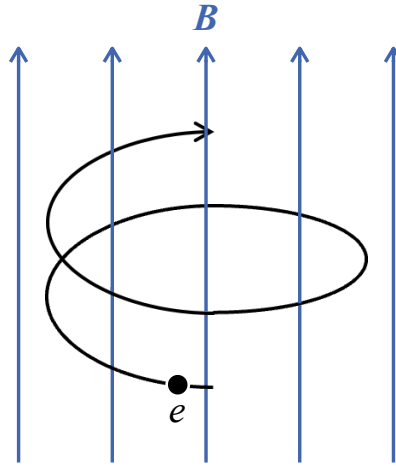


FIGURE 2.14: Spiral motion of an electron in a uniform magnetic field \mathbf{B} .

Integrating equation (2.12) for electrons with non-thermal distribution still yields a power-law energy spectrum. In conservative interpretation, its photon index is considered larger than 1.5 from observational studies. In the X-ray band, synchrotron emission is generally observed when relativistic electrons (on the order of TeV) are spiraling in a magnetic field on the order of μG or more (e.g., Koyama et al., 1995).

Inverse Compton scattering

The phenomenon in which photons collide with free electrons and transfer energy to the free electrons is called Compton scattering. On the other hand, when an electron with relativistic velocity collides with an optical and infrared photon, the electron transfers energy to the photon since the electron energy is much greater than that of the photon. This phenomenon is called inverse Compton scattering. When inverse Compton scattering is effective, low-energy photons gain energy through multiple collisions with high-energy electrons and are gradually knocked up into the high-energy band. As a result, we can observe X-ray and gamma-ray emissions.

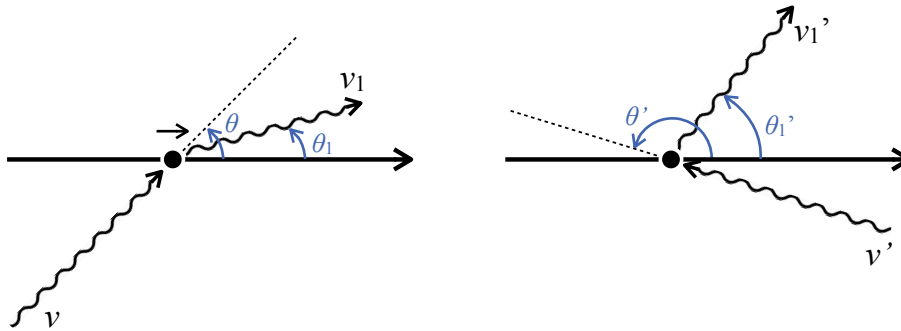


FIGURE 2.15: The geometries of an electron receiving energy from a photon in the observer's frame (left) and in the electron-rest frame (right).

Here, we consider the scattering in two systems: the observer's frame and the electron-rest frame. We denote the velocity of an electron as v , the frequency of the incident photon as ν in the observer's frame, and the frequency of the incident photon ν' in the electron-rest frame (figure 2.15). Let θ be the angle between the direction in which the electron moves and the direction of the incident photon, the frequencies in both frames have the following relationship because of the Doppler effect:

$$\nu' = \nu\gamma(1 - \beta\cos\theta). \quad (2.14)$$

We may assume $h\nu \ll mc^2$ in the electron-rest frame and thus the frequency does not vary before and after scattering (Tomson scattering). Accordingly, the frequency ν_1 after scattering in the observer's frame is written by

$$\nu_1 = \nu'_1\gamma(1 + \beta\cos\theta'_1) = \nu'\gamma(1 + \beta\cos\theta'_1). \quad (2.15)$$

From equations (2.14) and (2.15), we can see that the frequencies before and after scattering have the following relationship:

$$\nu_1 \sim \gamma^2 \nu. \quad (2.16)$$

Namely, a single inverse Compton scattering with a relativistic electron increases an incident photon energy by a factor of γ^2 .

The luminosity of the inverse Compton scattering from a single electron is given by

$$P_{\text{compt}} = \frac{4}{3} \sigma_{\text{T}} c \beta^2 \gamma^2 U_{\text{ph}}, \quad (2.17)$$

where U_{ph} is the energy density of the photon. Equation (2.17) is similar to the synchrotron emission, equation (2.13). In MSFRs, for example, infrared photons may be converted into X-ray photons through inverse Compton scattering by a few hundred MeV electrons. If it exists, the photon index of the obtained spectrum is still expected to be comparable to synchrotron emission (e.g., $\Gamma \gtrsim 1.5$).

2.3.3 Thermal emission

Thermal bremsstrahlung

Applying thermal distribution (i.e., Maxwell distribution) to equation (2.11) yields the spectrum of thermal bremsstrahlung. Some energetic mechanisms in MSFRs are believed to produce high-temperature plasma exceeding several MK, which emit thermal bremsstrahlung emission. When the electrons in plasma have a Maxwell distribution with temperature T , the probability dP that their velocities are between v and $v + dv$ is given by

$$dP \simeq v^2 \exp\left(-\frac{mv^2}{2kT}\right) dv, \quad (2.18)$$

where m is the mass of the electron and k is the Boltzmann constant. For equation (2.11), assuming the velocity range $0 < v < \infty$ and performing weighted average

with equation (2.18), we obtain

$$\frac{dW(T, \omega)}{d\omega dV dt} = \frac{\int_{v_{\min}}^{\infty} \frac{dW(v, \omega)}{d\omega dV dt} v^2 \exp\left(-\frac{mv^2}{2kT}\right) dv}{\int_0^{\infty} v^2 \exp\left(-\frac{mv^2}{2kT}\right) dv}. \quad (2.19)$$

Considering an electromagnetic wave with frequency ν , the relation $h\nu \leq mv^2/2$ should be satisfied since the moving particles must create a photon energy of $h\nu$ for the emission. Therefore, we set $v_{\min} = \sqrt{2h\nu/m}$. Using $d\omega = 2\pi d\nu$, we summarize equation (2.19) as follows:

$$\begin{aligned} \frac{dW}{dV dt d\nu} &\equiv \frac{2^5 \pi e^6}{3mc^3} \left(\frac{2\pi}{3km}\right)^{1/2} T^{-1/2} Z^2 n_e n_i e^{-h\nu/kT} \bar{g}_{ff}(T, \nu) \\ &= 6.8 \times 10^{-38} T^{-1/2} Z^2 n_e n_i e^{-h\nu/kT} \bar{g}_{ff}(T, \nu), \end{aligned} \quad (2.20)$$

where \bar{g}_{ff} is the Gaunt factor averaged over the electron velocity distribution and $\bar{g}_{ff} \sim (h\nu/kT)^{-0.4}$. Hence, the energy spectrum of thermal bremsstrahlung may be approximated by $E^{-0.4} e^{-E/kT}$ and the photon spectrum by $E^{-1.4} e^{-E/kT}$, respectively.

As shown in equations (2.11) and (2.20), the bremsstrahlung emission per unit volume and unit time is proportional to $n_e n_i$. Consequently, the energy emitted from the plasma of volume V per unit time is $n_e n_i V$. This value is called “emission measure (EM)” and is sometimes used as an index of the density or size of plasma gas. In most cases, n_i can be replaced by hydrogen density.

Line emission

Atoms and molecules have discrete energy levels because of the quantum-mechanical nature of the motion of the electrons. Line emissions are caused by the transition of electrons, which emits the energy equivalent to the difference between the two discrete levels. When electromagnetic waves are absorbed by the transition, they are called absorption lines. Both are characterized to appear only at specific energies on a spectrum, while thermal bremsstrahlung and other non-thermal mechanisms have continuous spectral shapes. For hydrogen atoms, when an electron excited to an energy level E_n (principal quantum number n) transitions to a lower

energy level E_m (principal quantum number m), the emission energy is given by

$$\Delta E = E_n - E_m = Rhc \left(\frac{1}{m^2} - \frac{1}{n^2} \right) \quad (2.21)$$

$$R = \frac{me^4}{8\epsilon_0^2 h^3 c} \quad (2.22)$$

where R is called Rydberg constant and ϵ_0 is the dielectric constant under a vacuum. For heavier elements with atomic number Z , it is known that the energies can be roughly expressed as follows:

$$\Delta E = E_n - E_m \sim Z^2 Rhc \left(\frac{1}{m^2} - \frac{1}{n^2} \right). \quad (2.23)$$

As for hydrogen and hydrogen-like ions, emission (absorption) lines by the transitions between $n = 1$ and higher levels are called Lyman series. Then, emission lines by the transitions from $n = 2, 3, 4, \dots$ are written by $\text{Ly}\alpha, \text{Ly}\beta, \text{Ly}\gamma, \dots$, respectively. The transition between $n = 1$ and $n = \infty$ (i.e., free electrons) is Lyman limit (13.6 eV). Emission (absorption) lines by the transitions between $n = 2, 3, 4, \dots$ and higher levels are called Balmer series, Paschen series, Brackett series, ..., respectively.

The transition processes become complex when ions have two or more electrons. Figure 2.16 shows the emission mechanism of helium-like ions. For example, w, x and y , and z are resonance, intercombination, and forbidden lines, respectively. Although they emit lines with subtly different energies, they cannot usually be distinguished without ultra-high energy resolution of several eV or more. The charge-coupled device (CCD) detector used in this thesis has a resolution of ~ 120 eV at 6 keV. Therefore, the sum of these lines is observed. Because of the transition on the K shell, emission lines from $n = 2, 3, 4, \dots$ to $n = 1$ are usually denoted as $\text{K}\alpha, \text{K}\beta, \text{K}\gamma, \dots$ lines, respectively. After the L shell, they are often written in the same way.

In optically thin thermal plasmas, ions are excited by collisions with free electrons. Since the lifetime of the excited state is much shorter than the average timescale of electron-ion collisions, the emission rate can be taken as equivalent to the excitation rate. Therefore, the intensity of the emission lines is proportional to $n_e n_i$, which determines the collision probability between electrons and ions. By comparing the intensity of the emission lines among different elements, we can derive relative abundance. That is useful for discussing the origin of thermal

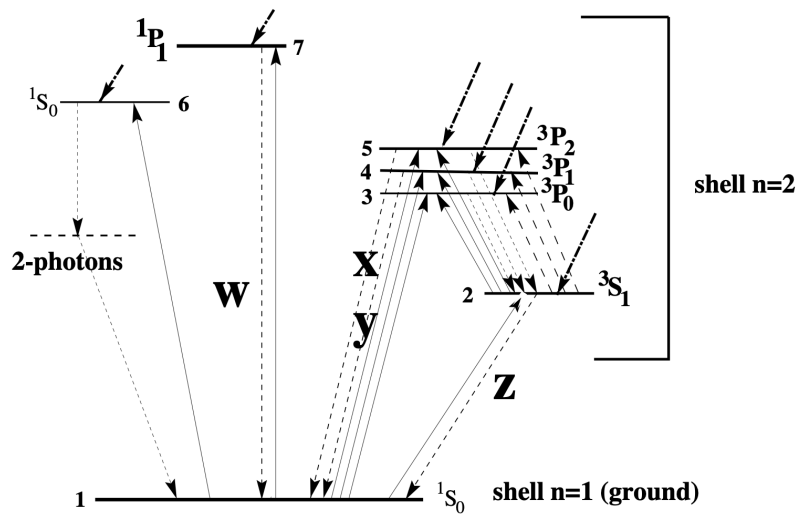


FIGURE 2.16: Simplified level scheme for helium-like ions, taken from Porquet et al. (2001). Full upward arrows, broken arrows, and thick skew arrows show collisional excitation transitions, radiative transitions, and recombination (radiative and dielectronic) + cascade processes, respectively.

plasmas in MSFRs (e.g., Hamaguchi et al., 2007; Ezoe et al., 2019).

2.3.4 X-rays from various stars

We here review the X-ray emission from stars. They can be said to be clumps of plasma. In the early soft X-ray studies of star-forming regions, the *Einstein* satellite (launched in 1978) established that most stars in various masses and evolutionary stages are X-ray sources, and the *ROSAT* satellite (launched in 1990) reinforced this view. Thus, a growing body of observation shows that most stars have hot plasma outside their photosphere and emit thermal bremsstrahlung with emission lines from various ions. The X-ray emission mechanism of stars seems to depend on their mass. However, they cannot be explained by a simple correlation with the mass.

High-quality observations, as exemplified by *Chandra* (launched in 1999), now accept the proposal that the X-ray emission of low-mass stars originates from surface convection zones and reconnection processes of magnetic field lines penetrating them. Low-mass stars often cause explosive events called flares, which show enormous X-ray enhancements on time scales of minutes to hours. On the other hand, X-rays from massive stars are believed to originate from stellar winds. Their intensity fluctuation is smaller than that of low-mass stars. When

it comes to intermediate-mass stars, there are no strong stellar winds; convection zones; and magnetic fields, suggesting that they do not emit X-rays. However, they have, in fact, been detected from some intermediate-mass stars, some of which have also produced flares. Flares are also observed in YSOs. These high-energy release mechanisms are not yet fully understood (see review for Güdel and Nazé, 2009). Table 2.4 shows the X-ray properties of stars and YSOs summarized in Ezoë (2004). Below we introduce the current understanding in more detail.

Cool stars

Coronal magnetic fields are known to be the origins of the X-ray emission in many F to M stars. The corona is the hot ($\gtrsim 10^8$ K) outer layer of the stellar atmosphere. In the case of the well-observed Sun, the corona is a hot region $\sim 2,000$ km above the photosphere. Unstable magnetic field lines extending in the corona collide with each other and cause magnetic reconnection. The energies generated at that time heat the coronal plasma to tens of million K and accelerate ions and electrons to relativistic velocity.

Most of the cool stars have outer convection zones and often also have inner radiative zones. In such stars, the interaction of convection and rotation produces and maintains magnetic fields at the base of the convection zones (called dynamo mechanism), causing multiple magnetic phenomena such as magnetic spots, a thin chromosphere, and flares in the photospheres. The heat in the corona is thus considered to be related to the magnetic field amplified by the dynamo mechanism and lifted to the surface by buoyancy-driven instabilities, called “Parker instability” (Parker, 1966).

The X-ray luminosity L_X of G to F stars depends on the rotational velocity as expected from a rotation-induced internal dynamo (Pallavicini et al., 1981; Walter, 1981). They are related by

$$L_X \sim 10^{27} (v \sin i)^2, \quad (2.24)$$

where v is the equatorial velocity and i is the rotation axis inclination angle with respect to the line of sight (see e.g., Pizzolato et al., 2003). This relationship becomes weaker as the spectral type approaches F and saturates at $L_X/L_{\text{bol}} \sim 10^{-3}$

TABLE 2.4: X-ray properties of young stellar objects (YSOs) and massive OB stars.

Class	kT (keV)	L_X^* (erg s ⁻¹)	$L_X/L_{\text{bol}}^\dagger$	Time Variability	Model [‡]
Massive YSOs	2–10	$10^{30}\text{--}10^{34}$	$10^{-8}\text{--}10^{-6}$	Yes	?
Intermediate-mass YSOs	0.5–10	$10^{30}\text{--}10^{32}$	$10^{-7}\text{--}10^{-3}$	Flare?	MR?
Low-mass YSOs	0.2–5 (quiescent)	$10^{28}\text{--}10^{31}$	$10^{-5}\text{--}10^{-3}$	Flare	MR
	1–10 (flare)	$10^{29}\text{--}10^{32}$	$10^{-4}\text{--}10^{-1}$		
Brown dwarfs	1–2.5	$10^{27}\text{--}10^{30}$	$10^{-5}\text{--}10^{-3}$	Flare	MR
OB stars	$\lesssim 1$	$10^{30}\text{--}10^{34}$	$10^{-4\pm 0.4}$		SW?
	+2–5 (a few stars)				

* Typical X-ray luminosity. Since X-ray emission from massive YSOs suffers large absorption, their luminosities cover typically 2–8 keV, while those of main-sequence OB stars 0.1–2 keV.

† The X-ray luminosity to bolometric luminosity ratio.

‡ Theoretical models. MR and SW mean magnetic reconnection and non-magnetically confined stellar wind models, respectively.

References;

low-mass YSOs: the ρ Ophiuchus cloud (Imanishi, Koyama, and Tsuboi, 2001; Imanishi, Tsujimoto, and Koyama, 2001; Imanishi, 2003), IC 348 (Preibisch and Zinnecker, 2001; Preibisch and Zinnecker, 2002), NGC 1333 (Getman et al., 2002), Orion Molecular Cloud 2/3 (Tsujimoto et al., 2002), intermediate-mass YSOs: Berghöfer et al. (1997) and Hamaguchi, Tsuboi, and Koyama (2000), OB stars: η Carina (Koyama et al., 1990; Tsuboi et al., 1997; Corcoran et al., 2000), λ Orionis (Corcoran et al., 1994), Cygnus OB2 star 5 (Kitamoto and Mukai, 1996).

although the cause is still unclear. In addition, L_X is known to decrease slightly for fast ($v \gtrsim 100 \text{ km s}^{-1}$) rotating bodies (Randich et al., 1996).

The L_X is also correlated with the coronal temperature T (e.g., Schrijver, Mewe, and Walter, 1984; Schmitt et al., 1990; Telleschi et al., 2005). Although the origins are unknown, it is related by

$$L_X \propto T^{4.5 \pm 0.3}. \quad (2.25)$$

The average coronal temperature of cool stars is $\sim 1.5\text{--}3 \times 10^6 \text{ K}$, although the variation is large. It may involve more frequent magnetic interactions on more active stars, leading to higher rates of magnetic energy release that heat the corona to higher temperatures. Thus, coronal activity is generally accepted as the X-ray generation mechanism of low-mass main-sequence stars.

Hot stars

Stars with masses of $>5M_\odot$ do not have surface convection like low-mass stars and are not considered to produce coronas and flares. O and early B stars have intense ultraviolet radiation and their outward momentum drives a strong outflow of $\sim 10^{-8}\text{--}10^{-5}M_\odot \text{ yr}^{-1}$ (Cassinelli, 1979; Kudritzki and Puls, 2000). The terminal wind velocity is typically $\sim 600\text{--}3000 \text{ km s}^{-1}$ and models have been proposed in which the fast stellar winds are the main sources of the X-ray emission (e.g., Lucy and White, 1980; Lucy, 1982; Puls, Owocki, and Fullerton, 1993; Hillier et al., 1993). Around massive stars, the high-speed gas causes internal shocks with the relatively low-speed gas surrounding them and emits X-rays. Therefore, dense shells are considered to form at certain radii. The observed temperatures are usually $<1 \text{ keV}$ and are roughly consistent with dynamical predictions. Absorption by stellar wind is relatively small (Sana et al., 2006; Zhekov and Palla, 2007).

The X-ray-to-bolometric luminosity ratio L_X/L_{bol} of hot stars is $\sim 10^{-7}$ which is smaller than that of cool stars, $L_X/L_{\text{bol}} \sim 10^{-6}\text{--}10^{-4}$. Shocks may be expected to exhibit large and short-term variability because unstable winds decay and grow over a short period of time. However, in fact, X-rays from hot stars are relatively stable. In order to match the model and observations, Feldmeier, Puls, and Pauldrach (1997) suggested wind fragmentation in which X-ray variability is smoothed over the whole emitting volume, resulting in a more constant X-ray

output. Thus, the wind shock scenario is now considered the X-ray generation mechanism of OB stars.

In contrast to the above theory, it has been reported that some MSFRs have high-temperature (>2 keV) X-ray sources (e.g., η Carina Nebula by Koyama et al., 1990; Tsuboi et al., 1997; Corcoran et al., 2000; Antokhin et al., 2008; λ Orionis by Corcoran et al., 1994; and Cygnus OB2 star 5 by Kitamoto and Mukai, 1996). The temperatures observed in these sources are slightly higher than the current wind shock scenario.

Chandra and *XMM-Newton* showed another possibility. That is narrow symmetric emission lines that suggest lower velocities than expected. In general, kinematic velocities of the sources appear in line widths because of the Doppler effect. In the wind shock scenario, the X-ray-emitting regions are considered to be located far above the photosphere. A *Chandra* observation found symmetric and unshifted emission lines from ζ Orionis (O9.7 Ib) with widths corresponding to ~ 430 km s $^{-1}$, much less than the typical terminal wind velocity of $\sim 2,000$ km s $^{-1}$ (Waldron and Cassinelli, 2001; Miller et al., 2002). They suggested that the X-rays are generated in dense regions of $\sim 10^{12}$ cm $^{-3}$. In other words, there may be X-ray-emitting regions near photospheres of the stars. Similar results have been obtained from some B stars (e.g., τ Scorpii by Mewe et al., 2003; Cohen et al., 2003; θ^1 Orionis A by Schulz et al., 2003). Thus, the true X-ray emission mechanism of OB stars is still under discussion.

Some hot and long-period binaries show non-thermal radio emission. That suggests there are relativistic electron populations in the winds. Diffuse shock acceleration processes probably accelerate such electrons near hydrodynamic shocks inside or between stellar winds (see De Becker, 2007). In such regions, inverse Compton scattering may boost a small fraction of ultraviolet photons to the X-ray energy band (Chen and White, 1991). In order to detect this non-thermal X-ray emission, it needs to be sufficiently strong compared to the thermal emission. Highly sensitive observations in both X-ray and gamma-ray bands are required to find this evidence.

YSOs

It is generally accepted that X-rays from low-mass YSOs (i.e., Classical T-Tauri stars and Weak T-Tauri stars) are emitted by magnetic coronae in the same way

as low-mass stars. The typical L_X/L_{bol} ratio is $\sim 10^4$ (e.g., Güdel et al., 2007; Sciortino, 2008), which is larger than that of typical low-mass main-sequence stars, $L_X/L_{\text{bol}} \sim 10^{-6}$ – 10^{-4} . Although flares are also often observed in T-Tauri stars (e.g., Stelzer et al., 2007; Imanishi, Koyama, and Tsuboi, 2001), they differ from low-mass main-sequence stars in that their peak luminosities are several orders of magnitude higher (10^{29} – 10^{32} erg s $^{-1}$), and their decay time scales are typically one order of magnitude longer (10–20 ks). In addition, unlike equation (2.24), there seems to be no clear correlation between the X-ray luminosity and the rotation velocity (Feigelson and Montmerle, 1999). On the other hand, Telleschi et al. (2007) reported the following relationship between the X-ray luminosity L_X and the stellar mass M :

$$L_X \propto M^{1.7 \pm 0.1}. \quad (2.26)$$

Understanding the behavior of YSOs is thus valuable in investigating whether they have a continuous X-ray emission mechanism with main-sequence stars and, if so, how it starts. However, mass accretion is basically continuing from disks, as described in subsection 2.1.2. Hence, the younger the central star, the more difficult it is to observe and the further from complete understanding.

In the case of massive YSOs, the evolution should be fast, as described in subsection 2.1.2, and they should have evolved into main-sequence OB stars before the end of accretion. Therefore, it is natural to assume that the dominant X-ray emission mechanism is the same as that of massive stars (i.e., wind shock scenario). However, this scenario cannot explain the observed ultra-high temperatures of $\gtrsim 10$ keV. Even if the magnetic reconnection scenario were applied, the L_X/L_{bol} ratio is $\sim 10^{-8}$ – 10^{-6} which is much lower than that of typical low-mass YSOs at quiescence ($\sim 10^{-4}$) and thus cannot be explained. *Chandra* spectroscopic observations proposed a model in which X-rays from massive YSOs consist of both stellar wind and magnetic contributions (e.g., Schulz et al., 2000; Kohno, Koyama, and Hamaguchi, 2002; Nakajima et al., 2003; Schulz et al., 2003). As the star evolves, the wind contribution may become dominant and settle at the temperature of the observed massive star.

Intermediate-mass YSOs are less likely to produce X-ray emission since they do not have as strong stellar winds as massive stars and do not have the convection zones and magnetic fields like low-mass stars. However, X-ray emission has actually been reported in some intermediate-mass YSOs (Zinnecker and Preibisch,

1994; Principe et al., 2017). These are also still under discussion. For example, Hamaguchi et al. (2001) proposed the magnetic reconnection scenario based on flare-like time variability and high L_X/L_{bol} ratios. Meanwhile, Feigelson et al. (2002) observed A and B stars in the Orion Nebula and argued that the X-rays might be explained by companion low-mass stars.

2.3.5 Diffuse X-rays from massive star-forming regions (MSFRs)

Since the *Uhuru* satellite detected X-rays from the Orion Nebula (Giacconi et al., 1974; Forman et al., 1978), MSFRs have become good targets for X-ray studies. *Einstein* was the first satellite with an X-ray imaging telescope sensitive to 0.1–4 keV (Giacconi et al., 1979). Ku and Chanan (1979) confirmed a significant X-ray flux in the Orion Nebula with *Einstein* and identified a number of stars, including the Orion Trapezium. However, they found that $\sim 35\%$ of the total X-ray emission remained unidentifiable as point sources on the image. It spatially extends $16'$ to the north and $15'$ to the west of the Trapezium, as shown in figure 2.17. Similar extended X-ray emission was also observed in the Carina Nebula and the Rosette Nebula (Seward and Chlebowski, 1982; Leahy, 1985).

ASCA (launched in 1993) was the first satellite with a telescope sensitive to the energy band above 2 keV (Tanaka, Inoue, and Holt, 1994). It observed hard X-ray emissions from multiple MSFRs and found that they can indeed be represented by thermal emissions of 3–9 keV (e.g., Yamauchi et al., 1996; Hofner and Churchwell, 1997; Sekimoto et al., 2000). These temperatures are higher than those of massive stars (table 2.4). Hence, it remained an open question whether the extended X-ray sources are massive YSOs, combinations of massive YSOs and low mass YSOs, a superposition of undetected point sources, or whether there is a mechanism that generates diffuse thermal plasma, such as winds.

As explained in subsection 2.3.3, one possible explanation for the extended X-ray emission is that energetic phenomena associated with massive stars and giant molecular clouds form hot plasmas. For example, spatially extended X-ray emission can be expected if the massive stellar winds collide with the surrounding gas and cause shocks. Considering the wind velocity of the most massive O stars, the post-shock energy is believed to be several keV, exceeding the X-ray luminosity of the massive star itself. Weaver et al. (1977) suggested that O stars have bubbles that are swept by the winds and expand, and their termination shocks become

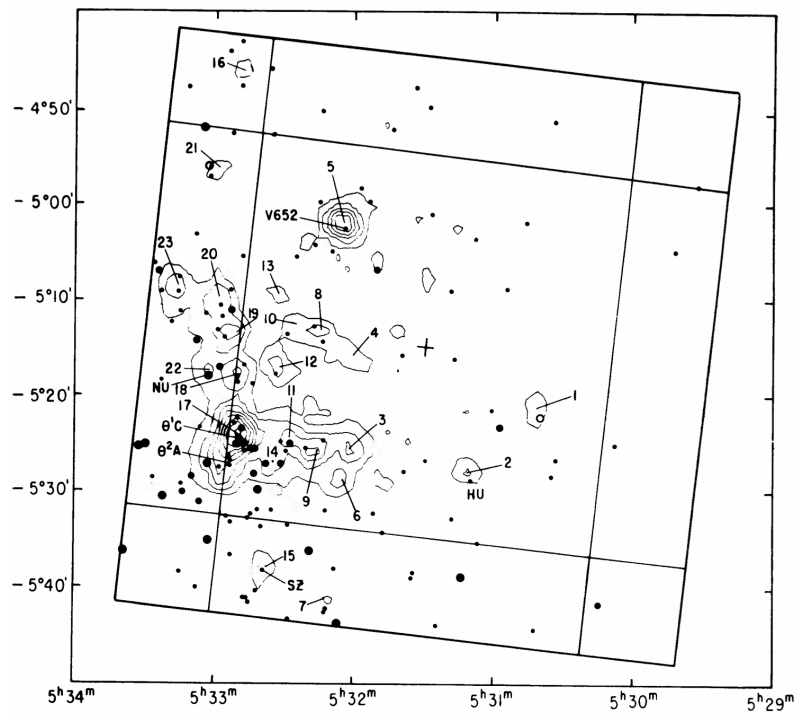


FIGURE 2.17: Contour map ($1^\circ \times 1^\circ$) of the Orion Nebula observed by *Einstein* (Ku and Chanan, 1979). The Trapezium (θ^1) is indicated $\sim 22'$ to the southeast of the center of the field. Bright nebular variables are represented as solid dots, and 23 discrete sources are labeled in the figure.

X-ray emission regions. Capriotti and Kozminski (2001) review the possible relationships between ionizing radiation and winds in H II regions. Thus, diffuse X-ray emission has theoretically been expected in H II regions excited by O stars since before.

If the high-energy diffuse phenomena described above are universal in star-forming regions, they would also affect star and planet formation. It may help us comprehend the poorly understood astrophysics of early massive stars and their emissions. However, due to the limited angular resolution of *ASCA* ($180''$, Serlemitsos et al., 1995), the X-ray sources could not be resolved, and it was not concluded whether the extended X-ray emission was truly diffuse or a superposition of faint point sources.

Chandra (launched in 1999) achieved angular resolution that is more than one order of magnitude better than previous satellites. It has extremely high point source resolution and eventually confirmed that the extended X-ray emission is truly diffuse. In addition to *Chandra*, *XMM-Newton* (launched in 1999) has a large effective area and high angular resolution (Jansen et al., 2001), and the *Suzaku* (launched in 2005) had good sensitivity to extended emission. In section 4.1, we summarize these X-ray observations of MSFRs in the 2000s. However, the issues mentioned in this section have not yet been fully resolved, and the origin of the diffuse X-rays is still under discussion.

In this thesis, we investigate the MSFR RCW 38, as the last report of these three satellite generations. This region is characterized by relatively hard X-ray emission and a mixture of numerous point sources. We utilize *Chandra* and *Suzaku*, which currently have the highest sensitivities for point sources and diffuse emission, respectively. In the next chapter, we present the characteristics of both satellites. The subsequent chapters introduce the recent reports of diffuse X-ray emissions and explain the purpose of this thesis.

Chapter 3

Instrumentation

To investigate the X-ray emission from the MSFR RCW 38, we analyze data from two X-ray astronomy satellites, *Chandra* and *Suzaku*. In this chapter, we briefly introduce the characteristics of both satellites. As we have reviewed, MSFRs have numerous point sources and extended X-ray emission. Therefore, it is important to use the best instruments for each X-ray source.

3.1 *Chandra*

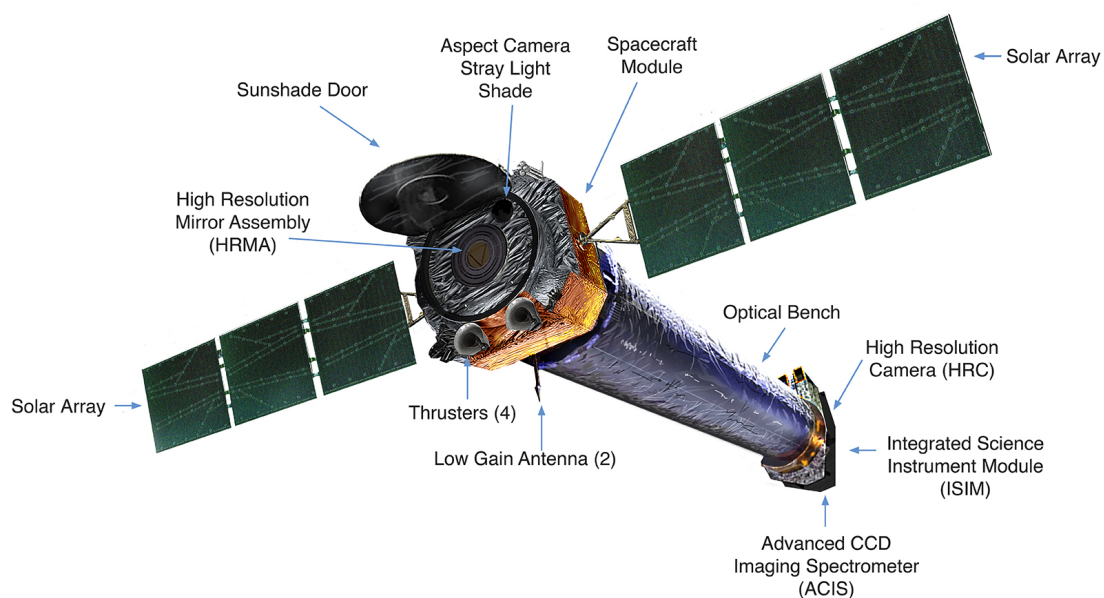


FIGURE 3.1: Schematic view of the *Chandra* X-ray observatory. Credit: NASA

The *Chandra* X-ray observatory (figure 3.1) is an X-ray astronomy satellite launched by NASA on 1999 July 23. It is one of the four NASA's Great Observatories series and was put into an elliptical orbit of apogee altitude of 138,800 km and perigee altitude of 10,100 km by the space shuttle *Columbia*. Its long orbital period (63.5 hrs) allows for long continuous observations.

Chandra has an X-ray telescope High Resolution Mirror Assembly (HRMA), two focal plane detectors Advanced CCD Imaging Spectrometer (ACIS) and High Resolution Camera (HRC), and two sets of X-ray grating systems (Weisskopf et al., 2002). *Chandra* has good sensitivity in the 0.1–10 keV band. Furthermore, it has an excellent angular resolution of $0''.5$, and its point-source sensitivity is 4×10^{-15} erg cm⁻² s⁻¹ in 10^4 s (0.4–6 keV). Multiple MSFRs, including our target RCW 38, have been observed with the HRMA and ACIS. We thus describe the HRMA and ACIS in the following subsection. Their basic performances are shown in table 3.1. For more information, see also The *Chandra* Proposers' Observatory Guide¹.

3.1.1 High Resolution Mirror Assembly (HRMA)

Figure 3.2 shows the appearance and schematic view of the HRMA. The HRMA adopts Wolter type-I configuration (Hans, 1952; Aschenbach, 1985) in which coaxial and confocal hyperboloid and paraboloid mirrors are combined. X-rays are collected through twice total reflections on their inner surfaces. Four pairs of mirrors are nested, and the diameter of the outermost mirror is 1.2 m. These eight mirrors are made of polished Zerodur glass on the surface, and iridium is deposited on the surface.

Figure 3.3 shows the on-axis effective area of the HRMA. The effective area is ~ 800 cm² in ~ 0.1 –2 keV and ~ 300 cm² above 2 keV, decreasing gradually with increasing energy and having little sensitivity above 10 keV. The sharp drop at 2 keV seen in figure 3.3 corresponds to the M-shell absorption edge of Ir.

3.1.2 Advanced CCD Imaging Spectrometer (ACIS)

The ACIS (figure 3.4) was developed by the Pennsylvania State University and the Massachusetts Institute of Technology Center for Space Research to perform imaging, spectroscopy, and time measurements of X-ray sources (Garmire et al.,

¹<https://cxc.harvard.edu/proposer/POG/html/index.html>

TABLE 3.1: Overview of *Chandra* capabilities.

HRMA	Focal length	10.1 m
	Ghost-free FOV	30' diameter
	Plate scale	0'.34 mm ⁻¹
	Effective area	800 cm ² at 1.5 keV
		100 cm ² at 8.0 keV
Angular resolution	0'.5 (half power diameter)	
ACIS-I	Array size	16'.9 × 16'.9
	Bandpass	0.1–10 keV
	Pixel grid	1024 × 1024
	Pixel size	24 μm × 24 μm
	Effective area	600 cm ² at 1.5 keV
		40 cm ² at 8.0 keV
	Minimum row readout time	2.8 ms
	Nominal frame time	3.2 sec (full frame)
	Allowable frame times	0.2 to 10.0 sec
	Frame transfer time	41 μs (per row)

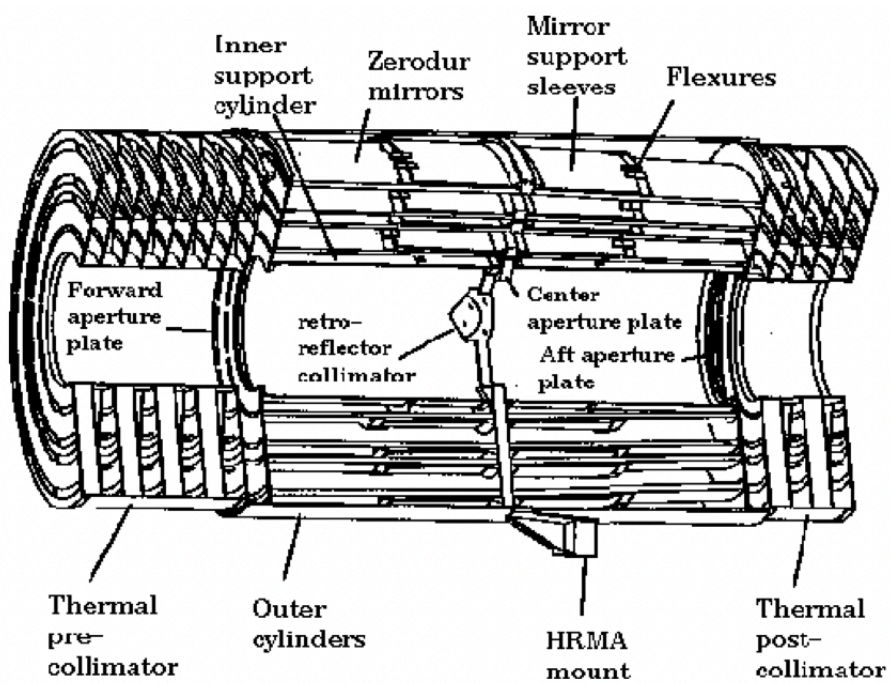
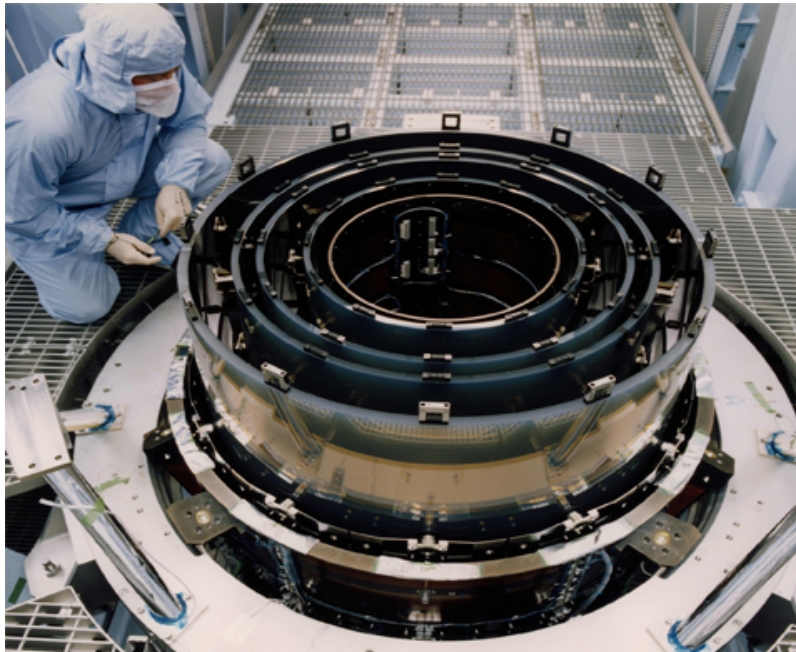


FIGURE 3.2: (top) Photograph of the High Resolution Mirror Assembly (HRMA). Credit: NASA/CXC/SAO. (bottom) Schematic view of the HRMA, taken from *The Chandra Proposers' Observatory Guide*.

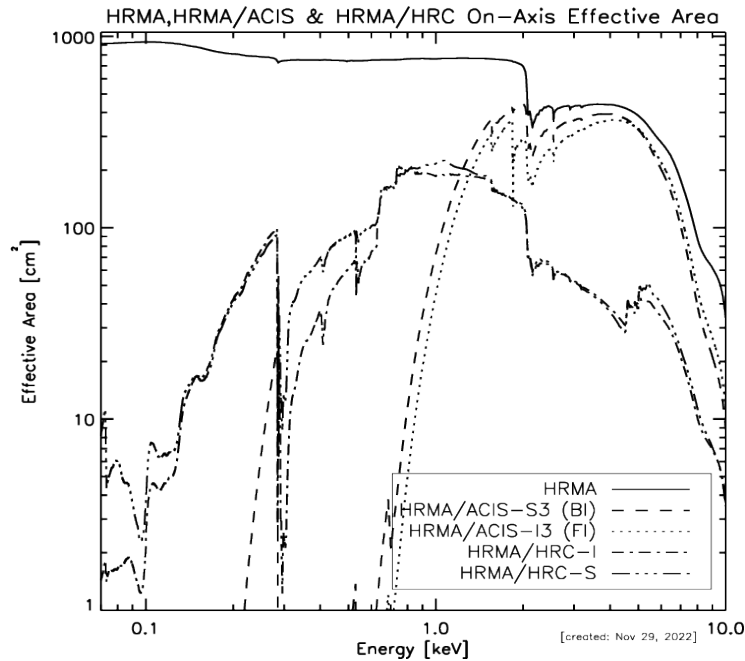


FIGURE 3.3: On-axis effective area versus X-ray energy of the *Chandra* HRMA, HRMA/Advanced CCD Imaging Spectrometer (ACIS), and HRMA/High Resolution Camera (HRC), taken from The *Chandra* Proposers' Observatory Guide.

2003). The ACIS consists of 10 planar CCDs. Four of them are arranged in a 2×2 array (ACIS-I) used for high-resolution imaging, while the others are arranged in a 1×6 array (ACIS-S) used for imaging or a grating spectrum read-out. RCW 38 was mainly observed with the ACIS-I. The present thesis thus deals with the ACIS-I. All ACIS-I detectors consist of front-illuminated (FI) CCDs.

Figure 3.5 shows the ACIS-I pre-launch energy resolution (full width at half maximum). Note that the energy resolution of the FI CCDs was actually degraded due to damage by charged particles as they passed through the radiation belt. It is also known that FI CCDs tend to have a poorer energy resolution the farther they are from the readout port.

3.2 *Suzaku*

The X-ray observatory *Suzaku* (figure 3.6) is the 5th Japanese X-ray astronomy satellite launched by JAXA with the M-V-6 rocket from JAXA's Uchinoura Space Center on 2005 July 10. It orbited in a near-circular orbit at an altitude of 570 km and was operated until 2015. It had a shorter orbital period (96 mins) than *Chandra* but had the advantage of low and stable background, as shown in figure 3.7.

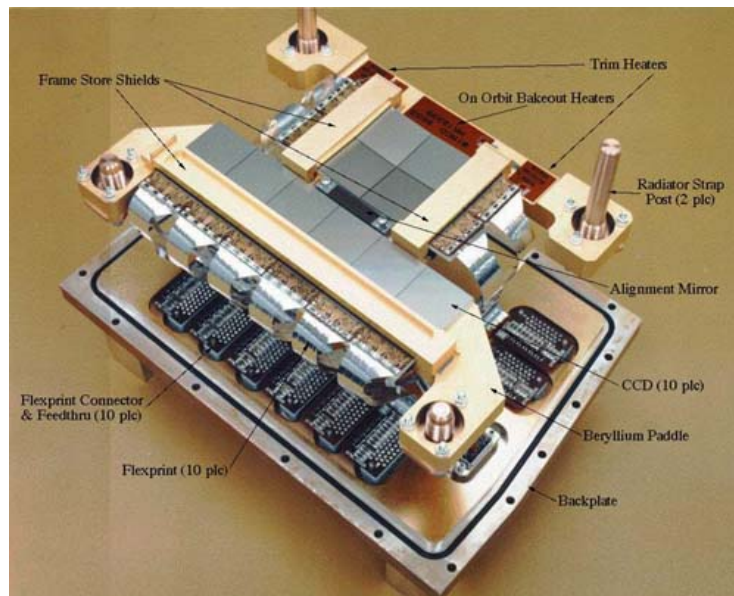


FIGURE 3.4: Photograph of the ACIS. Credit: NASA/CXC/SAO.

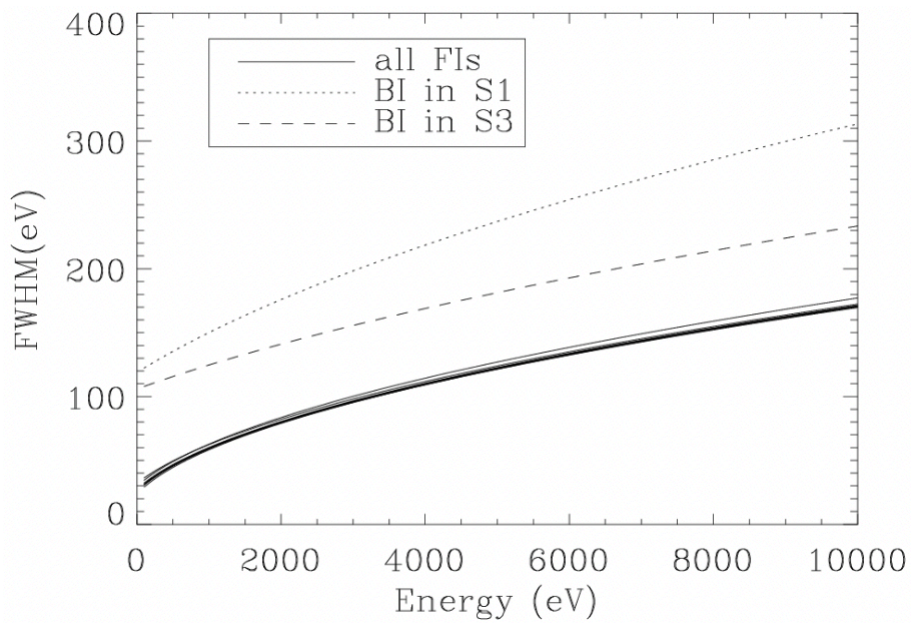


FIGURE 3.5: ACIS pre-launch energy resolution versus X-ray energy for the front-illuminated (FI) and back-illuminated (BI) CCDs, taken from The *Chandra* Proposers' Observatory Guide.

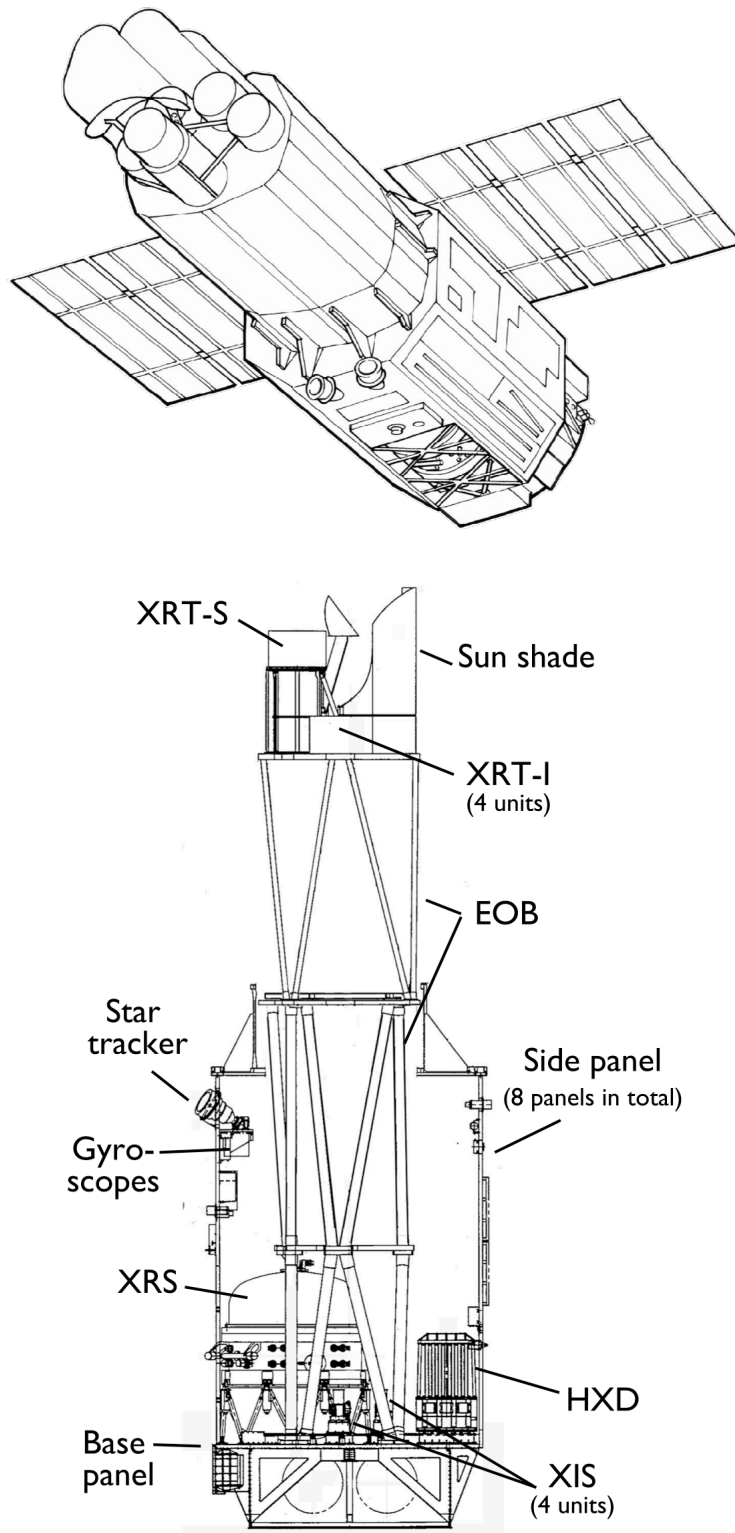


FIGURE 3.6: (top) Schematic view of the X-ray observatory *Suzaku*. (bottom) Side view of *Suzaku* with the internal structures after deployment of the extensible optical bench. Both are taken from Mitsuda et al. (2007).

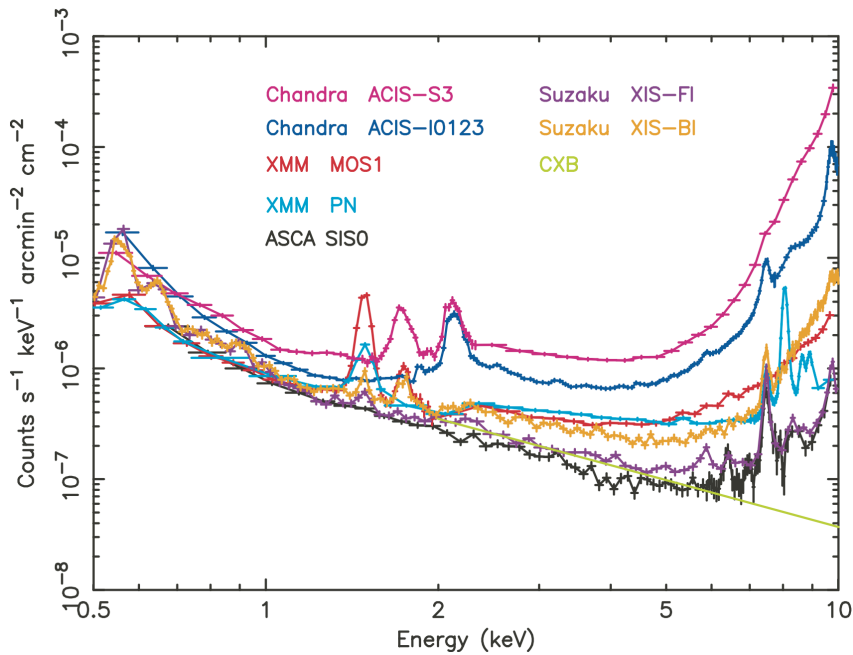


FIGURE 3.7: Background rates of detectors onboard X-ray astronomy satellites as a function of energy (Mitsuda et al., 2007). The rate is normalized with the effective area and the field of view (FOV), which is a good measure of the sensitivity determined by the background for spatially extended sources.

Suzaku's basic performances are shown in table 3.2. *Suzaku* has five X-Ray Telescopes (XRTs: Serlemitsos et al., 2007), four X-ray Imaging Spectrometers (XISs: Koyama et al., 2007), an X-Ray Spectrometer (XRS: Kelley et al., 2007), and a Hard X-ray Detector (HXD: Takahashi et al., 2007). *Suzaku* was designed to allow simultaneous observation of astronomical X-ray sources using six of these detectors and the XRTs. The XRS was a microcalorimeter with an excellent energy resolution of ~ 7 eV. However, the loss of liquid helium in the very early phase hampered its operation in orbit. The HXD is a non-imaging detector with sensitivity to broadband hard X-rays of 10–600 keV. In this thesis, we perform imaging and spectroscopic analysis using the XIS detectors and thus describe the XRT and XIS in the following subsection.

3.2.1 X-Ray Telescope (XRT)

The *Suzaku* XRT (figure 3.8) consists of five telescopes improved from the *ASCA* XRT and was developed by NASA/GSFC, Nagoya University, Tokyo Metropolitan University, and ISAS/JAXA. Four telescopes (XRT-I) focused on the XIS, and

TABLE 3.2: Overview of *Suzaku* capabilities (after Mitsuda et al., 2007).

XRT	Focal length	4.75 m
	FOV	17' × 17' at 1.5 keV
		13' × 13' at 8.0 keV
	Plate scale	0'.724 mm ⁻¹
	Effective area	440 cm ² at 1.5 keV
		250 cm ² at 8.0 keV
Angular resolution	2'.0 (half power diameter)	
XIS	FOV	17'.8 × 17'.8
	Bandpass	0.2–12 keV
	Pixel grid	1024 × 1024
	Pixel size	24 μm × 24 μm
	Energy resolution	~130 eV at 6.0 keV
		~60 eV at 1.5 keV
	Effective area (incl XRT-I)	330 cm ² (FI), 370 cm ² (BI) at 1.5 keV
		160 cm ² (FI), 110 cm ² (BI) at 8.0 keV
Time resolution	8 s (normal mode), 7.8 ms (P-sum mode)	



FIGURE 3.8: Photograph of *Suzaku's* X-Ray Telescope (XRT). Credit: NASA/GSFC

one (XRT-S) focused on the XRS. Wolter type-I optics approximated by two conical cones were adopted. Although the aperture is 40 cm, smaller than the HRMA, the reflection mirrors are made of 175 aluminum plates, are lightweight, and have a larger effective area. In order to enhance X-ray reflectivity, the gold layers are formed on the mirrors as reflection surfaces with a replication method (Serlemittos and Soong, 1996).

Figure 3.9 shows the point spread functions of the XRT-I, which represent the brightness distribution for a point source as a function of the radius from the detector center. The obtained angular resolutions (half power diameter) are $1'8$, $2'3$, $2'0$, and $2'0$ for the XRT-I0, -I1, -I2, and -I3, respectively. The effective area decreases with distance from the center of the field of view (FOV) due to the vignetting effect, as shown in figure 3.10.

3.2.2 X-ray Imaging Spectrometer (XIS)

The XIS was developed by the Massachusetts Institute of Technology, Kyoto University, Osaka University, Rikkyo University, Ehime University, and ISAS/JAXA. It is composed of four X-ray CCDs, as shown in 3.11. Three (XIS 0, 2, and 3) are FI types with a lower-level background and significant sensitivity in 1–10 keV

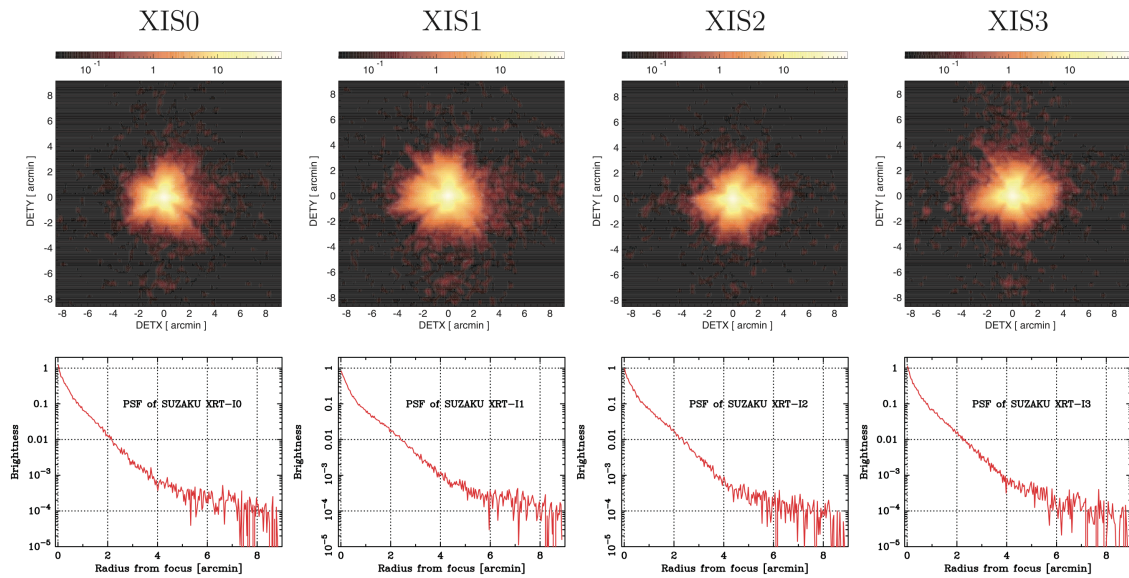


FIGURE 3.9: Image and point spread function of four XRT modules taken from Serlemitsos et al. (2007). All images are binned with 2×2 pixels, followed by smoothing with a Gaussian profile with $\sigma = 3$ pixels, where the pixel size is $24 \mu\text{m}$.

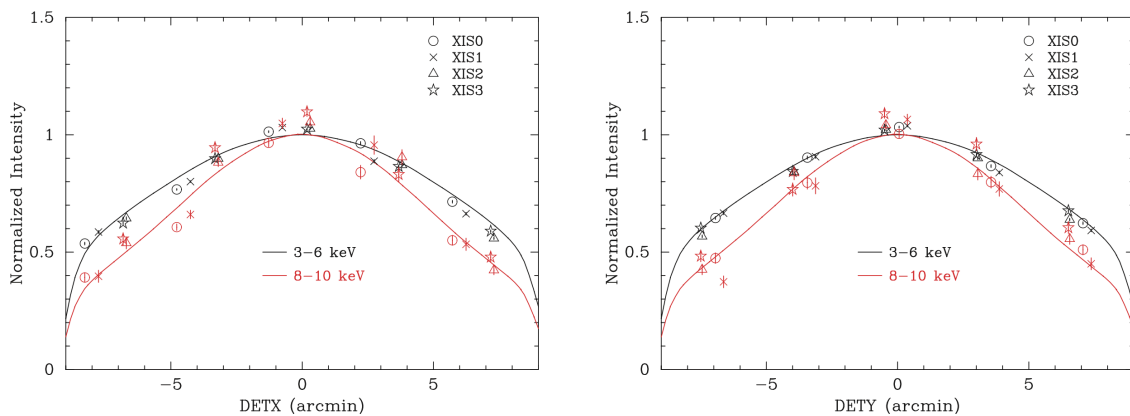


FIGURE 3.10: Vignetting curves of the four XRTs using the Crab Nebula taken during 2005 August 22–27 (Serlemitsos et al., 2007). The model curves were calculated with a ray-tracing simulator.



FIGURE 3.11: Photograph of the four X-ray Imaging Spectrometer (XIS) before installation onto *Suzaku*. Credit: NASA/GSFC

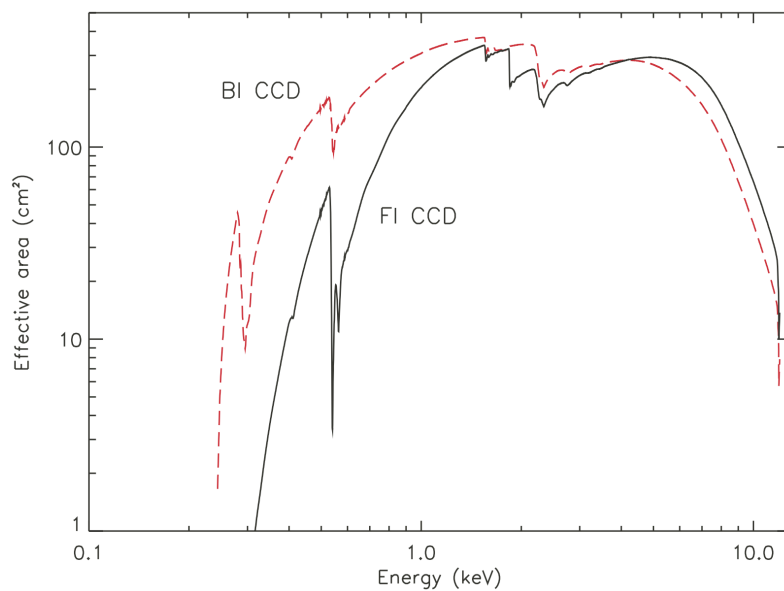


FIGURE 3.12: Effective area of one XRT + XIS system, for both the FI and BI CCDs (Mitsuda et al., 2007).

bands with moderate energy resolution. The other (XIS 1) is a back-illuminated (BI) type with superior sensitivity in the soft X-ray band (<1 keV). Figure 3.12 shows the effective area for both types of CCDs combined with the XRT. Some absorption edges also arise from optical blocking filters and gold on the XRT.

It is known that the XIS performance had gradually degraded immediately after launch due to damage caused by cosmic rays. In particular, the decrease in charge transfer efficiency was the most significant factor. CCD detectors read the energy by forwarding the photoelectrons stored in each pixel and counting the amount with the readout amplifier. Since this transfer is generally not perfect, it is necessary to compensate accordingly for the percentage of charge lost. However, because the loss of charge is a stochastic process, the energy resolution inevitably degrades as the number of transfers increases.

Chapter 4

Observations of MSFRs

4.1 Past reports of diffuse X-ray emission

The excellent angular resolution of *Chandra* has now established the existence of diffuse X-ray emission in multiple MSFRs. Table 4.1 summarizes the emission properties of MSFRs (H II regions) that are likely to exist, as reported by *Chandra*, *XMM-Newton*, or/and *Suzaku*. The diffuse X-ray emission is generally believed to come from hot plasmas, as described in subsection 2.3.5. However, diffuse X-rays in some regions exhibit a hard spectrum and are better explained by a non-thermal model. In this section, we describe each of these possibilities from specific examples and then introduce RCW 38 observations, which is the main target of this thesis.

4.1.1 Evidence for thermal emission

M 17

In the early *Chandra* observations, one of the clearest examples of diffuse X-ray emission associated with massive star formation is H II region M 17 on the edge of a massive molecular cloud at a distance of 1.6 kpc. Townsley et al. (2003) reported the observation of this region for 39 ks with the ACIS-I. The diffuse X-ray emission probably originates from stellar winds. M 17 is a powerful thermal radio source with a high degree of ionization. Its age is estimated to be ~ 1 Myr (Hanson, Howarth, and Conti, 1997; Povich et al., 2009). It has 100 stars earlier than B9, 14 of which are O stars. Some O4/O5 stars are concentrated in the center of the cluster and form a ring-like structure with a diameter of $\sim 1'$ called "Ring of

TABLE 4.1: Past reports of extended X-rays from MSFRs.

Region	Diffuse Area (pc ²)*	N _H (10 ²¹ cm ⁻²)	kT (keV) [†]	L _X (10 ³³ erg s ⁻¹) [‡]	Reference
Arches cluster	14	100	5.7	16	Yusef-Zadeh et al. (2002) [§]
Carina Nebula	1,200	2	0.2, 0.6	171	Hamaguchi et al. (2007) , Ezoe et al. (2009) Ezoe et al. (2019)
Cepheus B/OB3b	5	4.0, 1.0, 1.3	0.31, 0.35, 0.63	0.06	Townsley et al. (2011b) [§] , Townsley et al. (2011c) [§]
Hourglass (Lagoon Nebula)	0.04	5	0.8	≤0.7	Getman et al. (2006) [§]
M 17, Omega Nebula, W 38	42	11.1	0.63	3.4	Raww et al. (2002) [#]
NGC 2024	1<	4	0.13, 0.6	3.5	Townsley et al. (2003) [§]
NGC 3603	50	4.6	0.25	0.04	Hyodo et al. (2008)
NGC 3576 S	15.6	<11, 40	11	20	Ezoe et al. (2006a) [§]
NGC 3576 N	173.8	7	3.1	11	Moffat et al. (2002) [§]
NGC 6334, Cat's paw Nebula	45	13, 2.5	0.31, 0.53	12	Townsley (2009) [§] , Townsley et al. (2011c) [§]
Orion Nebula	>1.6	3.2, 13	0.11, 0.50, 0.67, $\Gamma = 2.1$	2	Townsley (2009) [§] , Townsley et al. (2011c) [§]
Onsala 2 G75.77+0.34	0.3	<10, >20	>1-10 or $\Gamma < 1$	0.055	Ezoe et al. (2006b) [§]
Onsala 2 G75.84+0.40	0.2	0.41	<0.2	0.17	Güdel et al. (2008) [#]
Quintuplet cluster	?	36	5.4	0.26 or 4.7	Skinner, Sokal, and Güdel (2019) [§]
RCW 38	2	42 or 62	2.2 or $\Gamma = 3.9$	≥3	Skinner, Sokal, and Güdel (2019) [§]
Rosette Nebula	47	38	10	1.6	Wang, Dong, and Lang (2006) [§]
Westerlund 1	150	9.5	0.2, $\Gamma = 1.6$	≤0.6	Wolk et al. (2002) [§]
Westerlund 2 (RCW 49)	39	2	0.06, 0.8	>30	Townsley et al. (2003) [§]
W 40	0.2	20	0.7, >3 or $\Gamma = 2$	3.0	Muno et al. (2006) [§]
W 49 A	0.3	4, 12	0.1, 0.8, 3.1 or $\Gamma = 2.3$	54	Townsley et al. (2005) [§]
W 51 A G49.5-0.4	88	10	0.1, 0.9, 4.2 or $\Gamma = 2.2$	0.02	Fujita et al. (2009)
30 Doradus, Tarantula Nebula	30,000	12	2.9	3	Kuhn et al. (2010) [§]
		22	0.66, >15	4.5	Tsujiimoto et al. (2006) [§]
		33	0.27, 4.3	10,000	Townsley et al. (2005) [§]
		510	7		Townsley et al. (2006) [§] , Townsley et al. (2011c) [§]

* Values are for reference only, as distances have not been sufficiently constrained in some regions.

† Temperature of diffuse plasma. If non-thermal emission exists, the photon index of the power-law model is noted.

‡ Absorption-corrected X-ray luminosities are noted for reference only.

§ *Chandra* observations.

|| *Suzaku* observations.

XMM-Newton observations.

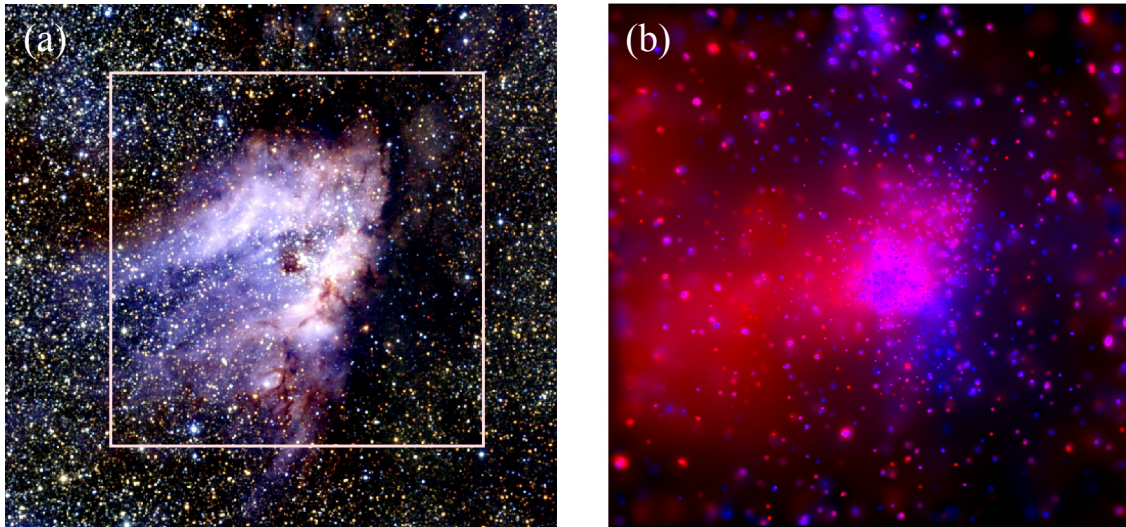


FIGURE 4.1: (a) The JHK_s three color near-infrared (NIR) image of the central region ($23' \times 25'$) of M 17 from the Two Micron All Sky Survey. The square shows the ACIS-I FOV. (b) Adaptively smoothed X-ray image of M 17, taken from the ACIS-I detector ($17' \times 17'$). Two colors correspond to 0.5–2 keV (red) and 2–8 keV (blue). Both images are derived from Townsley et al. (2003).

Fire”, as shown in figure 4.1a. The ionization front of the H II region is in contact with giant molecular clouds along two photo-dissociation regions.

Figure 4.1b shows an X-ray image of M 17 by *Chandra*. In the ACIS-I FOV, >900 point sources were detected. The diffuse emission is spatially concentrated eastward of the Ring of Fire, centrally filling the region delineated by the two bars seen in figure 4.1a. The diffuse emission appears to be independent of the distribution of the point sources. They also have different spectral shapes, as shown in figure 4.2. Townsley et al. (2003) reproduced the spectrum of the diffuse emission with a two-temperature absorbed thermal plasma model with $kT \sim 0.13$ and ~ 0.6 keV, $N_{\text{H}} \sim 4 \times 10^{21} \text{ cm}^{-2}$. The absorption-corrected X-ray luminosity was $\sim 3.4 \times 10^{33} \text{ erg s}^{-1}$ in 0.5–2 keV. In contrast, the point source sum spectrum showed a harder thermal plasma and higher absorption, fitted by $kT \sim 3$ keV and $N_{\text{H}} \sim 1.7 \times 10^{22} \text{ cm}^{-2}$. The point source luminosity was $\sim 1 \times 10^{34} \text{ erg s}^{-1}$, ~ 3 times higher than the diffuse component. They also reported that the temperature of the diffuse plasma did not vary from place to place. That would mean that the hot gas is hardly cooled by the ISM and flows out toward the direction of the lower-density side.

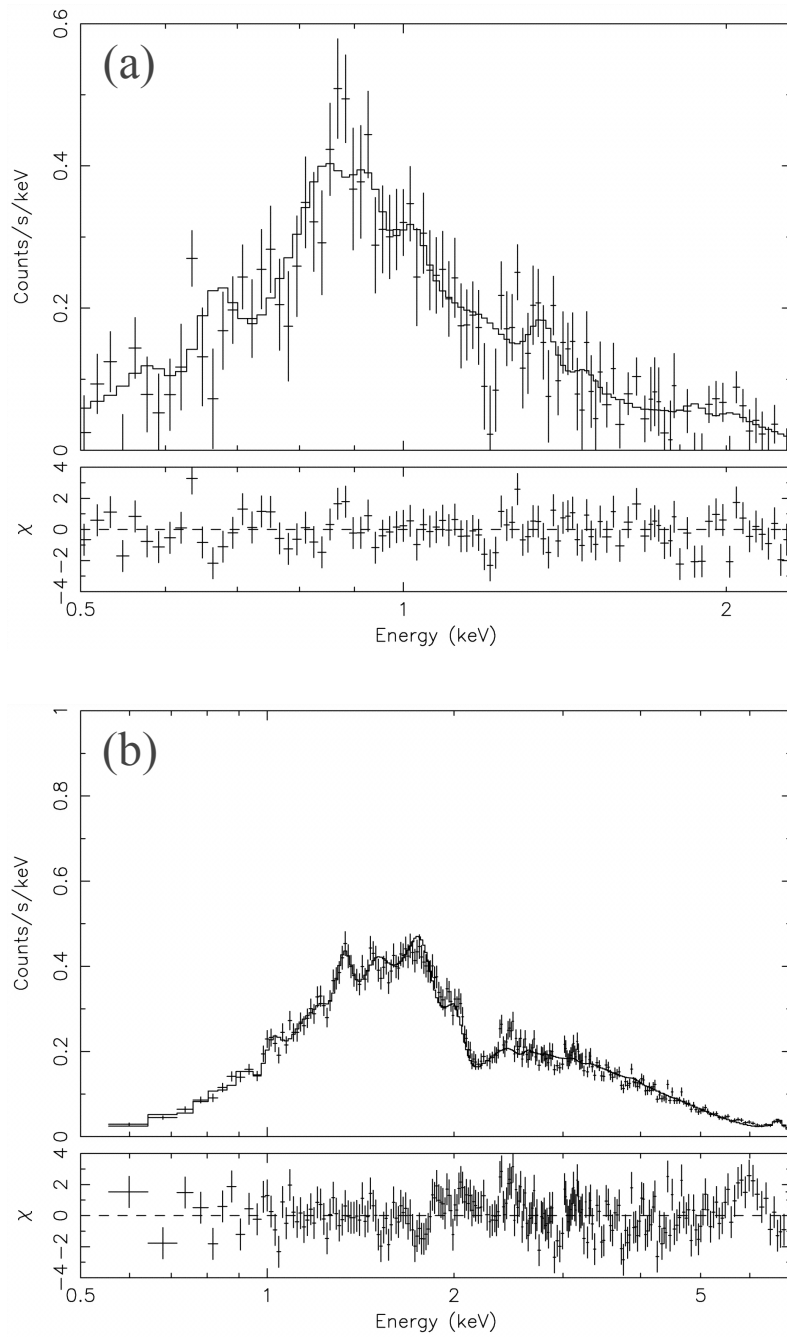


FIGURE 4.2: ACIS spectra of (a) soft diffuse emission and (b) point sources in M 17, taken from Townsley et al. (2003).

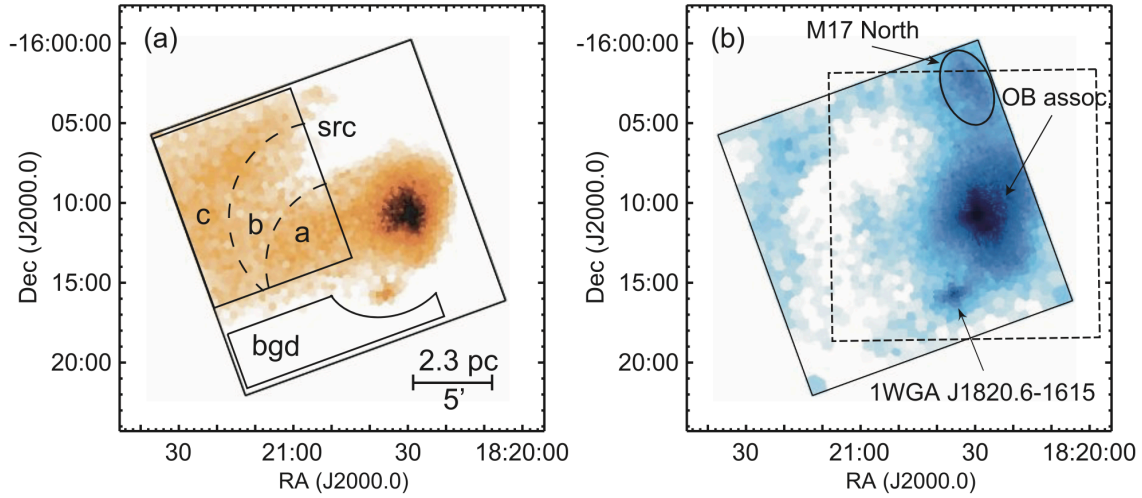


FIGURE 4.3: Adaptively binned XIS images of M 17 in the (a) 0.5–1.5 keV and (b) 1.5–5 keV bands, taken from Hyodo et al. (2008). The source and background regions for diffuse emission are shown by solid lines in (a). The ACIS-I field corresponding to figure 4.1 (b) is shown with the dashed square in (b).

Hyodo et al. (2008) reported 110 ks *Suzaku* XIS observation of M 17. *Suzaku* observed a slightly east region of the *Chandra* observation, as shown in figure 4.3. They showed that the diffuse emission had a comparable absorption ($\sim 4.5 \times 10^{21} \text{ cm}^{-2}$) and absorption-corrected luminosity ($\sim 3.5 \times 10^{33} \text{ erg s}^{-1}$ in 0.5–2 keV) to Townsley et al. (2003), however, it could be represented by a single plasma temperature ($\sim 0.3 \text{ keV}$). It is still considered soft X-rays heated by shock produced by stellar winds. They estimated the elemental abundances to be 0.1–0.3 solar with emission lines in the diffuse spectrum. These values also showed no significant difference by location. They considered that the diffuse plasma had already reached thermal equilibrium.

Carina

We also present the Great nebula in Carina, another diffuse soft X-ray emission report. It is slightly more distant ($\sim 2.3 \text{ kpc}$ by Smith, 2006b) but a much larger star-forming complex. The cluster age is estimated to be $\lesssim 1\text{--}6 \text{ Myr}$ (Feinstein, Fitzgerald, and Moffat, 1980; Sana et al., 2010). The cluster contains at least 66 O stars, 3 WR stars, and the bright blue variable η Carinae (Smith, 2006a; Corcoran et al., 2004; Smith and Brooks, 2008; Hamaguchi et al., 2018). An extensive X-ray survey, *Chandra* Carina Complex Project, was conducted to reveal over 10^4 X-ray

sources and diffuse emission. As shown in figure 4.4, a total of 22 mosaic images ($\sim 1.4 \text{ deg}^2$) were taken with the ACIS-I for 1.2 Ms (Townesley et al., 2011a). We can clearly see diffuse X-ray emission. The diffuse X-ray luminosity is $\sim 10^{35} \text{ erg s}^{-1}$, two orders of magnitude higher than that of M 17.

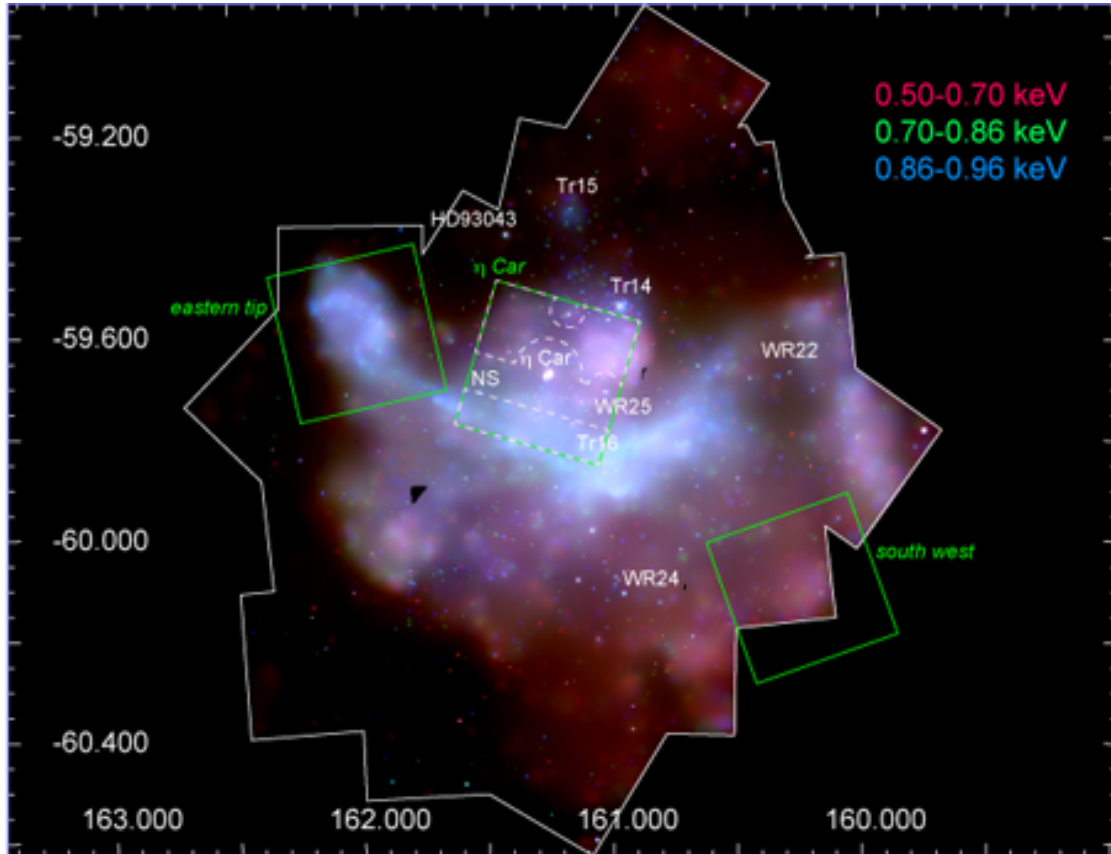


FIGURE 4.4: Adaptively smoothed three-color X-ray image of the Carina Nebula, provided by the *Chandra* Carina Complex Project (Townesley et al., 2011a). The names of white-labeled objects indicate major massive stellar clusters, massive O/Wolf-Rayet (WR) stars, and the middle-age neutron star. The three green boxes show the FOV of the *Suzaku* XIS observations. Taken from Ezoe et al. (2019).

After removing the point sources, Townesley et al. (2011b) divided the diffuse emission region into segments and analyzed their spectra in detail. As a result, almost all X-ray spectra could be reproduced by an absorbed ($N_{\text{H}} \sim 10^{21} \text{ cm}^{-2}$) multiple-temperature (typically three components of $kT \sim 0.1\text{--}1 \text{ keV}$) thermal plasma model. These models generally indicate similar absorptions and plasma

temperatures to the diffuse emission associated with M 17. However, the parameters are slightly variable depending on its position, and its morphology is likely more complex than M 17.

Although Townsley et al. (2011b) assumed a non-equilibrium ionized plasma as diffuse emission, some spectral lines could not be fitted well. One possible explanation for the line defects was the charge exchange. Charge exchange is a reaction in which highly ionized ions in thin hot plasmas take electrons from neutral particles through their collision (Lallement, 2004). The electrons are trapped in the high-excitation states of the ions. They immediately de-excited to the ground state by releasing emission lines corresponding to the energy difference. The charge exchange emission is likely to come from lighter elements such as oxygen and carbon, which are consistent with the energies of the line defects seen in the spectra. Such a reaction may occur when hot plasma comes into contact with the cold surrounding ISM.

Suzaku also observed this region three times. Each area is shown as green squares in figure 4.4: the region around η Carinae (Hamaguchi et al., 2007), the eastern tip region (Ezoe et al., 2009), and the southwest region (Ezoe et al., 2019). These papers also used the *Chandra* and *XMM-Newton* observations to estimate the point source contributions and modeled the diffuse X-ray emission on XIS. The spectra were reproduced by a two-temperature thermal plasma model with common absorption, typically $N_{\text{H}} \sim 2 \times 10^{21} \text{ cm}^{-2}$, $kT \sim 0.2$ and 0.6 keV .

As shown in figure 4.5, Hamaguchi et al. (2007) clearly showed that the XIS spectrum of the thermal plasma around η Carinae contains emission lines from various elements and diagnosed their abundance ratios. They suggested that the obtained ratios are closer to those of supernova remnants. Ezoe et al. (2019) also performed a detailed plasma diagnostic and showed that the abundance ratios are similar to OB stars and type II supernova remnants. Thus, they limited the origin of the diffuse emission. However, the conclusive evidence of the charge exchange suggested by *Chandra* was still not obtained.

Suzaku has a high sensitivity to extended sources and good energy resolution. Therefore, these reports are the most accurate results currently available for diffuse soft X-ray emission. Although these soft diffuse sources have been observationally and theoretically established as thermal plasmas, whether their origin is stellar wind, supernova remnants, or a mixture of them, including charge exchange emission, has not been settled.

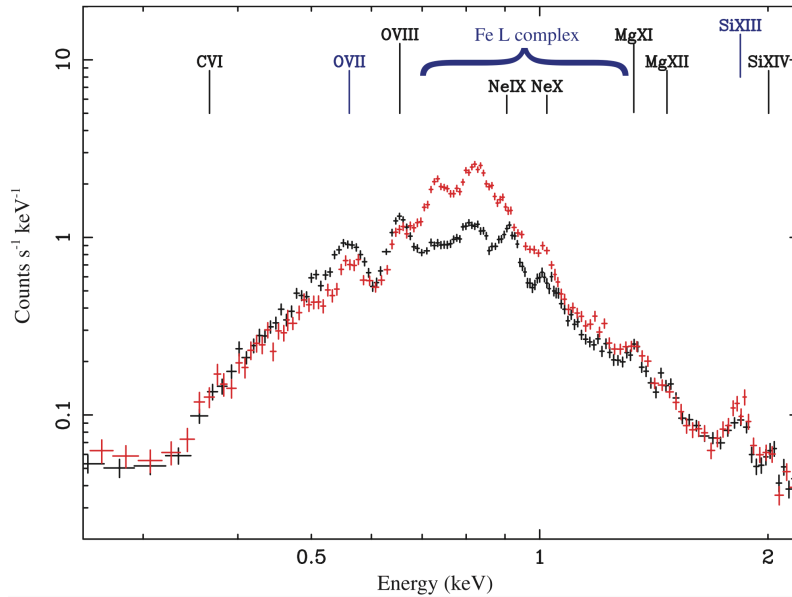


FIGURE 4.5: XIS spectra from the north (black) and south (red) of η Carinae, taken from Hamaguchi et al. (2007). The intensities are normalized. The above labels show detected emission lines.

4.1.2 Possibility of non-thermal origins

NGC 6334

The diffuse emission likely from thermal plasma is often observed below 2 keV, as seen in figures 4.2a and 4.5. However, some MSFRs have diffuse X-rays even at higher energy bands (2–8 keV). As an example, we here review the *Chandra* observation of NGC 6334. It is a giant molecular cloud and an H II region complex located at a distance of ~ 1.2 – 1.7 kpc (Neckel, 1978; Chibueze et al., 2014). It has star-forming cores named I–V in the FIR and A–F in the radio bands, each of which is considered to contain one or more young massive stars. The ages of the clusters are estimated to be 2 Myr or younger, although it probably depends on the location (Persi and Tapia, 2008; Fukui et al., 2018). This region was observed with the ACIS-I for 2×40 ks, as shown in figure 4.6.

Ezoe et al. (2006b) defined an extended emission region of $\sim 10' \times 18'$ ($\sim 6 \times 11$ pc²) within the ACIS-I FOV and analyzed the spectrum. Figure 4.7 compares the spectra of the diffuse X-ray emission and the sum of point sources. The diffuse component was about half the point source contribution and showed a hard spectrum. They divided the region into soft and hard X-ray regions and performed

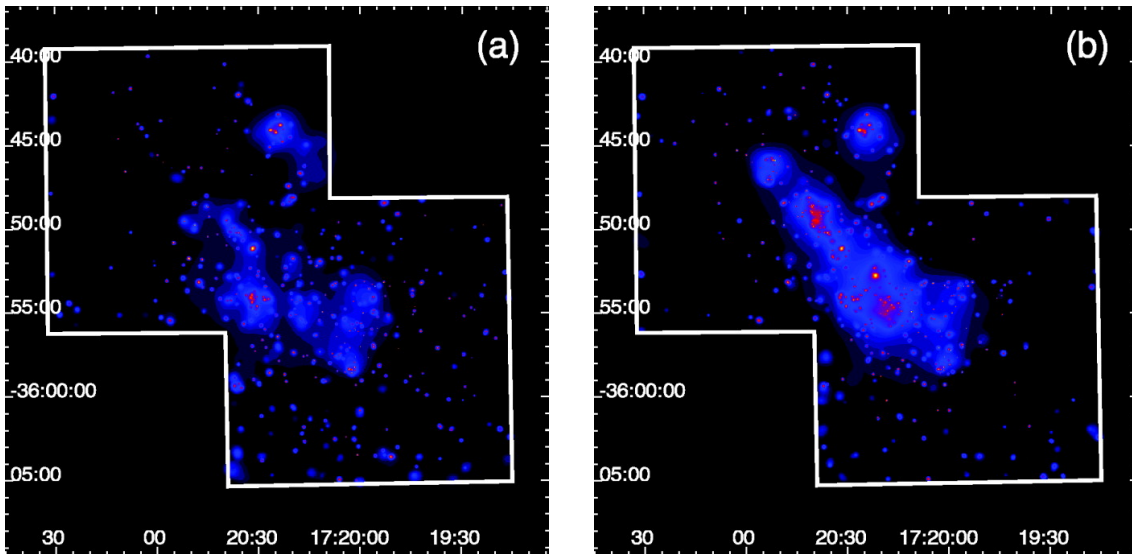


FIGURE 4.6: Adaptively smoothed ACIS-I images of NGC 6334 in the (a) 0.5–2 keV and (b) 2–8 keV bands, taken from Ezoë et al. (2006b). The intensities are plotted logarithmically.

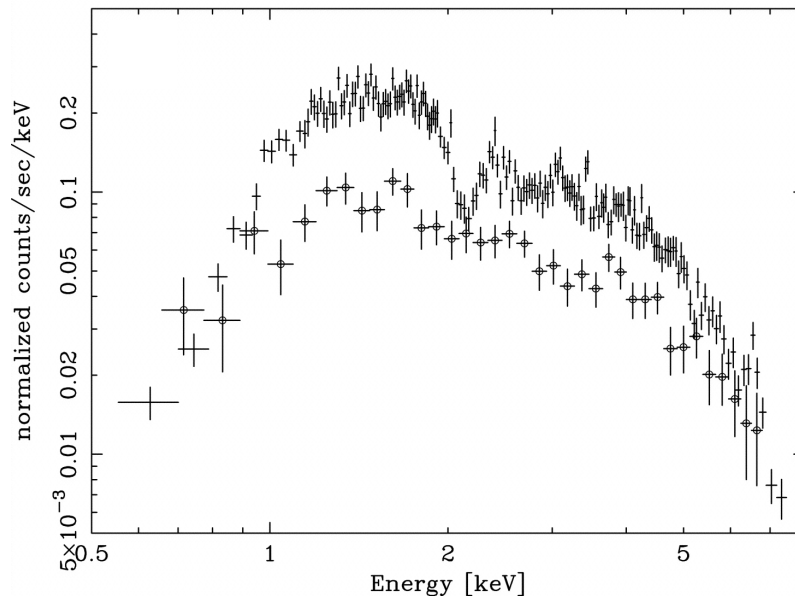


FIGURE 4.7: ACIS spectra of the diffuse component (circles) and summed point sources (crosses) in NGC 6334 (Ezoë et al., 2006b).

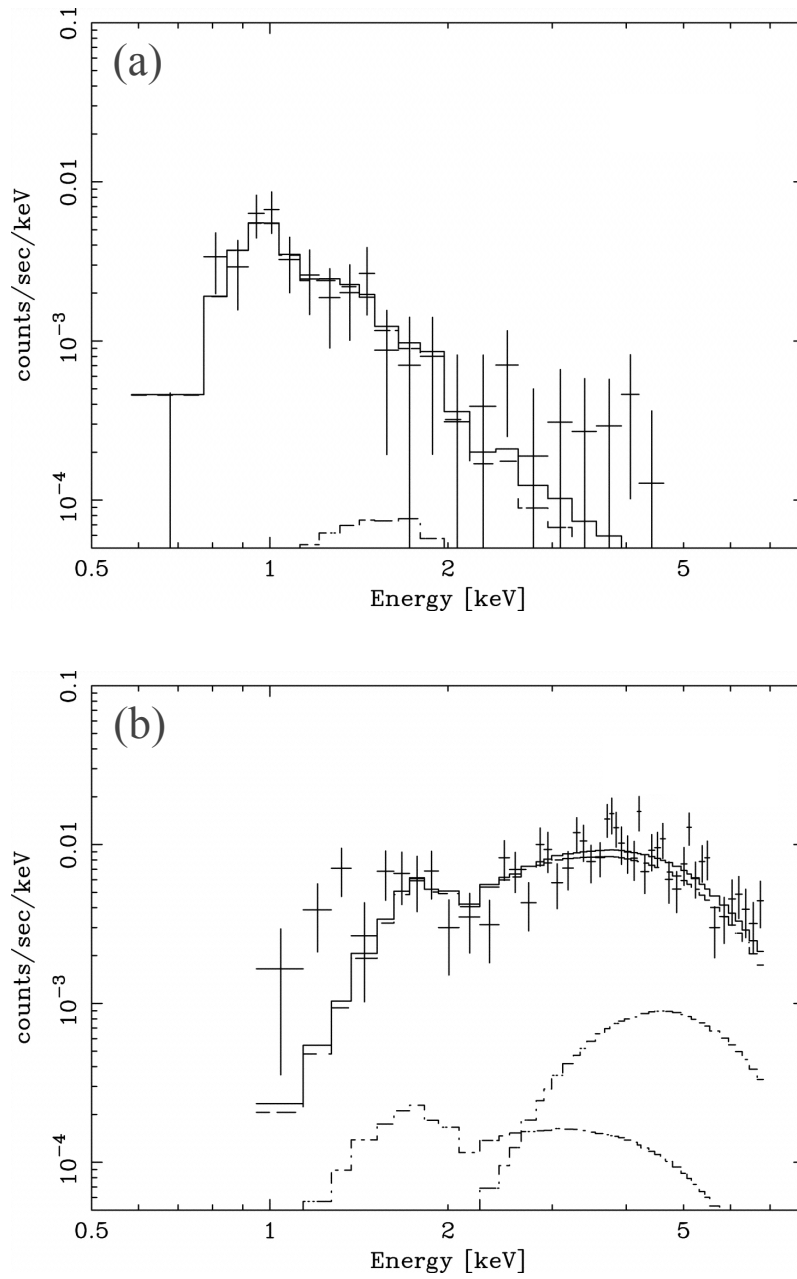


FIGURE 4.8: Examples of ACIS spectra of the diffuse component in (a) soft and (b) hard X-ray regions of NGC 6334 (Ezoe et al., 2006b).

the spectral analysis. They had distinctly different spectral shapes, as shown in figure 4.8. The soft X-ray regions were reproduced by thermal models with low N_{H} values (typically on the order of 10^{21}) and few keV plasmas, while the hard X-ray regions with high N_{H} values (typically on the order of 10^{22}) and ultra-high temperatures ($\gtrsim 4\text{--}10$ keV). They suspected these very hot components were too high for normal stellar plasma. They then attempted the power-law model on the hard regions and found that it reproduced the observed spectrum better than the thermal plasma model. That suggests there may be non-thermal particle acceleration in NGC 6334.

Possible non-thermal X-ray emitting mechanisms include bremsstrahlung, synchrotron emission, and inverse Compton scattering, as described in subsection 2.3.2. Since the photon index of the power-law model was relatively small ($\Gamma \sim 0.4\text{--}1$), Ezoe et al. (2006b) argued that the hard diffuse X-rays were consistent with bremsstrahlung by 10keV to several MeV electrons. The power-law model and the very hot thermal model are similar in shape, and the origin of these hard X-rays has not yet been settled. They discussed that the thermal interpretation is an order of magnitude less restrictive on energy supply than the non-thermal interpretation. Another important insight from the NGC 6334 observation is the suggestion that the gas pressure around massive stars is related to the hardness of the diffuse X-ray emission. This possibility is discussed in subsection 6.5.2 in detail.

RCW 49

We introduce another possible non-thermal origin, the giant H II region RCW 49, which is ionized by the OB association Westerlund 2. It has >10 massive stars, including 2 WR stars (WR20a and WR20b), an O6 star, and 5 O7 stars. Their age is estimated to be 2–3 Myr (Piatti, Bica, and Claria, 1998; Ascenso et al., 2007). As shown in figure 4.9a, RCW 49 is known to have two wind-blown shells (Whiteoak and Uchida, 1997). One is seen around WR20b and the other is located in the center of the OB association, which includes WR20a.

Townsley et al. (2005) reported 36 ks *Chandra* observation of Westerlund 2, as shown in figure 4.9b. They detected >500 point sources in the FOV. More than 100 of them were spatially coincident with the Westerlund 2 cluster. The distribution of the diffuse emission did not appear to be clearly associated with the cluster members. The point source and diffuse component could be classified

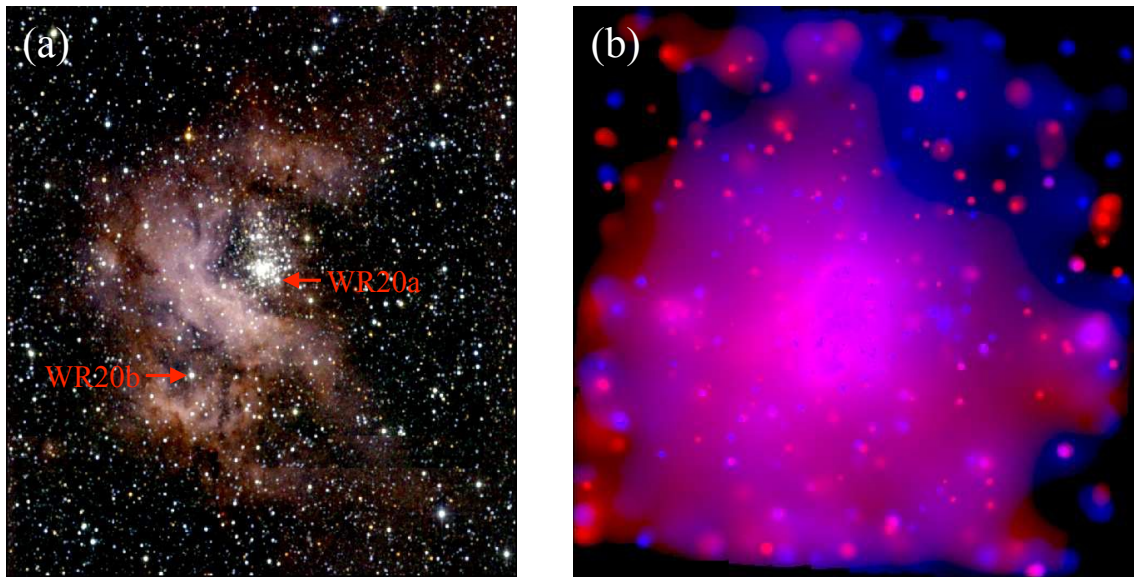


FIGURE 4.9: (a) The JHK_s three color NIR image ($\sim 16' \times 16'$) of RCW 49 centered on its ionizing cluster Westerlund 2. The arrows indicate the positions of two WR stars. (b) Adaptively smoothed X-ray image of RCW 49, taken from the ACIS-I detector ($17' \times 17'$). Two colors correspond to 0.5–2 keV (red) and 2–8 keV (blue). Both images are derived from Townsley et al. (2005)

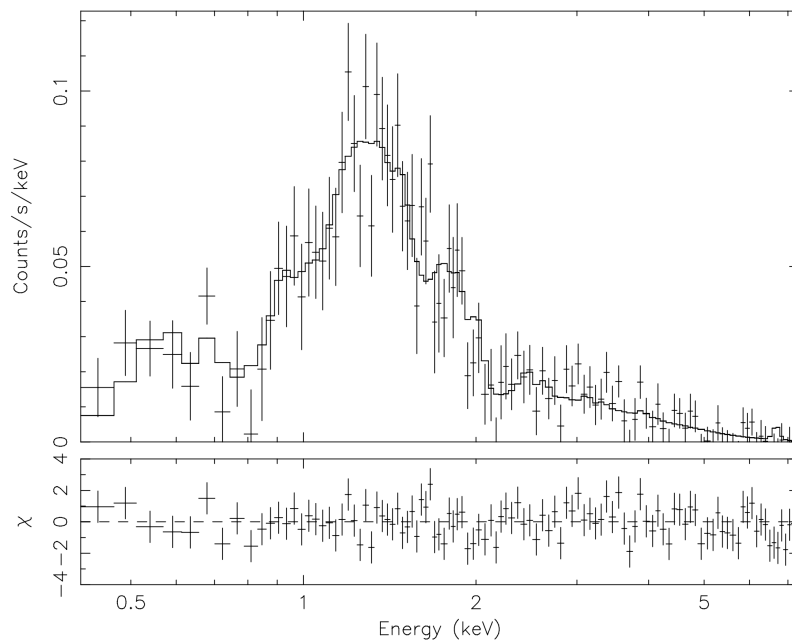


FIGURE 4.10: ACIS spectra of the diffuse emission in RCW 49 (Townsley et al., 2005).

into weak and strong absorption groups. The weakly absorbed diffuse component was reproduced as a thermal plasma model with $N_{\text{H}} \sim 4 \times 10^{21} \text{ cm}^{-2}$ and $kT \sim 0.1 \text{ keV}$. The other was reproduced with $N_{\text{H}} \sim 12 \times 10^{21} \text{ cm}^{-2}$, $kT \sim 0.8$ and 3.1 keV (figure 4.10). Absorption-corrected luminosities of each plasma component were 1.3×10^{33} , 0.8×10^{33} , and $0.9 \times 10^{33} \text{ erg s}^{-1}$ in 0.5–8 keV. Here, while the estimated distance to Westerlund 2 has a range of 2–8 kpc (e.g., Ascenso et al., 2007; Rauw et al., 2007), they assumed 2.3 kpc. In addition, they showed that the spectrum fit was also acceptable when the hottest component was replaced by a power law of $\Gamma = 2.3$.

Fujita et al. (2009) reported the results of *Suzaku* observation of this region. The spectrum of the diffuse emission was reproduced by similar three thermal ($kT \sim 0.1, 0.9,$ and 4 keV) or two thermal ($kT \sim 0.1$ and 1 keV) + non-thermal ($\Gamma \sim 2.2$) models as reported by Townsley et al. (2005). They focused on the non-thermal component because very-high-energy gamma-ray emission has been observed by H.E.S.S. in this region (Aharonian et al., 2007). That could support the existence of non-thermal particles. Furthermore, a sign of a past supernova explosion has also been reported (Fukui et al., 2009). Therefore, Fujita et al. (2009) discussed the possibility that the supernova explosion of a very massive star contributed to particle acceleration. A possible non-thermal scenario is synchrotron emission from accelerated TeV electrons.

4.2 RCW 38

As we have seen in the previous subsection, non-thermal extended X-ray signatures have been observed in multiple MSFRs. In those regions, the non-thermal (hard) components rarely show a strong presence alone and are often observed mixed with thermal components. The MSFR RCW 38 is a representative example reported to have dominant non-thermal X-ray emission by *Chandra*. Hence, this region is a good target for investigating unresolved hard X-ray components associated with young MSFRs.

In this thesis, we perform a combined *Chandra* and *Suzaku* study of the diffuse hard X-ray emission in RCW 38. In subsection 4.2.1, we introduce the basic properties and past observations of this region. Subsection 4.2.2 explain the motivation and method of our study. We present observation data of both X-ray satellites in subsection 4.2.3.

4.2.1 Basic properties and previous results

RCW 38 is a southern young ($\sim 0.1\text{--}1$ Myr) and embedded ($A_V \sim 10$ mag) MSFR located at a distance of 1.7 kpc from Earth (Muzzio, 1979; Avedisova and Palous, 1989; Winston et al., 2011; Getman et al., 2014). A dense molecular cloud envelopes a bright H II region. It is a bright source at multiple wavelengths, especially in the radio band. Figure 4.11 shows images of RCW 38 observed at various wavelengths. Optical light is strongly absorbed in the center of the region. Therefore, the investigation has been mainly performed on infrared, radio, and X-ray bands.

Two powerful infrared sources are well-known in RCW 38. The brightest at $10\ \mu\text{m}$ is called IRS 1, and the brightest at $2\ \mu\text{m}$ is called IRS 2 (Frogel and Persson, 1974). IRS 1 has another peak in the radio band and is believed to be a dust ridge extending from north to south over $0.1\text{--}0.2$ pc (Smith et al., 1999). On the other hand, IRS 2 is considered to be an O5.5 binary (DeRose et al., 2009). In the central region of RCW 38, two areas are cleared of dust and form cavities, as shown in figure 4.11c. One has a radius of 0.1 pc centered on IRS 2, and the other is a similar size and located just west of IRS 1. These cavities may have formed by feedback from the massive stars. In the radio band, Fukui et al. (2016) reported the presence of two major molecular clouds with different velocities. They proposed that the cloud-cloud collision triggered the formation of massive stars.

RCW 38 has just completed the ultracompact H II region phase. IRS 2 is the major ionization source. The cluster has $>1,300$ member stars, of which >30 have been considered OB stars (Lada and Lada, 2003; Wolk et al., 2006; Broos et al., 2013; Kuhn, Getman, and Feigelson, 2015). In terms of MSFRs with members of this class, RCW 38 is one of the nearest regions after the well-studied Orion Nebula Cluster (~ 0.4 kpc), which means a good target for investigating active star-forming sites.

In the 2000s, *Chandra* revealed the X-ray spatial structures of RCW 38 in detail. Wolk et al. (2002) first reported the discovery of extended X-ray emission. They detected ~ 190 distinct X-ray sources from the central $2'.5 \times 2'.5$ region with PWDetect code (Damiani et al., 1997). Even after removing these contributions, the X-ray counts in the central region were still 3 times higher than the $5'$ off-axis background. They suspected that there was some diffuse X-ray source.

They compared the extended emission with near-infrared K_s -band images and

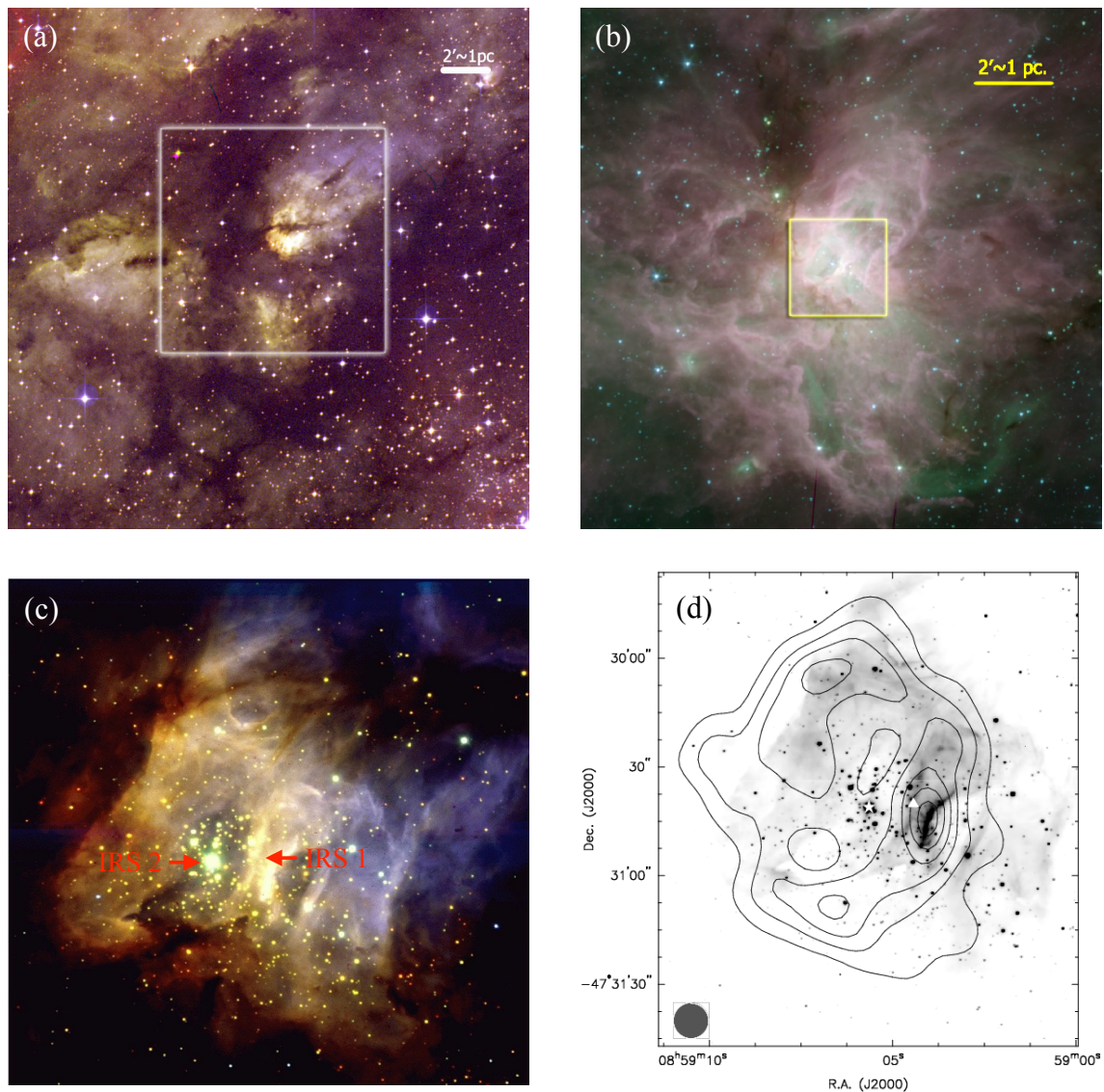


FIGURE 4.11: Observations of RCW 38 at various wavelengths (Wolk et al., 2008). (a) An optical image, about $20'$ (~ 10 pc) on a side. Blue plates are printed as blue, red plates are printed as yellow, and NIR data are printed in red from the digitized sky survey. The box corresponds to the field of (b). (b) Mid-infrared (MIR) image, about $11.5'$ (~ 5.6 pc) on a side, from *Spitzer* observations. The blue, green, and red correspond to 3.6 , 4.5 , and $5.6 \mu\text{m}$ emissions, respectively. The box is more detailed in (c) and (d). (c) A close-up of the central $2.5' \times 2.5'$ region, taken from Very Large Telescope. The Z band is shown in blue, the H band is green, and the K band is red. The arrows show bright infrared emission regions IRS 1 and IRS 2. (d) 6 cm radio continuum contours from Australia Telescope Compact Array overlain on the Very Large Telescope K-band image. The white triangle and star indicate the position of IRS 1 and IRS 2. The contour levels are 15%, 30%, 45%, 60%, 75%, and 90% of the peak emission. The synthesized beam of $10''$ is shown at the lower left.

showed that the spatial distribution differs from the point sources, as shown in figure 4.12. To ensure the extended emission differs from the point sources, they analyzed the spectra of IRS 2 and the extended emission. While the former was fitted only by a thermal bremsstrahlung model with $kT = 1.7$ keV and $N_{\text{H}} = 1.4 \times 10^{22} \text{ cm}^{-2}$, the latter could not be represented with the similar model because the spectrum drops off slowly toward the high-energy band, as shown in figure 4.13. The power law with the photon index of 1.6 and a weak thermal component of 0.19 keV with $N_{\text{H}} = 9.5 \times 10^{21} \text{ cm}^{-2}$ represented the data well. They concluded that this strange extended emission was truly diffuse.

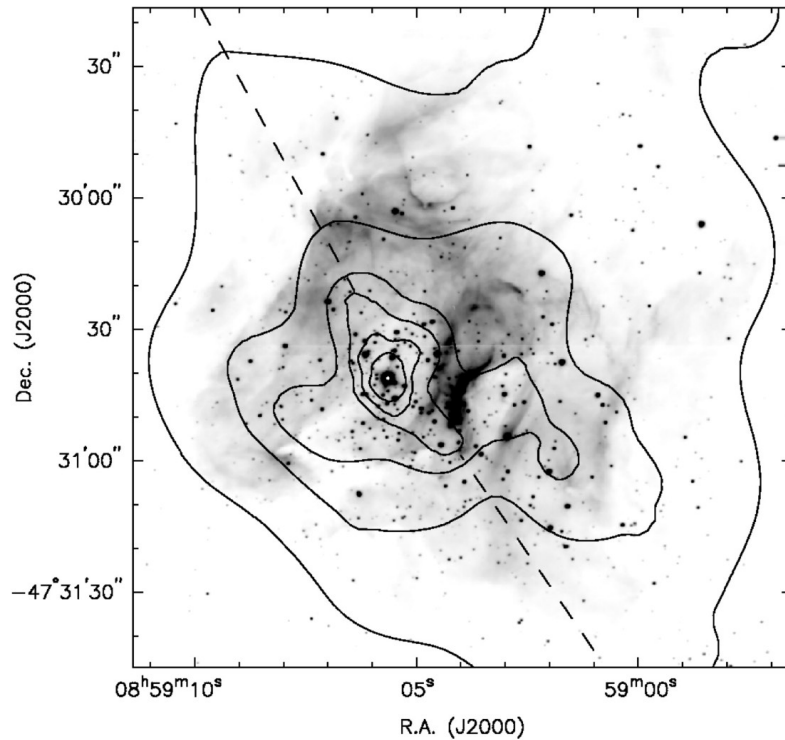


FIGURE 4.12: Extended X-ray contours (corresponding 0.16, 0.4, 0.8, 1.6, 3, and 5 X-ray counts pixel^{-1} outer to inner) overlaid on a K_s -band image of RCW 38, taken from Wolk et al. (2002). The image is $\sim 2'.5$ (~ 1.25 pc) on a side. O5.5 binary IRS 2 is centered on the contours.

Although diffuse thermal emissions associated with massive star formation had been detected with *Chandra*, a hard spectrum like RCW 38 was unprecedented at that time. Moreover, compared with subsequent reports of non-thermal emission (see subsection 4.1.2), the power-law model for this region is notable in that it can explain most of the diffuse emission. Wolk et al. (2002) further divided the region into four subregions (Outer NW, Inner NW, Core, SE) and fitted the

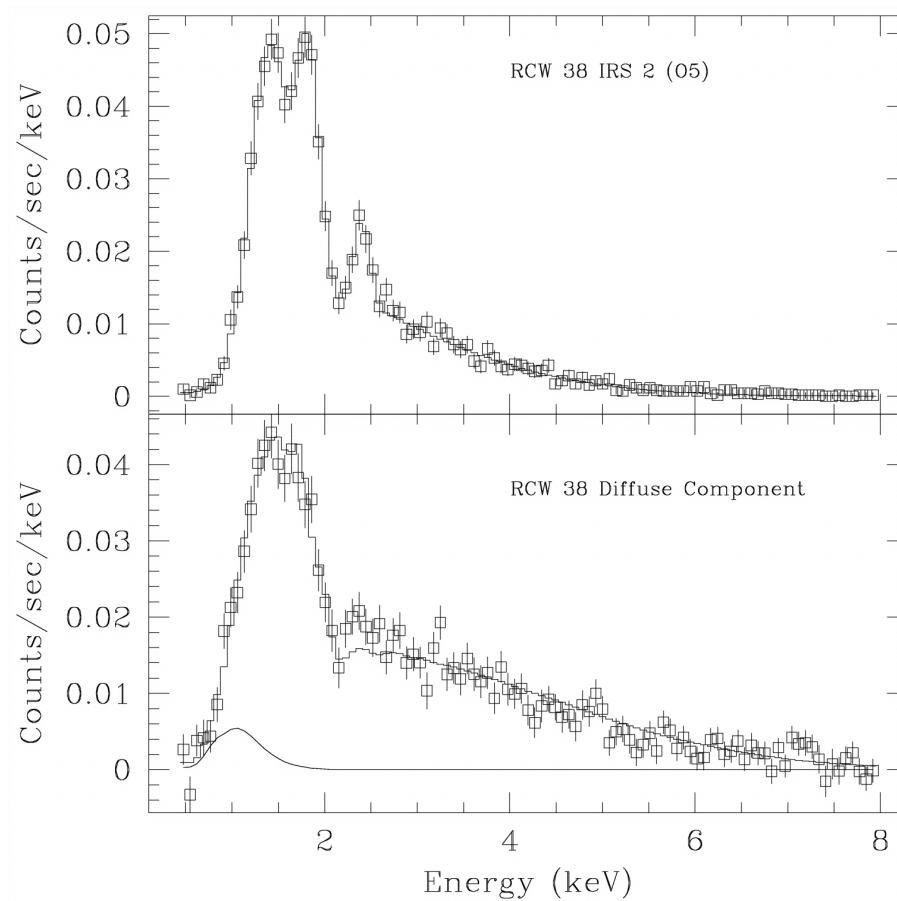


FIGURE 4.13: (top) X-ray spectrum of the O star IRS 2. An absorbed thermal bremsstrahlung model is fitted to the data. (bottom) X-ray spectrum of the diffuse emission in RCW 38. The data are fitted to an absorbed power law with a small thermal component (solid line). Taken from Wolk et al. (2002).

same model to each diffuse component, as shown in figure 4.14. As a result, they found that the absorption column density increased from $0.8 \times 10^{22} \text{ cm}^{-2}$ to $1.6 \times 10^{22} \text{ cm}^{-2}$ from northwest to southeast. This tendency was consistent with the NIR extinction data. The diffuse emission of each subregion was represented by a dominant non-thermal component of $\Gamma = 1.3\text{--}2.8$ and a thermal component of $kT = 0.2\text{--}1 \text{ keV}$. The photon indices Γ showed steeper (larger) values toward the center.

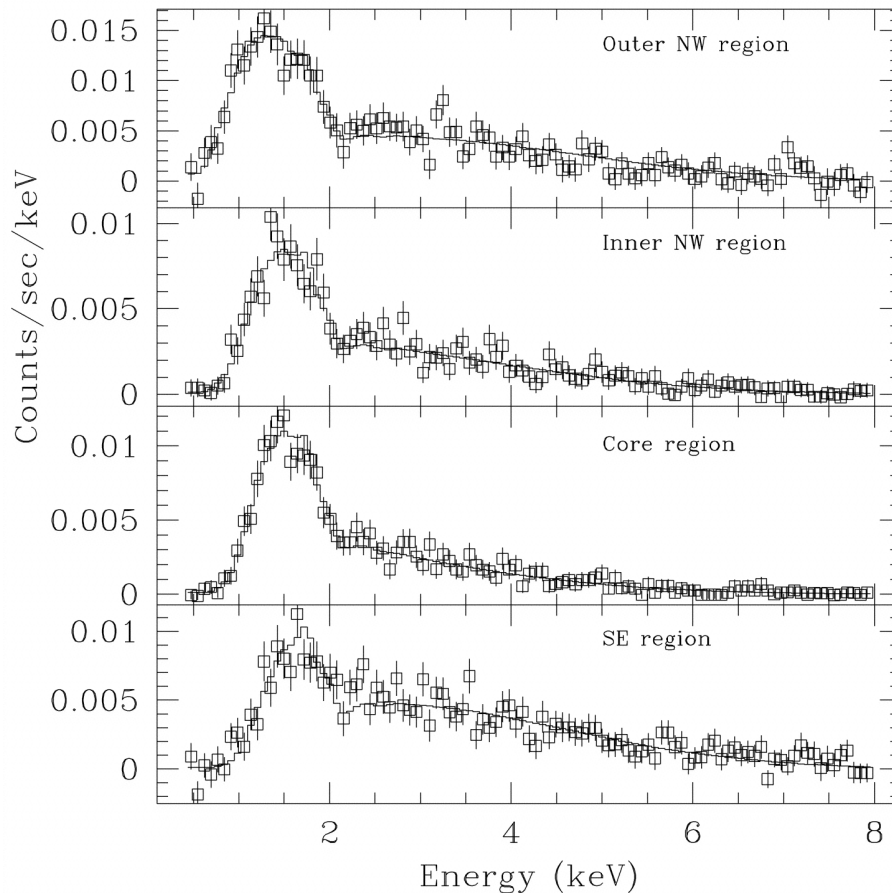


FIGURE 4.14: X-ray spectra of the diffuse emission from four subregions of RCW 38, taken from Wolk et al. (2002).

Objects with power-law X-ray spectra include, for example, supermassive black holes at the center of galaxies and supernova remnants (e.g., Band and Malkan, 1989; Bykov and Toptygin, 2001; Parizot et al., 2004). These X-ray emissions are believed to come from particles accelerated to extremely high energies. Such particles in MSFRs may be accelerated by fast stellar winds or supernova explosions

of massive stars. Wolk et al. (2002) argued that an embedded supernova remnant located $6'$ north of the cluster center, suggested by Two Micron All Sky Survey, could be a possible energy source and predicted the non-thermal emission mechanism of RCW 38 is synchrotron emission.

Wolk et al. (2006) focused on point sources in RCW 38 and reported a detailed study. Using `PWDetect` code, they identified 460 X-ray point-like sources with luminosities of 10^{30} – $10^{33.5}$ erg s^{-1} within the ACIS-I FOV ($17' \times 17'$). In addition, they developed “quartile analysis” referring to X-ray color and spatial properties, and divided the detected point sources into those associated with RCW 38 (members) and foreground/background sources (nonmembers). According to their analysis, 360 of the detected sources are stars in this cluster. Figure 4.15 shows the equatorial coordinate positions of the X-ray cluster members and nonmembers. While the nonmembers are almost uniformly distributed, the members are clustered around $\sim 10''$ (~ 0.1 pc) west of IRS 2, and the peak density is ~ 400 X-ray sources pc^{-1} . An estimate of the luminosity function suggests that this cluster contains at least 2,000 X-ray point sources, including undetected sources. Together with these results, Wolk et al. emphasize the conclusion that diffuse emission does exist. Their results are useful for the present thesis and are discussed again in subsections 5.2.2 and 6.2.1.

4.2.2 Motivations

The diffuse X-ray emission in RCW 38 had an impact because it showed an unprecedentedly hard spectrum. However, whether it includes contributions of the dark and undetected point sources was questioned (Townesley et al., 2003) because it resembles the point-source spectrum (i.e., thermal energy distribution). Indeed, we can see line-like structures in some subregions (e.g., ~ 7 keV in the Outer NW region, figure 4.14). However, the photon statistics and energy resolution need to be improved to resolve.

The origin of non-thermal X-ray emission is also still unclear. If the diffuse X-rays are the synchrotron emission, as suggested by Wolk et al. (2002), the presence of a magnetic field is required in addition to high-energy electrons. In RCW 38, the magnetic field strength was estimated to be 38 ± 3 μG by measuring the Zeeman effect (Bourke et al., 2001). The peak energy E_p of the synchrotron emission is known to be $E_p = 0.29h\nu_c = 0.29h \times 3\gamma^2 eB \sin\alpha / 2\pi mc$, based on equation 2.12. Assuming that this peak energy is consistent with the *Chandra* observation (figure

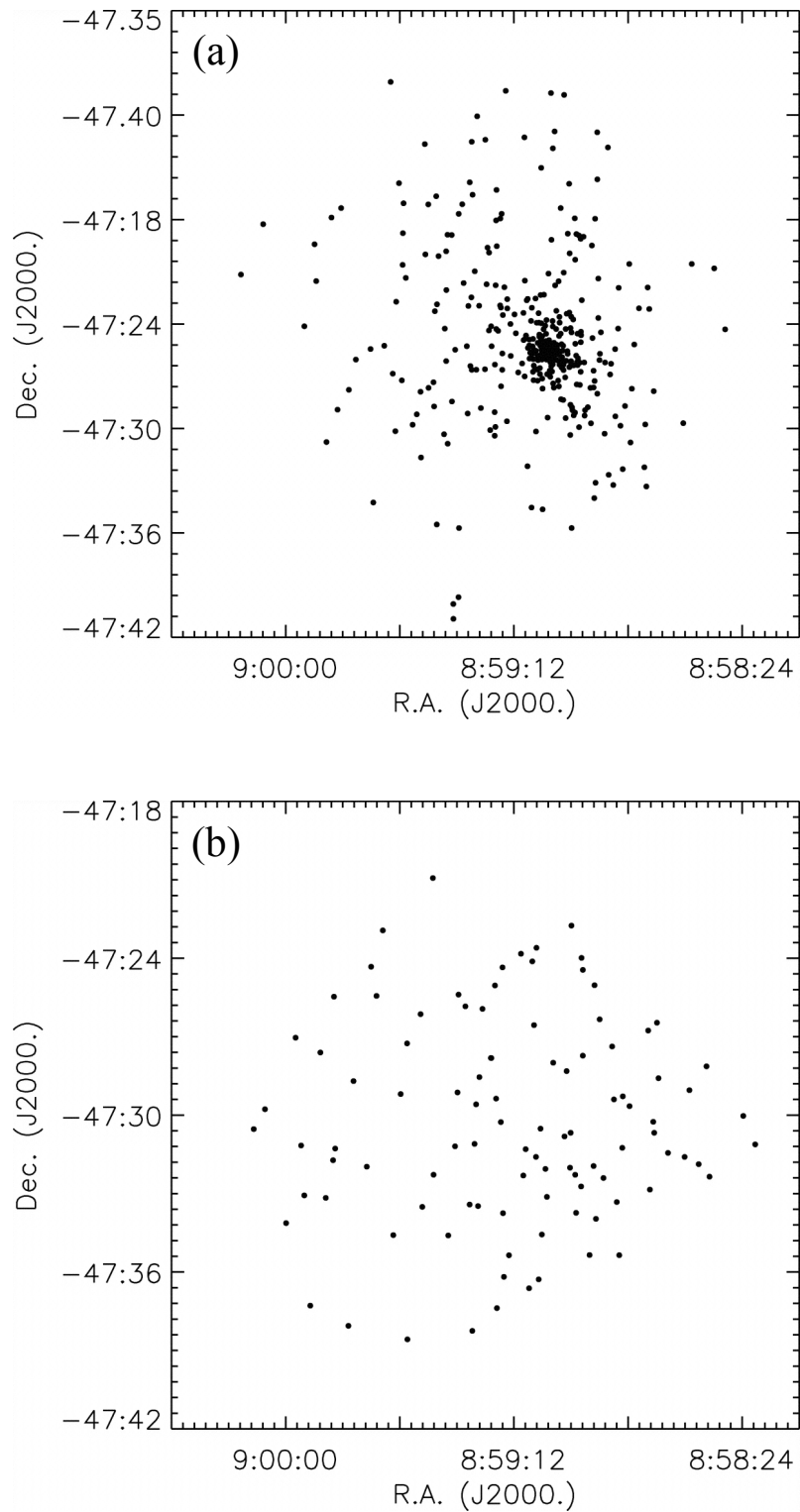


FIGURE 4.15: Position plots of (a) RCW 38 cluster members and (b) nonmembers, taken from Wolk et al. (2006).

4.13), the electron energy E_e can be roughly estimated as follows:

$$E_e \sim 30 \text{ TeV} \left(\frac{E_p}{1 \text{ keV}} \right)^{1/2} \left(\frac{B}{38 \mu\text{G}} \right)^{1/2}. \quad (4.1)$$

However, no such TeV sources have been detected in this region up to the present (e.g., TeVCat¹, see Horan and Wakely, 2008). Therefore, there is still no conclusive evidence of synchrotron emission in this region. Thus, the hard diffuse X-ray emission is not well understood, including its existence.

This thesis aims to investigate the diffuse X-ray emission in RCW 38. We examine the origin using spectra extracted from RCW 38 with *Suzaku* and *Chandra*. The emission line structures on the spectrum are important to distinguish whether X-ray emission is non-thermal or thermal. *Suzaku* is ideal for this purpose since it has a low background, a large effective area, and a superior spectral resolution.

In order to analyze the diffuse X-ray emission with *Suzaku*, we must separate the emission from contaminating sources. There are numerous point-like sources and astrophysical foreground and background emissions in the FOV. To extract the diffuse emission, we need to estimate their contribution and subtract them from the RCW 38 X-ray spectrum. *Chandra* has an excellent angular resolution and helps distinguish point source contributions. The diffuse emission in RCW 38 is mixed with bright point sources. Therefore, both satellites play complementary roles in this study.

It is useful to extract a reference spectrum from a blank region to remove foreground and background contributions. However, it is difficult to extract regions free from point sources and diffuse emission within the XIS FOV of RCW 38. Therefore, we used RX J0852.0-4622 NW offset observation near RCW 38 to estimate foreground and background emissions. Details of these observations are presented in the following subsection.

4.2.3 Observations

This thesis uses the following three observations to analyze the diffuse X-ray emission. Detailed information on the observations is given in table 4.2.

¹<http://tevcat.uchicago.edu>

(1) *Suzaku* observation of RCW 38

This is the main observation for analyzing the diffuse X-ray emission. RCW 38 was observed with the XRT and XIS for 72.2 ks.

(2) *Chandra* observation of RCW 38

This observation was first reported by Wolk et al. (2002). In this study, it is only used to estimate the contribution of point sources. RCW 38 was observed with the HRMA and ACIS-I for 96.7 ks.

(3) *Suzaku* observation of RX J0852.0-4622 NW offset

This is the region observed as the offset of a supernova remnant RX J0852.0-4622 (Hiraga et al., 2009; Takeda et al., 2016). The aim point is only 28' away from RCW 38. In our study, it is used to estimate foreground and background contributions. This offset region was observed with the XRT and XIS for 34.8 ks.

(1) *Suzaku* observation of RCW 38

RCW 38 was observed with the *Suzaku* XIS on 2008 November 18–19. In the *Suzaku* data analysis of RCW 38, we only use XIS 0, 1, and 3 because XIS 2 has not been in operation since 2006 November due to an accident². The XIS 0, 1, and 3 were operated in normal full-frame clocking mode with the spaced-raw charge injection (Nakajima et al., 2008; Uchiyama et al., 2009). We downloaded the data from the HEASARC archive (processing version 3.0.22.43) and analyzed the standard cleaned event data using the HEASoft analysis package version 6.30.

Figure 4.16 shows soft and hard X-ray images of RCW 38 observed with *Suzaku*. The center of the XIS image is almost consistent with the cluster center. The X-ray intensity decreases almost monotonically with increasing radius from the center. We define the emission region as a circle with a radius of 5'5 from the cluster center. The equatorial coordinates of the region center are $(\alpha, \delta)_{J2000.0} = (08^{\text{h}}59^{\text{m}}02^{\text{s}}.0, -47^{\circ}30'41''.0)$, which translates to galactic coordinates $(l, b) = (267^{\circ}56'04''.4, -1^{\circ}03'55''.6)$. In order to study the diffuse emission characteristics, the emission region with a central radius of 2'0 is defined as an inner region and the external annular region of 2'0–5'5 as an outer region.

²http://www.astro.isas.jaxa.jp/suzaku/doc/suzaku_td/

TABLE 4.2: Log of observations.

Data Set Name	Obs. ID	Date	Exposure	Aim Point (RA, Dec)_{J2000.0}	Satellite
RCW 38	503054010	2008 Nov. 18	72.2 ks	(08 ^h 59 ^m 03 ^s .4, -47°30'55".4)	<i>Suzaku</i>
	2556	2001 Dec. 10	96.7 ks	(08 ^h 59 ^m 20 ^s .7, -47°30'14".0)	<i>Chandra</i>
RX J0852.0-4622 NW offset	500010020	2005 Dec. 23	34.8 ks	(09 ^h 00 ^m 30 ^s .7, -47°54'36".7)	<i>Suzaku</i>

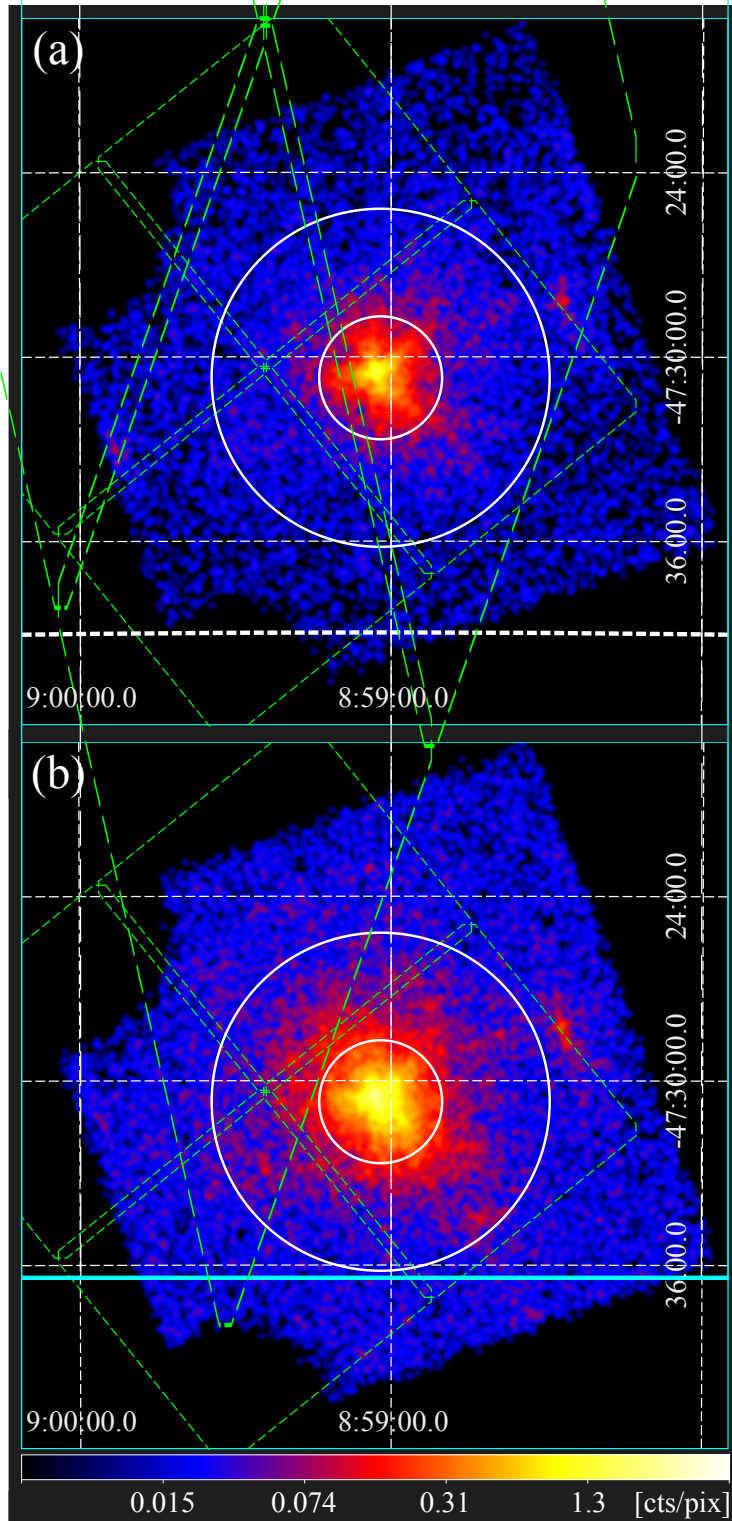


FIGURE 4.16: *Suzaku* XIS 0 + 3 image of RCW 38 in (a) 0.2–2 keV and (b) 2–10 keV. The two far-end corners of the ^{55}Fe calibration sources are removed. These images are smoothed by a Gaussian function with $\sigma = 5$ pixel. The circles correspond to the regions with a radius of 2'0 and 5'5, respectively. The green dashed regions correspond to the *Chandra* ACIS-I FOV.

(2) *Chandra* observation of RCW 38

Chandra observed RCW 38 on 2001 December 10–11, using the ACIS-I in a very faint mode. We downloaded the data from archives and analyzed them with *Chandra* Interactive Analysis of Observations³ (CIAO) software version 4.14. We reprocessed the data using the CIAO `chandra_repro` script. Figure 4.17 shows an X-ray image of RCW 38 observed with *Chandra*. We can see many point sources. At least 460 X-ray point sources in the FOV have already been identified (Wolk et al., 2006). The ellipse is the background extraction region for the point source analysis in subsection 5.2.2.

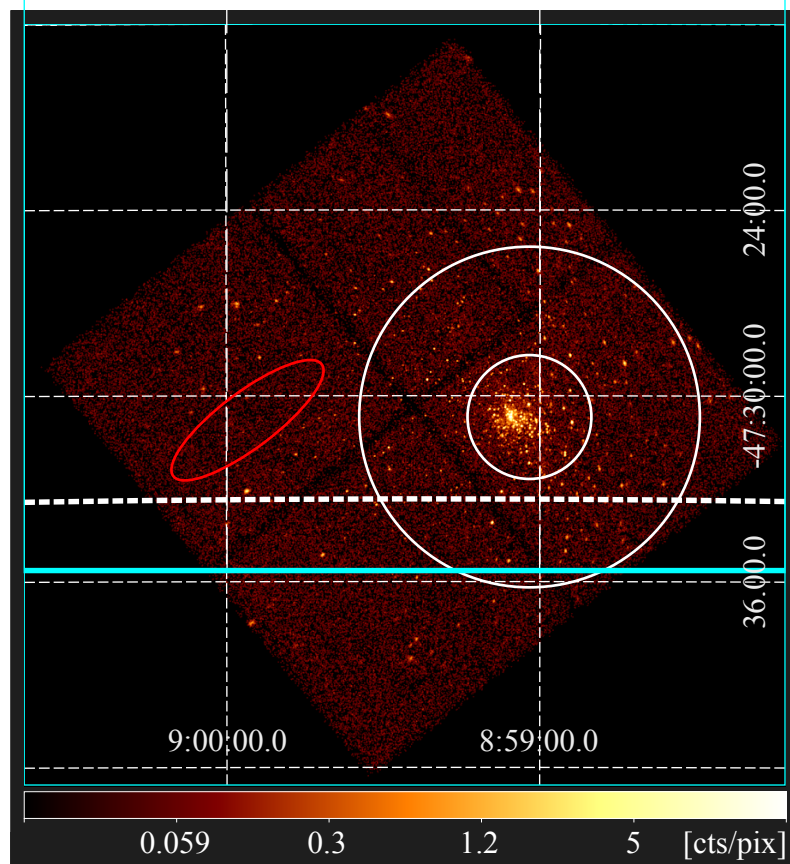


FIGURE 4.17: *Chandra* ACIS-I image of RCW 38. The image is smoothed by a Gaussian function with $\sigma = 2$ pixel. The circles are the same as in figure 4.16. The ellipse is the background region used in point-source spectral analysis.

³<https://cxc.harvard.edu/ciao/>

We used the CIAO `dmextract` tool to check the light curve of this observation, as shown in figure 4.18. An obvious background spike was seen while the background rate was mostly stable. We excluded 5σ outliers from the mean count rate in our spectral analysis. From the total of 96.7 ks observation of RCW 38, the duration of this background spike was only ~ 0.7 ks.

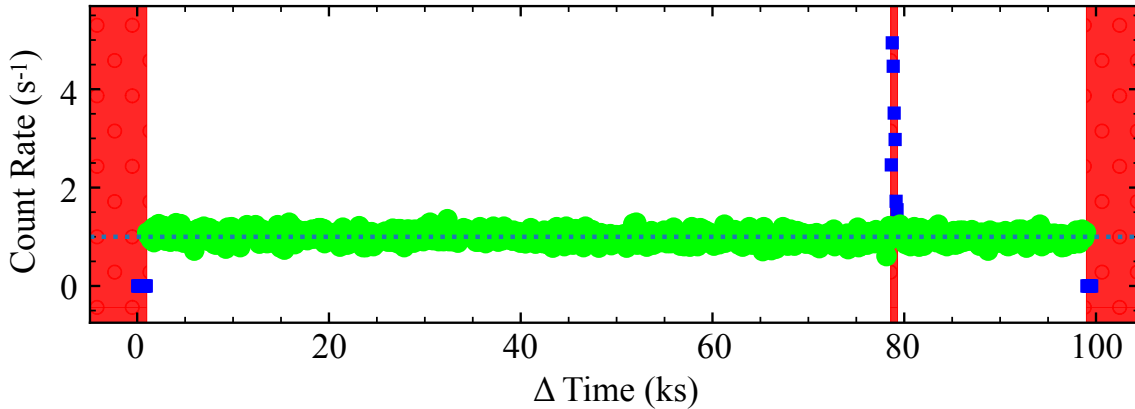


FIGURE 4.18: Light curve of the *Chandra* RCW 38 observation. The dotted line shows the mean count rate. The blue points represent outliers more than 5σ from the mean value.

(3) Offset observation

We utilized RX J0852.0-4622 NW offset observation to estimate astrophysical foreground and background emissions in our *Suzaku* spectral analysis. The equatorial coordinates of the aim point are $(\alpha, \delta)_{J2000.0} = (09^{\text{h}}00^{\text{m}}30^{\text{s}}.7, -47^{\circ}54'36''.7)$, which translates to galactic coordinates $(l, b) = (268^{\circ}23'55''.5, -1^{\circ}08'22''.9)$. It is very close to the *Suzaku* observation of RCW 38. The information on the observation is also included in table 4.2.

Figure 4.19 shows the X-ray image in 0.2–10keV observed with *Suzaku*. No obvious point sources have been reported in this area in any soft X-ray catalogs (e.g., ROSAT all-sky survey, see Boller et al., 2016). We can use the entire XIS FOV, excluding the two corners where the Fe calibration source is located. Hence, it is a suitable region for modeling foreground and background emissions. We downloaded the data from the archive. The XIS 0, 1, 2, and 3 were operated in normal full-frame clocking mode without spaced-raw charge injection during the RX J0852.0-4622 NW offset observation.

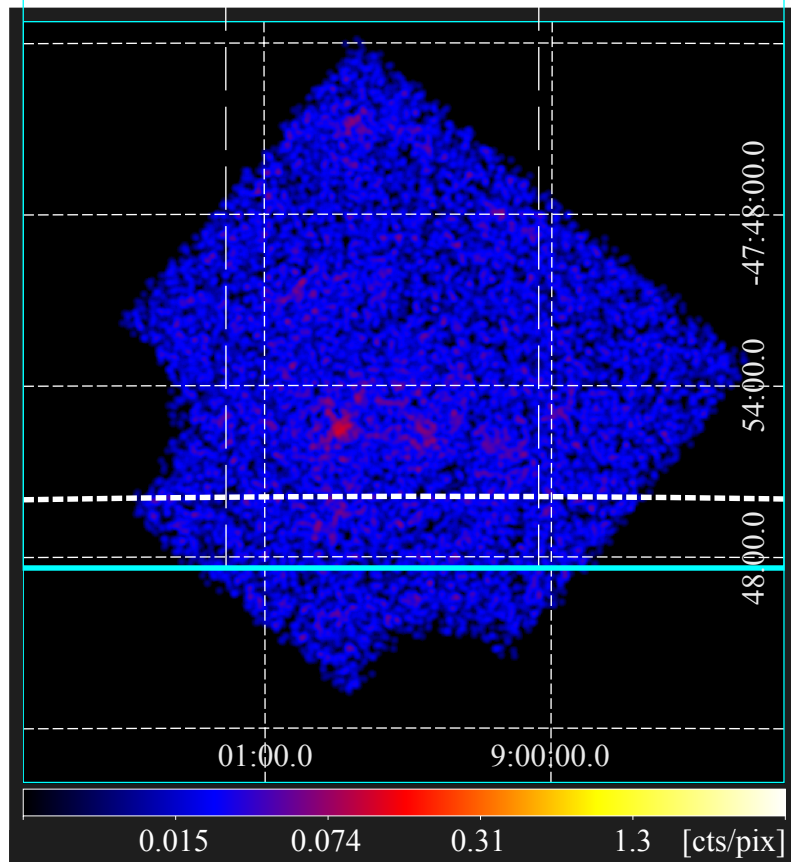


FIGURE 4.19: *Suzaku* XIS 0 + 3 image of the background region (RX J0852.0-4622 NW offset) in 0.2–10 keV. It is smoothed by a Gaussian function with $\sigma = 5$ pixel.

Chapter 5

Data analysis and results

In order to analyze the diffuse X-ray emission with *Suzaku*, we must separate the emission from contaminating sources. There are astronomical foreground and background sources, and point-like sources in the FOV. In addition, they are affected by the non-X-ray background (NXB), noise originating from cosmic rays. To extract the diffuse emission, we need to estimate these contributions. In this chapter, the following three-step spectral analysis is performed to ensure the diffuse X-ray emission: (1) background estimation, (2) modeling the X-ray point sources, and (3) analyzing the diffuse X-ray emission. For spectral fitting in this thesis, we used the XSPEC package (version 12.12.1).

5.1 Background estimation

In this section, we estimate the background contribution as a primary step in the spectral analysis. In our *Suzaku* X-ray study, there are two main types of backgrounds: (1) NXB caused by charged particles from space (Mizuno et al., 2004) and (2) astrophysical foreground and background X-ray emission.

5.1.1 Non-X-ray background (NXB)

The NXB is classified into two components: those in which the detector directly detects charged particles and those in which the detector detects X-rays generated by the reaction between the satellite equipment and the charged particles. The former is seen as a continuum component, and the latter as fluorescent X-rays on the XIS spectrum. These noises must be accurately subtracted from the data.

The NXB contribution can vary depending on its radiation environment. The XIS NXB database¹ is therefore publicly available to estimate the contribution. It is the event information observed with *Suzaku* toward night Earth, which can be considered pure NXB data since astrophysical foreground/background emission is blocked. We estimated the proper NXB using `xisnxbgen` software (Tawa et al., 2008) for both XIS data of RX J0852.0-4622 NW offset and RCW 38.

5.1.2 Astrophysical foreground and backgrounds

In order to model the astrophysical foreground and background emission, we extracted spectrum from the entire XIS FOV of the RX J0852.0-4622 NW offset region, excluding the Fe calibration source, as shown in figure 5.1. NXB was dominant in the high-energy band (>6 keV) in both types of detectors. To perform spectral analysis with XSPEC, we need to know the effect of complex telescopes and detector responses. We then made an auxiliary response file (ARF) using `xissimarfgen` version 2010-11-05. The `xissimarfgen` is a ray-tracing-based generation tool of ARFs for the XIS through Monte Carlo simulations (Ishisaki et al., 2007).

We here assumed contributions from three components, local hot bubble (LHB) as a foreground source, trans-absorption emission (TAE), and cosmic X-ray background (CXB) as background sources. LHB surrounds the solar system and is dominant in the soft X-ray band (Snowden et al., 1998). We used an astrophysical plasma emission code (`apec`) to represent LHB emission as a single thermal plasma model with $kT \sim 0.1$ keV. TAE is the emission from the galactic halo and is well explained by an absorbed (`phabs`) single thermal plasma model (`apec`) with $kT \sim 0.2$ keV (Yoshino et al., 2009). CXB is uniform and known to be modeled by an absorbed power-law model. We set the photon index Γ to 1.5 based on Miyaji et al. (1998) and Kushino et al. (2002). These absorptions were assumed to be common between TAE and CXB. Since the foreground and background sources were considered uniformly extended, the ARF was created by `xissimarfgen`, assuming that the source mode was “UNIFORM” and the source radius was $0' - 20'$.

We then fitted the above models to all XIS spectra. The best-fit parameters are described in table 5.1. The NXB subtracted spectrum and the best-fit models are shown in figure 5.2. LHB is dominant in the low-energy band (<0.7 keV). The fitted parameters of TAE and CXB are consistent with those in Yoshino et al.

¹<http://www.astro.isas.jaxa.jp/suzaku/analysis/xis/nte/>

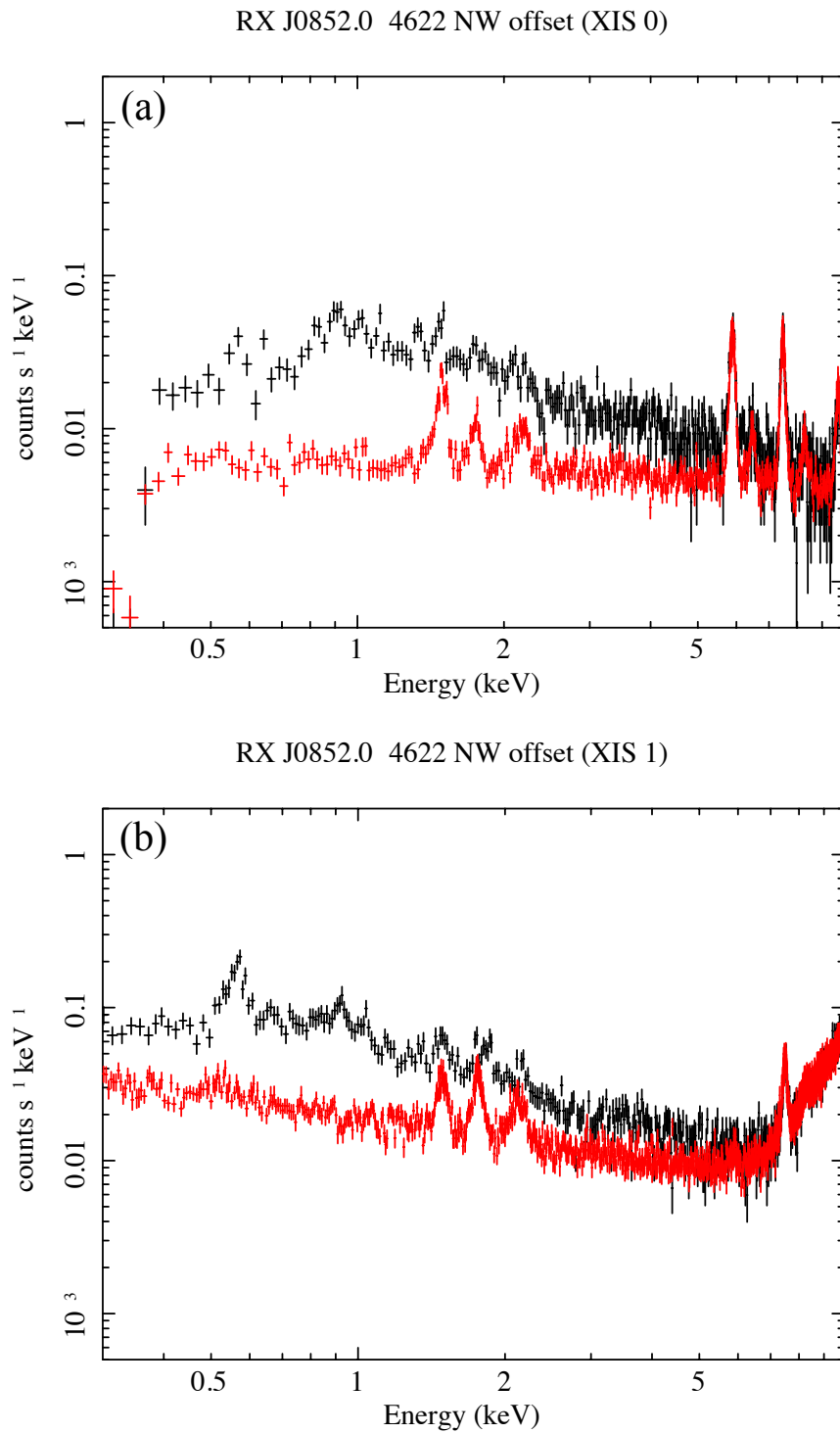


FIGURE 5.1: *Suzaku* XIS (a) FI and (b) BI spectra of RX J0852.0-4622 NW offset (black). The red spectra show NXB contribution, estimated from the night Earth observations.

TABLE 5.1: Spectral fits to astrophysical foreground/backgrounds.

Parameter	Unit	Value / error*
kT_{LHB}	(keV)	0.12 ± 0.01
Abundance	(solar)	1 (fixed)
Norm. ^{LHB}	(unit [†])	$(2.4 \pm 0.4) \times 10^{-3}$
N_{H}	(10^{22} cm^{-2})	0.69 ± 0.06
kT_{TAE}	(keV)	0.22 ± 0.02
Abundance	(solar)	1 (fixed)
Norm. ^{TAE}	(unit [†])	$2.3_{-0.8}^{+1.3} \times 10^{-2}$
Photon index		1.6 ± 0.1
Norm. ^{CXB}	(unit [‡])	$(1.7 \pm 0.1) \times 10^{-3}$
$\chi^2/\text{d.o.f.}$		1.16 (652)

* Errors are 90% confidence range.

† $10^{-14}/(4\pi D^2)EM$, where D is the distance to a target in cm and EM is the plasma emission measure in cm^{-3} .

‡ Photons $\text{keV}^{-1}\text{cm}^{-2} \text{ s}^{-1}$ at 1 keV.

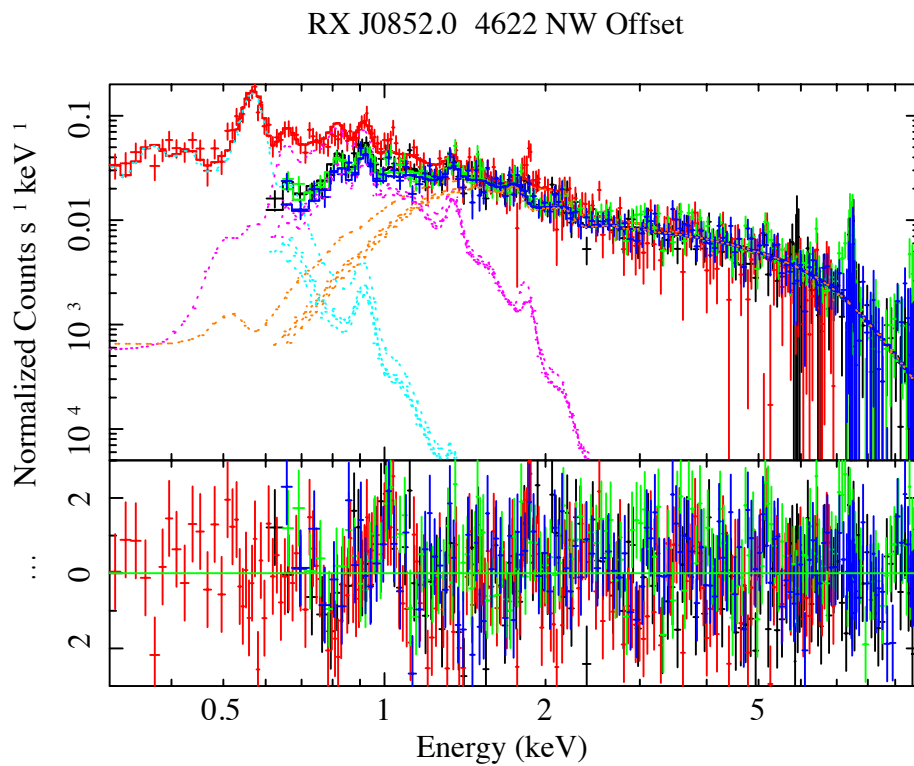


FIGURE 5.2: *Suzaku* XIS spectra of the RX J0852.0-4622 NW offset. The NXB is subtracted. The solid lines and data correspond with XIS 0 (black), XIS 1 (red), XIS 2 (green), and XIS 3 (blue). For astrophysical foreground/backgrounds, we assumed local hot bubble (LHB, dotted light blue lines), transabsorption emission (TAE, dotted magenta lines), and cosmic X-ray background (CXB, dotted orange lines).

(2009), Miyaji et al. (1998) and Kushino et al. (2002), respectively. The sum of the three components reproduces the obtained spectrum well with $\chi^2/\text{d.o.f.}$ of 1.16. Hence, we adopted these models and best-fit parameters, except for the hydrogen column density N_{H} , as the foreground/background emission.

5.2 *Chandra* spectra of point sources

In this section, we estimate the point-source contribution as a secondary step in the spectral analysis. The spectra of point-like sources can be well constrained by *Chandra* observation with high angular resolution. We attempt to model the point source spectrum of the RCW 38 emission region using the *Chandra* ACIS-I data.

5.2.1 Definition of extraction regions

Wolk et al. (2006) reported 460 X-ray point sources across the entire ACIS-I array, as described in subsection 4.2.1. Of the sources they reported, 205 are in our inner region and 159 are in our outer region. We adopted these point sources to extract the spectrum in this section. For the definition of their region sizes on the ACIS-I, we utilized CIAO `wavdetect` software to enclose point source extraction regions. It is a wavelet-based source detection algorithm (Freeman et al., 2002).

We first used the CIAO `fluximage` script to create a source image, a congruent exposure map, and a point spread function map. It was performed over the “broad” (0.5–7 keV) band to detect as many X-ray point sources as possible. Ellipses surrounded the point sources, and their size was determined by an enclosed-count fraction parameter selected by 0–1. After several attempts and checking by eye, we set the value to 0.68, which showed less false detection. `Wavdetect` was then performed under these conditions. As a result, 176 X-ray point sources in the inner region and 146 in the outer region were detected and consistent with Wolk et al. (2006). However, some dark sources reported by Wolk et al. were not successfully detected by `wavdetect` even if the parameters were changed. Therefore, we uniformly enclosed undetected 42 sources with a radius of $2''$, referring to table 1 in Wolk et al. (2006).

In contrast to the preceding results, we newly detected 46 weak point-like sources not listed in Wolk et al. (2006). These are considered to be due to differences in criteria for detection methods. We found that these X-ray sources did not significantly change the parameters and contributions of the spectral analysis discussed

in the following subsection. Therefore, these sources were not included in the spectral extraction to ensure consistency with their previous study.

We thus defined a total of 364 point source regions, as shown in figure 5.3. Since the central O5.5 binary IRS 2 has powerful emission in the X-ray band and appears to leak emission outside its defined region, the minor and major axes of this source region were expanded by 1.5 times (blue in figure 5.3). Starless regions can also be seen on the ACIS-I image. Thus, a background extraction region with an area of 8.5 arcmin² (red ellipse in figure 4.17) was created to consider both NXB and astrophysical foreground/backgrounds.

5.2.2 Spectral fitting to X-ray point sources

Spectra were extracted using the CIAO `specextract` tool from the inner and outer point source regions and background region, as shown in figure 5.4. A weighted response matrix file and an ARF were generated at the same time. The spectra of individual point sources in the FOV are known to be expressed with various models (Wolk et al., 2006). They are rarely represented by blackbody or power-law models but are well-fitted by thermal plasma models. Therefore, we attempted to represent all point sources in multiple-temperature plasma models in this subsection.

Point sources in the inner region

We first tried a two-temperature absorbed (phabs) thermal plasma (vapec + vapec) model for the point source sum spectrum in the inner region. The metal abundances except for He and Fe were tied. He was fixed at 1 solar, and Fe and other metals were initially set to 0.3 solar, the expected value for massive stars (Imanishi, Koyama, and Tsuboi, 2001; Getman et al., 2005). All parameters except He were set to free.

We then fitted the above models to the ACIS-I spectra from 1 to 8 keV. As a result, the X-ray spectrum was well reproduced by the two-temperature absorbed thermal plasma with $\chi^2/\text{d.o.f}$ of 1.07. The best-fitting parameters and the spectrum are shown in table 5.2 and figure 5.5a, respectively. The interstellar absorption $N_{\text{H}} = (1.6 \pm 0.1) \times 10^{22} \text{ cm}^{-2}$ is about twice higher than that of the offset region (table 5.1). The plasma temperatures are $kT = 0.86 \pm 0.12$ and 4.5 ± 0.4 keV, of

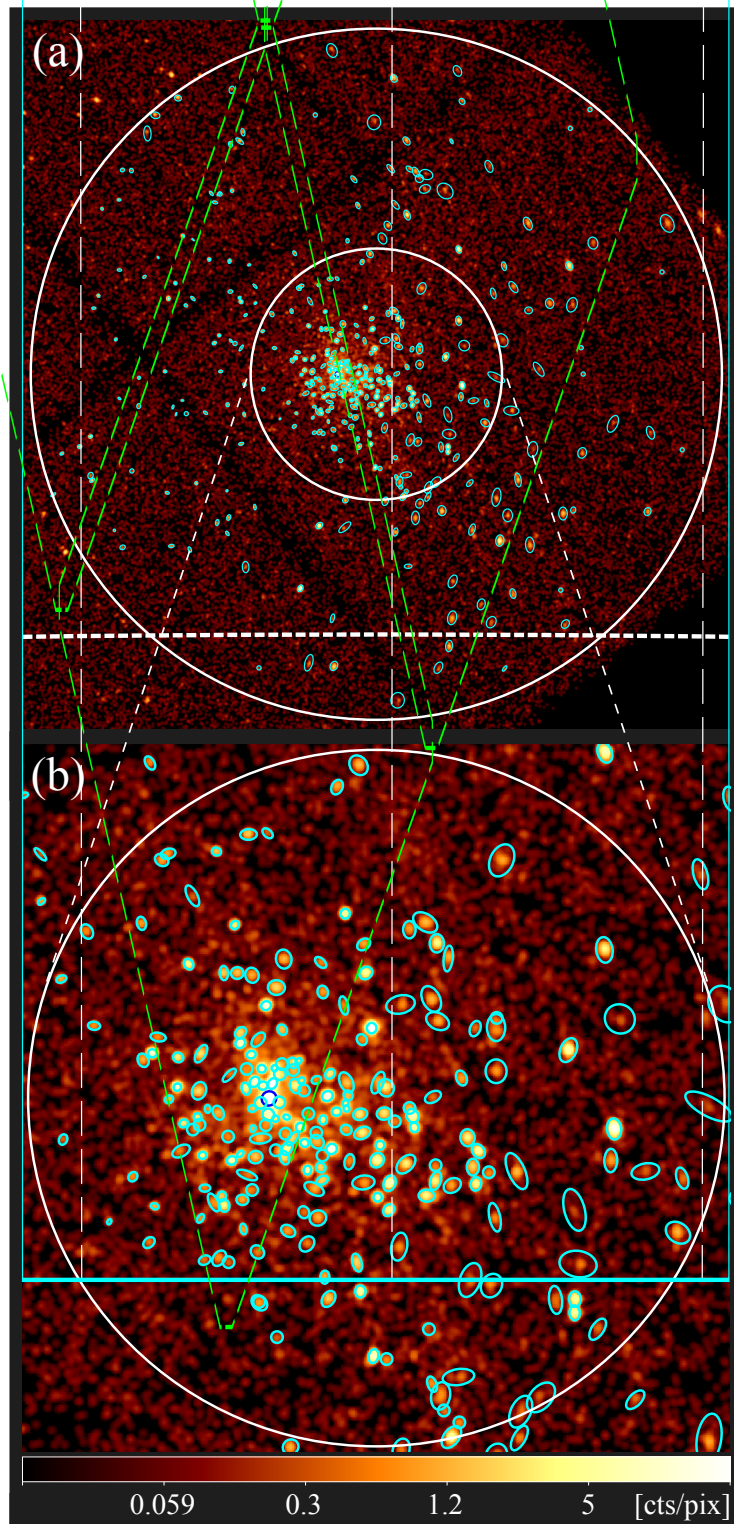


FIGURE 5.3: *Chandra* ACIS-I images of (a) the whole emission region and (b) a close-up view of the inner region. The images are smoothed by a Gaussian function with $\sigma = 2$ pixel. The cyan ellipses and circles show point source regions. The blue ellipse shows IRS 2.

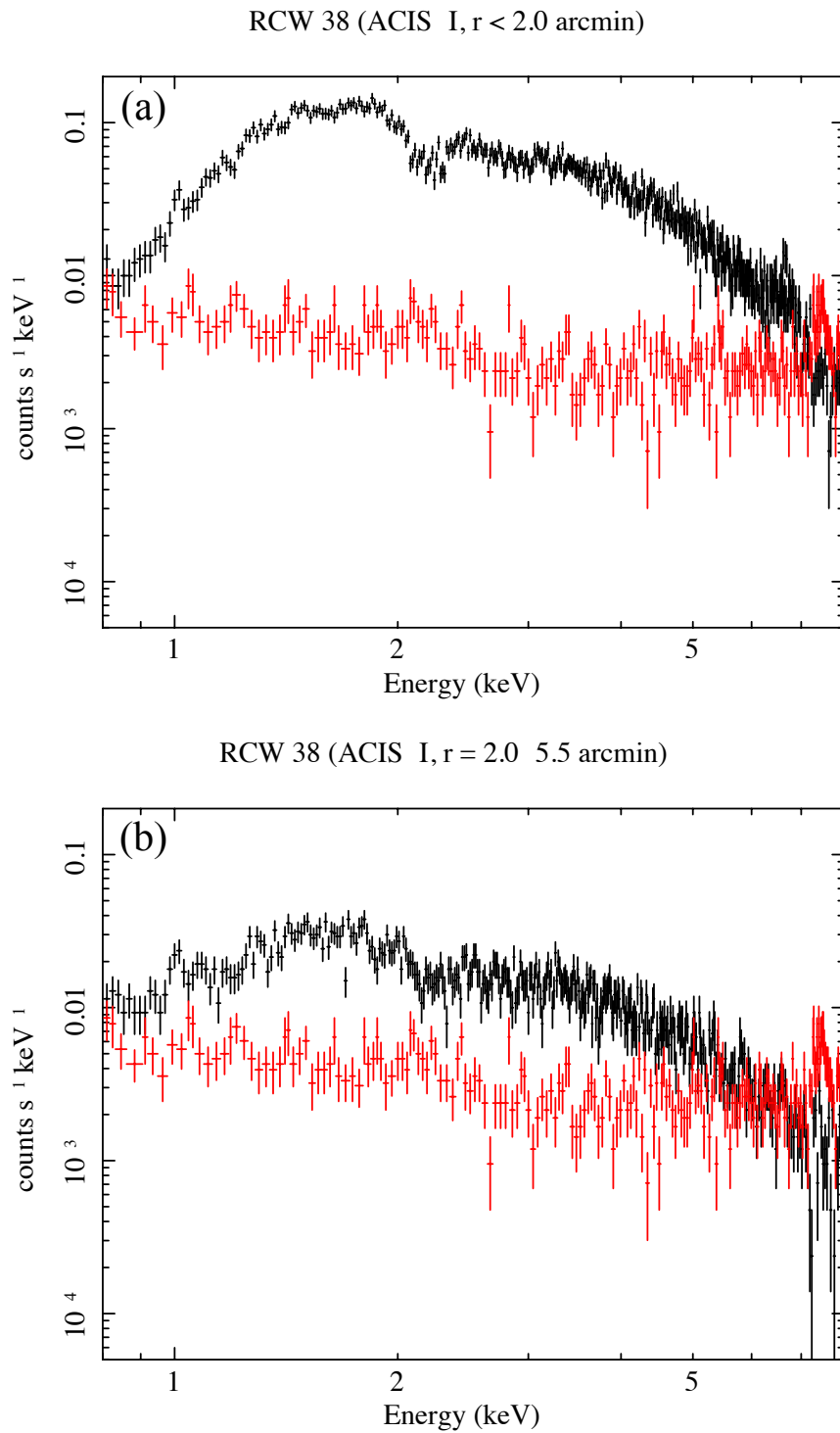


FIGURE 5.4: *Chandra* ACIS-I spectra from the point sources in the (a) inner and (b) outer regions of RCW 38 (black). The red spectra show the background contribution extracted from the starless region (red ellipse in figure 4.17).

TABLE 5.2: Spectral fits to X-ray point sources in RCW 38.

Parameter	Unit	Value / error*	
		Inner	Outer
N_{H}	(10^{22} cm^{-2})	1.6 ± 0.1	1.5 ± 0.2
kT_{low}	(keV)	0.86 ± 0.12	1.1 ± 0.1
Norm. ^{low}	(unit [†])	$2.4_{-0.9}^{+1.8} \times 10^{-3}$	$8.6_{-4.4}^{+6.1} \times 10^{-4}$
kT_{high}	(keV)	4.5 ± 0.4	$9.1_{-2.0}^{+3.0}$
Norm. ^{high}	(unit [†])	$(4.9 \pm 0.3) \times 10^{-3}$	$(1.0 \pm 0.1) \times 10^{-3}$
He	(solar)	1 (fixed)	1 (fixed)
Fe	(solar)	0.22 ± 0.05	0.39 ± 0.13
Other metal	(solar)	$0.65_{-0.26}^{+0.35}$	0.17 (< 0.52)
L_{X}^{\ddagger} in 1.0–8.0 keV	($10^{33} \text{ erg s}^{-1}$)	$2.4_{-0.2}^{+0.3}$	$0.65_{-0.09}^{+0.11}$
L_{X}^{\ddagger} in 0.3–8.0 keV	($10^{33} \text{ erg s}^{-1}$)	$3.7_{-0.3}^{+0.4}$	$0.96_{-0.14}^{+0.16}$
$\chi^2/\text{d.o.f.}$		1.07 (378)	1.09 (271)

* Errors are 90% confidence range.

† $10^{-14}/(4\pi D^2)EM$, where D is the distance to a target in cm and EM is the plasma emission measure in cm^{-3} .

‡ The total X-ray luminosity is corrected for absorption. A distance of 1.7 kpc is assumed.

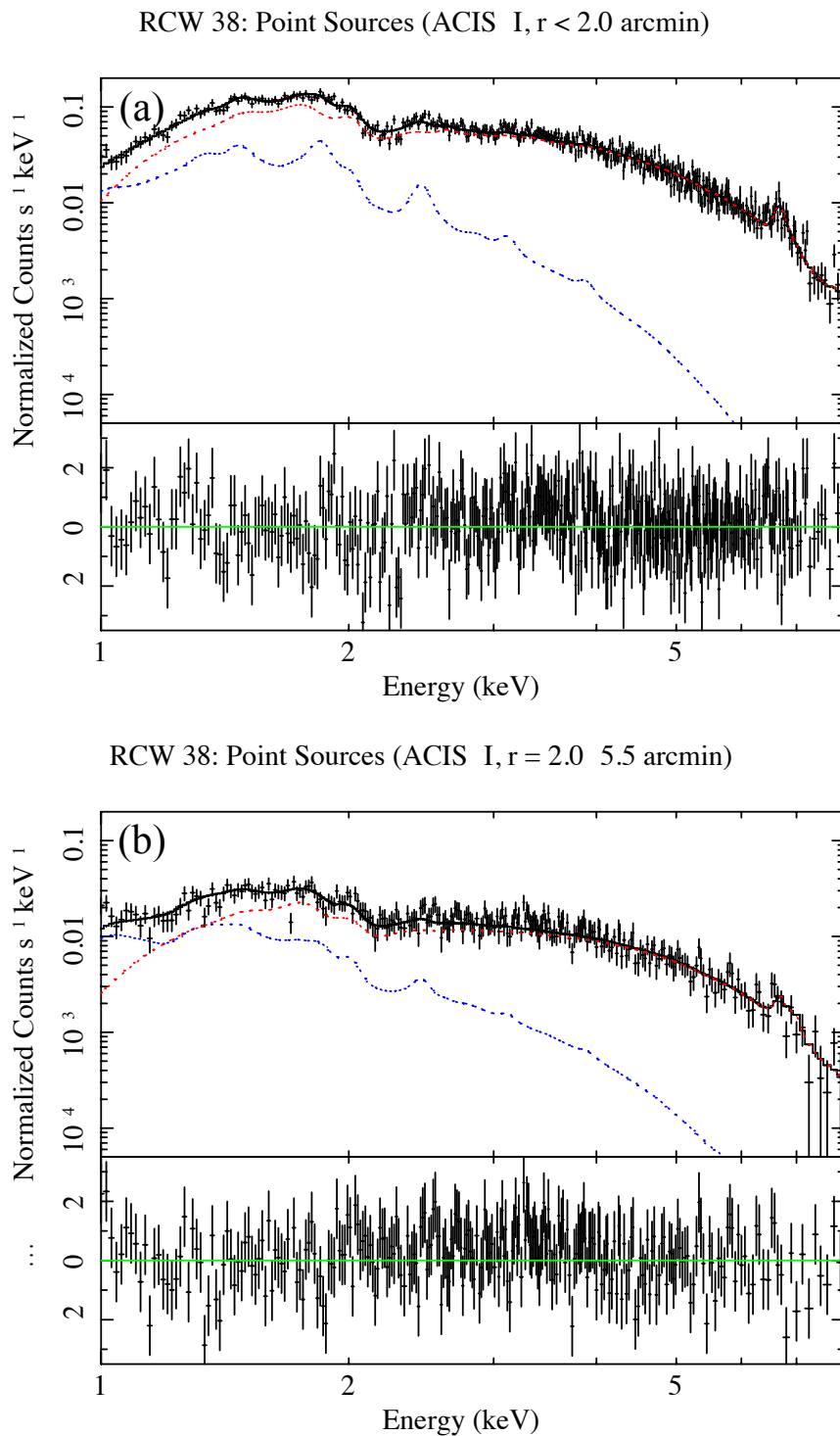


FIGURE 5.5: Background-subtracted *Chandra* ACIS-I spectra of point sources in the (a) inner and (b) outer regions of RCW 38. The blue and red dotted lines indicate low- and high-temperature thermal plasma models, respectively.

which the high-temperature component is dominant. The absorption-corrected luminosity is $2.4_{-0.2}^{+0.3} \times 10^{33}$ erg s⁻¹ in 1–8 keV.

Point sources in the outer region

We then fitted the same model as the inner region to the point source spectrum of the outer region. The initial values were also the same as those for the inner region. As a result, the spectrum was also well reproduced by the two-temperature absorbed plasma model, and the $\chi^2/\text{d.o.f.}$ was 1.09. The best-fit parameters are included in table 5.2.

Interstellar absorption $N_{\text{H}} = (1.5 \pm 0.2) \times 10^{22}$ cm⁻² and the elemental abundances are consistent with those of the inner region. The best-fitting plasma temperatures are $kT = 1.1 \pm 0.1$ and $9.1_{-2.0}^{+3.0}$ keV. The hot component is still dominant, as shown in figure 5.5b. However, its temperature is significantly higher than that of the inner region, indicating a harder spectrum. The absorption-corrected luminosity is $6.5_{-0.9}^{+1.1} \times 10^{32}$ erg s⁻¹ in 1–8 keV, ~ 4 times weaker than the sum of the point sources in the inner region.

Comparison with previous results

As mentioned in subsection 4.2.1, the X-ray point sources of RCW 38 have been well discussed by Wolk et al. (2006). They analyzed the spectra of all detected point sources separately and fitted one- or two-temperature thermal plasma models using Raymond and Smith (1977) code. Although absorptions of individual point sources were not constant, the typical values were $N_{\text{H}} \sim 10^{21}\text{--}10^{23}$ cm⁻², as shown in figure 5.6. Our results ($N_{\text{H}} \sim 1.5 \times 10^{22}$ cm⁻²) can be roughly interpreted as an average of these values.

As for the fitted plasma temperatures, the cluster members are most often represented by a few keV, as shown in figure 5.7. Here, it may appear peculiar that the high-temperature component in our point source modeling is extremely hot. They are even higher than the typical temperature of star-forming regions ($\lesssim 3$ keV, e.g., Preibisch et al., 2005). Furthermore, the temperatures of the inner and outer hot components are significantly different, the latter being considerably higher.

According to Wolk et al. (2006), the source density of RCW 38 cluster members decreases sharply from the cluster center and almost reaches the minimum at

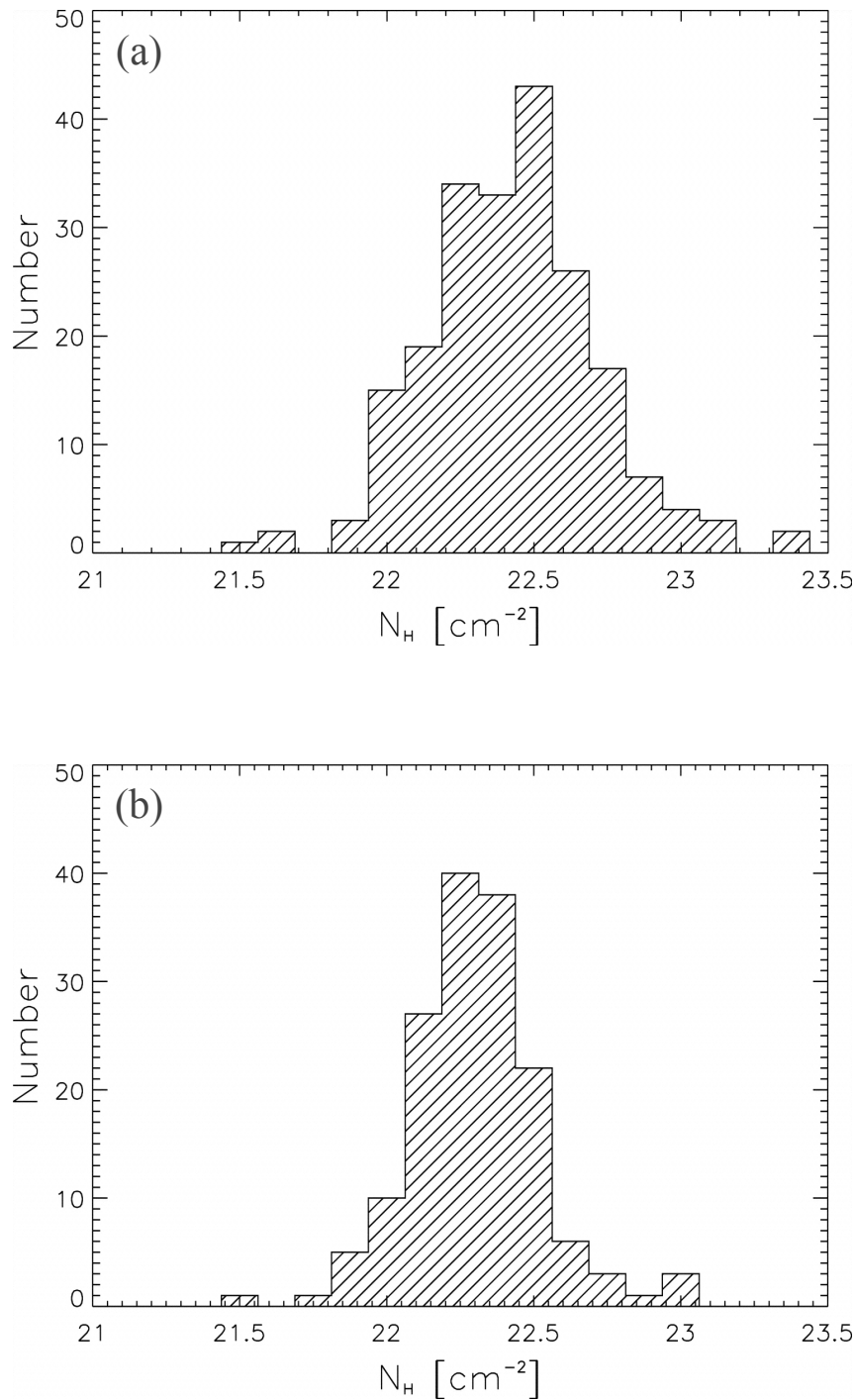


FIGURE 5.6: Histogram of absorption N_H derived through spectral fits of (a) the 209 bright cluster members and (b) the 157 faint cluster members within the RCW 38 ACIS-I observation (Wolk et al., 2006).

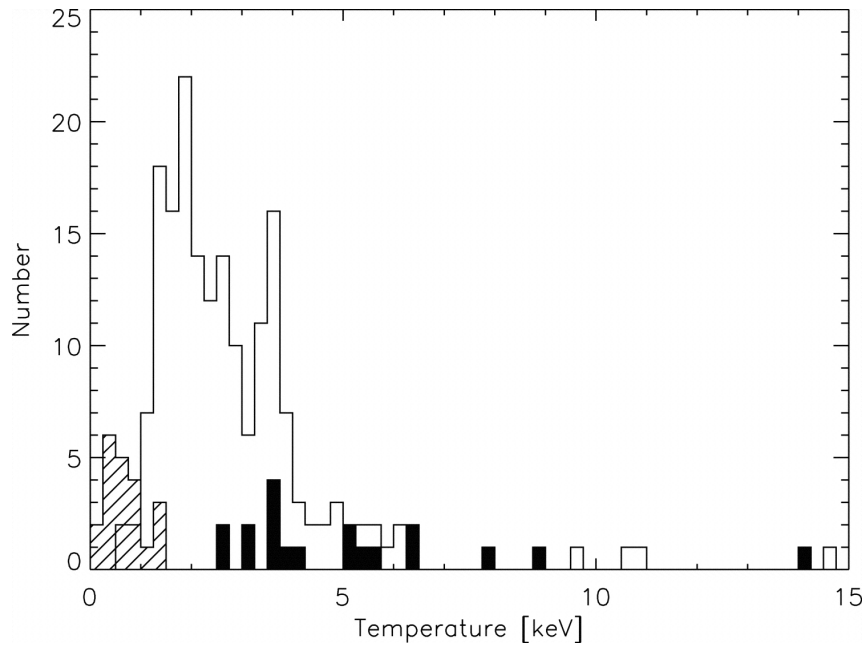


FIGURE 5.7: Histogram of plasma temperature kT for each cluster member, taken from Wolk et al. (2006). Fits for 188 sources fitted with one-temperature Raymond-Smith plasma are indicated by the open histogram. The hatched and filled histograms represent the low- and high-temperature components of the two-temperature fits, respectively.

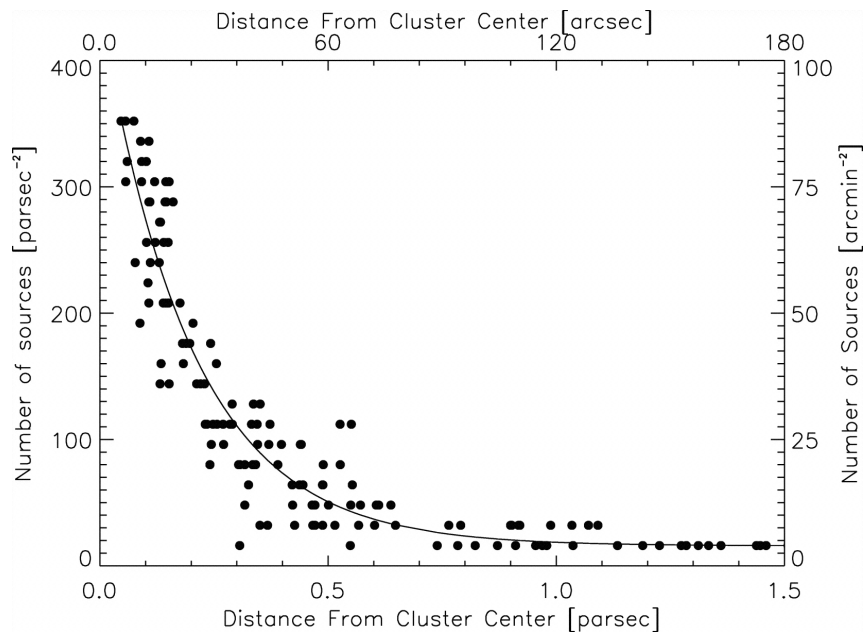


FIGURE 5.8: X-ray point source density profile of the RCW 38 cluster member as a function of distance from the cluster center (Wolk et al., 2006).

the radius of $2'$, as shown in figure 5.8. In contrast, nonmembers are uniformly distributed (figure 4.15). The nonmembers would have a harder spectrum than cluster members because they include hard X-ray-emitting objects, such as background active galactic nuclei, characterized as a power-law model. These sources may contribute observed hard spectrum. Indeed, the ratio of nonmembers is 42/159 ($\sim 26\%$) in the outer region, larger than 19/205 ($\sim 9\%$) in the inner region. Besides, 24 of the 159 sources ($\sim 15\%$) in the outer region were fitted by very hard (>10 keV) thermal plasma, while 19 of the 205 ($\sim 9\%$) in the inner region (see tables 5 to 9 in Wolk et al., 2006). Namely, emission from the nonmembers probably affects the hard component of the extracted point source spectrum.

5.3 Spectral analysis of diffuse X-ray emission with *Suzaku*

In this section, we evaluate the diffuse X-ray emission associated with RCW 38. First, the X-ray spectrum is extracted from the emission region with the *Suzaku* XIS. Next, we consider the contributions of the background and point source components estimated in the previous sections and quantify the residual component. Finally, spectral analysis is performed for the remaining diffuse component.

5.3.1 Background and point-source contributions

XIS spectra of backgrounds

As shown in black in figures 5.9 and 5.10, X-ray spectra were extracted with the XIS from the inner and outer regions, respectively. The spectra in the outer region are harder than in the inner region, which probably reflects the spectral shape of the point source emission. As in the analysis of the RX J0852.0-4622 offset region (section 5.1), *xisnxbgen* software was used to estimate the NXBs of both regions (red in figures 5.9 and 5.10). Since significant emission remained below 8 keV even after subtracting NXB, spectral analyses were performed in the energy band below this energy.

Figure 5.11 shows NXB-subtracted XIS spectra of the inner and outer regions. Black, red, and blue data correspond to XIS 0, 1, and 3, respectively. These spectra are considered to consist of astrophysical foreground/backgrounds, point sources, and diffuse component. In order to check the contribution of foreground

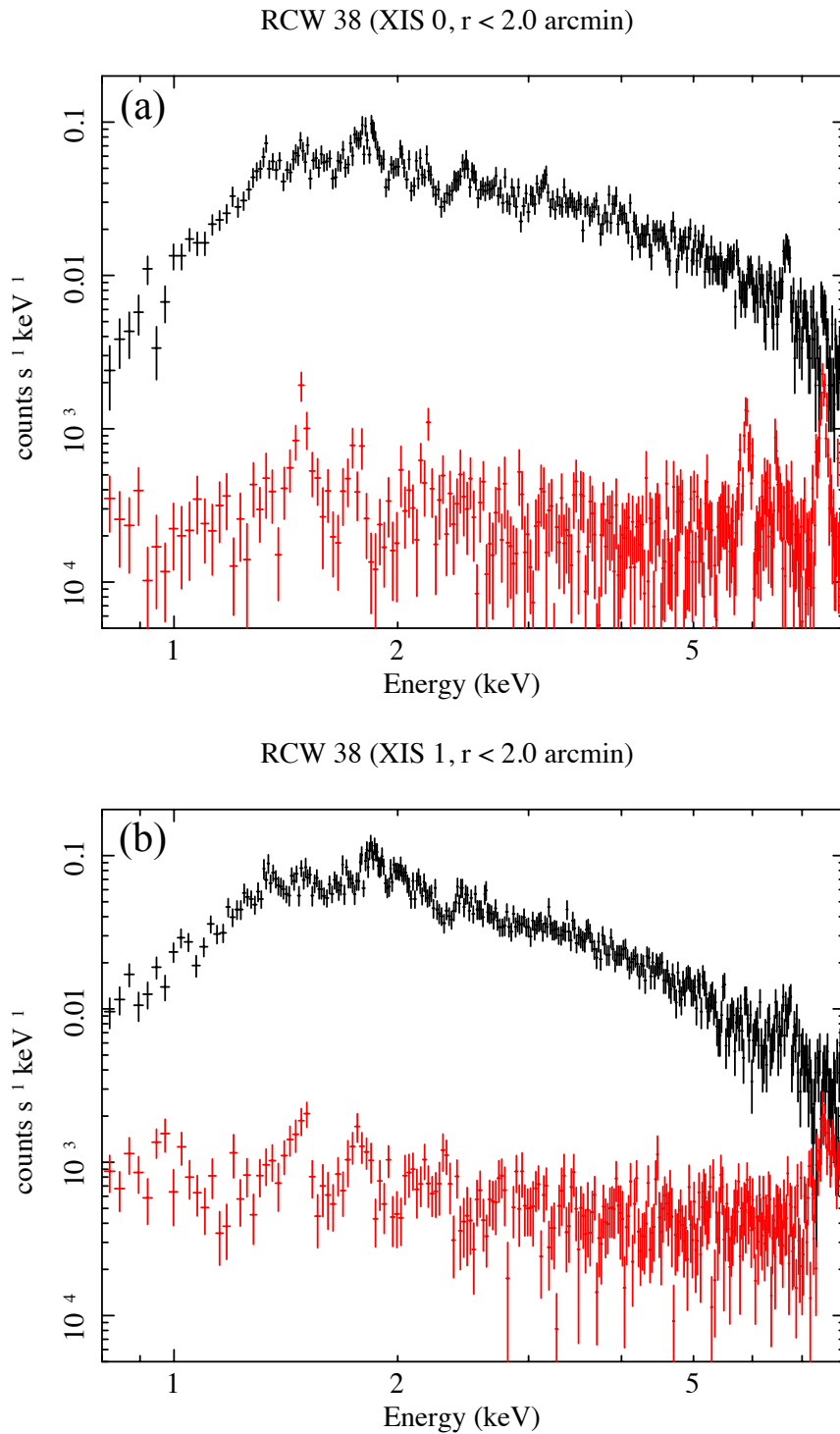


FIGURE 5.9: *Suzaku* XIS (a) FI and (b) BI spectra from the inner region of RCW 38 (black). The red spectra show NXB contribution, estimated from the night Earth observations.

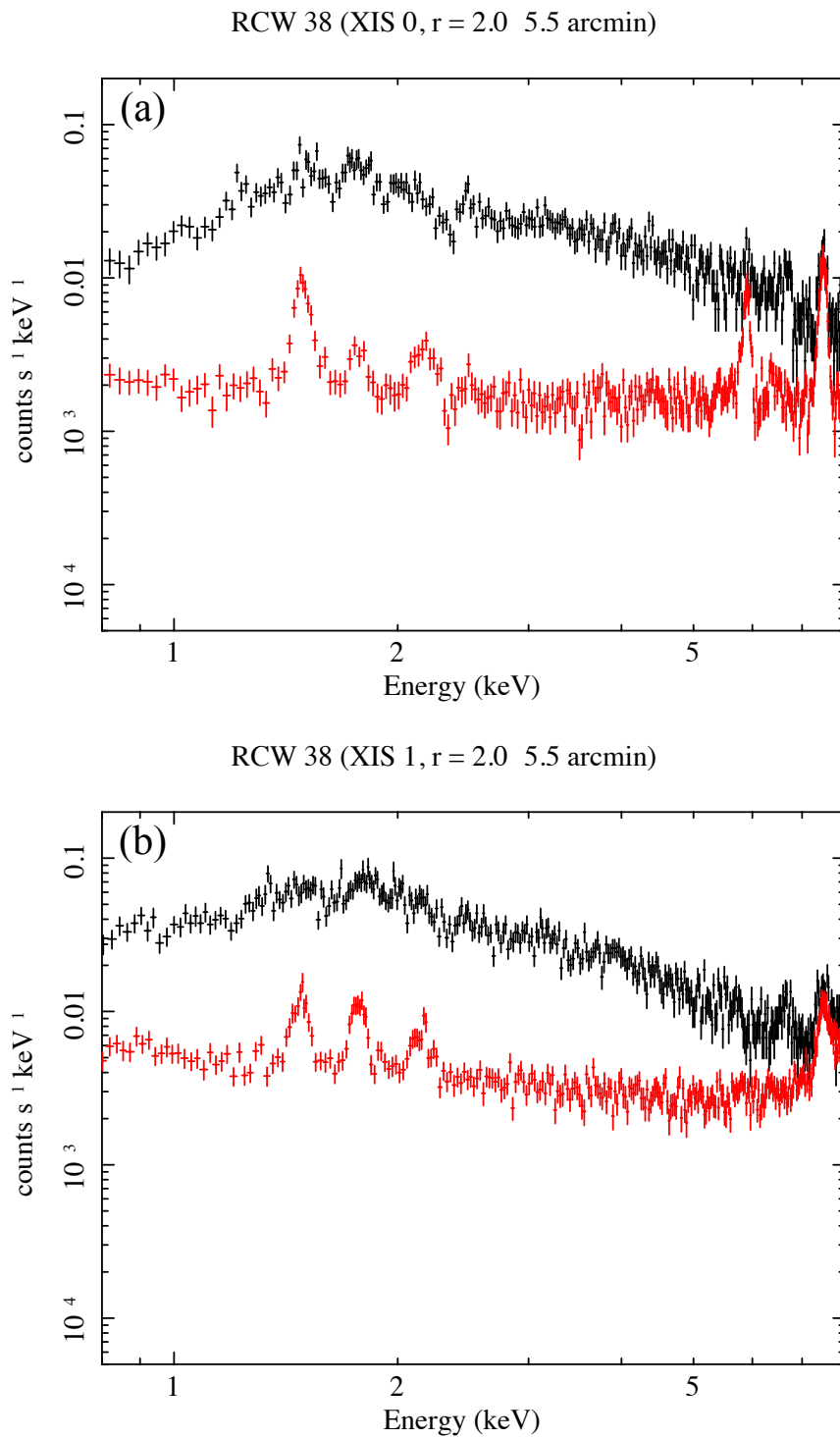


FIGURE 5.10: Same as figure 5.9 but for the outer region.

and background emission, we introduced the best-fitting model estimated in subsection 5.1.2 into the RCW 38 spectrum. The ARF for the foreground and background sources was generated again using `xissimarfgen` as in subsection 5.1.2, with source mode set to “UNIFORM” and source radius set to $0'–20'$. In 1–8 keV bands, we found that the foreground and background emissions account for $\sim 1\%$ and $\sim 10\%$ of the total spectra in the inner and outer regions, respectively (orange in figure 5.11).

XIS spectra of point sources

We next introduce best-fitting point source spectra estimated in subsection 5.2.2 to RCW 38 XIS spectra. The ARFs were also generated using `xissimarfgen` with the source mode set to “SKYFITS”. Images of the ACIS-I point source regions were input to take into account the positions and intensities of the point sources as accurately as possible.

We must consider the difference in point spread functions of the telescopes on-board both satellites. Point-like sources are detected on the larger area of XIS due to *Suzaku*'s larger point spread function (figure 3.9). Hence, part of the point source emission in the inner region escapes into the outer region, and likewise, some emission escapes from the outer region into the inner region. Therefore, we simulated the spread of point sources of each region using a Monte Carlo simulator `xissim` (Ishisaki et al., 2007). It can simulate the behavior of virtual photons based on the input point source images.

Figure 5.12a shows a simulation of the spread of the point sources located in the inner region. It was found that $\sim 24\%$ of the photons from the inner region were contained in the outer region. These photons do not extend beyond the outer region. Similarly, we simulated the spread of point sources in the outer region, as shown in figure 5.12b. As a result, it was found that $\sim 9\%$ of the photons from the outer region were included in the inner region. Although the same amount of photons also escapes outside the outer region, they are expected to cancel out with the photons spreading from outside the outer region to the outer region since the point source distribution is almost uniform near the outer boundary of the outer region (see figures 4.15 and 5.8).

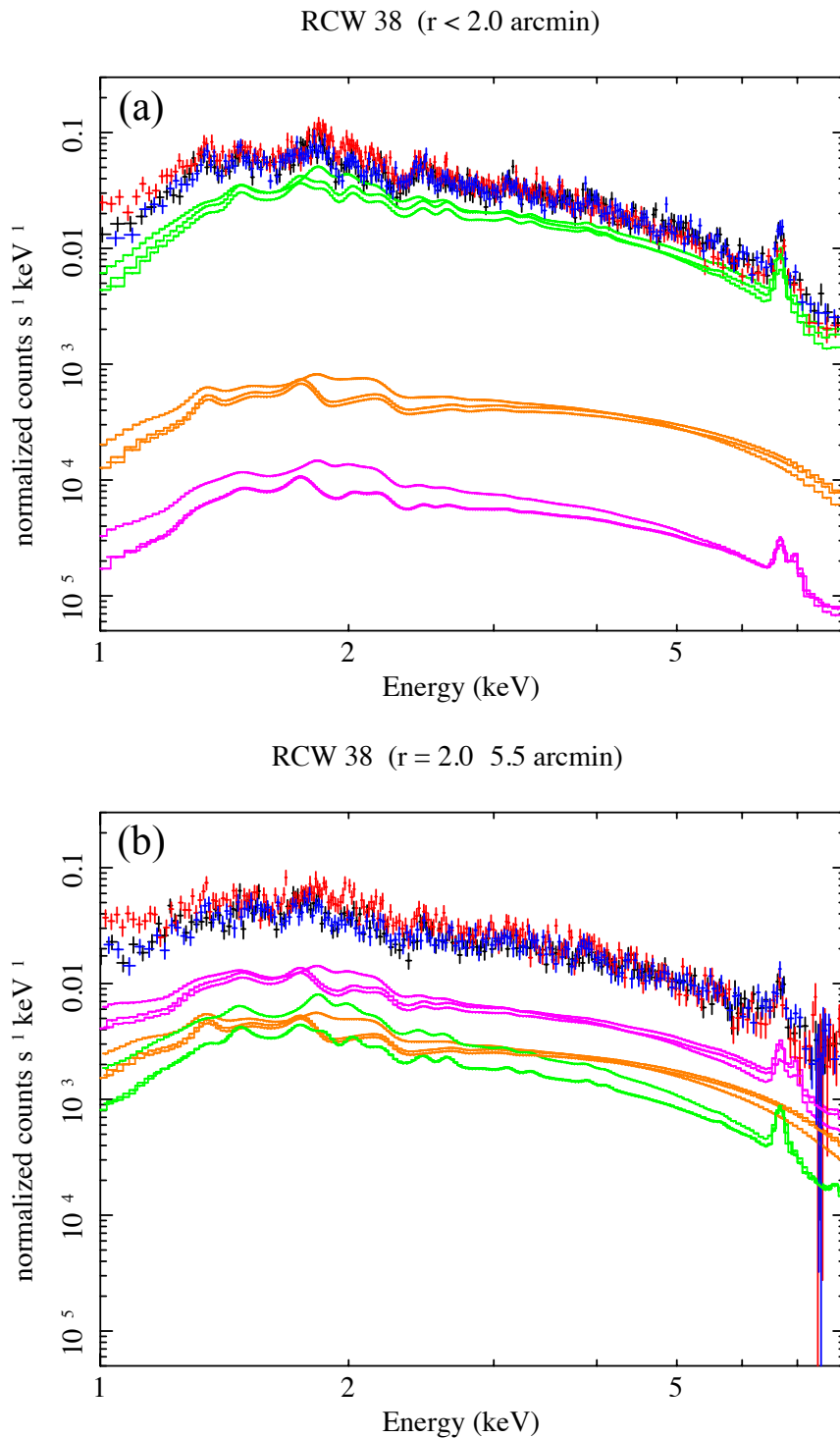


FIGURE 5.11: *Suzaku* XIS spectra of the (a) inner and (b) outer regions of RCW 38. The NXBs are subtracted. The solid lines and data correspond with XIS 0 (black), XIS 1 (red), and XIS 3 (blue). The orange lines indicate the best-fit models of foreground/background emission. The green and magenta lines indicate the contributions of point source emission from the inner and outer regions, respectively.

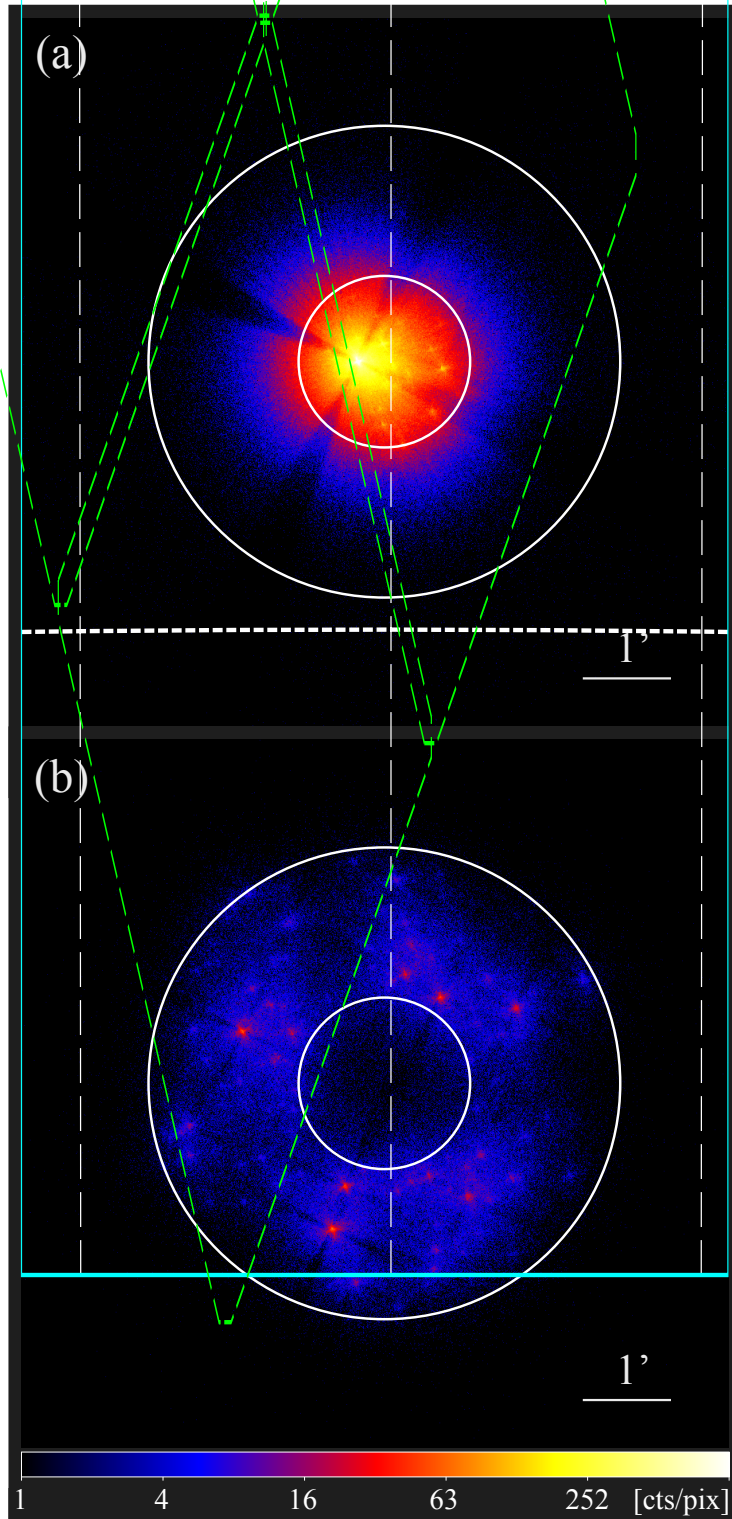


FIGURE 5.12: *Suzaku* XIS 0 + 3 images of the simulated point sources from the (a) inner and (b) outer regions of RCW 38. The exposure time was assumed to be 10,000 ks for photon statistics. The circles are the same as in figure 4.16.

We thus scaled the point source normalization taking into account the number of escaped photons and introduced the best-fit parameters of our *Chandra* analysis into the RCW 38 spectrum. As a result, the inner point source contributions dominate in the inner region, and their emission explains a large amount of the spectrum in 1–8 keV (green in figure 5.11a). On the other hand, point source emission escaping from the outer to the inner region was negligible (magenta in figure 5.11a). It was confirmed that $\sim 30\%$ of the emission remained in 1–8 keV even when foreground and background contributions were added to this emission.

In the outer region, point-source contributions from both the inner (green in figure 5.11b) and outer (magenta in figure 5.11b) regions have non-negligible contributions. However, the point source summed spectrum was weaker than in the inner region. We found that $\sim 40\%$ of the emission still remained in 1–8 keV even when foreground and background contributions were added. Therefore, the diffuse X-ray emission is most likely present in RCW 38. In the following subsection, a spectral analysis is performed, assuming that these residual components are diffuse emissions.

5.3.2 Spectral fitting in the inner region

We proceed to analyze the diffuse X-ray spectrum of RCW 38 with the XIS. The ARF for diffuse emission was generated by `xissimarfgem` assuming “UNIFORM” emission. The source radius was assumed to be $0'–20'$, but we show the results after correction using the actual area for the diffuse emission. First, we performed model fitting in the inner region.

Non-thermal model

We assumed a combined model of absorbed (`phabs`) thermal plasma (`vapex`) and non-thermal (`power_law`) models for the diffuse emission. It was the model first suggested by Wolk et al. (2002), as described in subsection 4.2.1. We call this a non-thermal model in the present thesis. The initial values were set according to the Overall region of table 1 in Wolk et al. (2002). The abundances of thermal plasma other than He were fixed at 0.3 solar, the expected value for massive stars, because thermal diffuse plasma is generally considered to be associated with massive stars in their cluster, as mentioned in subsection 4.1.1. We

assumed all emission components suffer the same amount of interstellar absorption and then used the same N_{H} value. Table 5.3 shows the astrophysical foreground/background and point source parameters assumed in the model fitting of the diffuse emission.

Table 5.4 shows the best-fitting parameters of the diffuse emission. The spectrum was represented by the thermal + non-thermal components with $\chi^2/\text{d.o.f.}$ of 1.30. Soft X-rays are relatively strongly affected by the absorption difference from the offset observation and unresolved point sources (see also subsection 6.2.2), which complicates the spectral fitting. Hence, this model was not perfect, however, the fit was acceptable when focusing on the high-energy band (>2.5 keV). The interstellar absorption was $N_{\text{H}} = 1.8 \pm 0.1$, which was consistent with our *Chandra* analysis in the inner region (table 5.2). The plasma temperature and the photon index were $kT = 0.93 \pm 0.06$ keV and $\Gamma = 1.9 \pm 0.2$, respectively. The photon index was consistent with the Overall region in Wolk et al. (2002), $\Gamma = 1.59 \pm 0.12$. The full spectrum (foreground/backgrounds + sum of point sources + diffuse component) is shown in figure 5.13a. The absorption-corrected luminosities of the thermal and non-thermal components were $(6.7 \pm 1.2) \times 10^{32}$ erg s $^{-1}$ and $4.8_{-1.3}^{+1.5} \times 10^{32}$ erg s $^{-1}$ in 1–8 keV, respectively. The summed luminosity of the diffuse component was ~ 2 times weaker than the summed point source luminosity.

Thermal model

We also checked if only thermal components could reproduce the diffuse emission. The abundances were set to the same values as in the fitting of the non-thermal model. As a result, we found that a two-temperature absorbed (phabs) thermal plasma (vapec + vapec) model could represent the spectrum with $\chi^2/\text{d.o.f.}$ of 1.25, as shown in table 5.5. The full spectrum is shown in figure 5.14a. Hereafter we call this a thermal model.

This new model required a higher plasma temperature $kT = 5.3_{-0.9}^{+1.2}$ keV in addition to 0.91 ± 0.06 keV. This high-temperature component corresponds with the power law of the non-thermal model, while the low-temperature component ($kT \sim 0.9$ keV) and the interstellar absorption ($N_{\text{H}} \sim 1.8 \times 10^{22}$ cm $^{-2}$) are common in both models. The absorption-corrected luminosities of the cool and hot components were $(6.1 \pm 1.1) \times 10^{32}$ erg s $^{-1}$ and $4.9_{-0.6}^{+0.8} \times 10^{32}$ erg s $^{-1}$ in 1–8 keV, respectively.

5.3.3 Spectral fitting in the outer region

Non-thermal model

We then proceeded to analyze the outer region. Although the area size is 6.6 times larger than the inner region, the unabsorbed point source luminosity is ~ 4 times weaker from our *Chandra* analysis and ~ 2 times weaker when escaped photons are taken into account. We tried to fit the spectrum with the same models, expecting the diffuse emission associated with the inner region. The initial values were set according to the best-fitting results of the inner region.

We thus found that the non-thermal model represents the spectrum with $\chi^2/\text{d.o.f.}$ of 1.30, as shown in table 5.4. The spectrum is shown in figure 5.13b. The thermal component have $kT = 1.1 \pm 0.2$ keV, slightly higher than the inner region. The photon index was 1.8 ± 0.1 . These basic parameters were consistent with those of the inner region. The interstellar absorption was $N_{\text{H}} = (1.4 \pm 0.1) \times 10^{22} \text{ cm}^{-2}$, and the absorption-corrected luminosities of the thermal and non-thermal components were $(3.3 \pm 1.0) \times 10^{32} \text{ erg s}^{-1}$ and $(6.4 \pm 1.4) \times 10^{32} \text{ erg s}^{-1}$ in 1–8 keV, respectively. However, the power-law model was not acceptable even when focusing only on the high-energy band. The most obvious factor is the Fe emission line defect at 6.7 keV.

Thermal model

We then tested the same spectral fitting for the thermal model. As a result, the two-temperature ($kT = 0.96 \pm 0.12$ and 4.9 ± 0.6 keV) thermal models represent the diffuse spectrum well with $\chi^2/\text{d.o.f.}$ of 1.22. This model was acceptable in the high-energy band. Both temperatures and absorptions agreed with those of the inner region within 90% errors, as shown in table 5.5. The spectrum is shown in figure 5.14b. The absorption-corrected luminosities of the cool and hot components were $(2.0 \pm 0.9) \times 10^{32} \text{ erg s}^{-1}$ and $(6.8 \pm 0.6) \times 10^{32} \text{ erg s}^{-1}$ in 1–8 keV, respectively.

Both models have a relatively cool ($kT \sim 1$ keV) plasma component and comparable interstellar absorption ($N_{\text{H}} \sim 1.4 \times 10^{22} \text{ cm}^{-2}$) as in our *Chandra* analysis, $N_{\text{H}} = (1.5 \pm 0.2) \times 10^{22} \text{ cm}^{-2}$. The significant difference was still the non-thermal

or the hot thermal component, as in the inner region. They were dominant, especially in the high-energy band. At this time, we can say that the thermal model shows better fitting than the non-thermal model.

TABLE 5.3: Parameters of the astrophysical foreground/background and point source emission assumed in the diffuse spectral analyses of tables 5.4 and 5.5.

Component	Parameter	Unit	Value	
			Inner	Outer
Astrophysical foreground/backgrounds	kT_{LHB}	(keV)	0.12	
	Abundance	(solar)	1	
	Norm. ^{LHB}	(unit*)	2.4×10^{-3}	
	N_{H}	(10^{22} cm^{-2})	(bind ₁)	(bind ₂)
	kT_{TAE}	(keV)	0.22	
	Abundance	(solar)	1	
	Norm. ^{TAE}	(unit*)	2.3×10^{-2}	
	Photon index		1.6	
	Norm. ^{CXB}	(unit [†])	1.7×10^{-3}	
Point sources from the inner region	N_{H}	(10^{22} cm^{-2})	(bind ₁)	(bind ₂)
	kT_{low}	(keV)	0.86	
	Norm. ^{low}	(unit*)	1.8×10^{-3}	5.7×10^{-4}
	kT_{high}	(keV)	4.5	
	Norm. ^{high}	(unit*)	3.7×10^{-3}	1.2×10^{-3}
	He	(solar)	1	
	Fe	(solar)	0.22	
	Other metal	(solar)	0.65	
Point sources from the outer region	N_{H}	(10^{22} cm^{-2})	(bind ₁)	(bind ₂)
	kT_{low}	(keV)	1.1	
	Norm. ^{low}	(unit*)	7.7×10^{-5}	7.8×10^{-4}
	kT_{high}	(keV)	9.1	
	Norm. ^{high}	(unit*)	9.3×10^{-5}	9.4×10^{-4}
	He	(solar)	1	
	Fe	(solar)	0.39	
	Other metal	(solar)	0.17	

* $10^{-14}/(4\pi D^2)EM$, where D is the distance to a target in cm and EM is the plasma emission measure in cm^{-3} .† Photons $\text{keV}^{-1}\text{cm}^{-2} \text{ s}^{-1}$ at 1 keV.

TABLE 5.4: Spectral fits to RCW 38 diffuse X-ray emission (non-thermal model).

Parameter	Unit	Value / error*	
		Inner	Outer
N_{H}	(10^{22} cm^{-2})	1.8 ± 0.1 (bind ₁)	1.4 ± 0.1 (bind ₂)
kT	(keV)	0.93 ± 0.06	1.1 ± 0.2
Norm. ^{thermal}	(unit [†])	$(4.1 \pm 0.7) \times 10^{-3}$	$(1.8 \pm 0.5) \times 10^{-4}$
Photon index		1.9 ± 0.2	1.8 ± 0.1
Norm. ^{non-thermal}	(unit [‡])	$(3.6 \pm 1.1) \times 10^{-4}$	$(4.5 \pm 1.0) \times 10^{-4}$
He	(solar)	1 (fixed)	1 (fixed)
Other metal	(solar)	0.3 (fixed)	0.3 (fixed)
$L_{\text{X}}^{\text{thermal}}$ in 1.0–8.0 keV [§]	($10^{33} \text{ erg s}^{-1}$)	0.67 ± 0.12	0.33 ± 0.10
in 0.3–8.0 keV [§]	($10^{33} \text{ erg s}^{-1}$)	1.8 ± 0.3	0.72 ± 0.22
$L_{\text{X}}^{\text{non-thermal}}$ in 1.0–8.0 keV [§]	($10^{33} \text{ erg s}^{-1}$)	$0.48_{-0.13}^{+0.15}$	0.64 ± 0.14
in 0.3–8.0 keV [§]	($10^{33} \text{ erg s}^{-1}$)	$0.71_{-0.19}^{+0.22}$	0.91 ± 0.20
$\chi^2/\text{d.o.f.}$		1.30 (716)	1.30 (634)

* Errors are 90% confidence range.

† $10^{-14}/(4\pi D^2)EM$, where D is the distance to a target in cm and EM is the plasma emission measure in cm^{-3} .

‡ Photons $\text{keV}^{-1}\text{cm}^{-2} \text{ s}^{-1}$ at 1 keV.

§ The X-ray luminosity is corrected for absorption. A distance of 1.7 kpc is assumed.

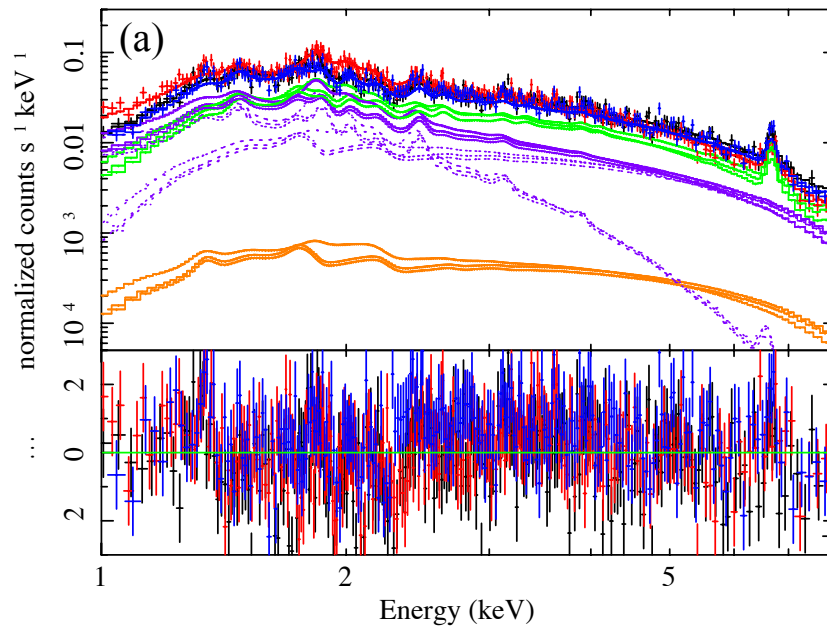
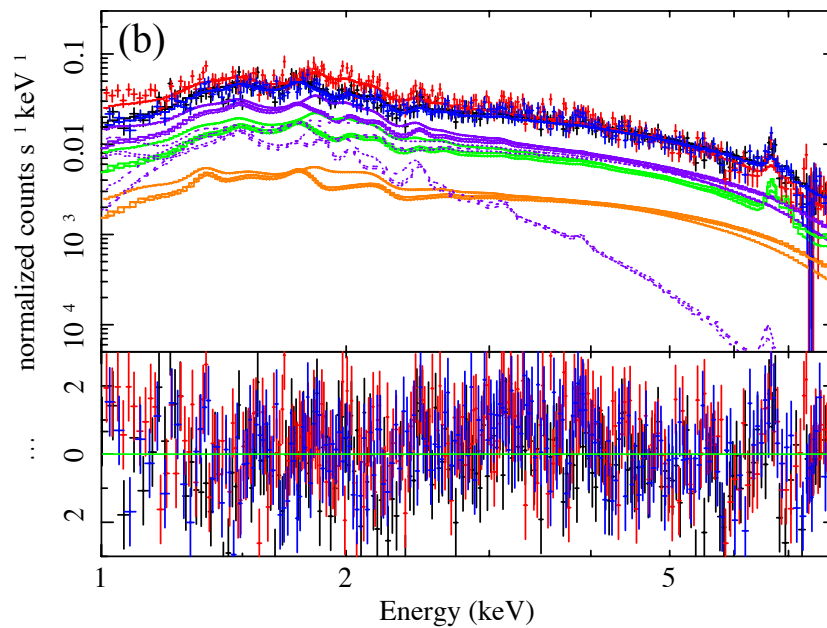
RCW 38: BKG + Point Sources + Diffuse component ($r < 2.0$ arcmin)RCW 38: BKG + Point Sources + Diffuse component ($r = 2.0 - 5.5$ arcmin)

FIGURE 5.13: *Suzaku* XIS spectra of the (a) inner and (b) outer regions of RCW 38. The NXBs are subtracted. The solid lines and data correspond with XIS 0 (black), XIS 1 (red), and XIS 3 (blue), respectively. The emission is divided into the following three components: astrophysical foreground/backgrounds (orange), summed point sources (green), and diffuse emission (purple). Absorbed power law and thermal plasma models were assumed for the diffuse emission. The separate components of the diffuse emission model are further indicated by the dotted lines.

TABLE 5.5: Spectral fits to RCW 38 diffuse X-ray emission (thermal model).

Parameter	Unit	Value / error*	
		Inner	Outer
N_{H}	(10^{22} cm^{-2})	1.8 ± 0.1 (bind ₁)	1.4 ± 0.1 (bind ₂)
kT_{low}	(keV)	0.91 ± 0.06	0.96 ± 0.12
Norm. ^{low}	(unit [†])	$(3.8 \pm 0.7) \times 10^{-3}$	$(1.2 \pm 0.5) \times 10^{-3}$
kT_{high}	(keV)	$5.3^{+1.2}_{-0.9}$	4.9 ± 0.6
Norm. ^{high}	(unit [†])	$(1.2 \pm 0.2) \times 10^{-3}$	$(1.7 \pm 0.2) \times 10^{-3}$
He	(solar)	1 (fixed)	1 (fixed)
Other metal	(solar)	0.3 (fixed)	0.3 (fixed)
$L_{\text{X}}^{\text{low}}$ in 1.0–8.0 keV [‡]	($10^{33} \text{ erg s}^{-1}$)	0.61 ± 0.11	0.20 ± 0.09
in 0.3–8.0 keV [‡]	($10^{33} \text{ erg s}^{-1}$)	1.7 ± 0.3	0.52 ± 0.21
$L_{\text{X}}^{\text{high}}$ in 1.0–8.0 keV [‡]	($10^{33} \text{ erg s}^{-1}$)	$0.49^{+0.08}_{-0.06}$	0.68 ± 0.06
in 0.3–8.0 keV [‡]	($10^{33} \text{ erg s}^{-1}$)	$0.64^{+0.11}_{-0.08}$	0.89 ± 0.08
$\chi^2/\text{d.o.f.}$		1.25 (716)	1.22 (634)

* Errors are 90% confidence range.

† $10^{-14}/(4\pi D^2)EM$, where D is the distance to a target in cm and EM is the plasma emission measure in cm^{-3} .

‡ The X-ray luminosity is corrected for absorption. A distance of 1.7 kpc is assumed.

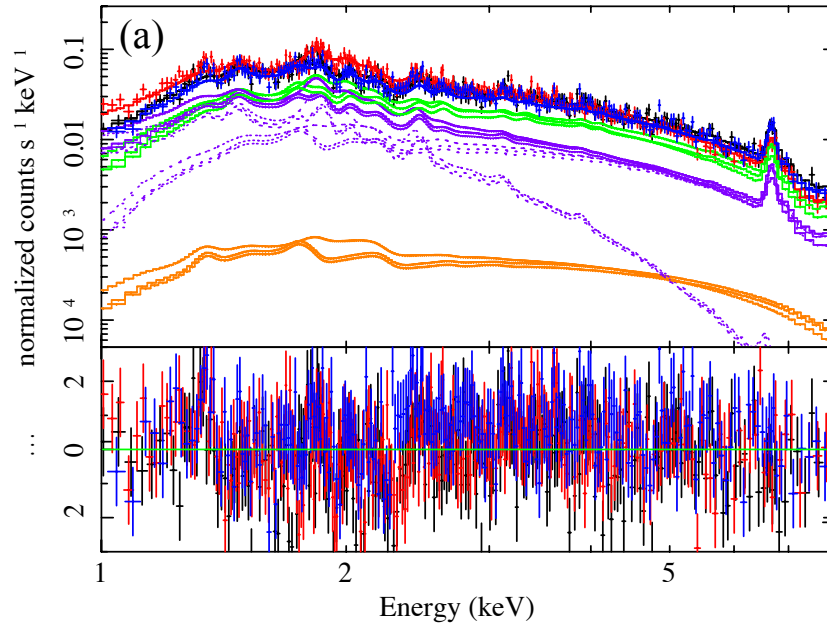
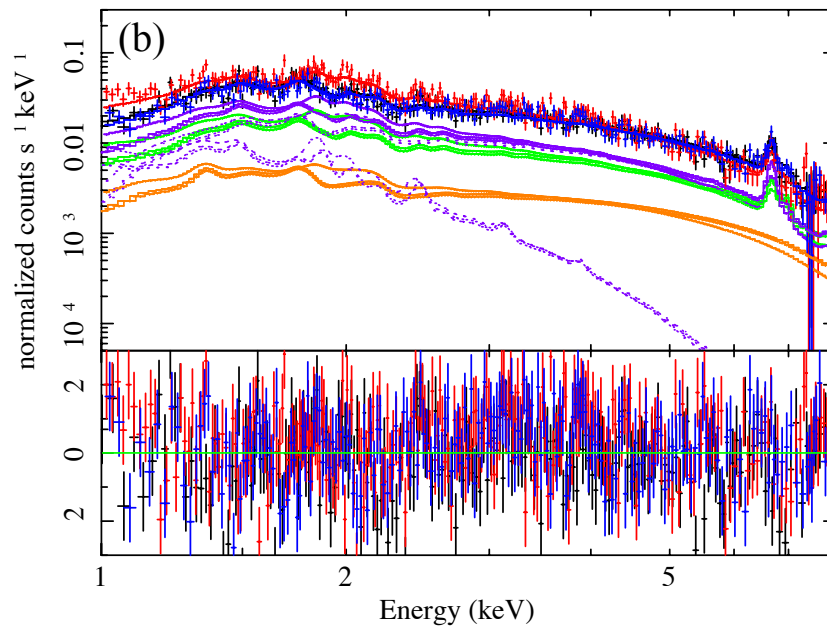
RCW 38: BKG + Point Sources + Diffuse component ($r < 2.0$ arcmin)RCW 38: BKG + Point Sources + Diffuse component ($r = 2.0 - 5.5$ arcmin)

FIGURE 5.14: Same as figure 5.13 but a two-temperature absorbed thermal plasma model was assumed for the diffuse emission.

Chapter 6

Discussion

6.1 Brief summary of obtained results

In order to reveal the hard diffuse X-ray emission seen in the MSFR RCW 38, we performed X-ray spectral analyses with *Suzaku* and *Chandra*, considering astrophysical foreground/backgrounds and point sources. In the inner region ($r < 2'.0$), we successfully detected the diffuse X-ray emission, although it contains bright point sources, such as O5.5 binary IRS 2. The X-ray spectrum of the diffuse emission could be represented by both the non-thermal model (absorbed thermal plasma at $kT = 0.93 \pm 0.06$ keV and power law of $\Gamma = 1.9 \pm 0.2$) and the thermal model (absorbed two-temperature plasma at $kT = 0.91 \pm 0.06$ and $5.3_{-0.9}^{+1.2}$ keV). The latter was first proposed in this study.

In the outer region ($r = 2'.0\text{--}5'.5$), it included the region not mentioned in previous studies, however, the *Suzaku* XIS significantly detected the point source and diffuse emissions. The diffuse emission was again represented by both the non-thermal model (absorbed thermal plasma at $kT = 1.1 \pm 0.2$ keV and power law of $\Gamma = 1.8 \pm 0.1$) and the thermal model (absorbed two-temperature plasma at $kT = 0.96 \pm 0.12$ and 4.9 ± 0.6 keV). The temperatures and photon index are consistent with the inner region. However, the thermal model was more favorable. The absorption-corrected luminosity of the diffuse emission was on the order of 10^{33} erg s⁻¹ in 1–8 keV in both the inner and outer regions. In this chapter, we will discuss these obtained results.

6.2 Contamination to diffuse components

6.2.1 Estimation of faint point source contribution

First of all, we must check the reliability of the diffuse X-ray emission in more detail because the contributions of undetected point sources can easily be imagined as contaminants of diffuse emission. Therefore, we compare the luminosities of expected undetectable X-ray point sources and the obtained diffuse emission in RCW 38.

Wolk et al. (2006) predicted the number of unresolved point sources. The detection limit luminosity of the unabsorbed point sources was estimated to be $L_X = 10^{30.75} \text{ erg s}^{-1}$ in 0.3–8 keV for the *Chandra* observation of RCW 38. They referred nominal “complete” X-ray luminosity function of the Orion Nebula Cluster parameterized by Feigelson et al. (2005) and normalized the lognormal distribution to fit the RCW 38 with $L_X > 10^{31.0} \text{ erg s}^{-1}$, as shown in figure 6.1. According to their estimation, there are $>2,000$ unresolved sources with X-ray luminosity of 10^{28} – $10^{31} \text{ erg s}^{-1}$ in RCW 38.

We thus calculated the total luminosity from figure 6.1. As a result, the absorption-corrected luminosity of unresolved sources was $\sim 2 \times 10^{33} \text{ erg s}^{-1}$ in 0.3–8 keV in the whole ACIS FOV ($17' \times 17'$). This number would be much smaller in our $r5/5$ (inner + outer) region and should thus be considered the upper limit. The total absorption-corrected luminosity of the diffuse X-rays was $\sim 2 \times 10^{33} \text{ erg s}^{-1}$ in 1–8 keV and $\sim 4 \times 10^{33} \text{ erg s}^{-1}$ in 0.3–8 keV (tables 5.4 and 5.5). The luminosity of the diffuse X-ray emission was larger than the sum of the undetectable sources by a factor of $\gtrsim 2$ in the latter energy band. Hence, it is most likely that at least a part of the extended emission is truly diffuse.

6.2.2 Possible uncertainties

We further consider the uncertainty of the point sources. It can be divided into four categories in our analysis. The first is the cross-calibration of *Suzaku* and *Chandra*. The possible difference in the intensity from the spectral fit between both satellites is $\sim 5\%$ (Tsujimoto et al., 2011). The second is the errors in the model fitting. The luminosity error bars were $\sim 10\%$ – 20% , as shown in table 5.2. The third is underestimation due to not including unresolved point sources. This is $\sim 40\%$, considering the luminosity of the undetected point sources described in the previous subsection. The last is overestimation due to including diffuse emission within the point source regions. This contribution is considered limited

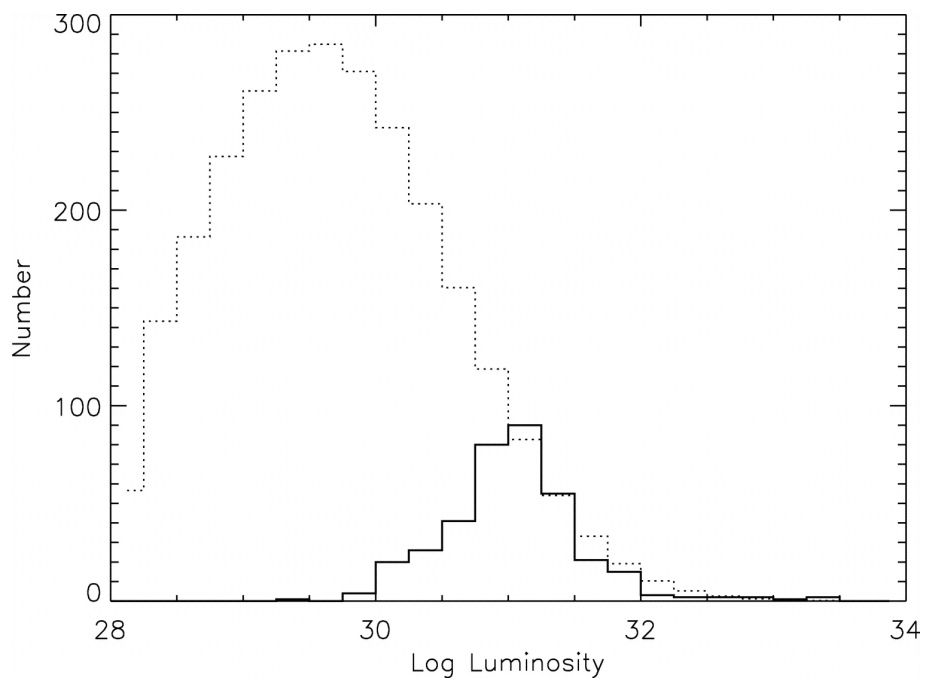


FIGURE 6.1: X-ray luminosity function of RCW 38, taken from Wolk et al. (2006). The solid line shows the 365 detected cluster members within the ACIS-I FOV. The dotted line shows the expected full distribution of X-ray luminosities assuming a lognormal distribution (after Feigelson et al., 2005).

because the percentages of the point source regions to the inner and outer regions are only 8% and 2%, respectively (figure 5.3).

Summarizing the above, we found that conservative considerations may overestimate point sources by up to $\sim 10\%$ – 20% or underestimate them by up to $\sim 40\%$ – 45% . We thus checked the best-fitting values of the diffuse parameter when the point-source intensity was changed by these amounts. As an example, tables 6.1 and 6.2 show the re-fitting parameters for the non-thermal model when the point source intensity is simply multiplied by 0.8, and figure 6.2 shows their spectra. The X-ray luminosity of the diffuse emission increased in both the inner and outer regions. However, the basic parameters (N_{H} , kT , and Γ) and χ^2 values showed no critical changes compared to table 5.4.

Similarly, the re-fitting parameters for the thermal model when the point source intensity is multiplied by 0.8 are shown in tables 6.1 and 6.3, and their spectra are in figure 6.3. As in the non-thermal model, the basic parameters (N_{H} , kT_{low} , and kT_{high}) and χ^2 values did not significantly change compared to table 5.5. The X-ray luminosity of the diffuse emission was simply increased in both the inner and outer regions. Therefore, we conclude that even if we were to overestimate the point sources due to uncertainty, it would not significantly affect the non-thermal and thermal models obtained in section 5.3. On the other hand, the total absorption-corrected luminosity of the diffuse emission of RCW 38 could be up to $\sim 3 \times 10^{33}$ erg s $^{-1}$ in 1–8 keV, considering the 90% errors.

Tables 6.4 and 6.5 show examples of the re-fitting parameters for the non-thermal model when the point source intensity is multiplied by 1.45. As shown in figure 6.4, we can see that there are still diffuse X-rays. However, most of the hard X-ray component in the inner region was explained by foreground/background and point source emission. As a result, the diffuse component was almost exclusively represented by a single-temperature ($kT = 0.88 \pm 0.08$ keV) thermal plasma, and the power law was negligible. The χ^2 value did not change significantly. In the outer region, the diffuse emission significantly remained in 1–8 keV bands. Its basic parameters were consistent with table 5.4. The point sources slightly compensated the residual of the Fe emission line, and $\chi^2/\text{d.o.f.}$ improved from 1.30 to 1.27.

Similarly, the re-fitting parameters for the thermal model when the point source intensity is multiplied by 1.45 are shown in tables 6.4 and 6.6, and their spectra are in figure 6.5. In the inner region, the diffuse emission was also mostly

TABLE 6.1: Same as table 5.3 but for tables 6.2 and 6.3. Point source contributions are scaled by a factor of 0.8 for the best-fitting model.

Component	Parameter	Unit	Value	
			Inner	Outer
Astrophysical foreground/backgrounds	kT_{LHB}	(keV)	0.12	
	Abundance	(solar)	1	
	Norm. ^{LHB}	(unit*)	2.4×10^{-3}	
	N_{H}	(10^{22} cm^{-2})	(bind ₃)	(bind ₄)
	kT_{TAE}	(keV)	0.22	
	Abundance	(solar)	1	
	Norm. ^{TAE}	(unit*)	2.3×10^{-2}	
	Photon index		1.6	
	Norm. ^{CXB}	(unit [†])	1.7×10^{-3}	
Point sources from the inner region	N_{H}	(10^{22} cm^{-2})	(bind ₃)	(bind ₄)
	kT_{low}	(keV)	0.86	
	Norm. ^{low}	(unit*)	1.4×10^{-3}	4.6×10^{-4}
	kT_{high}	(keV)	4.5	
	Norm. ^{high}	(unit*)	3.0×10^{-3}	9.4×10^{-4}
	He	(solar)	1	
	Fe	(solar)	0.22	
	Other metal	(solar)	0.65	
Point sources from the outer region	N_{H}	(10^{22} cm^{-2})	(bind ₃)	(bind ₄)
	kT_{low}	(keV)	1.1	
	Norm. ^{low}	(unit*)	6.2×10^{-5}	6.3×10^{-4}
	kT_{high}	(keV)	9.1	
	Norm. ^{high}	(unit*)	7.5×10^{-5}	7.5×10^{-4}
	He	(solar)	1	
	Fe	(solar)	0.39	
	Other metal	(solar)	0.17	

* $10^{-14}/(4\pi D^2)EM$, where D is the distance to a target in cm and EM is the plasma emission measure in cm^{-3} .† Photons $\text{keV}^{-1}\text{cm}^{-2} \text{ s}^{-1}$ at 1 keV.

TABLE 6.2: Same as table 5.4 (non-thermal model) but the point source contributions are scaled by a factor of 0.8 for the best-fitting model.

Parameter	Unit	Value / error*	
		Inner	Outer
N_{H}	(10^{22} cm^{-2})	1.8 ± 0.1 (bind ₃)	1.4 ± 0.1 (bind ₄)
kT	(keV)	0.95 ± 0.06	1.1 ± 0.1
Norm. ^{thermal}	(unit [†])	$(4.6 \pm 0.7) \times 10^{-3}$	$(1.9 \pm 0.5) \times 10^{-3}$
Photon index		1.9 ± 0.1	1.8 ± 0.1
Norm. ^{non-thermal}	(unit [†])	$(5.5 \pm 1.2) \times 10^{-4}$	$(5.1 \pm 1.0) \times 10^{-4}$
He	(solar)	1 (fixed)	1 (fixed)
Other metal	(solar)	0.3 (fixed)	0.3 (fixed)
$L_{\text{X}}^{\text{thermal}}$ in 1.0–8.0 keV [§]	($10^{33} \text{ erg s}^{-1}$)	0.77 ± 0.13	0.36 ± 0.10
in 0.3–8.0 keV [§]	($10^{33} \text{ erg s}^{-1}$)	2.0 ± 0.3	0.79 ± 0.23
$L_{\text{X}}^{\text{non-thermal}}$ in 1.0–8.0 keV [§]	($10^{33} \text{ erg s}^{-1}$)	$0.70^{+0.16}_{-0.14}$	0.74 ± 0.15
in 0.3–8.0 keV [§]	($10^{33} \text{ erg s}^{-1}$)	1.1 ± 0.2	1.0 ± 0.2
$\chi^2/\text{d.o.f.}$		1.33 (716)	1.32 (634)

* Errors are 90% confidence range.

† $10^{-14}/(4\pi D^2)EM$, where D is the distance to a target in cm and EM is the plasma emission measure in cm^{-3} .

‡ Photons $\text{keV}^{-1}\text{cm}^{-2} \text{ s}^{-1}$ at 1 keV.

§ The X-ray luminosity is corrected for absorption. A distance of 1.7 kpc is assumed.

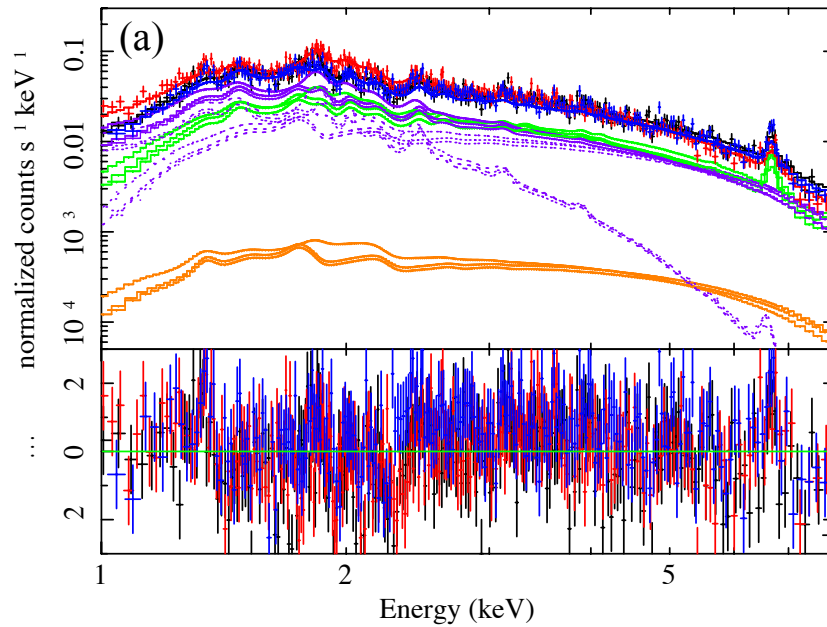
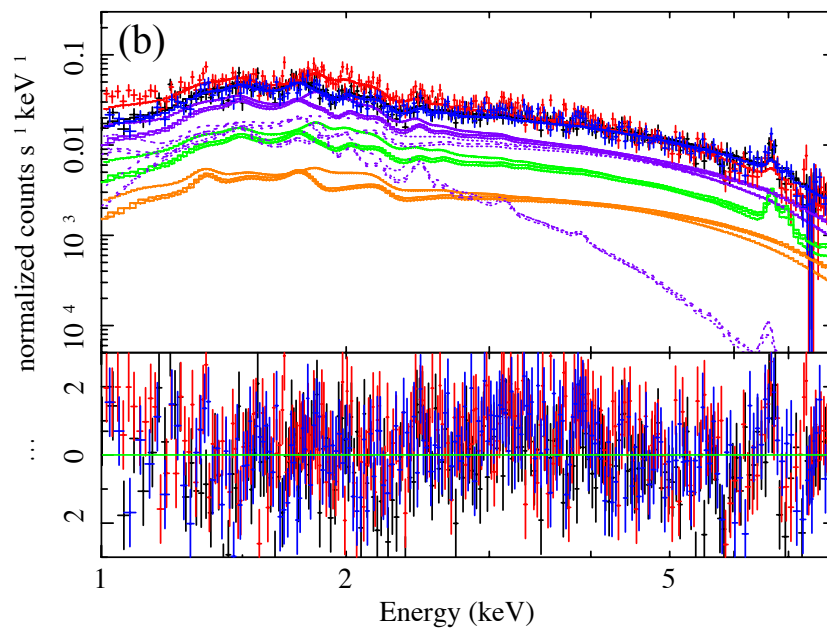
RCW 38: BKG + Point Sources + Diffuse component ($r < 2.0$ arcmin)RCW 38: BKG + Point Sources + Diffuse component ($r = 2.0 - 5.5$ arcmin)

FIGURE 6.2: Same as figure 5.13 but the point source contributions are scaled by a factor of 0.8 for the best-fitting model.

TABLE 6.3: Same as table 5.5 (thermal model) but the point source contributions are scaled by a factor of 0.8 for the best-fitting model.

Parameter	Unit	Value / error*	
		Inner	Outer
N_{H}	$(10^{22} \text{ cm}^{-2})$	1.8 ± 0.1 (bind ₃)	1.4 ± 0.1 (bind ₄)
kT_{low}	(keV)	0.91 ± 0.05	0.97 ± 0.10
Norm. ^{low}	(unit [†])	$(4.4 \pm 0.7) \times 10^{-3}$	$(1.3 \pm 0.5) \times 10^{-3}$
kT_{high}	(keV)	$5.1^{+0.8}_{-0.6}$	5.1 ± 0.6
Norm. ^{high}	(unit [†])	$(1.8 \pm 0.2) \times 10^{-3}$	$(1.9 \pm 0.1) \times 10^{-3}$
He	(solar)	1 (fixed)	1 (fixed)
Other metal	(solar)	0.3 (fixed)	0.3 (fixed)
$L_{\text{X}}^{\text{low}}$ in 1.0–8.0 keV [‡]	$(10^{33} \text{ erg s}^{-1})$	0.70 ± 0.11	0.23 ± 0.08
in 0.3–8.0 keV [‡]	$(10^{33} \text{ erg s}^{-1})$	2.0 ± 0.3	0.58 ± 0.21
$L_{\text{X}}^{\text{high}}$ in 1.0–8.0 keV [‡]	$(10^{33} \text{ erg s}^{-1})$	$0.71^{+0.08}_{-0.07}$	0.78 ± 0.06
in 0.3–8.0 keV [‡]	$(10^{33} \text{ erg s}^{-1})$	$0.92^{+0.11}_{-0.09}$	1.0 ± 0.1
$\chi^2/\text{d.o.f.}$		1.25 (716)	1.23 (634)

* Errors are 90% confidence range.

† $10^{-14}/(4\pi D^2)EM$, where D is the distance to a target in cm and EM is the plasma emission measure in cm^{-3} .

‡ The X-ray luminosity is corrected for absorption. A distance of 1.7 kpc is assumed.

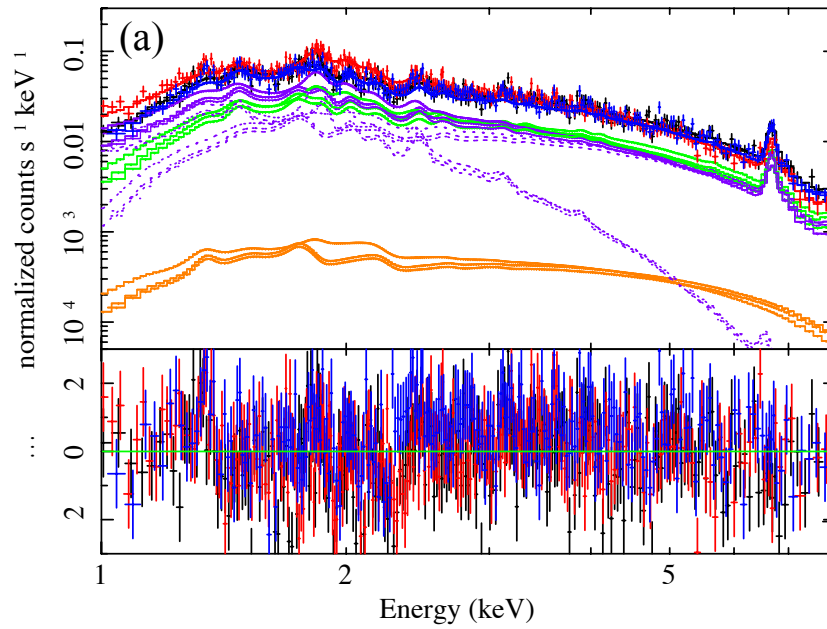
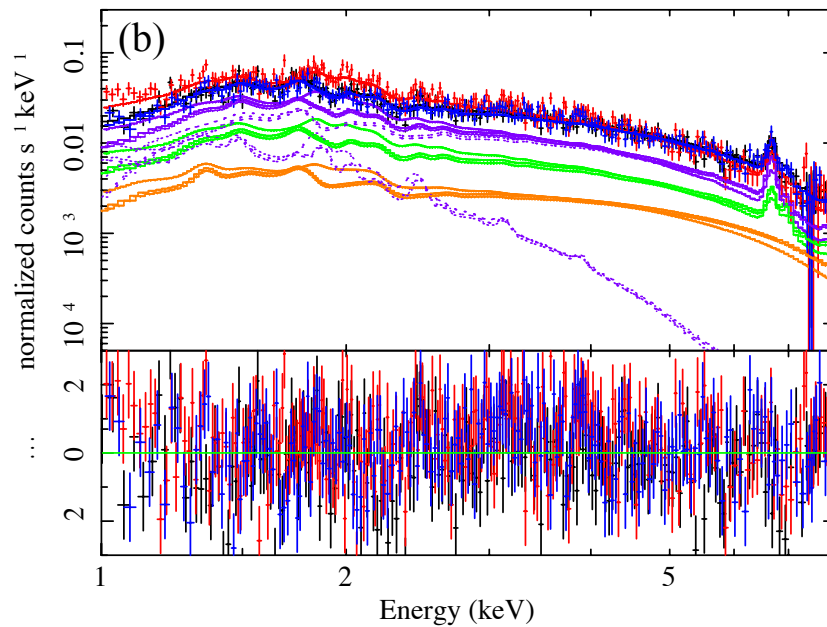
RCW 38: BKG + Point Sources + Diffuse component ($r < 2.0$ arcmin)RCW 38: BKG + Point Sources + Diffuse component ($r = 2.0 - 5.5$ arcmin)

FIGURE 6.3: Same as figure 5.14 but the point source contributions are scaled by a factor of 0.8 for the best-fitting model.

represented by the low-temperature ($kT = 0.87 \pm 0.08$ keV) component, and the high-temperature component was insignificant. The fit was slightly worse, and $\chi^2/\text{d.o.f.}$ was changed from 1.25 to 1.29. In the outer region, the basic parameters (N_{H} , kT_{low} , and kT_{high}) and χ^2 values did not significantly change compared to table 5.5. In summary, if the point sources were underestimated due to uncertainty, the parameters argued in section 5.3 also explain the diffuse X-ray emission in the outer region, while the hard X-ray emission becomes extremely weak or disappears in the inner region. We can say that the total absorption-corrected luminosity of the diffuse emission in RCW 38 would contribute at least $\sim 1 \times 10^{33}$ erg s⁻¹ in 1–8 keV, considering the 90% errors.

After all, we conclude that the diffuse emission truly exists in RCW 38. The thermal model can explain the emission significantly better than the non-thermal model with F-test confidence levels >90%, except for the case of the point source underestimation in the inner region. Therefore, at least in the outer region, we conclude that there is diffuse hard X-ray emission and that the thermal model fits better. Here, note that we assumed undetectable point sources and the resolved point sources have exactly the same spectral shape. Low-mass stars and YSOs are generally known to show softer emission than the spectral model we have assumed (e.g., Preibisch et al., 2005; Feigelson et al., 2005). Therefore, the estimates in this subsection are particularly conservative for hard X-rays.

6.3 Emission components

In our analysis, similar thermal plasma models of 0.9–1.1 keV were seen for point source (table 5.2) and diffuse emission models (tables 5.4 and 5.5). These may contain the contribution of undetected point sources. The total absorption-corrected X-ray luminosity of this low-temperature diffuse plasma within the $r_{5.5}$ circle was $\sim 2 \times 10^{33}$ erg s⁻¹ in 0.3–8 keV, which was comparable to the prediction of the undetected point sources. If this is true, the diffuse X-ray emission in RCW 38 would be dominant in the high-energy band because the low-temperature component is relatively soft emission.

In contrast to the preceding argument, it is quite possible for diffuse X-ray emission to have two emission components since RCW 38 has two major molecular clouds, as shown in figure 6.6. One has a ring-like shape surrounding IRS 2, and the other has a finger-like shape extending north-south across the inner and outer

TABLE 6.4: Same as table 5.3 but for tables 6.5 and 6.6. Point source contributions are scaled by a factor of 1.45 for the best-fitting model.

Component	Parameter	Unit	Value	
			Inner	Outer
Astrophysical foreground/backgrounds	kT_{LHB}	(keV)	0.12	
	Abundance	(solar)	1	
	Norm. ^{LHB}	(unit [*])	2.4×10^{-3}	
	N_{H}	(10^{22} cm^{-2})	(bind ₅)	(bind ₆)
	kT_{TAE}	(keV)	0.22	
	Abundance	(solar)	1	
	Norm. ^{TAE}	(unit [*])	2.3×10^{-2}	
	Photon index		1.6	
	Norm. ^{CXB}	(unit [†])	1.7×10^{-3}	
Point sources from the inner region	N_{H}	(10^{22} cm^{-2})	(bind ₅)	(bind ₆)
	kT_{low}	(keV)	0.86	
	Norm. ^{low}	(unit [*])	2.6×10^{-3}	8.3×10^{-4}
	kT_{high}	(keV)	4.5	
	Norm. ^{high}	(unit [*])	5.4×10^{-3}	1.7×10^{-3}
	He	(solar)	1	
	Fe	(solar)	0.22	
	Other metal	(solar)	0.65	
	Point sources from the outer region	N_{H}	(10^{22} cm^{-2})	(bind ₅)
kT_{low}		(keV)	1.1	
Norm. ^{low}		(unit [*])	1.1×10^{-4}	1.1×10^{-3}
kT_{high}		(keV)	9.1	
Norm. ^{high}		(unit [*])	1.3×10^{-4}	1.4×10^{-3}
He		(solar)	1	
Fe		(solar)	0.39	
Other metal		(solar)	0.17	

* $10^{-14}/(4\pi D^2)EM$, where D is the distance to a target in cm and EM is the plasma emission measure in cm^{-3} .

† Photons $\text{keV}^{-1}\text{cm}^{-2} \text{ s}^{-1}$ at 1 keV.

TABLE 6.5: Same as table 5.4 (non-thermal model) but the point source contributions are scaled by a factor of 1.45 for the best-fitting model.

Parameter	Unit	Value / error*	
		Inner	Outer
N_{H}	(10^{22} cm^{-2})	1.7 ± 0.1 (bind ₅)	1.4 ± 0.1 (bind ₆)
kT	(keV)	0.88 ± 0.08	1.0 ± 0.2
Norm. ^{thermal}	(unit [†])	$(2.6 \pm 0.7) \times 10^{-3}$	$(1.4 \pm 0.5) \times 10^{-3}$
Photon index		$1.3 (> 0.9)$	1.8 ± 0.2
Norm. ^{non-thermal}	(unit [†])	$0.61 (< 5.11) \times 10^{-5}$	$(3.0 \pm 0.9) \times 10^{-4}$
He	(solar)	1 (fixed)	1 (fixed)
Other metal	(solar)	0.3 (fixed)	0.3 (fixed)
$L_{\text{X}}^{\text{thermal}}$ in 1.0–8.0 keV [§]	($10^{33} \text{ erg s}^{-1}$)	0.39 ± 0.10	0.26 ± 0.10
in 0.3–8.0 keV [§]	($10^{33} \text{ erg s}^{-1}$)	1.1 ± 0.3	0.58 ± 0.22
$L_{\text{X}}^{\text{non-thermal}}$ in 1.0–8.0 keV [§]	($10^{33} \text{ erg s}^{-1}$)	$0.015 (< 0.125)$	0.41 ± 0.12
in 0.3–8.0 keV [§]	($10^{33} \text{ erg s}^{-1}$)	$0.018 (< 0.149)$	0.60 ± 0.17
$\chi^2/\text{d.o.f.}$		1.29 (718)	1.27 (634)

* Errors are 90% confidence range.

† $10^{-14}/(4\pi D^2)EM$, where D is the distance to a target in cm and EM is the plasma emission measure in cm^{-3} .

‡ Photons $\text{keV}^{-1}\text{cm}^{-2} \text{ s}^{-1}$ at 1 keV.

§ The X-ray luminosity is corrected for absorption. A distance of 1.7 kpc is assumed.

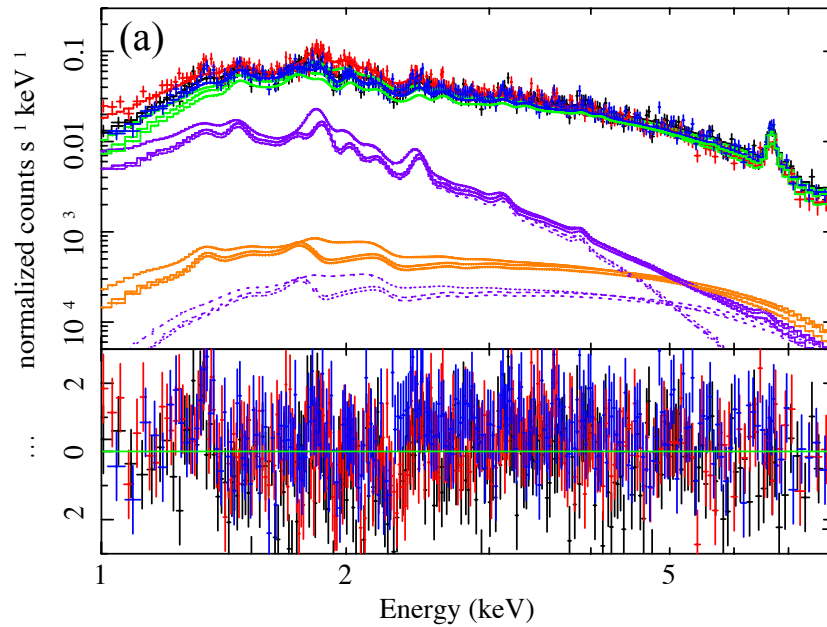
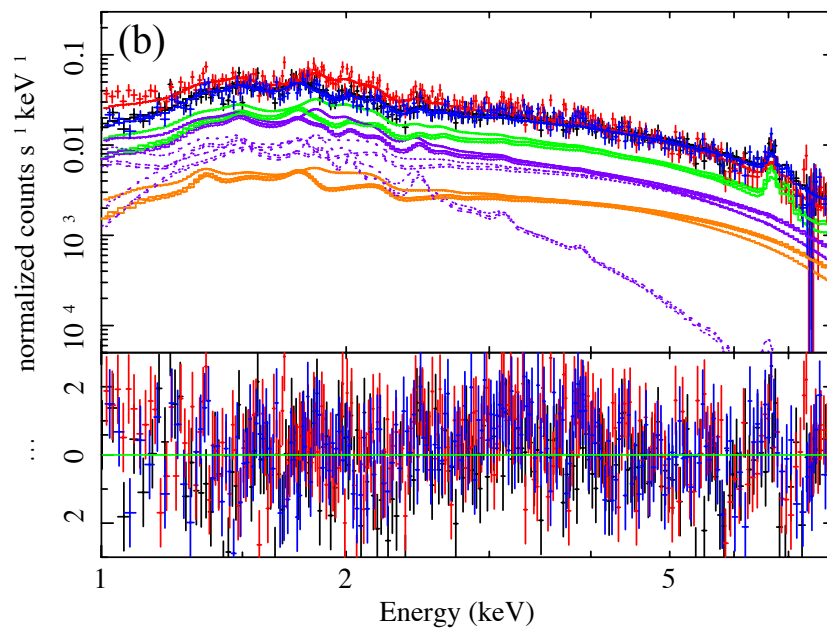
RCW 38: BKG + Point Sources + Diffuse component ($r < 2.0$ arcmin)RCW 38: BKG + Point Sources + Diffuse component ($r = 2.0 - 5.5$ arcmin)

FIGURE 6.4: Same as figure 5.13 but the point source contributions are scaled by a factor of 1.45 for the best-fitting model.

TABLE 6.6: Same as table 5.5 (thermal model) but the point source contributions are scaled by a factor of 1.45 for the best-fitting model.

Parameter	Unit	Value / error*	
		Inner	Outer
N_{H}	$(10^{22} \text{ cm}^{-2})$	1.7 ± 0.1 (bind ₅)	1.4 ± 0.1 (bind ₆)
kT_{low}	(keV)	0.87 ± 0.08	$0.93^{+0.17}_{-0.19}$
Norm. ^{low}	(unit [†])	$(2.6 \pm 0.7) \times 10^{-3}$	$8.4^{+5.2}_{-4.9} \times 10^{-4}$
kT_{high}	(keV)	12 (> 0)	$4.2^{+0.8}_{-0.6}$
Norm. ^{high}	(unit [†])	$0.37 (< 1.62) \times 10^{-4}$	$(1.2 \pm 0.2) \times 10^{-3}$
He	(solar)	1 (fixed)	1 (fixed)
Other metal	(solar)	0.3 (fixed)	0.3 (fixed)
$L_{\text{X}}^{\text{low}}$ in 1.0–8.0 keV [‡]	$(10^{33} \text{ erg s}^{-1})$	0.39 ± 0.10	0.14 ± 0.08
in 0.3–8.0 keV [‡]	$(10^{33} \text{ erg s}^{-1})$	1.2 ± 0.3	0.37 ± 0.22
$L_{\text{X}}^{\text{high}}$ in 1.0–8.0 keV [‡]	$(10^{33} \text{ erg s}^{-1})$	0.018 (< 0.078)	0.46 ± 0.06
in 0.3–8.0 keV [‡]	$(10^{33} \text{ erg s}^{-1})$	0.022 (< 0.095)	0.62 ± 0.08
$\chi^2/\text{d.o.f.}$		1.29 (716)	1.22 (634)

* Errors are 90% confidence range.

† $10^{-14}/(4\pi D^2)EM$, where D is the distance to a target in cm and EM is the plasma emission measure in cm^{-3} .

‡ The X-ray luminosity is corrected for absorption. A distance of 1.7 kpc is assumed.

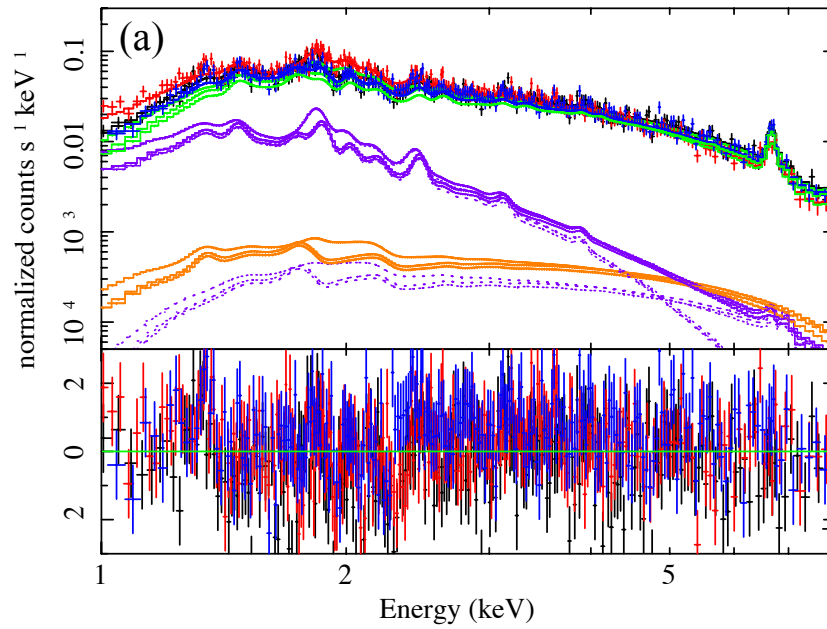
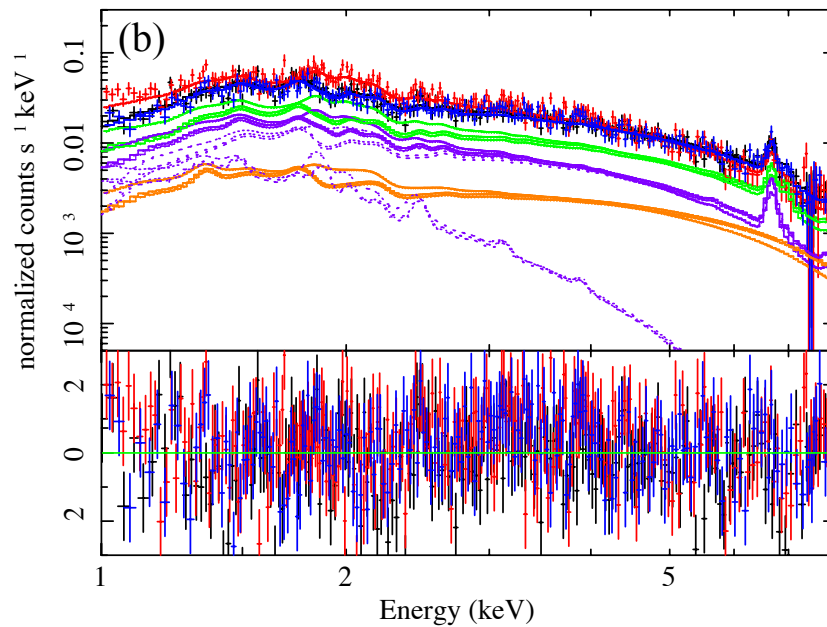
RCW 38: BKG + Point Sources + Diffuse component ($r < 2.0$ arcmin)RCW 38: BKG + Point Sources + Diffuse component ($r = 2.0 - 5.5$ arcmin)

FIGURE 6.5: Same as figure 5.14 but the point source contributions are scaled by a factor of 1.45 for the best-fitting model.

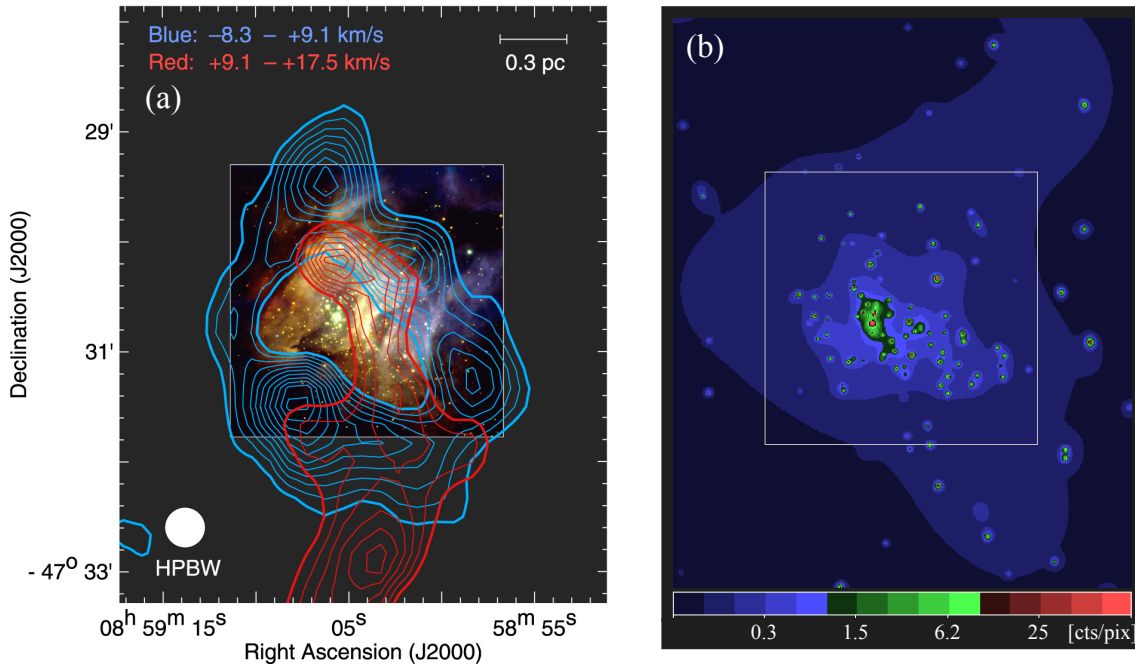


FIGURE 6.6: (a) Very Large Telescope image of RCW 38 (from Wolk et al., 2006) and the morphology of the molecular clouds derived from Fukui et al. (2016). The blue and red contours show $^{12}\text{CO } J = 3-2$ distributions of the ring cloud and the finger cloud, respectively. (b) *Chandra* RCW 38 image smoothed with the *csmooth* tool. The square corresponds to the FOV of the Very Large Telescope image.

regions (Fukui et al., 2016). Both clouds are on the order of several pc in size and move at different velocities. If the gas heating is caused by these ISM/wind collisions, it is reasonable to observe two or more separate emission components. The possibility of a mixture of thermal and non-thermal origins thus remains.

6.4 Comparison with previous non-thermal model

Wolk et al. (2002) argued that the diffuse X-ray emission could be explained by a thermal plasma of 0.2–1.0 keV and a power law of photon index 1.3–2.8. Although the luminosity was not mentioned in the paper, we converted their power-law model to an unabsorbed luminosity of $\sim 6 \times 10^{32} \text{ erg s}^{-1}$ in 1–8 keV using XSPEC. The X-ray spectrum in our region required a low temperature of 0.9–1.1 keV to represent the low-energy band, and a power law of photon index 1.8–1.9 was suitable for the high-energy band in the non-thermal model. The total absorption-corrected luminosity for the $r5'5$ circle was $(1.1 \pm 0.4) \times 10^{33} \text{ erg s}^{-1}$ for the best-fit power-law model. These are almost consistent with Wolk et al. (2002).

We also consider the case where the non-thermal emission exists only in the inner region because the outer region significantly favors the thermal model. The power-law luminosity is $4.8_{-1.3}^{+1.5} \times 10^{32} \text{ erg s}^{-1}$ in 1–8 keV. This value is still consistent with Wolk et al. (2002). As discussed in subsection 6.2.2, these luminosities may be scaled with the point source uncertainties. Thus, we can say that the non-thermal component of our analysis is generally consistent with their results.

6.5 Thermal scenario

In this thesis, it is newly discovered that a hot thermal component is seen in the entire or in the outer region of RCW 38. We discuss the possibility of thermal diffuse X-ray emission in this section. The discussion assumes that both temperatures contain diffuse emission components.

6.5.1 Thermal plasmas and energetics

The most likely origins of diffuse thermal plasma are shocks from massive stellar winds or past supernova remnants. These two scenarios can be distinguished by elemental abundances because the composition of the thermal plasma is determined by its source. Elemental abundances are estimated by precisely measuring the emission lines on the spectrum. Unfortunately, the diffuse X-ray emission in RCW 38 is strongly affected by bright point sources, making diagnosing difficult. A future satellite capable of both energy resolution superior to the XIS, such as a microcalorimeter (Ezoe, Ohashi, and Mitsuda, 2021), and point source separation (at least $30''$ in angular resolution) would make this verification possible in this region.

Here, we consider whether massive OB stars could be the origins as an example. It is believed that wind produces a strong shock at a radius where its ram pressure is equal to the external pressure (Castor, McCray, and Weaver, 1975; Weaver et al., 1977). The space between the shock and the contact discontinuity is filled with hot gas, which emits thermal X-ray emission. The kinematic luminosity L_w that can be supplied by the wind from a single massive star is obtained from the following:

$$L_w = \frac{1}{2} \dot{M} v_w^2 = 1 \times 10^{35} \text{ erg s}^{-1} \left(\frac{\dot{M}}{10^{-7} M_\odot \text{ yr}^{-1}} \right) \left(\frac{v_w}{2000 \text{ km s}^{-1}} \right)^2, \quad (6.1)$$

where $\dot{M} = 10^{-7} M_{\odot} \text{ yr}^{-1}$ is the standard mass loss rate (Vink, Koter, and Lamers, 2001) and $v_w = 2,000 \text{ km s}^{-1}$ is the typical wind velocity (Prinja, 1990). Since more than 30 OB stars were reported to be associated with RCW 38 (Wolk et al., 2006), there should be an energy supply of more than $10^{36} \text{ erg s}^{-1}$. On the other hand, our obtained luminosity of the diffuse emission is of the order of $10^{33} \text{ erg s}^{-1}$. The diffuse emission in RCW 38 can be explained if the wind is converted to X-ray luminosity with an efficiency of only $\sim 0.1\%$.

We then discuss what temperatures are possible for thermal plasma. The maximum temperature kT_s given behind the shock originating from the wind from a single OB star is given by

$$kT_s = \frac{3}{16} \mu m_H v_w^2 = 5 \text{ keV} \left(\frac{v_w}{2000 \text{ km s}^{-1}} \right)^2 \quad (6.2)$$

from the Rankine-Hugoniot relation, where $\mu = 0.62$ is the mean molecular weight and $m_H = 1.67 \times 10^{-27} \text{ kg}$ is the mass of the hydrogen. Multiple winds would make it even higher. Equation (6.2) shows that the observed temperatures ($kT = 0.91 \pm 0.06$ and $5.3_{-0.9}^{+1.2} \text{ keV}$ in the inner region, and $kT = 0.96 \pm 0.12$ and $4.9 \pm 0.6 \text{ keV}$ in the outer region) can be explained by assuming one or more massive OB stars with typical wind velocities.

6.5.2 Comparison with other MSFRs

Comparison with other MSFRs would be useful to consider the thermal interpretation. The low-temperature ($kT \sim 1 \text{ keV}$) thermal plasma emission was similar to other regions observed with *Suzaku* (e.g., $kT \sim 0.3 \text{ keV}$ in M 17 by Hyodo et al., 2008, $kT \sim 0.2$ and $\sim 0.6 \text{ keV}$ in the Carina Nebula by Hamaguchi et al., 2007; Ezoe et al., 2009; Ezoe et al., 2019, see subsection 4.1.1 for details). These plasmas showed almost uniform temperatures.

The high-temperature ($kT \sim 5 \text{ keV}$) components in RCW 38 were clearly higher than the past reports for M 17 and the Carina Nebula. As discussed in the previous subsection, such high temperatures can be reached in terms of energetics. Indeed, there are also reports suggesting the possibility of such high-temperature plasma (e.g., $kT \sim 4 \text{ keV}$ in RCW 49 by Fujita et al., 2009, see subsection 4.1.2 for details). However, it is still unclear what determines the plasma temperature and the brightness, even if they all are truly thermal emission. RCW 38 also has strong

interstellar absorption. That may be a clue to this question. From the *Chandra* observation of NGC 6334, it was reported that surface brightness and plasma temperature are related to the surrounding material which confines plasma sources, such as stellar winds (Ezoe et al., 2006b).

We then review the discussion in Ezoe et al. (2006b). We assume a situation in which a massive stellar wind in the center of the H II region spreads around and forms a hot bubble. Assuming that the energy of the stellar wind is equal to the displaced energy of the cold gas, the size of the expanding hot wind bubble R_b can be described as

$$\frac{1}{2}\dot{M}v_w^2t = \left(\frac{4}{3}\pi R_b^3\right)\frac{3}{2}p_s, \quad (6.3)$$

where t is the time since the wind started blowing and p_s is the thermal pressure of the surrounding material (Chevalier, 1999). Assuming that \dot{M} , v_w , and t are unchanged in equation (6.3), we expect $R_b \propto p_s^{-1/3}$, and hence $n_e \propto \dot{M}t/R_b^3 \propto p_s$, where n_e is the density of the X-ray emitting plasma. With this relationship, surface brightness S_X is described as

$$S_X \propto n_e^2 R_b \propto p_s^2 p_s^{-1/3} \propto p_s^{5/3}. \quad (6.4)$$

Furthermore, the absorption column density N_H should relate to surrounding pressure p_s , and then we may very roughly assume

$$S_X \propto N_H^{5/3}. \quad (6.5)$$

The above relation assumes thermal emission and a constant temperature, although its dependence on the cooling function $\Lambda(T)$ is rather weak ($T^{0.5}$). Indeed, the *Chandra* observation of NGC 6334 approximately satisfied this relationship. A similar positive correlation between kT and N_H was also reported. Presumably, stronger wind shocks would be formed in denser environments.

We test this relationship using the newly obtained results with *Suzaku*. However, time t should be treated as a variable parameter since it does not necessarily coincide in all regions. Then, using $R_b \propto p_s^{-1/3}t^{1/3}$ from equation (6.3), equation (6.5) is corrected as follows:

$$S_X t^{-1/3} \propto N_H^{5/3}. \quad (6.6)$$

We plotted the relationship between $S_X t^{-1/3}$ and N_H , as shown in figure 6.7. We corrected figure 14a in Ezoe et al. (2006b) using the expected time t . Furthermore, three *Suzaku* observations of thermal emission are added to the diagram. The N_H and S_X values were derived from X-ray spectral analyses, and t was estimated from other works. As a result, we can see a positive correlation. Although the error bars are large, they are approximately consistent with equation (6.6). Since the number of O stars can typically differ by one order of magnitude from region to region (Townsend et al., 2003), equation (6.6) may be changed to $S_X t^{-1/3} \dot{M}^{-1/3} \propto N_H^{5/3}$. However, the effect is rather weak, and this trend would still remain.

We next plotted the relationship between N_H and kT . To keep the analysis conditions the same, figure 6.8 shows only the results of multi-temperature plasma models in nearby ($\lesssim 6$ kpc) MSFRs observed with *Suzaku* and/or *Chandra*. The N_H and S_X values were determined from the respective X-ray observations. We initially did not find a positive correlation as seen in figure 14b in Ezoe et al. (2006b). This is because most studies have applied multiple temperature components with common absorption. Therefore, we focused only on the hottest component in each region. Then, we found a strong positive correlation between N_H and kT . They are approximated by a power law or linear function. That suggests that the pressure of the ISM around the plasmas determines the maximum temperature of the diffuse plasma.

The plasma temperature kT in figure 6.8 can be roughly regarded as an index of the hardness of the diffuse X-ray spectrum. That suggests that the pressure of the surrounding ISM may uniformly explain regional differences in X-ray spectral shape. Thus, one possible interpretation of the hard diffuse X-ray emission is that fast stellar winds or supernova remnants of massive stars formed in the cluster center scatter and collide with the surrounding dense ISM, converting kinetic energy into extremely hot plasma or possibly non-thermal particles.

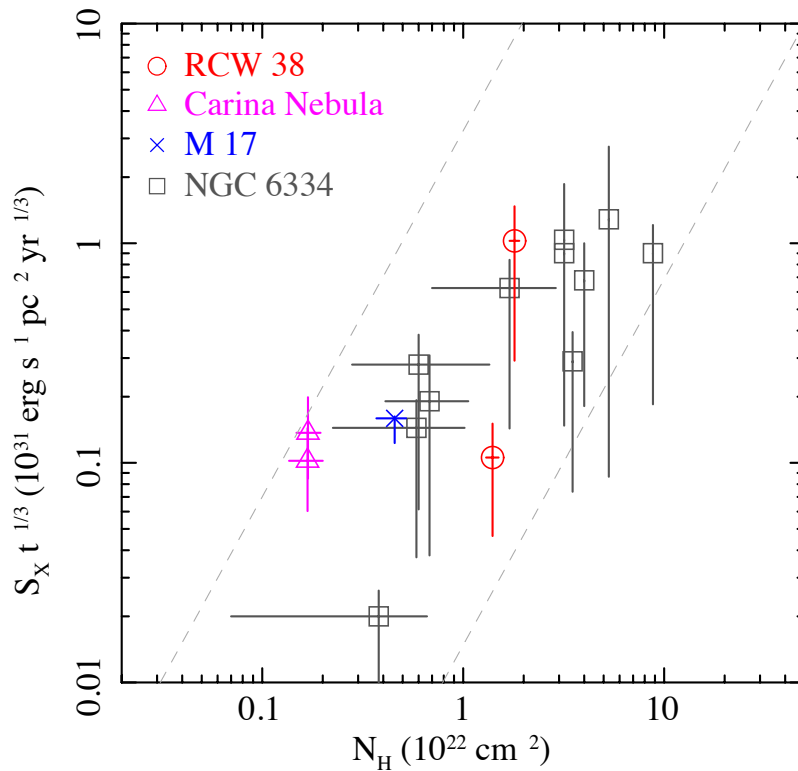


FIGURE 6.7: Unabsorbed age-corrected surface brightness versus absorption diagram for diffuse thermal plasma. The dashed lines show the prediction of $S_X t^{-1/3} \propto N_H^{5/3}$. N_H and S_X , and t values of RCW 38, the Carina Nebula, M 17, and NGC 6334 are referred to this work and Wolk et al. (2006), Ezoë et al. (2019) and Sana et al. (2010), Hyodo et al. (2008) and Hanson, Howarth, and Conti (1997), and Ezoë et al. (2006b) and Fukui et al. (2018), respectively.

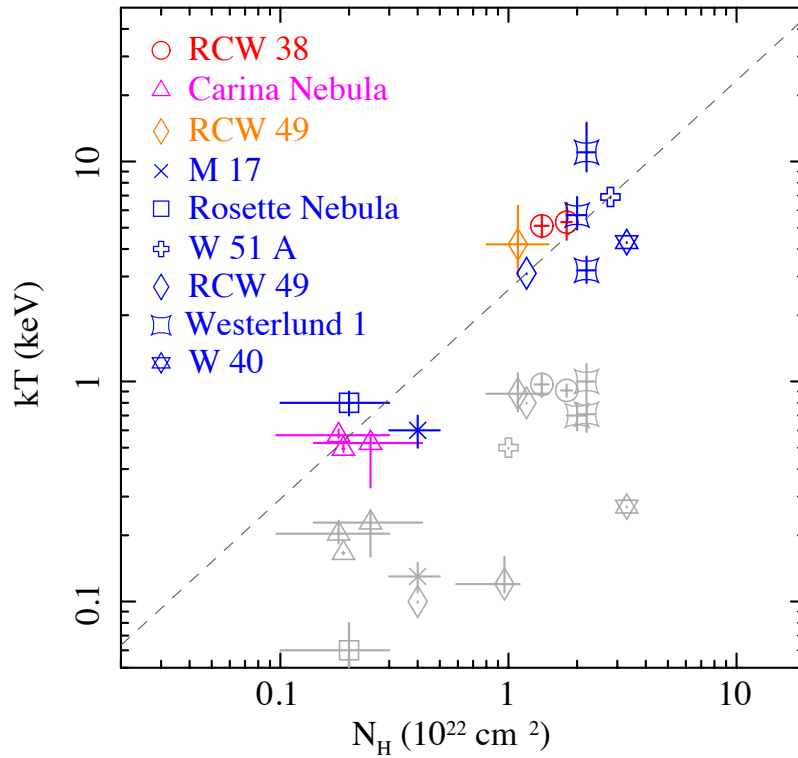


FIGURE 6.8: Temperature versus absorption diagram of diffuse thermal emission. Colored and gray data indicate high- and low-temperature components, respectively. The dashed line shows the fitted model ($kT = 2.6N_H^{0.95}$) to the high-temperature components. The results of RCW 38 (this work), the Carina Nebula (Hamaguchi et al., 2007; Ezoe et al., 2009; Ezoe et al., 2019), and RCW 49 (Fujita et al., 2009) are obtained with *Suzaku*. The results of M 17 and the Rosette Nebula (Townsend et al., 2003), W 51 A and RCW 49 (Townsend et al., 2005), Westerlund 1 (Muno et al., 2006), and W 40 (Kuhn et al., 2010) are obtained with *Chandra*. Of these, W 51 A, RCW 49 (*Chandra*), and W 40 should be used as reference only since the error bars are unknown.

Chapter 7

Conclusion

In this thesis, we investigated the diffuse X-ray emission associated with the formation of massive stars, which was revealed in the 2000s. Since the origins of power-law-like hard X-ray spectra were unsolved, we focused on nearby representative MSFR RCW 38 and studied it in detail using *Suzaku* and *Chandra*. We utilized nearby *Suzaku* offset observation and *Chandra* RCW 38 observation to estimate the contributions of astrophysical foreground/background and point source emission and quantified the diffuse X-ray components by introducing them into the *Suzaku* XIS spectrum of RCW 38. The results show that even after accounting for some uncertainty, there is indeed truly diffuse X-ray emission with an absorption-corrected luminosity of the order of 10^{33} erg s⁻¹ in 1–8 keV.

We divided the area into inner ($r < 2'.0$) and outer ($r = 2'.0\text{--}5'.5$) regions and performed a spectral analysis with *Suzaku*. In the inner region, the X-ray spectrum of this diffuse emission could be represented by the non-thermal model (absorbed thermal plasma at $kT = 0.93 \pm 0.06$ keV and power law of $\Gamma = 1.9 \pm 0.2$) and the thermal model (absorbed two-temperature plasma at $kT = 0.91 \pm 0.06$ and $5.3_{-0.9}^{+1.2}$ keV). The latter was first proposed in this study, while the former was consistent with the previous study (Wolk et al., 2002). In the outer region, the diffuse emission was again represented by the non-thermal model (absorbed thermal plasma at $kT = 1.1 \pm 0.2$ keV and power law of $\Gamma = 1.8 \pm 0.1$) and the thermal model (absorbed two-temperature plasma at $kT = 0.96 \pm 0.12$ and 4.9 ± 0.6 keV). Although the emission was strongly contaminated by undetectable point sources in the inner region, we concluded that the thermal model was more favorable than the non-thermal model, at least in the outer region.

The newly discovered hot component ($kT \sim 5$ keV) is higher than in the past reports for M 17 and the Carina Nebula. However, the obtained X-ray luminosity

and plasma temperature were consistently explained by the typical stellar winds ($\sim 2,000 \text{ km s}^{-1}$) from massive stars. We further show that the surface brightness and temperature of the thermal emission are positively correlated with the hydrogen column density. That suggests that the properties of the diffuse plasma strongly depend on the pressure of the ISM surrounding it.

Thus, our study showed that the thermal interpretation could be applied to RCW 38, a representative hard diffuse X-ray source. Furthermore, the plasma temperature correlated well with the surrounding material density along with other regions, supporting the stellar wind shock model as the origin of diffuse X-ray emission. While the non-thermal scenario is not ruled out, thermal emission turns out to be dominant in some areas of RCW 38. The spectral hardness, which varies from region to region, may be uniformly explained by the density of the surrounding ISM. For future studies, information on emission lines can provide clues to element abundances, which may lead to further discussions on non-thermal/thermal distinction and the origins of diffuse thermal X-ray emission.

Acknowledgements

The six years spent in my lab at Tokyo Metropolitan University (TMU) were fulfilling, but many difficulties also accompanied this voyage. I would like to extend my sincere thanks to everyone who supported me in overcoming all the challenges.

I would like to express my best gratitude to my supervisor, Dr. Yuichiro Ezoe, for his invaluable guidance, support, and encouragement throughout my Ph.D. journey. My experience under Ezoe-sensei has definitely made me grow a lot. I will never forget the last six years. I also acknowledge with appreciation the crucial role of Dr. Yoshitaka Ishisaki and Prof. Yutaka Fujita as members of my thesis committee. Their valuable feedback and suggestions allowed me to raise the quality of this thesis. Also, I would like to offer my special thanks to Dr. Takaya Ohashi, President of TMU, for his concern and kindness. I am looking forward to receiving my diploma with Ohashi-sensei's name on it. I also thank my excellent seniors and now lab staff, Dr. Kumi Ishikawa and Dr. Masaki Numazawa, for their daily support and thoughtful encouragement. I am also greatly indebted to Secretary Yuko Kawakami and the Physics Department office for accounting and paperwork. Dr. Hirokazu Odaka gave me constructive advice and suggestions many times on data analyses. Thanks to that, I have been able to complete this thesis. I also owe a lot to ISAS/JAXA nanoelectronics clean room and XRT team, Jun-ichi Nishizawa Memorial Research Center, Prof. Yoshiaki Kanamori, Dr. Kenji Hamaguchi, and other collaborating research institutes and companies. I am grateful for all their cooperation. Also, I want to thank my co-workers at TMU, Kazuma Takeuchi, Masaru Terada, Daiki Ishi, Maiko Fujitani, Ryota Otsubo, Takahito Itoyama, Mai Takeo, Tsubasa Umetani, Kanae Ohi, and all of the past and present members of our lab. Finally, a special gratitude I give to my family for respecting my wishes. Now I can go on my next voyage with confidence!

This research was also supported by Grant-in-Aid for Japan Society for the Promotion of Science Fellows Grant Number JP21J12023.

Bibliography

- Aharonian, Felix et al. (2007). "Detection of extended very-high-energy γ -ray emission towards the young stellar cluster Westerlund 2". In: *Astronomy & Astrophysics* 467.3, pp. 1075–1080.
- Anderson, LD et al. (2009). "The molecular properties of galactic H II regions". In: *The Astrophysical Journal Supplement Series* 181.1, p. 255.
- Andre, Philippe, Derek Ward-Thompson, and Mary Barsony (1993). "Submillimeter continuum observations of Rho Ophiuchi A-The candidate protostar VLA 1623 and prestellar clumps". In: *The Astrophysical Journal* 406, pp. 122–141.
- Antokhin, Igor I et al. (2008). "XMM-Newton X-ray study of early type stars in the Carina OB1 association". In: *Astronomy & Astrophysics* 477.2, pp. 593–609.
- Ascenso, J et al. (2007). "Near-IR imaging of Galactic massive clusters: Westerlund 2". In: *Astronomy & Astrophysics* 466.1, pp. 137–149.
- Aschenbach, B (1985). "X-ray telescopes". In: *Reports on Progress in Physics* 48.5, p. 579.
- Avedisova, VS and Jan Palous (1989). "Kinematics of star forming regions". In: *Bulletin of the Astronomical Institutes of Czechoslovakia* 40, pp. 42–52.
- Baldry, Ivan K and Karl Glazebrook (2003). "Constraints on a universal stellar initial mass function from ultraviolet to near-infrared galaxy luminosity densities". In: *The Astrophysical Journal* 593.1, p. 258.
- Bally, John and Hans Zinnecker (2005). "The birth of high-mass stars: Accretion and/or mergers?" In: *The Astronomical Journal* 129.5, p. 2281.
- Band, David L and Matthew A Malkan (1989). "Synthesis of accretion disk and nonthermal source models for active galactic nuclei". In: *The Astrophysical Journal* 345, pp. 122–134.
- Baraffe, Isabelle et al. (2003). "Evolutionary models for cool brown dwarfs and extrasolar giant planets. The case of HD 209458". In: *Astronomy & Astrophysics* 402.2, pp. 701–712.
- Berghöfer, TW et al. (1997). "X-ray properties of bright OB-type stars detected in the ROSAT all-sky survey." In: *Astronomy and Astrophysics* 322, pp. 167–174.

- Berrilli, F et al. (1992). "A study of the solar atmosphere with high-resolution spectroscopic images: Acquisition system". In: *Il Nuovo Cimento C* 15.5, pp. 519–526.
- Boller, Th et al. (2016). "Second ROSAT all-sky survey (2RXS) source catalogue". In: *Astronomy & Astrophysics* 588, A103.
- Bonnell, IA et al. (2001). "Competitive accretion in embedded stellar clusters". In: *Monthly Notices of the Royal Astronomical Society* 323.4, pp. 785–794.
- Bonnell, Ian A, Matthew R Bate, and Hans Zinnecker (1998). "On the formation of massive stars". In: *Monthly Notices of the Royal Astronomical Society* 298.1, pp. 93–102.
- Boulanger, F., P. Cox, and A. P. Jones (Jan. 2000). "Course 7: Dust in the Interstellar Medium". In: *Infrared Space Astronomy, Today and Tomorrow*. Ed. by F. Casoli, J. Lequeux, and F. David. Vol. 70, p. 251.
- Bourke, Tyler L et al. (2001). "New OH Zeeman measurements of magnetic field strengths in molecular clouds". In: *the Astrophysical Journal* 554.2, p. 916.
- Broos, Patrick S et al. (2013). "Identifying young stars in massive star-forming regions for the MYStIX project". In: *The Astrophysical Journal Supplement Series* 209.2, p. 32.
- Brussaard, PJ and HC Van de Hulst (1962). "Approximation formulas for nonrelativistic bremsstrahlung and average Gaunt factors for a Maxwellian electron gas". In: *Reviews of Modern Physics* 34.3, p. 507.
- Bykov, AM and IN Toptygin (2001). "A model of particle acceleration to high energies by multiple supernova explosions in OB associations". In: *Astronomy Letters* 27.10, pp. 625–633.
- Capriotti, Eugene R and Joseph F Kozminski (2001). "Relative Effects of Ionizing Radiation and Winds from O-Type Stars on the Structure and Dynamics of H ii Regions". In: *Publications of the Astronomical Society of the Pacific* 113.784, p. 677.
- Cassinelli, Joseph P (1979). "Stellar winds". In: *Annual Review of Astronomy and Astrophysics* 17, pp. 275–308.
- Castor, John, Richard McCray, and Robert Weaver (1975). "Interstellar bubbles". In: *Astrophysical Journal*, vol. 200, Sept. 1, 1975, pt. 2, p. L107-L110. 200, pp. L107–L110.
- Chen, Wan and Richard L White (1991). "Nonthermal X-ray emission from winds of OB supergiants". In: *The Astrophysical Journal* 366, pp. 512–528.
- Chevalier, Roger A (1999). "Supernova remnants in molecular clouds". In: *The Astrophysical Journal* 511.2, p. 798.

- Chibueze, James O et al. (2014). "Astrometry and Spatio-kinematics of H₂O Masers in the Massive Star-forming Region NGC 6334I (North) with VERA". In: *The Astrophysical Journal* 784.2, p. 114.
- Choudhuri, AR, M Schussler, and M Dikpati (1995). "The solar dynamo with meridional circulation." In.
- Churchwell, Ed (2002). "Ultra-compact HII regions and massive star formation". In: *Annual Review of Astronomy and Astrophysics* 40.1, pp. 27–62.
- Clark, P. C. et al. (May 2008). "The Conditions for Competitive Accretion". In: *Massive Star Formation: Observations Confront Theory*. Ed. by H. Beuther, H. Linz, and Th. Henning. Vol. 387. Astronomical Society of the Pacific Conference Series, p. 208.
- Cohen, David H et al. (2003). "High-resolution Chandra spectroscopy of τ Scorpii: a narrow-line X-ray spectrum from a hot star". In: *The Astrophysical Journal* 586.1, p. 495.
- Corcoran, MF et al. (1994). *ASCA solid state imaging spectrometer observations of O stars*. Tech. rep.
- Corcoran, MF et al. (2000). "The X-Ray spectral evolution of η Carinae as seen by ASCA". In: *The Astrophysical Journal* 545.1, p. 420.
- Corcoran, MF et al. (2004). "Waiting in the wings: reflected X-ray emission from the Homunculus nebula". In: *The Astrophysical Journal* 613.1, p. 381.
- Crowther, Paul A (2007). "Physical properties of Wolf-Rayet stars". In: *Annu. Rev. Astron. Astrophys.* 45, pp. 177–219.
- Dame, Thomas M, Dap Hartmann, and P Thaddeus (2001). "The Milky Way in molecular clouds: a new complete CO survey". In: *The Astrophysical Journal* 547.2, p. 792.
- Dame, TM et al. (1987). "A composite CO survey of the entire Milky Way". In: *The Astrophysical Journal* 322, pp. 706–720.
- Damiani, F et al. (1997). "A method based on wavelet transforms for source detection in photon-counting detector images. I. Theory and general properties". In: *The Astrophysical Journal* 483.1, p. 350.
- De Becker, Michaël (2007). "Non-thermal emission processes in massive binaries". In: *The Astronomy and Astrophysics Review* 14.3, pp. 171–216.
- DeRose, KL et al. (2009). "A Very Large Telescope/NACO Study of Star Formation in the Massive Embedded Cluster RCW 38". In: *The Astronomical Journal* 138.1, p. 33.

- Evans II, Neal J (1999). "Physical conditions in regions of star formation". In: *Annual Review of Astronomy and Astrophysics* 37.1, pp. 311–362.
- Ezoe, Y et al. (2006a). "The discovery of diffuse X-ray emission in NGC 2024, one of the nearest massive star-forming regions". In: *The Astrophysical Journal* 649.2, p. L123.
- Ezoe, Yuichiro (Mar. 2004). "Investigation of Diffuse Hard X-ray Emission Associated with the Formation of Massive Stars". PhD thesis. University of Tokyo.
- Ezoe, Yuichiro, Takaya Ohashi, and Kazuhisa Mitsuda (2021). "High-resolution X-ray spectroscopy of astrophysical plasmas with X-ray microcalorimeters". In: *Reviews of Modern Plasma Physics* 5.1, pp. 1–43.
- Ezoe, Yuichiro et al. (2006b). "Investigation of diffuse hard X-ray emission from the massive star-forming region NGC 6334". In: *The Astrophysical Journal* 638.2, p. 860.
- Ezoe, Yuichiro et al. (2009). "Suzaku and XMM-Newton observations of diffuse X-ray emission from the eastern tip region of the Carina Nebula". In: *Publications of the Astronomical Society of Japan* 61.sp1, S123–S136.
- Ezoe, Yuichiro et al. (2019). "Suzaku observation of diffuse X-ray emission from a southwest region of the Carina Nebula". In: *Publications of the Astronomical Society of Japan* 71.6, p. 122.
- Feigelson, Eric D and Thierry Montmerle (1999). "High-energy processes in young stellar objects". In: *Annual Review of Astronomy and Astrophysics* 37.1, pp. 363–408.
- Feigelson, Eric D et al. (2002). "X-ray-emitting young stars in the Orion nebula". In: *The Astrophysical Journal* 574.1, p. 258.
- Feigelson, Eric D et al. (2005). "Global X-ray properties of the Orion Nebula region". In: *The Astrophysical Journal Supplement Series* 160.2, p. 379.
- Feinstein, A, MP Fitzgerald, and AFJ Moffat (1980). "The young open cluster Trumpler 15 in the Eta Carinae complex". In: *The Astronomical Journal* 85, pp. 708–715.
- Feldmeier, Achim, J Puls, and AWA Pauldrach (1997). "A possible origin for X-rays from O stars." In: *Astronomy and Astrophysics* 322, pp. 878–895.
- Ferriere, Katia M (2001). "The interstellar environment of our galaxy". In: *Reviews of Modern Physics* 73.4, p. 1031.
- Field, GB, DW Goldsmith, and HJ Habing (1969). "Cosmic-ray heating of the interstellar gas". In: *The Astrophysical Journal* 155, p. L149.

- Forman, W et al. (1978). "The fourth Uhuru catalog of X-ray sources." In: *The Astrophysical Journal Supplement Series* 38, pp. 357–412.
- Freeman, Peter E et al. (2002). "A wavelet-based algorithm for the spatial analysis of Poisson data". In: *The Astrophysical Journal Supplement Series* 138.1, p. 185.
- Frogel, Jay A and S Eric Persson (1974). "Compact infrared sources associated with southern H II regions". In: *The Astrophysical Journal* 192, pp. 351–368.
- Fujita, Yutaka et al. (2009). "Suzaku Observation of Diffuse X-Ray Emission from the Open Cluster Westerlund 2: a Hypernova Remnant?" In: *Publications of the Astronomical Society of Japan* 61.6, pp. 1229–1235.
- Fukui, Y et al. (2016). "THE TWO MOLECULAR CLOUDS IN RCW 38: EVIDENCE FOR THE FORMATION OF THE YOUNGEST SUPER STAR CLUSTER IN THE MILKY WAY TRIGGERED BY CLOUD–CLOUD COLLISION". In: *The Astrophysical Journal* 820.1, p. 26.
- Fukui, Yasuo et al. (2009). "A peculiar jet and arc of molecular gas toward the rich and young stellar cluster westerlund 2 and a TeV gamma ray source". In: *Publications of the Astronomical Society of Japan* 61.4, pp. L23–L27.
- Fukui, Yasuo et al. (2018). "Molecular clouds in the NGC 6334 and NGC 6357 region: Evidence for a 100 pc-scale cloud–cloud collision triggering the Galactic mini-starbursts". In: *Publications of the Astronomical Society of Japan* 70.SP2, S41.
- Furukawa, Naoko et al. (2009). "Molecular clouds toward RCW49 and Westerlund 2: evidence for cluster formation triggered by cloud–cloud collision". In: *The Astrophysical Journal* 696.2, p. L115.
- Garmire, Gordon P et al. (2003). "Advanced CCD imaging spectrometer (ACIS) instrument on the Chandra X-ray Observatory". In: *X-Ray and Gamma-Ray Telescopes and Instruments for Astronomy*. Vol. 4851. SPIE, pp. 28–44.
- Getman, Konstantin V et al. (2002). "Chandra study of young stellar objects in the NGC 1333 star-forming cloud". In: *The Astrophysical Journal* 575.1, p. 354.
- Getman, Konstantin V et al. (2005). "Chandra Orion Ultradeep Project: observations and source lists". In: *The Astrophysical Journal Supplement Series* 160.2, p. 319.
- Getman, Konstantin V et al. (2006). "Chandra study of the cepheus B star-forming region: Stellar populations and the initial mass function". In: *The Astrophysical Journal Supplement Series* 163.2, p. 306.
- Getman, Konstantin V et al. (2014). "Age gradients in the stellar populations of massive star forming regions based on a new stellar chronometer". In: *The Astrophysical Journal* 787.2, p. 108.

- Giacconi, R et al. (1974). "The third UHURU catalog of X-ray sources". In: *The Astrophysical Journal Supplement Series* 27, p. 37.
- Giacconi, R et al. (1979). "The Einstein/HEAO 2/x-ray observatory". In: *The Astrophysical Journal* 230, pp. 540–550.
- Giacconi, Riccardo et al. (1962). "Evidence for x rays from sources outside the solar system". In: *Physical Review Letters* 9.11, p. 439.
- Goldsmith, Donald (2001). *Search for Life in the Universe, 3rd Ed.*
- Greene, Thomas P et al. (1994). "Further mid-infrared study of the rho Ophiuchi cloud young stellar population: Luminosities and masses of pre-main-sequence stars". In: *The Astrophysical Journal* 434, pp. 614–626.
- Güdel, Manuel and Yaël Nazé (2009). "X-ray spectroscopy of stars". In: *The Astronomy and Astrophysics Review* 17.3, pp. 309–408.
- Güdel, Manuel et al. (2007). "The XMM-Newton extended survey of the Taurus molecular cloud (XEST)". In: *Astronomy & Astrophysics* 468.2, pp. 353–377.
- Güdel, Manuel et al. (2008). "Million-degree plasma pervading the extended Orion nebula". In: *Science* 319.5861, pp. 309–312.
- Habets, GMHJ and JRW Heintze (1981). "Empirical bolometric corrections for the main-sequence". In: *Astronomy and Astrophysics Supplement Series* 46, pp. 193–237.
- Habing, HJ and FP Israel (1979). "Compact H II regions and OB star formation". In: *Annual Review of Astronomy and Astrophysics* 17, pp. 345–385.
- Hamaguchi, K, Y Tsuboi, and K Koyama (2000). "Hard X-ray detection from the core of the Monoceros R2 star forming region". In: *Advances in Space Research* 25.3-4, pp. 531–534.
- Hamaguchi, Kenji et al. (2001). "Magnetic activities on young stars". In: *Earth, planets and space* 53.6, pp. 683–687.
- Hamaguchi, Kenji et al. (2007). "Suzaku observation of diffuse X-ray emission from the Carina Nebula". In: *Publications of the Astronomical Society of Japan* 59.sp1, S151–S161.
- Hamaguchi, Kenji et al. (2018). "Non-thermal X-rays from colliding wind shock acceleration in the massive binary Eta Carinae". In: *Nature Astronomy* 2.9, pp. 731–736.
- Hans, Wolter (1952). "Spiegelsysteme streifenden Einfalls als abbildende Optiken für Röntgenstrahlen". In: *Annalen der Physik* 445.1-2, pp. 94–114.
- Hanson, MM, ID Howarth, and PS Conti (1997). "The young massive stellar objects of M17". In: *The Astrophysical Journal* 489.2, p. 698.

- Hau, George KT et al. (2008). "Is NGC 3108 transforming itself from an early- to late-type galaxy—an astronomical hermaphrodite?" In: *Monthly Notices of the Royal Astronomical Society* 385.4, pp. 1965–1972.
- Hayashi, Chushiro (1961). "Stellar evolution in early phases of gravitational contraction." In: *Publications of the Astronomical Society of Japan* 13.
- Hearnshaw, John B (1990). *The analysis of starlight: one hundred and fifty years of astronomical spectroscopy*. CUP Archive.
- Heger, Alexander et al. (2003). "How massive single stars end their life". In: *The Astrophysical Journal* 591.1, p. 288.
- Heney, LG, Robert Lelevier, and RD Levée (1955). "The early phases of stellar evolution". In: *Publications of the Astronomical Society of the Pacific* 67.396, pp. 154–160.
- Herbst, Eric (1995). "Chemistry in the interstellar medium". In: *Annual Review of Physical Chemistry* 46.1, pp. 27–54.
- Heyer, Mark and TM Dame (2015). "Molecular clouds in the Milky Way". In: *Annual Review of Astronomy and Astrophysics* 53, pp. 583–629.
- Hillier, DJ et al. (1993). "The 0.1-2.5-KEV X-Ray Spectrum of the O4F-STAR Zeta-Puppis". In: *Astronomy and Astrophysics* 276, p. 117.
- Hiraga, Junko S et al. (2009). "Search for Sc-K Line Emission from RX J0852.0 4622 Supernova Remnant with Suzaku". In: *Publications of the Astronomical Society of Japan* 61.2, pp. 275–281.
- Hofner, Peter and Ed Churchwell (1997). "Hard X-ray emission from the W3 core". In: *The Astrophysical Journal* 486.1, p. L39.
- Horan, Deirdre and S Wakely (2008). "TeVCat: An Online Catalog for TeV Astronomy". In: *AAS/High Energy Astrophysics Division# 10* 10, pp. 41–06.
- Hosokawa, Takashi, Harold W Yorke, and Kazuyuki Omukai (2010). "Evolution of massive protostars via disk accretion". In: *The Astrophysical Journal* 721.1, p. 478.
- Hyodo, Yoshiaki et al. (2008). "Suzaku Spectroscopy of Extended X-Ray Emission in M17". In: *Publications of the Astronomical Society of Japan* 60.sp1, S85–S93.
- Imanishi, Kensuke (Mar. 2003). "X-ray Study of Low-mass Young Stellar Objects in the ρ Ophiuchi Star-forming Region with". PhD thesis. Kyoto University.
- Imanishi, Kensuke, Katsuji Koyama, and Yohko Tsuboi (2001). "Chandra observation of the ρ Ophiuchi cloud". In: *The Astrophysical Journal* 557.2, p. 747.

- Imanishi, Kensuke, Masahiro Tsujimoto, and Katsuji Koyama (2001). "X-ray detection from Bona fide and candidate brown dwarfs in the ρ Ophiuchi cloud with Chandra". In: *The Astrophysical Journal* 563.1, p. 361.
- Ishisaki, Yoshitaka et al. (2007). "Monte Carlo simulator and ancillary response generator of Suzaku XRT/XIS system for spatially extended source analysis". In: *Publications of the Astronomical Society of Japan* 59.sp1, S113–S132.
- Jansen, F et al. (2001). "XMM-Newton observatory-I. The spacecraft and operations". In: *Astronomy & Astrophysics* 365.1, pp. L1–L6.
- Jeans, James Hopwood (1902). "I. The stability of a spherical nebula". In: *Philosophical Transactions of the Royal Society of London. Series A, Containing Papers of a Mathematical or Physical Character* 199.312-320, pp. 1–53.
- Kelley, Richard L et al. (2007). "The Suzaku high resolution x-ray spectrometer". In: *Publications of the Astronomical Society of Japan* 59.sp1, S77–S112.
- Kirkpatrick, J Davy (2005). "New spectral types L and T". In: *Annual Review of Astronomy and Astrophysics* 43, pp. 195–245.
- Kitamoto, Shunji and Koji Mukai (1996). "ASCA observation of Cygnus OB2 association". In: *Publications of the Astronomical Society of Japan* 48.6, pp. 813–818.
- Kohno, M, K Koyama, and K Hamaguchi (2002). "Chandra observations of high-mass young stellar objects in the Monoceros R2 molecular cloud". In: *The Astrophysical Journal* 567.1, p. 423.
- Koyama, Katsuji et al. (1990). "Hard X-ray emission from the Carina Nebula". In: *The Astrophysical Journal* 362, pp. 215–218.
- Koyama, Katsuji et al. (1995). "Evidence for shock acceleration of high-energy electrons in the supernova remnant SN1006". In: *Nature* 378.6554, pp. 255–258.
- Koyama, Katsuji et al. (2007). "X-ray imaging spectrometer (XIS) on board Suzaku". In: *Publications of the Astronomical Society of Japan* 59.sp1, S23–S33.
- Kraus, Stefan et al. (2010). "A hot compact dust disk around a massive young stellar object". In: *Nature* 466.7304, pp. 339–342.
- Kroupa, Pavel (2001). "On the variation of the initial mass function". In: *Monthly Notices of the Royal Astronomical Society* 322.2, pp. 231–246.
- Krumholz, Mark R et al. (2009). "The formation of massive star systems by accretion". In: *Science* 323.5915, pp. 754–757.
- Ku, WH-M and GA Chanan (1979). "Einstein observations of the Orion Nebula". In: *The Astrophysical Journal* 234, pp. L59–L63.
- Kudritzki, Rolf-Peter and Joachim Puls (2000). "Winds from hot stars". In: *Annual Review of Astronomy and Astrophysics* 38.1, pp. 613–666.

- Kuhn, Michael A, Konstantin V Getman, and Eric D Feigelson (2015). "The spatial structure of young stellar clusters. II. Total young stellar populations". In: *The Astrophysical Journal* 802.1, p. 60.
- Kuhn, Michael A et al. (2010). "A Chandra observation of the obscured star-forming complex W40". In: *The Astrophysical Journal* 725.2, p. 2485.
- Kuiper, Rolf et al. (2010). "Circumventing the radiation pressure barrier in the formation of massive stars via disk accretion". In: *The Astrophysical Journal* 722.2, p. 1556.
- Kurtz, S. (Oct. 2002). "Ultracompact HII Regions". In: *Hot Star Workshop III: The Earliest Phases of Massive Star Birth*. Ed. by P. Crowther. Vol. 267. Astronomical Society of the Pacific Conference Series, p. 81. arXiv: [astro-ph/0111351](https://arxiv.org/abs/astro-ph/0111351) [astro-ph].
- Kurtz, Stan (2005). "Hypercompact HII regions". In: *Proceedings of the International Astronomical Union* 1.S227, pp. 111–119.
- Kurtz, STAN et al. (2000). "Hot molecular cores and the earliest phases of high-mass star formation". In: *Protostars and Planets IV* 299.
- Kushino, Akihiro et al. (2002). "Study of the X-ray background spectrum and its large-scale fluctuation with ASCA". In: *Publications of the Astronomical Society of Japan* 54.3, pp. 327–352.
- Lada, Charles J and Elizabeth A Lada (2003). "Embedded clusters in molecular clouds". In: *Annual Review of Astronomy and Astrophysics* 41.1, pp. 57–115.
- Lada, Charles J and BA Wilking (1984). "The nature of the embedded population in the Rho Ophiuchi dark cloud-Mid-infrared observations". In: *The Astrophysical Journal* 287, pp. 610–621.
- Lallement, R (2004). "The heliospheric soft X-ray emission pattern during the ROSAT survey: Inferences on Local Bubble hot gas". In: *Astronomy & Astrophysics* 418.1, pp. 143–150.
- Larson, Richard B (2003). "The physics of star formation". In: *Reports on Progress in Physics* 66.10, p. 1651.
- Leahy, DA (1985). "Einstein observations of the Rosette nebula and the Mon OB2 association". In: *Monthly Notices of the Royal Astronomical Society* 217.1, pp. 69–75.
- Ledrew, Glenn (2001). "The real starry sky". In: *Journal of the Royal Astronomical Society of Canada* 95, p. 32.

- Licquia, Timothy C and Jeffrey A Newman (2015). "Improved estimates of the Milky Way's stellar mass and star formation rate from hierarchical Bayesian meta-analysis". In: *The Astrophysical Journal* 806.1, p. 96.
- Lucy, L B_ and RL White (1980). "X-ray emission from the winds of hot stars". In: *The Astrophysical Journal* 241, pp. 300–305.
- Lucy, LB (1982). "X-ray emission from the winds of hot stars. II". In: *The Astrophysical Journal* 255, pp. 286–292.
- Madau, Piero and Mark Dickinson (2014). "Cosmic star formation history". In: *arXiv preprint arXiv:1403.0007*.
- Maeda, Keiichi and Yukikatsu Terada (2016). "Progenitors of type Ia supernovae". In: *International Journal of Modern Physics D* 25.10, p. 1630024.
- Maeder, André and Georges Meynet (1987). "Grids of evolutionary models of massive stars with mass loss and overshooting-Properties of Wolf-Rayet stars sensitive to overshooting". In: *Astronomy and Astrophysics* 182, pp. 243–263.
- McKee, Christopher F and Jonathan C Tan (2003). "The formation of massive stars from turbulent cores". In: *The Astrophysical Journal* 585.2, p. 850.
- Mewe, R et al. (2003). "High-resolution XMM-Newton X-ray spectra of τ SCOR-PII". In: *Advances in Space Research* 32.6, pp. 1167–1173.
- Miller, Glenn E and John M Scalo (1979). "The initial mass function and stellar birthrate in the solar neighborhood". In: *The Astrophysical Journal Supplement Series* 41, pp. 513–547.
- Miller, NA et al. (2002). "New challenges for wind shock models: the Chandra spectrum of the hot star δ Orionis". In: *The Astrophysical Journal* 577.2, p. 951.
- Mitsuda, Kazuhisa et al. (2007). "The X-ray observatory Suzaku". In: *Publications of the Astronomical Society of Japan* 59.sp1, S1–S7.
- Miyaji, T et al. (1998). "The cosmic X-ray background spectrum observed with ROSAT and ASCA". In: *arXiv preprint astro-ph/9803320*.
- Mizuno, Tsunefumi et al. (2004). "Cosmic-ray background flux model based on a gamma-ray large area space telescope balloon flight engineering model". In: *The Astrophysical Journal* 614.2, p. 1113.
- Moffat, AFJ et al. (2002). "Galactic Starburst NGC 3603 from X-rays to Radio". In: *The Astrophysical Journal* 573.1, p. 191.
- Morgan, William Wilson and Philip Childs Keenan (1973). "Spectral classification". In: *Annual Review of Astronomy and Astrophysics* 11, p. 29.
- Morgan, WW, Philip C Keenan, and Edith Kellman (1943). *An atlas of stellar spectra*. Vol. 5. Chicago: University of Chicago Press.

- Muno, Michael P et al. (2006). "Diffuse, nonthermal X-ray emission from the galactic star cluster Westerlund 1". In: *The Astrophysical Journal* 650.1, p. 203.
- Muzzio, JC (1979). "Photometric study of faint early-type stars in the southern Milky Way". In: *The Astronomical Journal* 84, pp. 639–649.
- Myers, Andrew T et al. (2013). "The fragmentation of magnetized, massive star-forming cores with radiative feedback". In: *The Astrophysical Journal* 766.2, p. 97.
- Nakajima, Hiroshi et al. (2003). "X-ray observation on the Monoceros R2 star-forming region with the Chandra ACIS-I array". In: *Publications of the Astronomical Society of Japan* 55.3, pp. 635–651.
- Nakajima, Hiroshi et al. (2008). "Performance of the charge-injection capability of Suzaku XIS". In: *Publications of the Astronomical Society of Japan* 60.sp1, S1–S9.
- Neckel, Th (1978). "UBV, VRI and H β observations of stars in the H II regions NGC 6334 and NGC 6357". In: *Astronomy and Astrophysics* 69, pp. 51–56.
- Nishimura, Atsushi et al. (2018). "FOREST Unbiased Galactic plane Imaging survey with the Nobeyama 45 m telescope (FUGIN). III. Possible evidence for formation of NGC 6618 cluster in M 17 by cloud–cloud collision". In: *Publications of the Astronomical Society of Japan* 70.SP2, S42.
- Ohama, Akio et al. (2010). "Temperature and density distribution in the molecular gas toward westerlund 2: Further evidence for physical association". In: *The Astrophysical Journal* 709.2, p. 975.
- Palla, Francesco and Steven W Stahler (1993). "The pre-main-sequence evolution of intermediate-mass stars". In: *The Astrophysical Journal* 418, p. 414.
- (1999). "Star formation in the Orion nebula cluster". In: *The Astrophysical Journal* 525.2, p. 772.
- Pallavicini, R et al. (1981). "Relations among stellar X-ray emission observed from Einstein, stellar rotation and bolometric luminosity". In: *The Astrophysical Journal* 248, pp. 279–290.
- Parizot, E et al. (2004). "Superbubbles and energetic particles in the Galaxy-I. Collective effects of particle acceleration". In: *Astronomy & Astrophysics* 424.3, pp. 747–760.
- Parker, E. N. (Sept. 1966). "The Dynamical State of the Interstellar Gas and Field". In: *The Astrophysical Journal* 145, p. 811. DOI: [10.1086/148828](https://doi.org/10.1086/148828).
- Persi, P and M Tapia (2008). "Star Formation in NGC 6334". In: *Handbook of Star Forming Regions, Volume II* 5, p. 456.

- Piatti, AE, E Bica, and JJ Claria (1998). "Fundamental parameters of the highly reddened young open clusters Westerlund 1 and 2". In: *Astronomy and Astrophysics Supplement Series* 127.3, pp. 423–432.
- Pizzolato, N et al. (2003). "The stellar activity-rotation relationship revisited: Dependence of saturated and non-saturated X-ray emission regimes on stellar mass for late-type dwarfs". In: *Astronomy & Astrophysics* 397.1, pp. 147–157.
- Porquet, D et al. (2001). "Line ratios for helium-like ions: Applications to collision-dominated plasmas". In: *Astronomy & Astrophysics* 376.3, pp. 1113–1122.
- Povich, Matthew S et al. (2009). "The Extended Environment of M17: A Star Formation History". In: *The Astrophysical Journal* 696.2, p. 1278.
- Preibisch, Thomas and Hans Zinnecker (2001). "Deep Chandra X-ray observatory imaging study of the very young stellar cluster IC 348". In: *The Astronomical Journal* 122.2, p. 866.
- (2002). "X-ray properties of the young stellar and substellar objects in the IC 348 cluster: the Chandra view". In: *The Astronomical Journal* 123.3, p. 1613.
- Preibisch, Thomas et al. (2005). "The origin of T Tauri X-ray emission: new insights from the Chandra Orion Ultradeep Project". In: *The Astrophysical Journal Supplement Series* 160.2, p. 401.
- Principe, DA et al. (2017). "The multiple young stellar objects of HBC 515: An X-ray and millimeter-wave imaging study in (pre-main sequence) diversity". In: *Astronomy & Astrophysics* 598, A8.
- Prinja, RK (1990). "Similarities in the wind characteristics of hot stars". In: *Astronomy and Astrophysics* 232, pp. 119–125.
- Puls, J, SP Owocki, and AW Fullerton (1993). "On the synthesis of resonance lines in dynamical models of structured hot-star winds". In: *Astronomy and Astrophysics* 279, pp. 457–476.
- Randich, S et al. (1996). "The X-ray properties of the young open cluster around alpha Persei." In: *Astronomy and Astrophysics* 305, p. 785.
- Rauw, Grégor et al. (2002). "An-observation of the Lagoon Nebula and the very young open cluster NGC 6530". In: *Astronomy & Astrophysics* 395.2, pp. 499–513.
- Rauw, Grégor et al. (2007). "Early-type stars in the core of the young open cluster Westerlund 2". In: *Astronomy & Astrophysics* 463.3, pp. 981–991.
- Raymond, John C and Barham W Smith (1977). "Soft X-ray spectrum of a hot plasma". In: *Astrophysical Journal Supplement Series*, vol. 35, Dec. 1977, p. 419–439. *Research supported by the University of Wisconsin*; 35, pp. 419–439.

- Rybicki, George B and Alan P Lightman (1991). *Radiative processes in astrophysics*. John Wiley & Sons.
- Rybicki, George B. and Alan Paige Lightman (1979). *Radiative processes in astrophysics*. J. Wiley and sons.
- Ryter, Ch E (1996). "Interstellar extinction from infrared to X-rays: an overview". In: *Astrophysics and Space Science* 236.2, pp. 285–291.
- Salpeter, Edwin E (1955). "The luminosity function and stellar evolution." In: *The Astrophysical Journal* 121, p. 161.
- Sana, Hugues et al. (2006). "An XMM–Newton view of the young open cluster NGC 6231–II. The OB star population". In: *Monthly Notices of the Royal Astronomical Society* 372.2, pp. 661–678.
- Sana, Hugues et al. (2010). "A MAD view of Trumpler 14". In: *Astronomy & Astrophysics* 515, A26.
- Scalo, John (Jan. 1998). "The IMF Revisited: A Case for Variations". In: *The Stellar Initial Mass Function (38th Herstmonceux Conference)*. Ed. by Gary Gilmore and Debbie Howell. Vol. 142. Astronomical Society of the Pacific Conference Series, p. 201. arXiv: [astro-ph/9712317](https://arxiv.org/abs/astro-ph/9712317) [astro-ph].
- Scalo, John M (1986). "The stellar initial mass function". In: *Fundamentals of cosmic physics* 11, pp. 1–278.
- Schmitt, JHMM et al. (1990). "Einstein Observatory coronal temperatures of late-type stars". In: *The Astrophysical Journal* 365, pp. 704–728.
- Schrijver, CJ, R Mewe, and FM Walter (1984). "Coronal activity in F-, G-, and K-type stars. II-Coronal structure and rotation". In: *Astronomy and Astrophysics* 138, pp. 258–266.
- Schulz, Norbert S et al. (2003). "X-ray modeling of very young early-type stars in the Orion Trapezium: signatures of magnetically confined plasmas and evolutionary implications". In: *The Astrophysical Journal* 595.1, p. 365.
- Schulz, NS et al. (2000). "X-ray line emission from the hot stellar wind of θ 1 Orionis C". In: *The Astrophysical Journal* 545.2, p. L135.
- Sciortino, S (2008). "Results and perspectives of young stellar object long look programs". In: *Astronomische Nachrichten* 329.2, pp. 214–217.
- Sekimoto, Yutaro et al. (2000). "Hard X-ray emission from massive star clusters in a giant molecular cloud NGC 6334". In: *Publications of the Astronomical Society of Japan* 52.5, pp. L31–L35.
- Serlemitsos, Peter J and Yang Soong (1996). "Foil X-ray mirrors". In: *Astrophysics and Space Science* 239.2, pp. 177–196.

- Serlemitsos, Peter J et al. (1995). "The X-ray telescope on board ASCA". In: *Publications of the Astronomical Society of Japan* 47, pp. 105–114.
- Serlemitsos, Peter J et al. (2007). "The x-ray telescope onboard Suzaku". In: *Publications of the Astronomical Society of Japan* 59.sp1, S9–S21.
- Seward, FD and T Chlebowski (1982). "X-ray emission from the Carina Nebula and the associated early stars". In: *The Astrophysical Journal* 256, pp. 530–542.
- Skinner, Stephen L, Kimberly R Sokal, and Manuel Güdel (2019). "Chandra Observations of the Massive Star-forming Region Onsala 2". In: *The Astrophysical Journal* 871.1, p. 116.
- Smith, Craig H et al. (1999). "Mid-infrared imaging and spectroscopy of the southern HII region RCW 38". In: *Monthly Notices of the Royal Astronomical Society* 303.2, pp. 367–379.
- Smith, Nathan (2006a). "Erratum: A census of the Carina Nebula–I. Cumulative energy input from massive stars". In: *Monthly Notices of the Royal Astronomical Society* 368.4, pp. 1983–1984.
- (2006b). "The structure of the Homunculus. I. Shape and latitude dependence from H2 and [Fe II] velocity maps of η Carinae". In: *The Astrophysical Journal* 644.2, p. 1151.
- Smith, Nathan and Kate J Brooks (2008). "The Carina Nebula: A Laboratory for Feedback and Triggered Star Formation". In: *arXiv preprint arXiv:0809.5081*.
- Snowden, SL et al. (1998). "Progress on establishing the spatial distribution of material responsible for the 1/4 keV soft X-ray diffuse background local and halo components". In: *The Astrophysical Journal* 493.2, p. 715.
- Spitzer, Lyman (1978). *Physical processes in the interstellar medium*. New York: Wiley Interscience. DOI: [10.1002/9783527617722](https://doi.org/10.1002/9783527617722).
- Stahler, Steven W (1988). "Understanding young stars: a history". In: *Publications of the Astronomical Society of the Pacific* 100.634, p. 1474.
- Stelzer, B et al. (2007). "A statistical analysis of X-ray variability in pre-main sequence objects of the Taurus molecular cloud". In: *Astronomy & Astrophysics* 468.2, pp. 463–475.
- Strom, Karen M et al. (1989). "Circumstellar material associated with solar-type pre-main-sequence stars–A possible constraint on the timescale for planet building". In: *The Astronomical Journal* 97, pp. 1451–1470.
- Strömgren, Bengt (2013). "86. The Physical State of Interstellar Hydrogen". In: *A Source Book in Astronomy and Astrophysics, 1900–1975*. Harvard University Press, pp. 588–592.

- Suzuki, Takeru K et al. (2013). "Saturation of Stellar Winds from Young Suns". In: *Publications of the Astronomical Society of Japan* 65.5, pp. 98–98.
- Tak, FFS Van der (2004). "Hot molecular cores and high mass star formation". In: *Symposium-International Astronomical Union*. Vol. 221. Cambridge University Press, pp. 59–66.
- Takahashi, Tadayuki et al. (2007). "Hard X-ray detector (HXD) on board Suzaku". In: *Publications of the Astronomical Society of Japan* 59.sp1, S35–S51.
- Takeda, Sawako et al. (2016). "Suzaku observations of the hard X-ray spectrum of Vela Jr.(SNR RX J0852. 0- 4622)". In: *Publications of the Astronomical Society of Japan* 68.SP1, S10.
- Tanaka, Kei EI and Taishi Nakamoto (2011). "Direct Stellar Radiation Pressure at the Dust Sublimation Front in Massive Star Formation: Effects of a Dust-free Disk". In: *The Astrophysical Journal Letters* 739.2, p. L50.
- Tanaka, Yasuo, Hajime Inoue, and Stephen S Holt (1994). "The X-ray astronomy satellite ASCA". In: *Publications of the Astronomical Society of Japan* 46, pp. L37–L41.
- Tawa, Noriaki et al. (2008). "Reproducibility of non-X-ray background for the X-ray imaging spectrometer aboard Suzaku". In: *Publications of the Astronomical Society of Japan* 60.sp1, S11–S24.
- Telleschi, Alessandra et al. (2005). "Coronal evolution of the Sun in time: high-resolution X-ray spectroscopy of solar analogs with different ages". In: *The Astrophysical Journal* 622.1, p. 653.
- Telleschi, Alessandra et al. (2007). "X-ray emission from T Tauri stars and the role of accretion: inferences from the XMM-Newton extended survey of the Taurus molecular cloud". In: *Astronomy & Astrophysics* 468.2, pp. 425–442.
- Townsley, Leisa K (2009). "An x-ray tour of massive star-forming regions with Chandra". In: *Massive Stars from Pop III and GRBs to the Milky Way*, pp. 60–73.
- Townsley, Leisa K et al. (2003). "10 MK gas in M17 and the Rosette nebula: X-ray flows in galactic H ii regions". In: *The Astrophysical Journal* 593.2, p. 874.
- Townsley, Leisa K et al. (2006). "A Chandra ACIS study of 30 Doradus. I. Superbubbles and supernova remnants". In: *The Astronomical Journal* 131.4, p. 2140.
- Townsley, Leisa K et al. (2011a). "An introduction to the chandra carina complex project". In: *The Astrophysical Journal Supplement Series* 194.1, p. 1.
- Townsley, Leisa K et al. (2011b). "The Chandra Carina Complex Project: Deciphering the enigma of Carina's diffuse X-ray emission". In: *The Astrophysical Journal Supplement Series* 194.1, p. 15.

- Townsley, Leisa K et al. (2011c). "The integrated diffuse X-ray emission of the Carina Nebula compared to other massive star-forming regions". In: *The Astrophysical Journal Supplement Series* 194.1, p. 16.
- Townsley, LK et al. (2005). "Parsec-scale X-ray flows in high-mass star-forming regions". In: *Proceedings of the International Astronomical Union* 1.S227, pp. 297–302.
- Tsuboi, Yohko et al. (1997). "ASCA observations of Eta Carinae". In: *Publications of the Astronomical Society of Japan* 49.1, pp. 85–92.
- Tsujimoto, M et al. (2006). "Hard x-rays from ultracompact H II regions in w49a". In: *The Astrophysical Journal* 653.1, p. 409.
- Tsujimoto, Masahiro et al. (2002). "X-ray Properties of Young Stellar Objects in OMC-2 and OMC-3 from the Chandra X-ray Observatory". In: *The Astrophysical Journal* 566.2, p. 974.
- Tsujimoto, Masahiro et al. (2011). "Cross-calibration of the X-ray instruments on-board the Chandra, INTEGRAL, RXTE, Suzaku, Swift, and XMM-Newton observatories using G21. 5–0.9". In: *Astronomy & Astrophysics* 525, A25.
- Turner, Barry E (1988). "Molecules as probes of the interstellar medium and of star formation". In: *Galactic and Extragalactic Radio Astronomy*. Springer, pp. 154–199.
- Uchiyama, Hideki et al. (2009). "New CTI correction method for spaced-row charge injection of the Suzaku x-ray imaging spectrometer". In: *Publications of the Astronomical Society of Japan* 61.sp1, S9–S15.
- Vink, Jorick S, Alex de Koter, and HJGLM Lamers (2001). "Mass-loss predictions for O and B stars as a function of metallicity". In: *Astronomy & Astrophysics* 369.2, pp. 574–588.
- Waldron, Wayne L and Joseph P Cassinelli (2001). "Chandra discovers a very high density X-ray plasma on the O star ζ Orionis". In: *The Astrophysical Journal* 548.1, p. L45.
- Walter, FM (1981). "On the coronae of rapidly rotating stars. II-A period-activity relation in G stars". In: *The Astrophysical Journal* 245, pp. 677–681.
- Wang, Peng et al. (2009). "Outflow feedback regulated massive star formation in parsec-scale cluster-forming clumps". In: *The Astrophysical Journal* 709.1, p. 27.
- Wang, Q Daniel, Hui Dong, and Cornelia Lang (2006). "The interplay between star formation and the nuclear environment of our Galaxy: deep X-ray observations of the Galactic centre Arches and Quintuplet clusters". In: *Monthly Notices of the Royal Astronomical Society* 371.1, pp. 38–54.

- Weaver, ROBERT et al. (1977). "Interstellar bubbles. II-Structure and evolution". In: *The Astrophysical Journal* 218, pp. 377–395.
- Weidner, Carsten and JS Vink (2010). "The masses, and the mass discrepancy of O-type stars". In: *Astronomy & Astrophysics* 524, A98.
- Weisskopf, MC et al. (2002). "An overview of the performance and scientific results from the Chandra X-Ray Observatory". In: *Publications of the Astronomical Society of the Pacific* 114.791, p. 1.
- Whiteoak, JBZ and KI Uchida (1997). "High-resolution radio observations of RCW 49." In: *Astronomy and Astrophysics* 317, pp. 563–568.
- Williams, Jonathan P, Leo Blitz, and Christopher F McKee (1999). "The structure and evolution of molecular clouds: from clumps to cores to the IMF". In: *arXiv preprint astro-ph/9902246*.
- Williams, Rik J, Smita Mathur, and Fabrizio Nicastro (2005). "Galactic Corona or Local Group Intergalactic Medium?" In: *arXiv preprint astro-ph/0511621*.
- Winston, Elaine et al. (2011). "The structure of the star-forming cluster RCW 38". In: *The Astrophysical Journal* 743.2, p. 166.
- Wolfire, Mark G and Joseph P Cassinelli (1987). "Conditions for the formation of massive stars". In: *The Astrophysical Journal* 319, pp. 850–867.
- Wolk, Scott J et al. (2002). "Discovery of Nonthermal X-Ray Emission from the Embedded Massive Star-forming Region RCW 38". In: *The Astrophysical Journal* 580.2, p. L161.
- Wolk, Scott J et al. (2006). "X-ray and infrared point source identification and characteristics in the embedded, massive star-forming region RCW 38". In: *The Astronomical Journal* 132.3, p. 1100.
- Wolk, Scott J et al. (2008). "X-ray and IR point source identification and characteristics in the embedded, massive star-forming region RCW 108". In: *The Astronomical Journal* 135.2, p. 693.
- Wood, Douglas OS and Ed Churchwell (1989). "The morphologies and physical properties of ultracompact H II regions". In: *The Astrophysical Journal Supplement Series* 69, pp. 831–895.
- Yamauchi, Shigeo et al. (1996). "Broad-band X-ray observations of the Orion region with ASCA". In: *Publications of the Astronomical Society of Japan* 48.5, pp. 719–737.
- Yang, Hui et al. (1996). "The violent interstellar medium of ngc 604". In: *The Astronomical Journal* 112, p. 146.

- Yorke, Harold W and Peter Bodenheimer (1999). "The formation of protostellar disks. III. The influence of gravitationally induced angular momentum transport on disk structure and appearance". In: *The Astrophysical Journal* 525.1, p. 330.
- Yoshino, Tomotaka et al. (2009). "Energy spectra of the soft x-ray diffuse emission in fourteen fields observed with Suzaku". In: *Publications of the Astronomical Society of Japan* 61.4, pp. 805–823.
- Yusef-Zadeh, F et al. (2002). "Detection of X-ray emission from the Arches cluster near the Galactic center". In: *The Astrophysical Journal* 570.2, p. 665.
- Zhang, Han (Jan. 2018). "Mid-infrared polarimetry: Insights into magnetic fields and dust grain properties in young stellar objects and protoplanetary disks". PhD thesis. University of Florida.
- Zhekov, Svetozar A and Francesco Palla (2007). "X-rays from massive OB stars: thermal emission from radiative shocks". In: *Monthly Notices of the Royal Astronomical Society* 382.3, pp. 1124–1132.
- Zinnecker, H and Th Preibisch (1994). "X-ray emission from Herbig Ae/Be stars: a ROSAT survey". In: *Astronomy and Astrophysics* 292, pp. 152–164.
- Zinnecker, Hans and Harold W Yorke (2007). "Toward understanding massive star formation". In: *Annu. Rev. Astron. Astrophys.* 45, pp. 481–563.